

UNIVERSITÀ DEGLI STUDI DI PADOVA



DIPARTIMENTO DI INGEGNERIA INDUSTRIALE

Scuola di Dottorato di Ricerca in
Scienza e Ingegneria dei Materiali
Ciclo XXV

Innovative Materials and Systems for Solid State Hydrogen Storage

Direttore della Scuola:
Ch.mo Prof. Gaetano Granozzi

Supervisore:
Ch.mo Prof. Amedeo Maddalena

Cosupervisore:
Ch.mo Prof. Giovanni Principi


Dottorando:
Giovanni Capurso

Innovative Materials and Systems for Solid State Hydrogen Storage

Giovanni Capurso


PhD Thesis

UNIVERSITY OF PADOVA - DEPARTMENT OF INDUSTRIAL ENGINEERING
MATERIAL SCIENCE AND ENGINEERING DOCTORAL SCHOOL
Innovative Materials and Systems for Solid State Hydrogen Storage
Giovanni Capurso (<mailto:giovanni.capurso@gmail.com>)
January 2013

Typeset using L^AT_EX 2_ε with L^yX 2.0.5 on  Mac OS X.

This is the grayscale version with hyperlinks, optimized for screen reading. It was then converted to PDF/A following ISO 19005-1:2005 standard and this may have corrupted hyperlinks.

For other versions or any question use the contact above.

Uploaded on PaDUA@research database with Open Access .

Ai miei genitori.

Abstract

The research presented in this doctoral thesis concerns with the development of novel materials and systems for solid state hydrogen storage.

The first group of works presented is on alkaline and alkaline-earth borohydrides. The possibility to enhance their properties with the help of nanosupports has been widely explored. An attempt to improve the dehydrogenation kinetics of lithium borohydride has been made dispersing this material on the surface of modified nanotubes and graphite. The resulting nanoconfined material displayed a decreased decomposition temperature in comparison with pure material and further decreasing was observed when the surface area of the supports was increased. An analogous experiment was performed to investigate this effect in combination with the assets of a reactive hydride composite, where two materials are mixed to obtain a compound with a lower decomposition enthalpy. The effect of the mixture was beneficial in presence of the support, due to lower temperature melting. For calcium borohydride an ordered mesoporous carbon was used after chemical activation. The increased properties of this support resulted in lower decomposition temperature and improved reversibility for a number of cycles at different pressure values.

The second research line is focused on magnesium hydride. To improve its kinetic properties a zirconium-nickel alloy was investigated to evaluate its influence on the reaction rate, both in absorption and desorption. The degradation observed in experimental reactors, of different magnesium hydride powders catalyzed with a transition metal oxide, motivated the fabrication of pellets with the addition of a binding agent, to obtain mechanical resistance, still allowing hydrogen diffusion. Each pellet was supposed to behave as an independent system, so they were also tested in a small reactor. Several hydrogen absorption/desorption cycles were performed to compare the behaviour of the small reactor with the laboratory data obtained on smaller quantity of powdered and pelletized specimens.

Finally, the feasibility of a vehicular hydrogen tank system was investigated using an interstitial metal hydride as storage material. Apart from material basic characterization, two different kinds of experiment were performed. Static tests (measurements with automatic flow control and constant settings) were used to evaluate whether the requirements for desorption are met by the tank set-up. Then, dynamic tests were designed and applied on the tank, where the hydrogen flow was fluctuating following a hypothetical on-road trial. It was possible to underline the heat management issues of high-demanding performances and to analyze some solutions for that. Different cycles were carried out on the tank to find the ideal setting for high average and peak flows in a realistic experiment.

Sommario

L'attività di ricerca presentata in questa tesi di dottorato riguarda lo sviluppo di nuovi materiali e sistemi per lo stoccaggio di idrogeno allo stato solido.

Il primo gruppo di attività presentate è sui boroidruri di metalli alcalini e alcalino-terrosi. È stata ampiamente esplorata la possibilità di migliorare le loro proprietà con l'ausilio di nanosupporti. Un tentativo di migliorare la cinetica di decomposizione del litio boroidruro è stato fatto disperdendo tale materiale sulla superficie di nanotubi di carbonio e grafite modificati. Il materiale nanoconfinato risultante ha mostrato una temperatura di decomposizione inferiore, se paragonato al materiale puro e un'ulteriore diminuzione è stata osservata aumentando l'area superficiale del supporto. Un esperimento analogo è stato eseguito per osservare questo effetto in combinazione con i vantaggi di un *reactive hydride composite*, nel quale due materiali sono combinati per ottenere un composto con una minor entalpia di decomposizione. L'effetto del composto è stato positivo in presenza del supporto, grazie alla minor temperatura di fusione. Per il calcio boroidruro è stato usato carbone mesoporoso dopo attivazione chimica. Le migliorate proprietà di questo supporto hanno dato una minor temperatura di decomposizione e una migliorata reversibilità per vari cicli a diverse pressioni.

La seconda linea di ricerca si focalizza sull'idruro di magnesio. Per migliorare le sue proprietà cinetiche, è stata testata una lega zirconio-nickel, al fine di valutare la sua influenza sulla velocità di reazione in assorbimento e desorbimento. Il degrado di altre polveri di magnesio idruro catalizzate con un ossido metallico in reattori sperimentali ha motivato la produzione di pastiglie con l'aggiunta di un agente legante, per ottenere resistenza meccanica, consentendo comunque la diffusione dell'idrogeno. Era previsto che ogni pastiglia si comportasse come un sistema indipendente, infatti, sono state testate in un piccolo reattore. Diversi cicli di assorbimento e desorbimento sono stati effettuati per paragonare la risposta del reattore con dati di laboratorio ottenuti su minori quantità di polvere o pastiglie.

Infine, è stata sperimentata la realizzabilità di un serbatoio di idrogeno veicolare usando un idruro di un metallo interstiziale. Oltre alla caratterizzazione di base del materiale, sono stati realizzati due tipi di esperimenti. Test statici (misure con controllo automatico di flusso e impostazioni costanti) sono stati usati per valutare se il serbatoio soddisfacesse i requisiti di rilascio di idrogeno. Test dinamici sono stati progettati e applicati al serbatoio, dove il flusso di idrogeno era variabile seguendo un'ipotetica prova su strada. È stato possibile evidenziare i problemi legati allo scambio di calore per le prestazioni di maggior consumo e analizzare alcune possibili soluzioni. Cicli diversi sono stati effettuati sul serbatoio in esperimenti realistici, per trovare le impostazioni ideali per alti valori di flusso medio e di picco.

Contents

Abstract	vii
Sommario	ix
1 Introduction	1
1.1 Hydrogen Properties	4
1.2 Hydrogen as an Energy Carrier	5
References	7
2 Hydrogen Storage in Metal and Complex Hydrides	9
2.1 Hydrides Properties	9
2.1.1 Sorption Dynamics	9
2.1.2 Thermodynamics of Hydrides	11
2.1.3 Stability of Hydrides	13
2.1.4 Kinetics	15
2.2 Metal Hydrides	16
2.2.1 Intermetallic Hydrides	16
2.2.2 Magnesium Hydride	18
2.3 Complex Hydrides	20
2.3.1 Complex Borohydrides	20
2.3.2 Lithium Borohydride	23
2.3.3 Magnesium Borohydride	24
2.3.4 Calcium Borohydride	25
2.3.5 Alanates	26
2.3.6 Amides/Imides	26
2.4 Conclusions	27
References	29
3 Synthesis and Characterization Techniques	35
3.1 Samples Preparation	35
3.1.1 Ball Milling	35
3.1.2 Sample Handling	38
3.2 Structural Characterization	39
3.2.1 X-Ray Diffraction	39
3.2.2 Scanning Electron Microscopy	41
3.2.3 Pores and Surface Characterization	42
3.3 Functional Properties Characterization	45
3.3.1 Differential Scanning Calorimetry	45
3.3.2 Hydrogen a/d Characterization	47
References	51

4	Nanosupported Borohydride Compounds	53
4.1	Advantages of Nanosupports	54
4.2	Preparation and Characterization of Samples	55
4.2.1	Lithium, Magnesium and Mixed Borohydrides	55
4.2.2	Calcium Borohydride on Mesoporous Carbon	56
4.3	Analysis of Experimental Outcomes	57
4.3.1	Characterization of Carbonaceous Supports	57
4.3.2	Properties of Studied Borohydride Mixtures	61
4.3.3	Nanoconfined Samples and Mixtures Samples	63
4.3.4	Calcium Borohydride	72
4.4	Observations on Nanosupported Borohydrides	74
	References	77
5	Magnesium Hydride Based Materials and Systems	81
5.1	Seeking a Novel Catalyst	82
5.1.1	Preparation of Zirconium-Nickel Catalyzed Magnesium Hydride Sam- ples	82
5.1.2	Analysis of Experimental Results	82
5.2	Development of Magnesium Hydride-Based Pellets	88
5.2.1	Preparation of Pellets	89
5.2.2	Results Analysis	89
5.2.3	Overall Properties of Magnesium Hydride-Based Pellets	95
5.2.4	Experimental Reactor for Magnesium Hydride-Based Pellets	96
5.2.5	Performances of the Reactor	97
5.2.6	Towards Magnesium Hydride-Based Tanks	100
	References	101
6	Room Temperature Hydride Storage System	105
6.1	Introduction	106
6.1.1	Purpose	106
6.2	Material Choice	107
6.2.1	Structural Characterization	107
6.2.2	Hydrogen a/d Properties	108
6.3	Storage System Development	114
6.3.1	Requirements	114
6.3.2	Experimental Set-Up	114
6.3.3	Static Tests	117
6.3.4	Dynamic Tests	121
6.4	Conclusions	125
7	Final Remarks	129
	Nomenclature	133
	Curriculum Vitæ	135
	Acknowledgments	139

1

Chapter 1

Introduction

Abstract. This introductory chapter provides a brief perspective of a hydrogen based economy, describing the possible advantages of such an energy carrier. Fossil fuels could be referred as power sources, on the other hand, clean power generation is linked to natural fluxes and therefore the increase of renewable sources makes inevitable the necessity of large energy storage. The physico-chemical properties of hydrogen are presented, as a useful tool for the following matters, and the different stages of a hydrogen cycle are mentioned, presenting the problem of its storage.

Energy is a key aspect in human development and, therefore, thermodynamics is a fundamental knowledge to understand the processes that allow mankind to control and transform it. The laws of thermodynamics help to understand that energy cannot be created or destroyed, but just its transformation and conversion is possible in order to be used, stored or transported in the most effective and convenient way.

From a thermodynamical outlook Earth can be approximated by a closed system, in which there is no transfer of matter, but energy can be exchanged. The planet receives a considerable amount of energy every day from solar irradiation [1, 2, 3] and the ability to convert this energy is what, basically, differentiates living from dead matter: plants developed the photosynthesis and were used as biomass by humans to obtain heat, food and therefore work. Solar energy was also used to travel thanks to wind and sails or to work in waterwheels and windmills. A huge amount of it, that was spontaneously accumulated in fossil fuels, hydrocarbon based energy carriers, was later used to start the industrial revolution with the steam engine and to develop enormously over the last century thanks to several more efficient ways to convert energy into mechanical work. The massive use of hydrocarbons has altered the natural carbon cycle, because their combustion increased the amount of carbon emitted to such a level that plants were not able to absorb [4].

Society is now starting to develop the consciousness that the combustion of fossil fuels leads to climate changes [5] and that these reserves of accumulated solar energy will not last forever. The former point is well supported by evidences, as temperature is being monitored and an increase of the average value can be noticed. Since the planet can receive

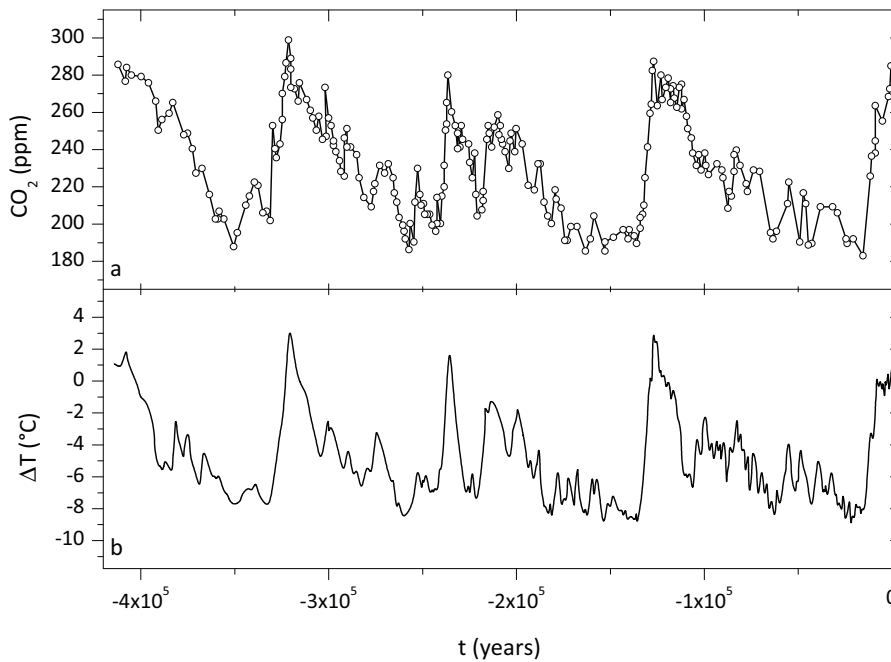


Figure 1.1: Climatic and atmospheric history can be retrieved from antarctic ice: here atmospheric CO_2 concentration (a) and temperature variations (b) are shown over time. Adapted from [8].

energy from solar irradiation and now, even in a period of decreasing solar activity, the temperature on Earth is increasing, there must be something that prevents some of the heat to be dispersed back in the outer space: an unnatural grow of the greenhouse gases. Carbon dioxide is one of them and its anthropogenic production highly increased with the exploitation of hydrocarbons. The increment of its concentration in the atmosphere is one of the main responsible for temperature rising [6, 7]. An investigation of the climate and atmospheric history from the ice core in Antarctica has shown that the variations in the temperature on the Earth can be correlated with the variations in the concentration of greenhouse gases in the atmosphere [8].

As it can also be seen in figure 1.1, in the last thousands of years the carbon dioxide concentration has been rising and in the last centuries many observatories have been monitoring this value in the atmosphere [9], which is rising with a rate higher than $1.5 \text{ ppm year}^{-1}$ [10]. In recent times the values of CO_2 concentration have exceeded historical data by far, as it is clearly shown by figure 1.2.

Regarding the latter matter, there is a debate over the prediction of the fuels reserves [11]. Extrapolation of the energy consumption shows that the demand will soon exceed the supply [12], as it already happened in the United States in the seventies, proving the theory of M. K. Hubbert [13].

No matter how much fossil fuel is left, it is necessary to develop a world sustainable energy economy for the future. As today, most of the energy demand is covered by energy carriers; however, all renewable energy sources deliver energy fluxes and a synthetic energy carrier is therefore needed. The research for a sustainable energy carrier can be solved by hydrogen [14], as it fulfills most of the requirements and it can be inserted in a closed

cycle, similar to the natural ones (e. g. nitrogen, water) [15].

The use of hydrogen to produce energy, both in combustion processes or in electrochemical reactions, implies the reaction of H_2 with O_2 to obtain water as by-product, without production of pollutants or greenhouse gases. This energy carrier can be produced in a great variety of processes, starting from fossil fuels with a control over greenhouse gases emission or extracting it from water with the release of pure oxygen. Energy must be spent in order to separate hydrogen from the molecules to which it is bond. Extracting it from hydrocarbons with CO_2 capture can represent just a starting scenario, but the most convenient strategy is to exploit renewable energies to dissociate water. The possibility to accumulate energy producing hydrogen is very convenient for most of the technologies based on renewable sources, which deliver variable fluxes of energy, as already mentioned. In addition, with this opportunity, energy production can be optimized even in big traditional plants, avoiding fluctuations due to the daily different demand of power, just storing the excess energy.

Furthermore, it is possible to produce hydrogen wherever water and energy are available. Taking in account renewable energy sources, this allow the first diffusion of hydrogen based systems especially in places where fossil fuels are expensive or unavailable, or the power grid is unreachable. There is no harm for natural equilibrium, because all the water consumed is going back in its cycle when hydrogen is transformed back to energy [15].

Hydrogen has the highest specific energy among fuels and represents the arrival point in the evolution of fuels used in history [16]: the carbon to hydrogen atoms ratio $Q_H = \frac{m}{n+m}$ has been reducing with the time in hydrocarbons C_nH_m , as it is shown in figure 1.3. Moreover, it is possible to notice how the boiling point T_B has been reducing, bringing the state from liquid to gaseous; this allowed a better distribution and storage, as previously happened with the transition from firewood and coal to liquid fuels.

This already high specific energy is also the one with the highest *exergy*¹ content, because electrochemical conversion is almost free from friction and thermal losses, so the *anergy* is reduced to the minimum [18]. Even considering a transitional scenario, where hydrogen is partly produced starting from

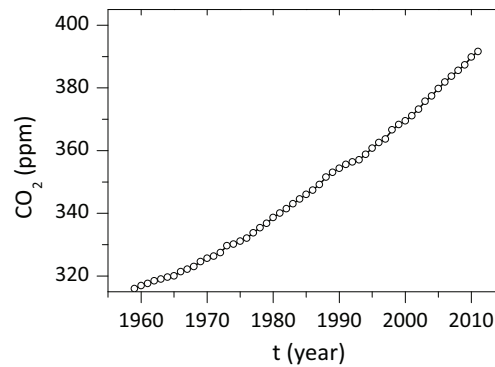


Figure 1.2: CO_2 concentration from 1960 to the present. Data recorded at Mauna Loa observatory in Hawaii [10].

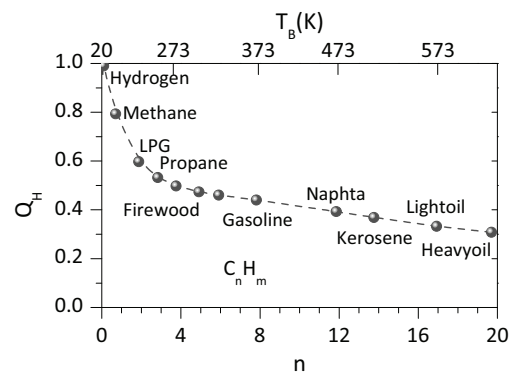


Figure 1.3: Energetic transition from hydrocarbons to hydrogen (see text for details). Adapted from [16].

¹The maximum fraction of an energy form which (in a reversible process) can be transformed into work is called *exergy*. The remaining part is called *anergy* [17].

hydrocarbons or with conventional energy, a future energetic hydrogen based economy is realistic [14].

1.1 Hydrogen Properties

Hydrogen is the most common element in the universe. Some estimations say it is more than 90 % of it [19], but for sure it is present in the Sun and stars and is the main source of energy in the thermonuclear fusion processes. However, in the Earth’s atmosphere its presence is quite scarce, due to its very low weight for attraction by the Earth’s gravitational field. H_2 is the tenth most abundant element on Earth’s crust, but it does not reach 0.15 % in weight. It can be found bond to all the elements of the periodic table with exclusion of noble gases, so that it is the most present element in chemical compounds: water, living matter as carbohydrates and proteins, many organic compounds, hydrocarbon, ammonia, and acids.

It was discovered in 1766 by Henry Cavendish, who analyzed the gas produced by the reactions of metals and acids; the name *hydrogen* (from ancient Greek ὕδωρ, *hydor*, “water”, and the root γεν- of γίγνομαι, *gìghnomai*, “to generate”) was later proposed by Antoine Lavoisier.

Hydrogen is the first and the lightest element of Mendeleev’s periodic table. Three different isotopes are known in nature:

- 1_1H proper hydrogen, *protium*, is the 99.985 % of the total and consists of a single proton-electron couple;
- 2_1H *deuterium*, also indicated by chemical symbol D, is the 0.015 %;
- 3_1H *tritium* is present only in traces and is radioactive.

Property	Value	Unit
Atomic weight	1.007 94	u
Atomic radius	0.53	Å
Covalent radius	0.37	Å
van der Waals radius	1.20	Å
Electronegativity	2.2	(Pauling Scale)
First ionization energy	1 312.06	kJ mol ⁻¹

Table 1.1: Atomic hydrogen properties.

The atomic hydrogen properties belong to the most common isotope and are reported in table 1.1. The electron configuration allows the creation of bonding both losing an electron and creating H^+ cation or gaining an electron to have the hydride anion H^- . Covalent bonding can also occur, especially with non metallic elements. The small radius of the atom is responsible for hydrogen bond, a form of medium-strength non-covalent bonding which is critical to the stability of many biological molecules.

Molecular hydrogen is a diatomic gas in standard conditions and its properties are listed in table 1.2.

Property	Value	Unit
Molecular mass	2.015 88	u
Bond length	0.746	Å
Dissociation energy, E_{diss}	431.58	kJ mol ⁻¹
Triple point	temperature	13.96 K
	pressure	7.3 kPa
Critical point	temperature, T_c	32.98 K
	pressure, P_c	1.31 kPa
Boiling point	20.39	K
Density at b. p., ρ_l	70.811	kg m ⁻³
Density at STP	0.089 9	kg m ⁻³
Thermal conductivity	0.182 6	W m ⁻¹ K ⁻¹

Table 1.2: Molecular hydrogen properties.

The equation of state for H₂ gas follows the ideal gases law at low densities:

$$pV = nRT \quad (1.1)$$

where p is the pressure, V the volume, n the moles, T the absolute temperature, and R the gas constant (8.314 472 m³ Pa K⁻¹ mol⁻¹ [20]).

At higher densities (which can be found at standard conditions or in practical interest settings) van der Waals equation is a better approximation of the real hydrogen behaviour:

$$p = \frac{nRT}{V - nb} - a \frac{n^2}{V^2} \quad (1.2)$$

where parameters a and b are defined as:

$$a \equiv \frac{27 R^2 T_c^2}{64 P_c} \quad b \equiv \frac{1}{8} R \frac{T_c}{P_c} \quad (1.3)$$

and are related to the distance from the critical point (defined by T_c and P_c , as in table 1.2) of the considered status [21].

1.2

Hydrogen as an Energy Carrier

As already mentioned, among the numerous advantages of using hydrogen there is also the possibility of having this carrier inserted in a natural closed cycle. The main part of it are:

production, where energy is used to extract hydrogen from the molecules where is bound to other elements;

storage, to have the possibility to transport and distribute the carrier, and to have access to energy at the most convenient time and place;

use, to extract the energy using thermal or electrochemical device for the conversion of hydrogen.

In this work, efforts are focused on the second step, therefore production and utilization topics will not be considered in depth.

Hydrogen is now produced mainly from hydrocarbons, with reactions like the steam methane reforming or the partial oxidation of hydrocarbons. All these processes yield to quite high efficiency in production [22], but cannot be accounted in a sustainable scenario, as they exploit fossil fuels or biomass [23]. Electrolysis allows to use electricity from clean energy [24], e. g. from photovoltaic [25]. Water molecules can be split also using biological reactors [26, 27]. More techniques and details can be found in the specific literature [28, 29].

The conversion of hydrogen back to energy is possible through combustion or electrochemical reaction. In both cases H_2 is recombined with O_2 , but the efficiency of the latter is theoretically higher: this is the reason why most of the vehicular or stationary applications of hydrogen as energy vector make use of fuel cells. There are different kinds of possible electrolytes, which allow the distinction of fuel cells in categories: alkaline fuel cells uses KOH [30], proton exchange membrane (PEM) fuel cells have a solid polymer [31], molten carbonate fuel cells use a mixture of molten carbonate salts [32]. For a comprehensive outlook of fuel cells and production technologies, the book edited by D. Stolten [33] is a very useful tool.

The storage issue is often indicated as the main technological hinder in hydrogen economy [34, 35]. Owing to the very low density of H_2 (see table 1.2) the use of this carrier is possible only increasing the pressure of its gaseous state, reducing the temperature to reach the liquid state, or reducing the distance between atoms and molecules, thanks to the interaction with other materials. The physical storage of hydrogen in high-pressure cylinders is a mature technology [36], its safety is comparable to other fuels [18], but it presents some limitations in the maximum density available [37]. The liquid storage allows to reach an higher value of density (see ρ_l in table 1.2) and cryogenic storage systems are also an established technology [38], but the energy required for liquefaction and the boil-off make this solution effective only in limited applications [39]. Adsorption on high specific surface area materials is also possible and the quantity stored is proportional to the surface of the considered material, but appreciable sorption capacities are possible only at cryogenic temperature [40, 41].

Some of the other possible solutions available will be analyzed in the following chapters, with a particular emphasis on storing hydrogen in the atomic form — in metal and complex hydrides — with the attempt of increasing the hydrogen density to the highest levels [42].

References

- 1 Noia M., Ratto C.F., Festa R., Solar irradiance estimation from geostationary satellite data: I. Statistical models, *Solar Energy*, **51** (1993) 449–456. (Cited on page 1)
- 2 Noia M., Ratto C.F., Festa R., Solar irradiance estimation from geostationary satellite data: II. Physical models, *Solar Energy*, **51** (1993) 457–465. (Cited on page 1)
- 3 Mubiru J., Banda E.J.K.B., Estimation of monthly average daily global solar irradiation using artificial neural networks, *Solar Energy*, **82** (2008) 181–187. (Cited on page 1)
- 4 Stucki S., “The Carbon Cycle and Biomass Energy”, in: *Hydrogen as a Future Energy Carrier*, Züttel A., Borgschulte A., Schlapbach L. (eds), (2008) Wiley-VCH, Weinheim. Chap. 3.2, 37–43. (Cited on page 1)
- 5 Rosa E.A., Dietz T., Climate Change and Society: Speculation, Construction and Scientific Investigation, *International Sociology*, **13** (1998) 421–455. (Cited on page 1)
- 6 Arrhenius S., On the Influence of Carbonic Acid in the Air upon the Temperature of the Ground, *Philosophical Magazine and Journal of Science*, **41** (1896) 237–276. (Cited on page 2)
- 7 Uppenbrink J., Arrhenius and Global Warming, *Science*, **272** (1996) 1122. (Cited on page 2)
- 8 Petit J. R., Jouzel J., Raynaud D., Barkov N.I., Barnola J.-M., Basile I., Bender M., Chappellaz J., Davisk M., Delaygue J., Delmotte M., Kotlyakov V.M., Legrand M., Lipenkov V.Y., Lorius C., Pépin L., Ritz C., Saltzman E., Stievenard M., Climate and atmospheric history of the past 420 000 years from the Vostok ice core, Antarctica, *Nature*, **399** (1999) 429–436. (Cited on page 2)
- 9 Wallén, C.C., Global monitoring of carbon dioxide in the atmosphere, *Environment International*, **2** (1979) 351–355. (Cited on page 2)
- 10 Hofmann D.J., Butler J.H., Tans P.P., A new look at atmospheric carbon dioxide, *Atmospheric Environment*, **43** (2009) 2084–2086. (Cited on pages 2 and 3)
- 11 Hall C., Tharakan P., Hallock J., Cleveland C., Jefferson M., Hydrocarbons and the evolution of human culture, *Nature*, **426** (2003) 318–322. (Cited on page 2)
- 12 Johnson H.R., Crawford P.M., Bunger J.W., Assessment of Strategic Issues, *Strategic Significance of America’s Oil Shale Resource*, U.S. Department of Energy, **I** (2004). (Cited on page 2)
- 13 Hubbert M.K., The energy resources of the Earth, *Scientific American*, **225** (1971) 60–70. (Cited on page 2)
- 14 Barreto L., Makihiraa A., Riaha K., The hydrogen economy in the 21st century: a sustainable development scenario, *International Journal of Hydrogen Energy*, **28** (2003) 267–284. (Cited on pages 2 and 4)
- 15 Speight J.D., “The Hydrogen Cycle”, in: *Hydrogen as a Future Energy Carrier*, Züttel A., Borgschulte A., Schlapbach L. (eds), (2008) Wiley-VCH, Weinheim. Chap. 3.3, 43–67. (Cited on page 3)
- 16 Ohta T., Some thoughts about the hydrogen civilization and the culture development, *International Journal of Hydrogen Energy*, **31** (2006) 161–166. (Cited on page 3)
- 17 Honerkamp J., *Statistical Physics: An Advanced Approach with Applications*, (2002) Springer-Verlag, Berlin Heidelberg. (Cited on page 3)
- 18 Winter C.-J., Energy policy is technology politics — The hydrogen energy case (with an eye particularly on safety comparison of hydrogen energy to current fuels), *International Journal of Hydrogen Energy*, **31** (2006) 1623–1631. (Cited on pages 3 and 6)
- 19 Suess H., Urey, H., Abundances of the Elements, *Reviews of Modern Physics*, **28** (1956) 53–74. (Cited on page 4)
- 20 Mohr P.J., Taylor B.N., Newell D.B., CODATA Recommended Values of the Fundamental Physical Constants: 2006, *Reviews of Modern Physics*, **80** (2008) 633–730. (Cited on page 5)
- 21 Elliot J.R., Lira C.T., *Introductory Chemical Engineering Thermodynamics*, (1998) Prentice-Hall, Upper Saddle River. (Cited on page 5)
- 22 Kothari R., Comparison of environmental and economic aspects of various hydrogen production methods, *Renewable and Sustainable Energy Reviews*, **12** (2008) 553–563. (Cited on page 6)
- 23 Ni M., Leung D.Y.C., Leung M.K.H., Sumathy K., An overview of hydrogen production from biomass, *Fuel Processing Technology*, **87** (2006) 461–472. (Cited on page 6)
- 24 Holladay J.D., Hu J., King D.L., Wang Y., An overview of hydrogen production technologies,

- Catalysis Today*, **139** (2009) 244–260. (Cited on page 6)
- 25 Tributsch H., Photovoltaic hydrogen generation, *International Journal of Hydrogen Energy*, **33** (2008) 5911–5930. (Cited on page 6)
- 26 Levin D.B., Pitt L., Love M., Biohydrogen production: prospects and limitations to practical application, *International Journal of Hydrogen Energy*, **29** (2004) 173–185. (Cited on page 6)
- 27 Kosourov S., Patrusheva E., Ghirardi M.L., Seibert M., Tsygankov A., A comparison of hydrogen photoproduction by sulfur-deprived *Chlamydomonas reinhardtii* under different growth conditions. *Journal of Biotechnology*, **128** (2007) 776–787. (Cited on page 6)
- 28 Turner J., Sverdrup G., Mann M.K., Maness P.-C., Kroposki B., Ghirardi M., Evans R.J., Blake D., Renewable Hydrogen Production, *International Journal of Energy Research*, **32** (2008) 379–407. (Cited on page 6)
- 29 Irvine J., Theme issue: materials chemistry for hydrogen storage and generation, *Journal of Materials Chemistry*, **18** (2008) 2295–2297. (Cited on page 6)
- 30 Lin B.Y.S., Kirk D.W., Thorpe S.J., Performance of alkaline fuel cells: A possible future energy system?, *Journal of Power Sources*, **161** (2006) 474–483. (Cited on page 6)
- 31 Jing F., Hou M., Shi W., Fu J., Yu H., Ming P., Yi B., The effect of ambient contamination on PEMFC performance, *Journal of Power Sources*, **166** (2007) 172–176. (Cited on page 6)
- 32 Farooque M., Maru H.C., Carbonate fuel cells: Milliwatts to megawatts, *Journal of Power Sources*, **160** (2006) 827–834. (Cited on page 6)
- 33 Stolten D. (ed.), *Hydrogen and Fuel Cells*, (2010) Wiley-VCH, Weinheim. (Cited on page 6)
- 34 Ross D.K., Hydrogen storage: The major technological barrier to the development of hydrogen fuel cell cars, *Vacuum*, **80** (2006) 1084–1089. (Cited on page 6)
- 35 Felderhoff M., Weidenthaler C., von Helmolt R., Eberle U., Hydrogen storage: the remaining scientific and technological challenges, *Physical Chemistry Chemical Physics*, **9** (2007) 2643–2653. (Cited on page 6)
- 36 Irani R.S., Hydrogen storage: High-pressure gas containment, *MRS bulletin*, **27** (2002) 680–682. (Cited on page 6)
- 37 Züttel A., Materials for hydrogen storage, *Materials Today*, **6** (2003) 24–33. (Cited on page 6)
- 38 Wolf J., Liquid-hydrogen technology for vehicles, *MRS Bulletin*, **27** (2002) 684–687. (Cited on page 6)
- 39 Sarkar A., Banerjee R., Net energy analysis of hydrogen storage options. *International Journal of Hydrogen Energy*, **30** (2005) 867–877. (Cited on page 6)
- 40 Nijkamp M.G., Raaymakers J.E.M.J., van Dillen A.J., De Jong K.P., Hydrogen storage using physisorption — materials demands. *Applied Physics A*, **72** (2001) 619–623. (Cited on page 6)
- 41 Schlapbach L., Züttel A., Hydrogen-storage materials for mobile applications, *Nature*, **414** (2001) 353–358. (Cited on page 6)
- 42 von Helmolt R., Eberle U., Fuel cell vehicles: Status 2007, *Journal of Power Sources*, **165** (2007) 833–843. (Cited on page 6)

2 Chapter 2

Hydrogen Storage in Metal and Complex Hydrides

Abstract. This chapter presents the theoretical aspects bond to most of the materials used in solid state hydrogen storage, focusing on hydrides. The sorption mechanism and reaction kinetics are delineated, along with a general analysis on thermodynamics and stability of the hydrogen containing compounds. A state-of-the-art review of metal and complex hydride is also provided: synthesis, structures and thermodynamics are described, research works to improve a/d kinetics and properties are presented. In this overview of the principal classes of solid-state hydrogen materials, particular care is given to introduce those that will be analyzed and implemented, thanks to experimental work, in the following chapters.

Most of the elements on the periodic table form hydrides or compounds containing hydrogen, some of which can be used for hydrogen storage, transport and delivery. Differently from compressed gas, liquid storage or H_2 molecules physisorption, in these materials hydrogen is found in the atomic form, chemically bound to other elements. Consequently, a hydrogen storage system based on hydrides, or compounds containing them, depends strongly on the characteristics of the considered material.

Before presenting the various classes of materials, considered the most interesting for storage purposes, and the particular ones that have been object of this research work, some background information is necessary.

2.1 Hydrides Properties

2.1.1 Sorption Dynamics

The sorption process is the result of the interaction between gaseous hydrogen and a solid-state material and can be described with the help of a simplified one-dimensional potential

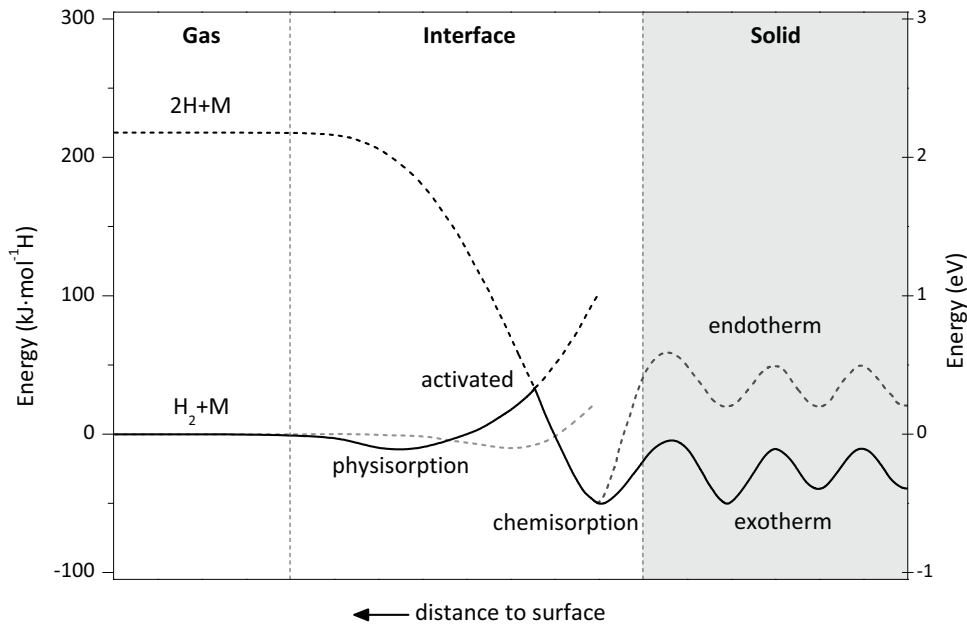


Figure 2.1: Lennard-Jones potential energy curves for hydrogen activated chemisorption on a metal surface and endothermic and exothermic solution in the bulk material. Adapted from [1].

energy curve (Lennard-Jones potential) for a metal, as shown in figure 2.1.

Faraway from the surface, the difference in the potential between a hydrogen molecule and two hydrogen atoms is the dissociation energy (E_{diss} in table 1.2). The first attractive interaction of H_2 approaching the metal surface is the van der Waals force, leading to the physisorption ($E_{phys} \approx 10 \text{ kJ mol}^{-1} H_2$) at about one hydrogen molecule radius from the metal surface, approximately 0.2 nm. Not all the molecules colliding with the surface will remain attached, depending on the geometry of the surface involved in the collision. Nearer to the metal surface hydrogen has to overcome an activation barrier for dissociation and formation of the hydrogen metal bond. The height of the activation barrier depends on the surface elements involved. Hydrogen atoms, sharing their electron with the metal atoms at the surface, are then in the chemisorbed state ($E_{chem} \approx 50 \text{ kJ mol}^{-1} H_2$). The chemisorbed hydrogen atoms may have a high surface mobility, interact with each other and form surface phases at a sufficiently high coverage. In the next step the chemisorbed hydrogen atom can move inside the subsurface layer. Then hydrogen can diffuse through interstitial sites in the bulk of the metal host overcoming another barrier that is of the order of $10 \text{ kJ mol}^{-1} H_2$ [2].

The hydrogen is exothermically dissolved (solid-solution, called α -phase) in the metal at a concentration $c_H < 0.1$ ($c_H = N_H/N_M$, where N_H and N_M are the number of hydrogen and metal atoms, respectively). The metal lattice expands proportionally to c_H by about 2 to 3 \AA^3 per hydrogen atom [3]. At greater hydrogen concentrations in the host metal ($c_H > 0.1$) a strong H–H interaction, due to the lattice expansion, becomes important and the hydride phase (β -phase) nucleates and grows. Most of the time $c_H = 1$ in the hydride phase [4] and the volume difference between the coexisting α - and the β -phase can reach

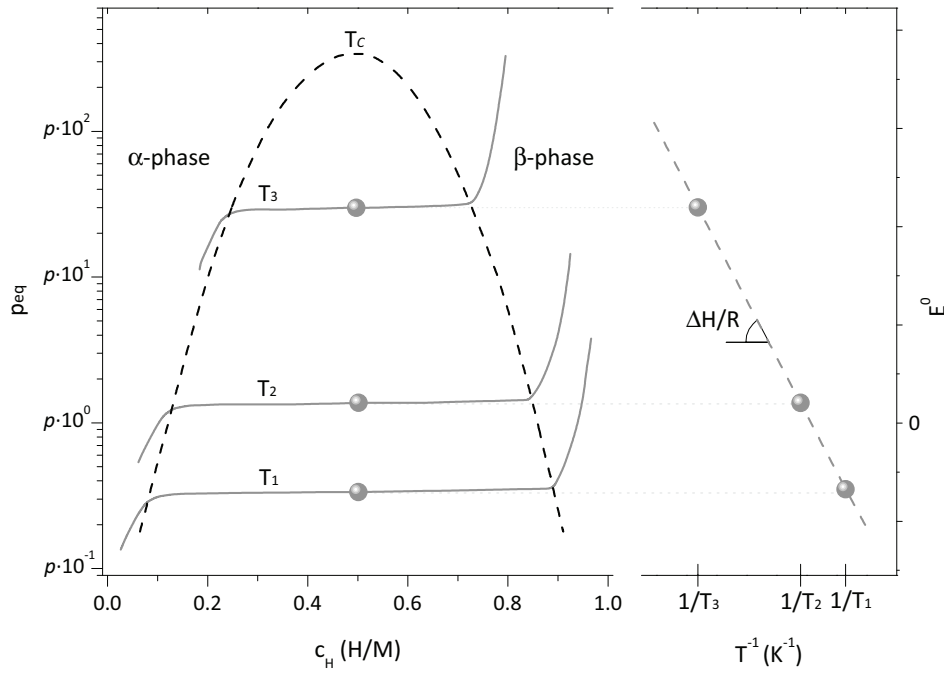


Figure 2.2: Generic pressure composition isotherm and relative van't Hoff plot.

in many cases up to 10–20% of the metal lattice. Consequently, a large stress is built up at the phase boundaries and often leads to decrepitation of brittle host metals, as in the last of the steps that will be shown in figure 2.4 at page 15. The final hydride is a powder with a typical particle size of 10 to 100 μm [5].

2.1.2 Thermodynamics of Hydrides

In contact with hydrogen, a generic hydride-forming metal M will form a metal hydride following the reaction:



where Q is the heat of reaction of hydride formation. The thermodynamic aspects of reaction (2.1) are easily described by pressure-composition isotherm (PCI); a schematic PCI curve is shown in figure 2.2.

At low concentration ($x \ll 1$) hydrogen begins to dissolve in the metal lattice and forms the α -phase. Hydrogen is then randomly distributed in the metal host lattice and the concentration varies slowly following the temperature. The α -phase has the same crystal structure as the starting metal. The condition for thermodynamic equilibrium is given by:

$$\frac{1}{2}\mu_{H_2}(p, T) = \mu_H(p, T, c_H) \quad (2.2)$$

where μ_{H_2} is the chemical potential of molecular hydrogen, μ_H is the chemical potential of atomic hydrogen in solution in the metal and c_H is the hydrogen concentration.

The concentration increases with pressure, until nucleation of β -phase occurs. Now

the system has three phases (α , β and hydrogen gas) and two components (metal and hydrogen). From the Gibbs phase rule, the degree of freedom f is:

$$f = C - P + 2 \quad (2.3)$$

where C is the number of components and P is the number of phases. As a consequence, in the two-phase region concentration increases while hydrogen pressure is constant. Once the complete disappearance of the α -phase has been reached and pure β -phase is present, the system has two degrees of freedom. Hydrogen enters into solid solution in the β -phase and the hydrogen pressure rises with concentration again [6].

The phase rule (2.3) requires pressure to be constant at any temperature below the critical temperature. The change in Gibbs free energy of the process ΔG^0 , summarized by reaction (2.1), are expressed by the following equations:

$$\Delta G^0 = RT \ln p_{\text{eq}} \quad (2.4)$$

$$\Delta G^0 = \Delta H^0 - T\Delta S^0 \quad (2.5)$$

where R is the gas constant, T the absolute temperature, p_{eq} the equilibrium pressure, ΔH^0 is the enthalpy change of hydride formation and ΔS^0 the entropy change of hydride formation. In equation (2.4) the activity of solid-states such as metals is set to 1.

From (2.4) and (2.5) the following equation is obtained:

$$\ln p_{\text{eq}} = \frac{\Delta H^0}{RT} - \frac{\Delta S^0}{R} \quad (2.6)$$

The plot of the hydrogen equilibrium pressure versus the reciprocal of the absolute temperature $1/T$ is called van't Hoff plot. The slope and the intercept with the y -axis of the the plot give ΔH^0 and ΔS^0 , respectively.

In general, the difference in standard entropy between a metal and its hydride is very small and is of the order of $10 \text{ J K}^{-1} \text{ mol}^{-1}$. The change in entropy with hydride formation S^0 is mainly provided by the loss of the standard entropy of hydrogen gas ($130.86 \text{ J K}^{-1} \text{ mol}^{-1}$), which means that ΔS^0 can be assumed to be a constant and does not depend on the nature of the materials that absorb hydrogen. Therefore (2.6) can be rewritten as

$$\ln p_{\text{eq}} = \frac{\Delta H^0}{RT} + K \quad (2.7)$$

where $K = -\Delta S^0/R$ is a constant and does not depend on the hydrogen storage material. A sufficient number of sets of temperatures and equilibrium pressures are needed for calculation of the enthalpy of hydride formation when using the van't Hoff equation (2.6). While, by using (2.7) only a few values of T and p_{eq} are required to calculate ΔH^0 . This method is very convenient to use to obtain a first impression of thermodynamic properties of a given metal-hydrogen system. Because the difference in standard entropy between metal and hydrogen is of the order of $10 \text{ J K}^{-1} \text{ mol}^{-1}$, ΔS^0 calculated using the van't Hoff plot, is usually around $-110 \text{ J K}^{-1} \text{ mol}^{-1}$ [7].

2.1.3

Stability of Hydrides

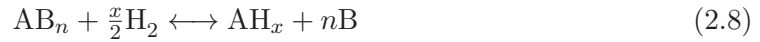
Most of the natural elements can form hydrides, but the only metallic element reacting with hydrogen at ambient temperature and moderate H_2 pressure is vanadium. Because of this, alloys are preferentially used for hydrogen storage purpose. However, the alloy-hydrogen system is less simple than the metal-hydrogen system, mainly because the interstitial sites have different chemical and geometrical configurations.

Still, semi-empirical models can be used to have physical insight on the hydride formation of some systems.

2.1.3.1 Rule of Reversed Stability

A model which gives reasonably good agreement between the calculated and experimental heat of formation was developed by Miedema and coworkers [8, 9, 10, 11].

Considering a binary alloy AB_n , where element A easily forms a hydride and element B does not form any hydride, element A is assumed to form a hydride following reaction (2.1): at a given temperature T , this reaction has a hydrogen equilibrium pressure p_{eq} . Considering now a solid solution of this metal A with the non-hydride forming metal (B), the relative partial molar free energy of A in the alloy is ΔG_A . If the resulting alloy AB_n reacts with hydrogen as



then, the hydrogen pressure equilibrium of reaction (2.8) is given by

$$p = p_{eq} \exp\left(\frac{-2\Delta G_A}{xRT}\right) \quad (2.9)$$

Since ΔG_A is always negative, p is always higher than p_{eq} . As a consequence, the formation of a solid solution with a non-forming hydride has the effect of making the AH_x hydride less stable. The considered relation is valid when the alloy decomposes upon hydrogenation. However, most of the time the AB_n alloy will not decompose upon hydrogenation, but instead it reacts as a ternary hydride:



Generally, the equilibrium pressure of reaction (2.10) will be higher than in reaction (2.1).

In Miedema's model it is assumed that, in a compound of metals A and B, their atomic cells are similar to the atomic cells of the pure metals. After hydrogenation the hydrogen atoms will bond with an A atom, but they will also be positioned close to B atoms: the atomic contact between A and B that gave the heat of formation of the binary compound is therefore gone. The contact surface is about the same for $A-H$ and B_n-H , so that the ternary hydride AB_nH_{m+p} is energetically equivalent to a physical mixture of AH_m and B_nH_p [12]. From these considerations, a semi-empirical relation for the heat of formation of a ternary hydride can be written as [11]:

$$\Delta H (AB_nH_{x+y}) = \Delta H (AH_x) + \Delta H (B_nH_y) - \Delta H (AB_n) \quad (2.11)$$

which is usually referred as Miedema's *rule of reversed stability* and states that the heat of formation of a ternary hydride is the difference between the sum of the heat of formation

Formula	H ₂ (wt.%)	ΔH (kJ mol ⁻¹ H ₂)	Desorption T for 0.1 MPa (°C)
Mg ₂ FeH ₆	5.5	98	320
Ca ₄ Mg ₄ Fe ₃ H ₂₂	5.0	122	395
Mg ₂ NiH ₄	3.6	64	250
CaMgNiH ₄	3.2	129	405

Table 2.1: Hydrogen storage properties of selected complex transition metal hydrides. Adapted from [15].

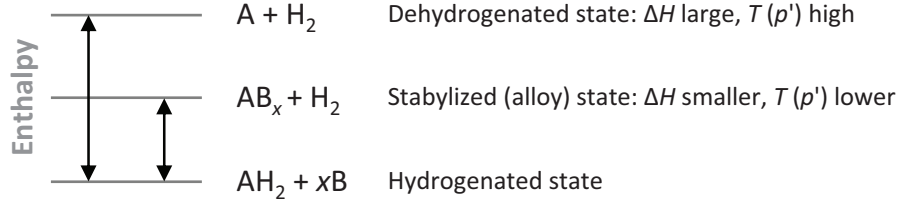


Figure 2.3: Concept of destabilization of a hydride, introducing a different phase to favour alloy formation. Adapted from [13].

of the elemental hydrides and the enthalpy of formation of the alloy. Because atom A is an hydride-forming element, ΔH (AH_x) is negative and has a large absolute value, while ΔH (B_nH_y) is small (or even positive) and may be ignored. Because of the minus sign associated with the alloy enthalpy of formation, when the alloy is more stable (enthalpy more negative) the right-hand term becomes more positive and the ternary hydride becomes more unstable. Therefore, Miedema's rule asserts that *less stable alloys form more stable hydrides*.

2.1.3.2 Destabilized and Reactive Hydrides

The rule of reversed stability can be usefully applied to find hydrides with a low enthalpy of formation: the ΔH of the hydride is reduced by the enthalpy of formation of the second compound from the initial phase. As depicted in figure 2.3, it is the application of reaction (2.8) backwards to obtain a more stable hydride. So the term *destabilization* of a hydride is used when a metal hydride AH_n is mixed with a species B that can form an alloy with the species A during dehydrogenation [13, 14]. The properties of some complex transition metal hydrides are reported in table 2.1.

The reduction of ΔH leads to a higher plateau pressure at the same temperature. This means that, from a thermodynamic and practical point of view, the destabilized system will work at a lower temperature to provide the hydrogen pressure required.

This concept was brought further with the introduction of *reactive hydride composite* approach [16, 17]: during the endothermic dehydrogenation reactions of two or more hydrides (typically a complex hydride with a binary one), the exothermic formation of a number of compounds proceeds and the total reaction enthalpy is hence reduced [18, 19]. In spite of the lower ΔH of reaction, in some cases the dehydrogenated compounds can react during hydrogenation, too, forming the starting hydride at more moderate conditions [20]. A short list of reactive hydride composites and their properties is reported in table 2.2.

Reactive Hydride Composite	H ₂ (wt.%)	ΔH (kJ mol ⁻¹ H ₂)	Ref.
MgH ₂ + 2 LiBH ₄	11.4	46	[21]
2 NaBH ₄ + MgH ₂	7.9	62	[22]
NaBH ₄ + 2 MgH ₂	7.7	69	[23]
Ca(BH ₄) ₂ + MgH ₂	7.7	47	[24]

Table 2.2: Reactive hydride composites and their enthalpies.

2.1.4 Kinetics

Hydrogen adsorption/desorption (a/d) mechanism in a metal/hydride system is a complicated process based on different steps briefly described in figure 2.4 and in section 2.1.1. The overall reaction kinetics is limited by the slowest step, the rate-limiting step. In the laboratory scale and development of new materials, it is recommended that heat and mass transport do not represent this step. This translates in good care in the design and use of the sample holder in order to ensure maximum heat conduction and minimal hydrogen flow resistance. On the other hand, for practical and prototypical applications, heat and mass transport will be extremely important parameters.

For hydride characterization, the curve of kinetics for a given reaction is the transformed fraction (also, the a/d hydrogen) versus time. The dependence of this curve on pressure and temperature should be investigated in order to deduce the rate-limiting steps of the reaction. In the case of hydrogen-metal reaction, the situation is particularly complex because of the heat of reaction, relatively fast reaction rates, poor thermal conductivity of the hydride phase, and embrittlement of the products. Sample size, particle size, surface properties, and the purity of the solid and gas phases are also factors that could have an important impact on the kinetics of a given sample. All these facts make a simple kinetic equation useless and the comparison of different experiments a difficult task [6].

The aim of mathematical analysis is to individuate the limiting step comparing the experimental data with some theoretical models, obtained assuming that a slowest step is

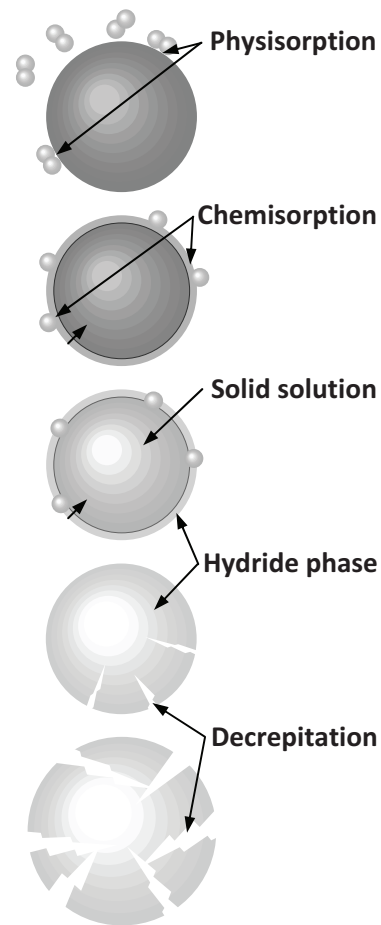


Figure 2.4: Absorption process steps.

present. Most models were elaborated to describe homogeneous reaction kinetics, namely the evolution of reactions in which all the reactants are in the same physical state. The direct reactions between the metal and gaseous hydrogen are solid-gas-phase reactions, which differ in some aspects from homogeneous reactions. However, it is possible to take for granted the fact that they can be described within the same theoretical framework of homogeneous reactions [25], in order to analyze the data in a mathematically accessible way.

In solid-state reactions, the fraction of a material that has reacted — the fractional reaction α — is used as a parameter for representing the change in the concentration of that substance in the original solid. The rate of a solid-state reaction can be expressed by means of the following general law:

$$\frac{d\alpha}{dt} = A \exp\left(-\frac{E}{RT}\right) f(\alpha) \quad (2.12)$$

where A is the pre-exponential factor of Arrhenius, E the activation energy, R the gas constant, T the absolute temperature and $f(\alpha)$ a kinetic model function depending on the reaction mechanism [25, 26]. There are several models that result in functions which can be used to analyze hydrogenation/dehydrogenation kinetics; an exhaustive list is reported in [26].

2.2

Metal Hydrides

Metals, intermetallic compounds and alloys generally react with hydrogen and form mainly solid metal–hydrogen compounds. Hydrides exist as ionic, polymeric covalent, volatile covalent and metallic hydrides. The demarcation between the various types of hydrides is not sharp, they merge into each other according to the electronegativities of the elements concerned. This section describes metals and intermetallic compounds which form metallic hydrides with hydrogen.

Electropositive elements such as yttrium, scandium, the lanthanides, actinides and elements belonging to the group of titanium and vanadium are the most reactive and can easily form hydrides. The crystal structure of the formed hydride phase remains unchanged with respect to that of the host metal, where hydrogen is contained in octahedral, tetrahedral interstitial sites, or a combination of both. This is the reason why these compounds are also called interstitial metal hydrides. Only a small number of transition metals has no stable hydrides. Most of these hydrides are generally not suitable for practical applications in the storage field. There are exception, as magnesium hydride, which will be described later.

2.2.1

Intermetallic Hydrides

Intermetallic compounds present more appealing properties. In general, the hydride formula is $A_nB_mH_p$, in which varying the elemental composition it is possible to change the hydrogen absorbing properties of the material, following the concepts described in section 2.1.3. The element labelled as A is typically a rare earth or alkaline earth metal, tending to form a stable hydride, while element B is a transition metal, which only

forms unstable hydrides. It has been found that in several intermetallic compounds for which the ratio of the molar amount of component B and component A takes the values $m/n = 0.5, 1, 2, 5$, the $c_H = N_H/N_M$ ratio can be higher than 2 [1].

AB₅

AB₅ alloys are characterized by a hexagonal crystal structure. Element A is usually one of the lanthanides, Ca, Y, or Zr, but for industrial applications mischmetal (a generic name used for an alloy of rare earth elements in various naturally-occurring proportions) is mostly used. The B site is mainly nickel but substitution with other transition elements is possible. By substitution on the A and B sites, hydrogen storage properties such as plateau pressure and slope, hysteresis, resistance to cycling and contamination can be controlled. In many instances the improvement of one property may lead to the deterioration of another. Thus, optimization by multiple substitution is an active field of research of AB₅ alloys. LaNi₅ has been the most studied in this family of compounds, absorbing around 1.5 wt.% H₂ hydrogen and easily activated. The operating temperature and pressure are always very close to ambient. The drawbacks of these systems are the low gravimetric hydrogen capacity and the degradation after relatively few a/d cycles [27].

AB₂ Laves Phases

The AB₂ type alloys are a vast and versatile group, considered quite interesting for hydrogen storage for its thermodynamics properties which make them usable at ambient temperature already. The crystalline structures consist of three types, which are named after the representatives cubic MgCu₂ (C15), hexagonal MgZn₂ (C14) and hexagonal MgNi₂ (C36); they all have sub-structures ascribable to Laves phases, which is also an alternative name for this group of alloys. Laves phases form the largest group of intermetallics and thus have a wide range of properties. Their stability depends on various factors such as: geometry, packing density, valence electron concentration, or the difference in electronegativity. However, these concepts are of limited value for the prediction of new alloys [28]. Element A can be Ti, Zr, Hf or Th, but Laves phases have been recognized to be attractive hydrogen storage materials, when Ti [29] and Zr are used [30, 31, 32], while with a rare earth the compound tends to disproportionation and amorphization. Element B is typically a 3d element or combination of them: in order to achieve optimum hydrogen storage properties, multicomponent systems Zr_{1-x}T_x(Mn, Cr)_{2-y}M_y (where T = Ti, Y, Hf, Sc, Nb and M = V, Mo, Mn, Cr, Fe, Co, Ni, Cu, Al, Si, Ge) are usually used. They generally have relatively good hydrogen storage capacity and kinetics, long cycling life and low cost, but are usually too stable at room temperature and are sensitive to gas impurities [27, 33, 34]. Small amounts of oxygen can cause a permanent loss of capacity for an AB₂ compound. A profitable characteristic is the metal segregation at the surface: this leaves a greater abundance of B on the surface that favours the adsorption and dissociation of hydrogen molecules [35].

AB

The AB family is represented mainly by ZrNi, the first intermetallic compound with storage properties to be known, and TiFe, the first application of an intermetallic compound in a hydrogen powered car [5]. The last compound has a capacity of around 1.9 wt.% H₂

and its constituents are very cheap. However, the process of activation of this material is problematic for the easy formation of a titanium oxide layer and high temperatures and pressures are also required to achieve a reversible maximum capacity (the alloys present two plateaux). These difficulties have contributed to the abandonment of such materials [27].

A₂B

A₂B type alloys have mostly C16 cubic structure, with B usually a transition metal. The material with the best performance among the alloys of this family is Mg₂Ni, able to absorb about 3.6 wt.% H₂. The operating temperatures allowing plateau pressures higher than 0.1 MPa are above 250 °C, but the presence of Ni, which plays a catalytic activity for the adsorption and dissociation of hydrogen, allows favourable a/d kinetics [35].

2.2.2

Magnesium Hydride

Magnesium is an attractive medium for hydrogen storage, thanks to its H₂ gravimetric capacity of 7.6 wt.% and a volumetric density higher than that of hydrocarbons [36]. Magnesium, one of the alkaline earth metals, is the eighth most abundant element on the Earth's crust [37]; being so accessible, it can be considered a low cost material. Mg based hydrides have interesting functional properties, such as heat resistance, vibration absorption, reversibility and cyclability [33]. Magnesium hydride differs to other metal hydrides according to the type of M–H bonds, crystal structure and properties, and is similar to ionic hydrides of alkali and others alkaline earth metals [38].

Metallic Mg crystal structure is hcp, while in normal conditions β-MgH₂ has a tetragonal crystal structure of the rutile type [39] (with $a = b = 4.501 \text{ \AA}$ and $c = 3.010 \text{ \AA}$, space group P4₂/mnm [40, 41]). In specific conditions of high pressure it undergoes polymorphic transformations [41] to form γ-MgH₂, metastable at ambient temperature and pressure, having an orthorhombic structure (with $a = 4.5213 \text{ \AA}$, $b = 5.4382 \text{ \AA}$ and $c = 4.9337 \text{ \AA}$, space group Pbcn [40]) and then α-MgH₂ with a hexagonal structure (with $a = c = 4.7902 \text{ \AA}$ and space group Pa $\bar{3}$ [41]).

β-MgH₂ is a rather stable compound, with ΔH of formation of $-74.5 \text{ kJ mol}^{-1}$ [42], resulting in an hydride decomposition and hydrogen release that can take place at temperatures above 300 °C for an equilibrium pressure of interest for practical applications. This is a major drawback for a material that is candidate for the use in hydrogen tanks for vehicular applications.

Moreover, the hydrogenation and dehydrogenation reactions for pure magnesium are very slow. As described in sections 2.1.1 and 2.1.4, there are several factors which can influence a reaction of this kind and Mg presents various of them. The first impediment could be surface oxidation MgO of magnesium exposed to air [43] and thus to start hydrogen absorption, the oxide layer should be embrittled by activation. The process may consist in cyclic heating and cooling in vacuum or hydrogen pressure, but even after this, magnesium could form hydride completely after several hours [43]. Moving further in the chemisorption process, the slow kinetics can be justified by the low *sticking coefficient* of hydrogen on the Mg ($\sim 10^{-6}$). That implies that, after the impact, a very small fraction of H₂ molecules remains stucked to the surface [44]. Another cause of the slow rate of hydrogenation is the low dissociation rate of hydrogen molecules on the metal surface [45].

The activation barrier for the dissociation of hydrogen depends strongly on the geometry of the adsorption site and a clean surface of pure magnesium needs a very high energy for dissociation. Additionally, the diffusion of dissociated hydrogen atoms within metal hydride is very slow. In section 2.1.2, it was shown how the growth rate of MgH_2 phase depends on the hydrogen pressure since the thermodynamic driving force for the reaction increases with it. Nevertheless, if the initial hydrogenation process is fast enough, a surface MgH_2 -layer that blocks the hydrogen penetration is formed [46, 47]. The growth of the magnesium hydride phase occurs with a sluggish motion of the Mg-MgH_2 interface [48] resulting from the hydrogen diffusion along this interface rather than through the hydride layer [49]. When the hydride thickness reaches 30–50 μm , the reaction stops almost completely [43], requiring to use powder rather than bulk material for hydrogenation [38].

2.2.2.1 Improvement of MgH_2 Hydrogen a/d Properties

Mg-based systems have to be adequately treated in order to improve the sorption properties. Studies are focused to reduce the desorption temperature and to obtain faster re/dehydrogenation kinetics, which can be influenced modifying surface and grain size by milling and/or adding other transition metal and their oxides, as catalysts or alloying elements.

The surface is an important factor for hydrogen kinetics. At the beginning is not the limiting step, but after a partial formation of MgH_2 layer it becomes important as the diffusion coefficient in the hydride is much smaller than in Mg [50]. The high energy ball milling, which relies on mechanical impact and friction to refine powder materials and obtain nano-crystalline material, is a possible way to overcome this problem. Milling can produce structural defects, phase and/or crystallinity change [51]. A heavily damaged or amorphous structure possesses different hydriding characteristics from the crystalline counterpart. In general, hydrogen atoms occupy similar interstitial sites in the amorphous structure to those in the crystalline structure, but the binding energy of the interstitial site varies, owing to lattice distortion in the non-crystalline status. It has been assessed that nano-structured materials can yield much better results for storing high content of hydrogen with fast kinetics [43].

The use of catalysts in the Mg-based materials is also decisive to improve kinetic properties. The use of one or more catalysts is often associated to high energy ball milling, which not only allows the reduction of grain size to nanoscale, but also allows the uniform dispersion of the catalyst within the material. The main classes of catalysts used in these systems are transition metals and their oxides [44, 52].

The catalytic activity of these metals or alloys occurs in one of the stages of the a/d process, which is likely the dissociation of the hydrogen molecule at the metal surface [52]. The activation barrier of dissociative process, mentioned also in section 2.1.1, is the Pauli repulsion due to overlapping of the hydrogen molecule electronic orbital with the s -band of the substrate [53]. This repulsion is lowered by the presence of a transition metal, for the presence of d -type orbitals incompletely filled, which are more localized than s -band. In this way the system does not pass through the physisorption of the molecule, but hydrogen is absorbed directly as dissociated [53]. This mechanism shows how some transition metals absorb hydrogen by dissociation, while simple and noble metals cannot.

In addition to these transition metals, their oxides also appear to be excellent catalysts for magnesium, if processed with high energy ball milling. Transition metal oxides (such

as Nb_2O_5 , V_2O_5 , TiO_2 , Al_2O_3 , Fe_3O_4 , Cr_2O_3 , La_2O_3) may also show catalytic properties outranking those of constituting transition metals [38, 54, 55]. The mechanisms that these oxides exploit in their catalytic activity is not solved yet, but it is probably associated to the possibility of the transition elements to have different valence states, resulting in different electronic configurations.

Alloying with other transition metal is also a method which has shown a solution to reduce the desorption temperature and to remove other thermodynamic constraints. In this case, rules similar to (2.11) applies, as there is the creation of a new species. It is then possible to tailor properties of magnesium creating a very wide range of intermetallic compounds [27, 38].

2.3 Complex Hydrides

Complex hydrides are salt-like materials in which hydrogen is covalently bound to the central atoms. In this way there is the formation of a crystal structure consisting of so-called complex anions. In general, complex hydrides have the chemical formula $\text{A}_x\text{Me}_y\text{H}_z$. Compounds where position A is preferably occupied by elements of the alkaline and alkaline earth metals, and Me is either boron or aluminum are known and have been already deeply investigated. Nevertheless, another possibility is that complex hydrides are built by transition metal cations. Complex metal hydrides have been known for more than 50 years, but for many years they were not taken into account for reversible hydrogen storage due to the high kinetic barriers of the decomposition which needed high temperatures. This perspective changed in 1997 when Bogdanović and Schwickardi discovered that the kinetic barrier of the decomposition of the complex metal hydride NaAlH_4 can be lowered by the addition of Ti catalysts and that the material becomes reversible close to useful technical conditions [56]. Moreover, they showed not only that catalysts can improve the kinetics of dehydrogenation, but also that re-hydrogenation becomes possible under mild conditions. This finding stimulated the publication of an impressive number of papers focusing on the synthesis and the properties of complex hydrides. The major goal is to understand the basic steps of dehydrogenation and re-hydrogenation and the role played by catalysts. Many complex metal hydrides have high hydrogen gravimetric storage capacities and some of them are commercialized. Some complex hydride systems, such as $\text{Al}(\text{BH}_4)_3$, have an extremely high volumetric hydrogen density of up to 150 kg m^{-3} , much higher than the volumetric density of 70 kg m^{-3} of liquid hydrogen. This makes complex transition metal hydrides interesting as potential storage materials [57].

2.3.1 Complex Borohydrides

In 1939 Schlesinger *et al.* prepared $\text{Al}(\text{BH}_4)_3$, the first example of a complex metal borohydride [58]. In the following years the Schlesinger group prepared different new complex borohydride compounds, but most of the results were published later [59]. Nowadays some of the complex borohydrides (NaBH_4 , KBH_4) are widely used in organic synthesis for the reduction of aldehydes or ketones to alcohols [60]. One important property of complex borohydrides is the high gravimetric H_2 density. The low atomic weight of boron and the high amount of bound hydrogen make this complex system interesting for hydrogen

	Molecular weight (g mol^{-1})	Melting point ($^{\circ}\text{C}$)	Decomposition T ($^{\circ}\text{C}$)	Hydrogen content (wt.%)
LiBH_4	21.8	275	320 [75]	18.4
NaBH_4	37.8	505	450 [81]	10.6
KBH_4	53.9	585	584 [82]	7.4
$\text{Be}(\text{BH}_4)_2$	38.6	–	–	20.7
$\text{Mg}(\text{BH}_4)_2$	53.9	–	320 [85]	14.8
$\text{Ca}(\text{BH}_4)_2$	69.8	–	360 [95]	11.5

Table 2.3: Physical properties of alkaline and alkaline earth metals borohydrides. Adapted from [57].

storage. $\text{Be}(\text{BH}_4)_2$ is the known compound with the highest hydrogen content (more than 20 wt.%), but its high toxicity excludes this material from any use as a practical storage solution. Most of the metal borohydrides show high stability to temperature, making the liberation of hydrogen difficult. They cannot be decomposed with the waste heat of a PEM fuel cell, which makes their use impractical, especially in vehicular application. Another important disadvantage is the poor reversibility under moderate technical conditions. Some physical properties of the most important complex borohydrides are listed in table 2.3.

2.3.1.1 Thermodynamics and Stability of Borohydrides

In the study of hydrogen storage in metal hydrides, the chemical potential of gaseous H_2 is considered equal to that of hydrogen dissolved in the metal in the two-phase regime, as in (2.2). This leads to a constant equilibrium pressure of hydrogen at constant temperature (plateau pressure). The PCI plots were only recently achieved for complex hydrides, revealing the existence of a two-phase regime also for the decomposition and formation of complex hydrides [56, 61]. Elevated temperature or catalysts are required to reach quasi-equilibrium conditions.

The explanation for the plateaux is similar to that for metal hydride: the chemical potential of hydrogen in the various phases remains unaltered and only the amount of the corresponding phases changes. So, from isotherms determined at various temperatures, van't Hoff plots of the corresponding plateau pressures reveal the full set of thermodynamic parameters, that is enthalpy and entropy of reaction.

The thermodynamic characterization by means of PCI measurements has been reported for only a few complex hydrides. An empirical model has been developed to describe the stability of complex hydrides. In case of metal borohydrides the stability is in relation to the localization of the charge on the anion. The enthalpy of formation of a series of borohydrides was calculated by means of density functional theory (DFT) and

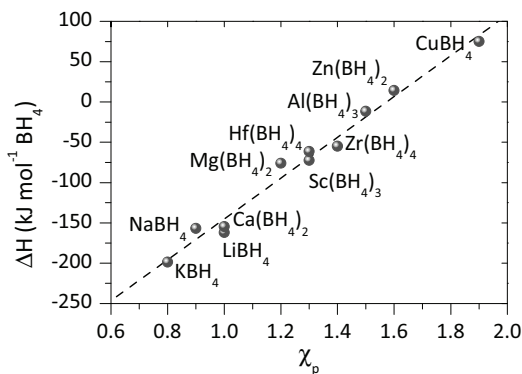


Figure 2.5: Link between the heat of formation ΔH and the Pauling electronegativity χ_p of the cation for various borohydrides. Adapted from [63].

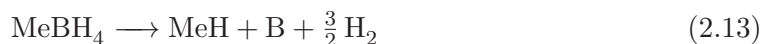
a linear relationships between the enthalpy of formation and the electronegativity was found [62].

In fact, the properties of the bonds and the characteristics of metal borohydride systems strongly depend on the electronegativity difference between the metal atom and boron ($\chi = 2.01$). While for the compounds NaBH_4 ($\chi_{\text{Na}} = 0.93$) and KBH_4 ($\chi_{\text{K}} = 0.82$) the electronegativity difference is large, the difference between Al ($\chi = 1.47$) and B in covalently bound aluminum borohydride is much smaller. As a consequence, $\text{Al}(\text{BH}_4)_3$ is a liquid at room temperature. The same behavior is observed for $\text{Be}(\text{AlH}_4)_2$ with the same small electronegativity difference between Be ($\chi = 1.47$) and B. In this compound the $[\text{BH}_4]^-$ units are covalently bonded via hydrogen bridges to beryllium. Theoretical calculations of a series of various metal borohydrides have shown that in all cases the bond between the metal cation and the $[\text{BH}_4]^-$ anion is an ionic bond and that charge transfer from the metal cation to the anion governs the stability of the metal borohydrides [62]. Figure 2.5 shows the linear relation between the heat of formation of $\text{Me}(\text{BH}_4)_n$ and the Pauling electronegativity χ_p of the metal cation Me, as predicted by first-principles calculations [62, 63].

Furthermore, the experimentally measured decomposition temperature of the borohydrides decreases with the increasing electronegativity. Mixed metal borohydrides may be synthesized with the composition properties that approach the average of those of the single metal borohydride [62, 64].

2.3.1.2 Decomposition of Complex Borohydrides

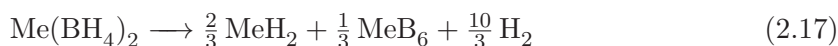
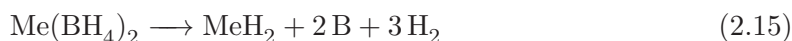
Dealing with the decomposition of alkali metal borohydrides to form metal hydrides, the reaction can be described as follows:



with the release of 1.5 mol H_2 . There is also a possibility where hydrogen is released completely and metal boride is produced.



For alkaline earth borohydrides the following decomposition reactions are possible:



with the production of alkaline earth metal hydride and boron metal, the formation of metal boride or a combination of the formation of the hydride and a metal boride compound. Another possible pathway to the release of hydrogen during the decomposition of metal borohydride compounds is the formation of diborane or heavier boranes. These volatile compounds have the disadvantage of polluting the catalyst or the membrane of a fuel cell. In the case of a potential reversible reaction, the storage capacity of the system is reduced over time. Above all, diborane and other volatile boranes are highly toxic. Thermal desorption studies revealed for Li-, Na, and K-borohydrides the formation of alkali hydride as decomposition products above 430 °C. While Mg-, Sc, and Zr-borohydrides

decompose through the formation of intermediate phases and/or borides, $\text{Zn}(\text{BH}_4)_2$ decomposes directly to elemental Zn [62].

2.3.2

Lithium Borohydride, LiBH_4

LiBH_4 is one of the most used compounds in organic chemistry as a reducing agent for aldehydes, ketones, acid chlorides, lactones, epoxides and esters [65]. After $\text{Be}(\text{BH}_4)_2$, LiBH_4 has the second highest hydrogen content (18.4 wt.%) of all alanates and borohydrides. With this hydrogen content it could be a very attractive hydrogen storage material: in fact, it is one of the most interesting and studied complex hydrides.

2.3.2.1 Synthesis and Crystal Structure

LiBH_4 was first prepared by the reaction of ethyl lithium with diborane [66], and can be also prepared by metathesis reaction starting from NaBH_4 and Li halides or chlorides [67, 68]. Under rigorous conditions of temperature between 550 and 700 °C and hydrogen pressures between 3 and 15 MPa, LiBH_4 can be prepared in a direct synthesis starting from lithium (or lithium hydride) and boron [69]. More recently, LiBH_4 has been directly synthesized from a mixture of elements exposed to hydrogen at 700 °C and 15 MPa [20] and it has been demonstrated the possibility of the formation of LiBH_4 at room temperature [70] by high energy reactive milling of the decomposition products of the dehydrogenation reaction:



The first crystal structure analysis of LiBH_4 was performed in 1947, with the conclusion that the space group of the room temperature structure is Pcmn [71]. After re-investigation of the structure using synchrotron X-ray powder diffraction data, orthorhombic symmetry was confirmed. The space group is Pnma with cell dimensions $a = 7.178\,58 \text{ \AA}$, $b = 4.436\,86 \text{ \AA}$ and $c = 6.803\,21 \text{ \AA}$ at 25 °C [72]. The tetrahedral $[\text{BH}_4]^-$ anions are strongly distorted with respect to bond lengths and bonds angles and are aligned along two orthogonal directions. LiBH_4 shows a phase transition at 118 °C to a hexagonal structure (space group $\text{P6}_3\text{mc}$) with $a = 4.276\,31 \text{ \AA}$, $b = 4.436\,86 \text{ \AA}$ and $c = 6.948\,44 \text{ \AA}$ at 135 °C. The phase transition is endothermic with a transition enthalpy of 4.18 kJ mol^{-1} .

2.3.2.2 Decomposition of LiBH_4

In the first thermal desorption experiments under ambient pressure and in a hydrogen atmosphere up to 1 MPa several endothermic peaks were observed [73, 74]. The first two peaks at 110 and 280 °C describe a structural phase transformation and the melting of the material. The main amount of hydrogen (80 wt.%) is liberated from the molten LiBH_4 in a temperature range between 320 and 380 °C. Under these conditions, one hydrogen atom remains in the structure of LiH. More advanced experiments have shown different stages of hydrogen liberation [75, 76]. In the range between 100 and 200 °C a small amount of hydrogen (0.3 wt.%) is released. After melting at 280 °C (without hydrogen release) an additional 1 wt.% H_2 is released at about 320 °C. After this decomposition reaction, a second hydrogen release step is observed starting at 400 °C. Up to 600 °C an overall amount of 9 wt.% hydrogen is produced. This is half of the total hydrogen in LiBH_4 ,

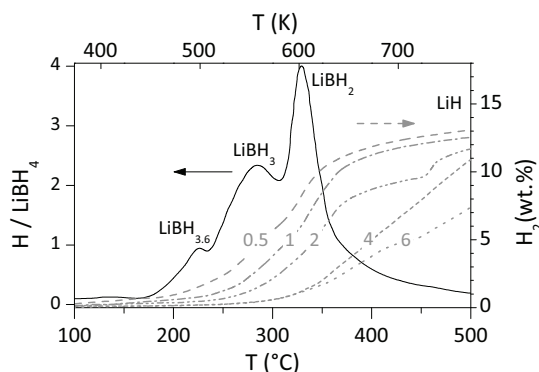


Figure 2.6: Integrated thermal desorption spectra for catalyzed LiBH_4 obtained for various heating rates, from 0.5 to 6°C min^{-1} . Adapted from [77].

resulting in a product with the general composition LiBH_2 . It can be generally concluded that LiBH_4 releases only 13.4 wt.% H_2 when decomposed according to reaction (2.18), starting above 300°C and having a maximum desorption rate between 400 and 500°C , as it is shown in figure 2.6. Not all the theoretical hydrogen content can be easily released, due to the high stability of LiH which desorbs hydrogen only above 730°C [77]. It was shown by Raman spectroscopy, X-ray diffraction studies, and NMR investigations that, during the decomposition of LiBH_4 , the boron hydride cluster $[\text{B}_{12}\text{H}_{12}]^{2-}$ is formed as an intermediate [78, 79].

In principle, re-hydrogenation of the decomposition products LiH and B to LiBH_4 is possible. Besides the high dehydrogenation temperature, the problem of using LiBH_4 as a hydrogen storage material is the complexity of the recycling mechanism: as reported by Orimo *et al.* [80], reaction (2.18) is reversible only in extreme pressure and temperature conditions (35 MPa H_2 and 600°C).

2.3.3

Magnesium Borohydride, $\text{Mg}(\text{BH}_4)_2$

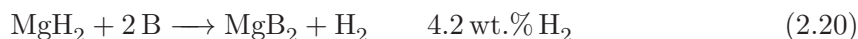
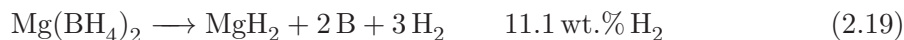
2.3.3.1 Synthesis and Crystal Structure

With a hydrogen content of 14.8 wt.%, $\text{Mg}(\text{BH}_4)_2$ seems to be interesting for hydrogen storage, but the high thermal stability (decomposition temperature around 300°C) makes it less suitable. Starting from MgCl_2 and LiBH_4 , $\text{Mg}(\text{BH}_4)_2$ was prepared in ether solution. After drying at 145°C a solvent free crystalline material was obtained, which was used for high-resolution X-ray diffraction studies [83, 84]. The evaluation of several mechanochemical and wet chemical preparation methods showed that solvent-free and pure α - $\text{Mg}(\text{BH}_4)_2$ can only be obtained by direct wet chemical synthesis [85].

Qualitatively, the crystal structure of $\text{Mg}(\text{BH}_4)_2$ is similar to that of other borohydrides, but a closer look in more detail shows a very complex crystal structure. Each Mg^{2+} atom in the hexagonal structure (space group $P6_1$) is coordinated by eight H atoms from four $[\text{BH}_4]^-$ tetrahedra. Each Mg dodecahedra is linked by $[\text{BH}_4]^-$ bridges to four neighboring dodecahedra forming a network [83, 84].

2.3.3.2 Decomposition

During thermal treatment, α -Mg(BH₄)₂ first undergoes a phase transformation at about 190 °C before it further decomposes in several steps to MgH₂, Mg, and MgB₂ (reactions (2.19) and (2.20)) [85]. The weight loss between 290 and 500 °C is 13 wt.% H₂ with a maximum release between 300 and 400 °C. Small amounts of B₂H₆ were detected by mass spectrometric measurements. The decomposition mechanism can be described as follows:



For the first decomposition step the formation of [B₁₂H₁₂]²⁻ anion as a possible intermediate phase is discussed [86]. Different enthalpy values in the range -40 to 57 kJ mol⁻¹ H₂ for the first decomposition step at about 277 °C have been determined from experimental data [86, 87, 88]. From DFT calculations a reaction enthalpy of 38 kJ mol⁻¹ H₂ at 27 °C was confirmed [89]. Cycling experiments performed at 350 °C under 10 MPa hydrogen lead to re-absorption of more than 3 wt.% hydrogen, showing that the second decomposition step is reversible [85, 88].

2.3.4

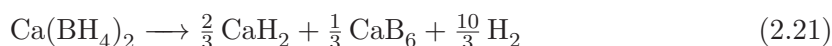
Calcium Borohydride, Ca(BH₄)₂

2.3.4.1 Synthesis and Crystal Structure

Calcium borohydride, Ca(BH₄)₂, contains 11.5 wt.% H₂. It can be prepared by reacting calcium hydride or alkoxides with diborane or by reaction in THF [90, 91, 92]. Starting from ball-milled CaH₂ added to triethylamine borazane complex, Ca(BH₄)₂ and CaH₂ were obtained as by-products after heating to 140 °C, cooling and washing with n-hexane [93]. Without any solvent, Ca(BH₄)₂ can be obtained by ball milling of CaH₂ and MgB₂ and subsequent hydrogenation at elevated temperatures [18]. Mechano-chemical synthesis from a mixture of CaCl₂ and LiBH₄/NaBH₄ under an argon pressure of 0.1 MPa has been reported to produce calcium borohydride and chlorides as by-phases [94]. Recently, calcium borohydride was prepared under rather harsh conditions by reacting ball-milled CaB₆ and CaH₂ at 70 MPa hydrogen pressure and heating to 400–440 °C [95]. The crystal structure of α -Ca(BH₄)₂ (space group Fddd) consists of Ca²⁺ atoms each coordinated octahedrally by six [BH₄]⁻ anions. Each [BH₄]⁻ has three Ca²⁺ neighbors [96]. While the bond between Ca and [BH₄]⁻ has a ionic character, the internal bonding of [BH₄]⁻ is covalent. This crystal structure has been proved to undergo polymorphic transformation when heated [97].

2.3.4.2 Decomposition

The decomposition reaction with a hydrogen release of 9.6 wt.% and an enthalpy change of 32 kJ mol⁻¹ H₂ was predicted to be [96]:



Starting from THF educt and removing the solvent in vacuum at elevated temperatures leads to the formation of the solvent-free low temperature α -phase (orthorhombic). Riktor *et al.* proposed the existence of another orthorhombic low temperature form called the

γ -form [93]. However, since the given lattice parameters are very similar to the values of the α -form and no further structure details were provided, the existence of such a phase is questionable. Further heating of the α -phase leads to transformation into the β -form (tetragonal) at about 170 °C [97, 98]. The β -form decomposes in two endothermic steps between 360 and 500 °C into an unidentified intermediate phase and CaH_2 . Interestingly, Ronnebro and Majzoub observed CaH_2 and CaB_6 as final products of the dehydrogenation at 400 °C, corresponding to the educts. From this, they conclude a reversible system with 9.6 wt.% H_2 capacity [95]. However, the synthesis conditions and therewith the conditions for hydrogen loading of 70 MPa H_2 and 400 °C might be too challenging for any application. Even the positive influence of Ti and Nb catalysts on the desorption temperatures (with TiCl_3 as a catalyst, the dehydrogenation temperature decreases by about 50 °C [99]) and the re-adsorption properties at a pressure lower than 9 MPa cannot hide the fact that the reaction temperature of 350 °C held for 24 h is unreasonable for reloading a hydrogen storage tank in mobile applications [99, 100].

2.3.5

Alanates

Alanates are complex hydrides where hydrogen is bound covalently to Al, forming the $[\text{AlH}_4]^-$ anion, which form a ionic bond with a metallic cation. The most representative compound of this group is sodium alanate, a medium temperature complex hydride with quite a high reversible hydrogen content (5.6 wt.% H_2) at moderate conditions. When compared to room temperature hydrides and to MgH_2 , sodium alanate offers a suitable compromise with relatively high gravimetric capacity at a temperature around 125 °C. The thermal decomposition of sodium alanate, releasing hydrogen, has been known for many years, but it presents very slow kinetics. NaAlH_4 was the first complex hydride to be studied for its achievable reversible storage, once catalyzed with titanium compounds [56]. It is reversibly formed in a two step reaction within the technically suitable range of up to 125 °C:



releasing 5.6 wt.% H_2 . If further release of hydrogen coming from NaH is considered, the total amount is increased to 7.4 wt.% H_2 . However, due to the high decomposition temperature of NaH (> 400 °C), for practical applications only the hydrogen coming from (2.22) and (2.23) is taken into account. The thermodynamic equilibrium of the reacting system was studied in detail by Bogdanović [101].

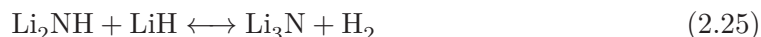
Other alanates are being studied for hydrogen storage, including LiAlH_4 , KAlH_4 , $\text{Mg}(\text{AlH}_4)_2$ and $\text{Ca}(\text{AlH}_4)_2$, but their decomposition temperatures are slightly higher [33, 102].

2.3.6

Amides/Imides

The lithium amide/imide system ($\text{LiNH}_2/\text{Li}_2\text{NH}$) is based on principles similar to borohydrides and alanates, but the molecular geometry is different because of the different coordination number of nitrogen. In LiNH_2 the two hydrogen atoms are covalently stabilized inside the $[\text{NH}_2]^-$ anion and this is bond to the positive Li^+ . The release of hydrogen

proceeds following the reactions:



The two reactions yield to a gravimetric density of 10.4 wt.% H₂, but reaction (2.25) is hardly reversible at room temperature, due to its high formation enthalpy. Reaction (2.24) does not present this problem and can be used to reversibly store H₂ up to 5.2 wt.%, below 200 °C [103].

2.4

Conclusion: a Materials Selection Approach

Hundreds of hydrides have been studied so far for the potential practical use in hydrogen storage. The assessment is usually carried out considering the following points:

- hydrogen capacity, both considering volumetric and gravimetric H₂ density;
- range of operating pressure and temperature;
- kinetics of the a/d processes;
- reversibility and degradation of properties after repeated cycles;
- cost of the material and of the system.

The first point is often graphically represented in charts similar to that in figure 2.7 [1, 36], where the different classes of hydrides are available for a first comparison of their properties. Most of the efforts in research are being focused to try to profitably use materials in the top right corner. This section of the chart was also pointed as ultimate target to address practical requirements [104]. The second point of the list can also be represented in two dimensions by the various van't Hoff plots of the considered hydrides, as shown in figure 2.8. The desired range of operative conditions (temperature and pressure close to the atmospheric) is not likely to include any of the known hydrides with best capacity performance. An acceptable compromise is to be found, because an *ideal* material for hydrogen storage does not exist, as well as for any other application.

The materials selection approach — developed for mechanical design by Ashby [105, 106] — suggests that is always possible to find the *best* solution for a specific application, taking into account the properties exploited in utilization. The selection procedure is based on indexing the characteristics of specific candidates or class of materials, optimizing the combination of multiple requirements and considering the process, too [107, 108]. From the indexes, a wide range of properties charts can be prepared, which are conceptually the same way of classifying the hydrides in figure 2.7. Since Ashby's method is suitable for several applications, recently even in the environmental field [109], an attempt to develop a similar, but simply qualitative approach for hydrogen storage materials is outlined in this work.

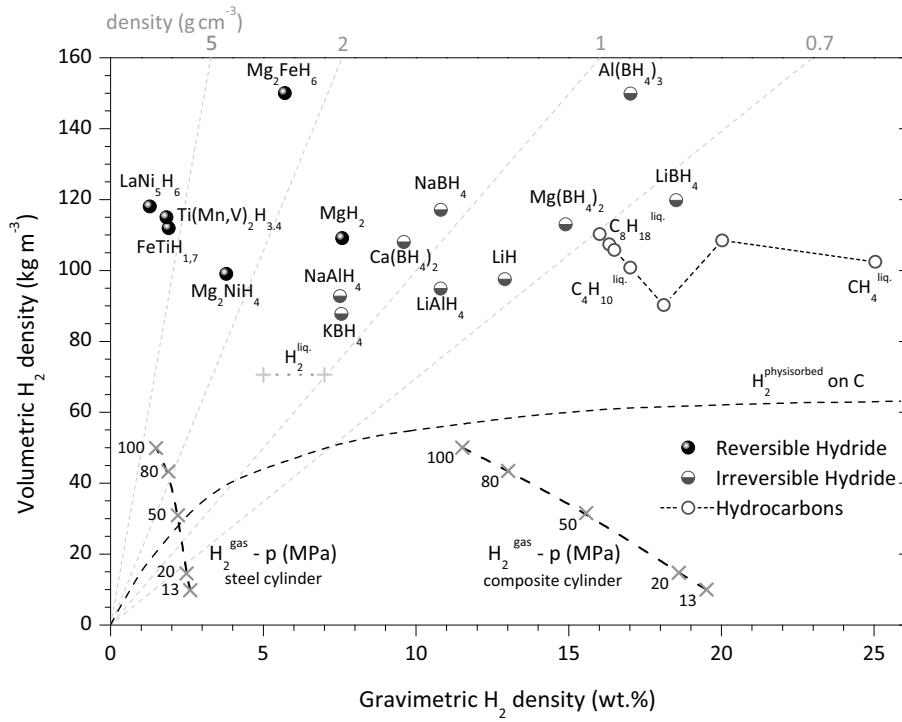


Figure 2.7: Density of hydrogen in different storage materials and technologies.

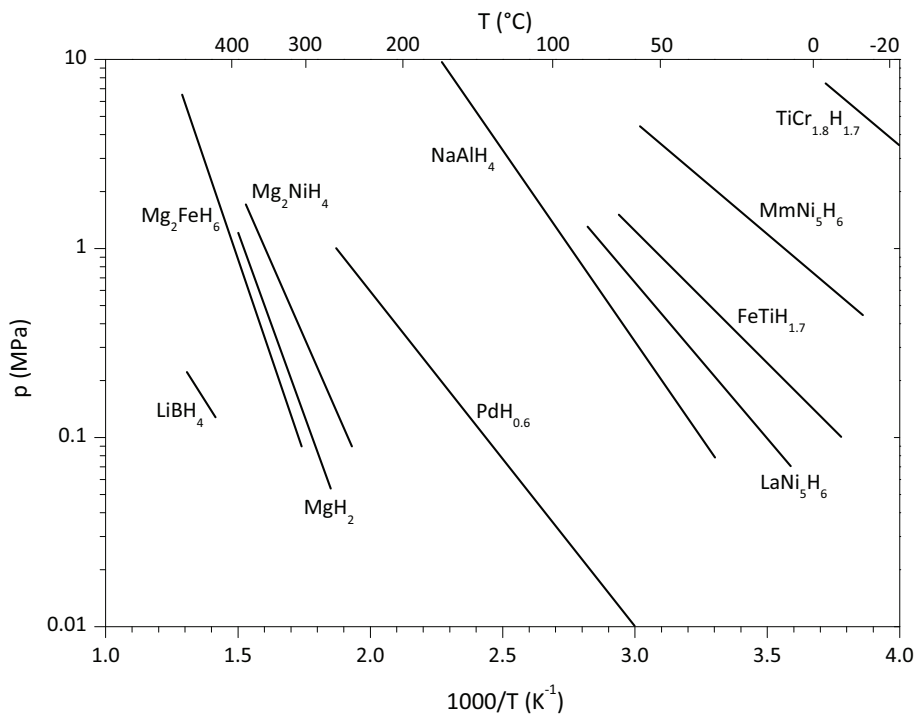


Figure 2.8: Van't Hoff plot of some technically important hydrides according to [101].

References

- 1 Züttel A., Materials for hydrogen storage, *Materials Today*, **6** (2003) 24–33. (Cited on pages 10, 17, and 27)
- 2 David E., An overview of advanced materials for hydrogen storage. *Journal of Materials Processing Technology*, **162-163** (2005) 169–177. (Cited on page 10)
- 3 Fukai Y., Site occupancy and phase stability of some metal hydrides, *Zeitschrift für Physikalische Chemie*, **164** (1989) 165–174. (Cited on page 10)
- 4 Züttel A., Wenger P., Sudan P., Mauron Ph., Orimo S., Hydrogen density in nanostructured carbon, metals and complex materials, *Material Science and Engineering: B*, **108** (2004) 9–18. (Cited on page 10)
- 5 Züttel A., “Metal Hydrides”, in: *Hydrogen as a Future Energy Carrier*, Züttel A., Borgschulte A., Schlapbach L. (eds), (2008) Wiley-VCH, Weinheim. Chap. 6.3, 188–195. (Cited on pages 11 and 17)
- 6 Huot J., “Metal Hydrides”, in: *Handbook of Hydrogen Storage*, Hirscher M. (ed.), (2010) Wiley-VCH, Weinheim. Chap. 4, 81–116. (Cited on pages 12 and 15)
- 7 Akiba E., “Metal Hydrides”, in: *Hydrogen and Fuel Cells*, Stolten D. (ed.), (2010) Wiley-VCH, Weinheim. Chap. 19, 395–413. (Cited on page 12)
- 8 Miedema A.R., The electronegativity parameter for transition metals: Heat of formation and charge transfer in alloys, *Journal of the Less Common Metals*, **32** (1973) 117–136. (Cited on page 13)
- 9 Miedema A.R., Buschow K.H.J., van Mal H.H., Which intermetallic compounds of transition metals form stable hydrides?, *Journal of the Less Common Metals*, **49** (1976) 463–472. (Cited on page 13)
- 10 Bouten P.C.P., Miedema A.R., On the heats of formation of the binary hydrides of transition metals, *Journal of the Less Common Metals*, **71** (1980) 147–160. (Cited on page 13)
- 11 van Mal H.H., Buschow K.H.J., Miedema A.R., Hydrogen absorption in LaNi_5 and related compounds: Experimental observations and their explanation, *Journal of the Less Common Metals*, **35** (1974) 65–76. (Cited on page 13)
- 12 Ivey D.G., Northwood D.O., Storing energy in metal hydrides: a review of the physical metallurgy, *Journal Material Science*, **18** (1983) 321–347. (Cited on page 13)
- 13 Vajo J.J., Olson G.L., Hydrogen storage in destabilized chemical systems, *Scripta Materialia*, **56** (2007) 829–834. (Cited on page 14)
- 14 Vajo J.J., Mertens F., Ahn C.C., Bowman R.C., Fultz B., Altering Hydrogen Storage Properties by Hydride Destabilization through Alloy Formation: LiH and MgH_2 Destabilized with Si, *Journal of Physical Chemistry B*, **108** (2004) 13977–13983. (Cited on page 14)
- 15 Yvon K., “Complex Transition Metal Hydrides”, in: *Hydrogen as a Future Energy Carrier*, Züttel A., Borgschulte A., Schlapbach L. (eds), (2008) Wiley-VCH, Weinheim. Chap. 6.4, 195–203. (Cited on page 14)
- 16 Barkhordarian G., Klassen T., Bormann R., *Composite Material Storing Hydrogen, and Device for the Reversible Storage of Hydrogen*, (2004) International Patent Application WO 2006/063 627. (Cited on page 14)
- 17 Vajo J.J., Mertens F.O., Skeith S., Balogh M.P., *Reversible Hydrogen Storage System and Methods for Use Thereof*, (2004) International Patent Application WO 2005/097 671. (Cited on page 14)
- 18 Barkhordarian G., Klassen T., Dornheim M., Bormann R., Unexpected kinetic effect of MgB_2 in reactive hydride composites containing complex borohydrides, *Journal of Alloys and Compounds*, **440** (2007) L18–L21. (Cited on pages 14 and 25)
- 19 Vajo J.J., Skeith S.L., Mertens F., Reversible Storage of Hydrogen in Destabilized LiBH_4 , *Journal of Physical Chemistry B*, **109** (2005) 3719–3722. (Cited on page 14)
- 20 Friedrichs O., Buchter F., Borgschulte A., Remhof A., Zwicky C.N., Mauron Ph., Biemann M., Züttel A., Direct synthesis of $\text{Li}[\text{BH}_4]$ and $\text{Li}[\text{BD}_4]$ from the elements, *Acta Materialia*, **56** (2008) 949–954. (Cited on pages 14 and 23)
- 21 Bösenberg U., Doppiu S., Mosegaard L., Borgschulte A., Eigen N., Barkhordarian G., Jensen T.R., Cerenius Y., Gutfleisch O., Klassen T., Dornheim M., Bormann R., Hydrogen sorption properties of MgH_2 - LiBH_4 composites, *Acta Materialia*, **55** (2007) 3951–3958. (Cited on page 15)
- 22 Pistidda C., Barkhordarian G., Rzeszutek A., Garroni S., Bonatto Minella C., Baró M.D., Nolis P., Bormann R., Klassen T., Dornheim

- M., Activation of the reactive hydride composite $2\text{NaBH}_4 + \text{MgH}_2$, *Scripta Materialia*, **64** (2011) 1035–1038. (Cited on page 15)
- 23 Garroni S., Milanese C., Girella A., Marini A., Mulas G., Menéndez E., Pistidda C., Dornheim M., Suriñach S., Baró M.D., Sorption properties of $\text{NaBH}_4/\text{MH}_2$ ($\text{M} = \text{Mg}, \text{Ti}$) powder systems, *International Journal of Hydrogen Energy*, **35** (2010) 5434–5441. (Cited on page 15)
 - 24 Siegel D.J., Wolverson C., Ozoliņš V., Thermodynamic guidelines for the prediction of hydrogen storage reactions and their application to destabilized hydride mixtures, *Physical Review B*, **76** (2007) 134102. (Cited on page 15)
 - 25 Koga N., Tanaka H., A physico-geometric approach to the kinetics of solid-state reactions as exemplified by the thermal dehydration and decomposition of inorganic solids, *Thermochimica Acta*, **388** (2002) 41–61. (Cited on page 16)
 - 26 Gotor F.J., Criado J.M., Malek J., Koga N., Kinetic Analysis of Solid-State Reactions: The Universality of Master Plots for Analyzing Isothermal and Nonisothermal Experiments, *Journal of Physical Chemistry A*, **104** (2000) 10777–10782. (Cited on page 16)
 - 27 Bououdina M., Grant D., Walker G., Review on hydrogen absorbing materials — structure, microstructure, and thermodynamic properties, *International Journal of Hydrogen Energy*, **31** (2006) 177–182. (Cited on pages 17, 18, and 20)
 - 28 Stein F., Palm M., Sauthoff G., Structure and stability of Laves phases. Part I. Critical assessment of factors controlling Laves phase stability, *Intermetallics*, **12** (2004) 713–720. (Cited on page 17)
 - 29 Töpler J., Feucht K., Results of a Test Fleet with Metal Hydride Motor Cars, *Zeitschrift für Physikalische Chemie*, **164** (1989) 1451–1461. (Cited on page 17)
 - 30 Shaltiel D., Jacob I., Davidov D., Hydrogen absorption and desorption properties of AB_2 Laves-phase pseudobinary compounds, *Journal of the Less Common Metals*, **53** (1977) 117–131. (Cited on page 17)
 - 31 Shoemaker D.P., Shoemaker C.B., Concerning atomic sites and capacities for hydrogen absorption in the AB_2 Friauf-Laves phases, *Journal of the Less Common Metals*, **68** (1979) 43–58. (Cited on page 17)
 - 32 Ivey D.G., Northwood D.O., Hydriding properties of $\text{Zr}(\text{Fe}_x\text{Cr}_{1-x})_2$ intermetallic compounds, *International Journal of Hydrogen Energy*, **11** (1986) 583–591. (Cited on page 17)
 - 33 Sakintuna B., Lamari-Darkrim F., Hirscher M., Metal hydride materials for solid hydrogen storage: a review, *International Journal of Hydrogen Energy*, **32** (2007) 1121–1140. (Cited on pages 17, 18, and 26)
 - 34 Bououdina M., Soubeyroux J.L., de Rango P., Fruchart D., Phase stability and neutron diffraction studies of the laves phase compounds $\text{Zr}(\text{Cr}_{1-x}\text{Mo}_x)_2$ with $0.0 \leq x \leq 0.5$ and their hydrides, *International Journal of Hydrogen Energy*, **25** (2000) 1059–1068. (Cited on page 17)
 - 35 Dantzer P., Properties of intermetallic compounds suitable for hydrogen storage applications, *Materials Science and Engineering: A*, **329-331** (2002) 313–320. (Cited on pages 17 and 18)
 - 36 Schlapbach L., Züttel A., Hydrogen-storage materials for mobile applications, *Nature*, **414** (2001) 353–358. (Cited on pages 18 and 27)
 - 37 Anderson D.L., Composition of the Earth, *Science* **243** (1989) 367–370. (Cited on page 18)
 - 38 Jain I.P., Lal C., Jain A., Hydrogen storage in Mg: a most promising material, *International Journal of Hydrogen Energy*, **35** (2010) 5133–5144. (Cited on pages 18, 19, and 20)
 - 39 Zachariassen W.H., Holley C.E., Stampfer J.F., Neutron diffraction study of magnesium deuteride, *Acta Crystallographica*, **16** (1963) 352–353. (Cited on page 18)
 - 40 Bortz M., Bertheville B., Böttger G., Yvon K., Structure of the high pressure phase γ - MgH_2 by neutron powder diffraction, *Journal of Alloys and Compounds*, **287** (1999) L4–6. (Cited on page 18)
 - 41 Vajeeston P., Ravindran P., Kjekshus A., Fjellvåg H., Pressure-Induced Structural Transitions in MgH_2 , *Physical Review Letters*, **89** (2002) 175506. (Cited on page 18)
 - 42 Imamura H., Masanari K., Kusuhara M., Katsumoto H., Sumi T., Sakata Y., High hydrogen storage capacity of nanosized magnesium synthesized by high energy ball-milling, *Journal of Alloys and Compounds*, **386** (2005) 211–216. (Cited on page 18)
 - 43 Zaluska A., Zaluski L., Strom-Olsen J.O., Nanocrystalline magnesium for hydrogen storage, *Journal of Alloys and Compounds*, **288** (1999) 217–225. (Cited on pages 18 and 19)
 - 44 Oelerich W., Klassen T., Bormann R., Metal oxides as catalysts for improved hydrogen sorption in nanocrystalline Mg-based materials, *Journal of Alloys and Compounds* **315** (2001), 237–242. (Cited on pages 18 and 19)

- 45 Schlapbach L., Shaltiel D., Oelhafen P., Catalytic effect in the hydrogenation of Mg and Mg compounds: surface analysis of Mg–Mg₂Ni and Mg₂Ni, *Material Research Bulletin*, **14** (1979) 1235–1246. (Cited on page 18)
- 46 Luz Z., Genossar J., Rudman P.S., Identification of the diffusing atom in MgH₂, *Journal of the Less Common Metals*, **73** (1980) 113–118. (Cited on page 19)
- 47 Krozer A., Kasemo B., Equilibrium hydrogen uptake and associated kinetics for the Mg–H₂ system at low pressures, *Journal of Physics: Condensed Matter*, **1** (1989) 1533–1538. (Cited on page 19)
- 48 Stioiu M., Grayevski A., Resnik A., Shaltiel D., Kaplan N., Macroscopic and microscopic kinetics of hydrogen in magnesium-rich compounds, *Journal of the Less Common Metals*, **123** (1986) 9–24. (Cited on page 19)
- 49 Vigeholm B., Kjoller J., Larsen B., Pedersen A.S., Formation and decomposition of magnesium hydride, *Journal of the Less Common Metals*, **89** (1983) 135–44. (Cited on page 19)
- 50 Sholl D.S., Using density functional theory to study hydrogen diffusion in metals: a brief overview, *Journal of Alloys and Compounds*, **446** (2007) 462–468. (Cited on page 19)
- 51 Berube V., Radtke G., Dresselhaus M., Chen G., Size effects on the hydrogen storage properties of nanostructured metal hydrides: a review. *International Journal of Energy Research*, **31** (2007) 637–663. (Cited on page 19)
- 52 Hanada N., Ichikawa T., Fujii H., Catalytic effect of nanoparticle 3d-transition metals on hydrogen storage properties in magnesium hydride MgH₂ prepared by mechanical milling. *Journal of Physical Chemistry B*, **109** (2005) 7188–7194. (Cited on page 19)
- 53 Harris J., Andersson S., H₂ dissociation at metal surfaces, *Physical Review Letters*, **55** (1985) 1583–1586. (Cited on page 19)
- 54 Barkhordarian G., Klassen T., Bormann R., Fast hydrogen sorption kinetics of nanocrystalline Mg using Nb₂O₅ as catalyst. *Scripta Materialia*, **49** (2003) 213–217. (Cited on page 20)
- 55 Gupta R., Agresti F., Lo Russo S., Madalena A., Palade P., Principi G., Structure and hydrogen storage properties of MgH₂ catalysed with La₂O₃, *Journal of Alloys and Compound*, **450** (2008) 310–313. (Cited on page 20)
- 56 Bogdanović B., Schwickardi M., Ti-doped alkali metal aluminium hydrides as potential novel reversible hydrogen storage materials, *Journal of Alloys and Compound*, **253–254** (1997) 1–9. (Cited on pages 20, 21, and 26)
- 57 Weidenthaler C., Felderhoff M., “Complex Hydrides”, in: *Handbook of Hydrogen Storage*, Hirscher M. (ed.), (2010) Wiley-VCH, Weinheim. Chap. 5, 117–157. (Cited on pages 20 and 21)
- 58 Schlesinger H.I., Sanderson R.T., Burg A.B., A Volatile Compound of Aluminum, Boron and Hydrogen, *Journal of the American Chemical Society*, **61** (1939) 536. (Cited on page 20)
- 59 Schlesinger H.I., Brown H.C., Abraham B., Bond A.C., Davidson N., Finholt A.E., Gilbreath J.R., Hoekstra H., Horvitz L., Hyde E.K., Katz J.J., Knight J., Lad R.A., Mayfield D.L., Rapp L., Ritter D.M., Schwartz A.M., Sheft I., Tuck L.D., Walkeret A.O., New Developments in the Chemistry of Diborane and the Borohydrides, *Journal of the American Chemical Society*, **75** (1953) 186–190. (Cited on page 20)
- 60 Brown H.C., *Organic Syntheses via Boranes*, (1975) John Wiley & Sons, Inc., New York. (Cited on page 20)
- 61 Mauron Ph., Buchter F., Friedrichs O., Remhof A., Biemann M., Zwicky C.N., Züttel A., Stability and reversibility of Li[BH₄], *Journal of Physical Chemistry B*, **112** (2008) 906–910. (Cited on page 21)
- 62 Nakamori Y., Miwa K., Ninomiya A., Li H., Ohba N., Towata S., Züttel A., Orimo S., Correlation between thermodynamical stabilities of metal borohydrides and cation electronegativities: First-principles calculations and experiments, *Physical Review B*, **74** (2006) 045 126. (Cited on pages 22 and 23)
- 63 Miwa K., Ohba N., Towata S., Nakamori Y., Züttel A., Orimo S., First-principles study on thermodynamical stability of metal borohydrides: Aluminum borohydride Al(BH₄)₃, *Journal of Alloys and Compound*, **446–447** (2007) 310–314. (Cited on pages 21 and 22)
- 64 Nickels E.A., Jones M.O., David W.I., Johnson S.R., Lowton R.L., Sommariva M., Edwards P.P., Tuning the decomposition temperature in complex hydrides: synthesis of a mixed alkali metal borohydride, *Angewandte Chemie International Edition* **47** (2008) 2817–2819. (Cited on page 22)
- 65 Fieser M., *Reagents for Organic Synthesis*, **14** (1989) John Wiley & Sons, Inc., New York. (Cited on page 23)

- 66 Schlesinger H.I., Brown H.C., Metallo Borohydrides. III. Lithium Borohydride, *Journal of the American Chemical Society*, **62** (1940) 3429–3435. (Cited on page 23)
- 67 Brown H.C., Choi Y.M., Narasimhan S., Addition Compounds of Alkali Metal Hydrides. 22. Convenient Procedures for the Preparation of Lithium Borohydride from Sodium Borohydride and Borane-Dimethyl Sulfide in Simple Ether Solvents, *Inorganic Chemistry*, **21** (1982) 3657–3661. (Cited on page 23)
- 68 Schlesinger H.I., Brown H.C., Hyde E.K., The Preparation of Other Borohydrides by Metathetical Reactions Utilizing the Alkali Metal Borohydrides, *Journal of the American Chemical Society*, **75** (1953) 209–213. (Cited on page 23)
- 69 Goerrig D., *Verfahren zur herstellung von boranaten*, (1958) German Patent 1 077 644. (Cited on page 23)
- 70 Agresti F., Khandelwal A., Evidence of formation of LiBH₄ by high-energy ball milling of LiH and B in a hydrogen atmosphere, *Scripta Materialia*, **60** (2009) 753–755. (Cited on page 23)
- 71 Harris P.M., Meibohm E.P., The Crystal Structure of Lithium Borohydride LiBH₄, *Journal of the American Chemical Society*, **69** (1947) 1231–1232. (Cited on page 23)
- 72 Soulié J.-Ph., Renaudin G., Černý R., Yvon K., Lithium boro-hydride LiBH₄: I. Crystal structure, *Journal of Alloys and Compound*, **346** (2002) 200–205. (Cited on page 23)
- 73 Fedneva E.M., Alpatova V.L., Mikheeva V.I., LiBH₄ Complex Hydride Materials, *Russian Journal of Inorganic Chemistry*, **9** (1964) 826. (Cited on page 23)
- 74 Staninevich D.S., Egorenko G.A., *Russian Journal of Inorganic Chemistry*, **13** (1988) 341. (Cited on page 23)
- 75 Züttel A., Wenger P., Rentsch S., Sudan P., Mauron Ph., Emmenegger Ch., LiBH₄ a new hydrogen storage material, *Journal of Power Sources*, **118** (2003) 1–7. (Cited on pages 21 and 23)
- 76 Züttel A., Rentsch S., Fischer P., Wenger P., Sudan P., Mauron Ph., Emmenegger Ch., Hydrogen storage properties of LiBH₄, *Journal of Alloys and Compound*, **356–357** (2003) 515–520. (Cited on page 23)
- 77 Züttel A., Borgschulte A., Orimo S., Tetrahydroborates as new hydrogen storage materials, *Scripta Materialia*, **56** (2007) 823–828. (Cited on page 24)
- 78 Orimo S., Nakamori Y., Ohba N., Miwa K., Aoki M., Towata S., Züttel A., Experimental studies on intermediate compound of LiBH₄, *Applied Physics Letters*, **89** (2006) 021 920. (Cited on page 24)
- 79 Hwang S.J., Bowman R.C., Reiter J.W., Rijssenbeck J., Soloveichik G.L., Zhao J.C., Kabbour H., Ahn C.C., NMR Confirmation for Formation of [B₁₂H₁₂]₂ Complexes during Hydrogen Desorption from Metal Borohydrides, *Journal of Physical Chemistry Letters*, **112** (2008) 3164–3169. (Cited on page 24)
- 80 Orimo S., Nakamori Y., Kitahara G., Miwa K., Ohba N., Towata S., Züttel A., Dehydriding and rehydriding reactions of LiBH₄, *Journal of Alloys and Compound*, **404–406** (2005), 427–430. (Cited on page 24)
- 81 Urgnanai J., Torres F.J., Palumbo M., Baricco M., Hydrogen release from solid state NaBH₄, *International Journal of Hydrogen Energy*, **33** (2008) 3111–3115. (Cited on page 21)
- 82 Orimo S., Nakamori Y., Züttel A., Material properties of MBH₄ (M = Li, Na, and K) *Materials Science and Engineering: B*, **108** (2004) 51–53. (Cited on page 21)
- 83 Černý R., Filinchuk Y., Hagemann H., Yvon K., Magnesium Borohydride: Synthesis and Crystal Structure, *Angewandte Chemie*, **119** (2007) 5867–5869. (Cited on page 24)
- 84 Her J.H., Stephens P.W., Gao Y., Soloveichik G.L., Rijssenbeck J., Andrus M., Zhao J.C., Structure of unsolvated magnesium borohydride Mg(BH₄)₂, *Acta Crystallographica B*, **63** (2007) 561–568. (Cited on page 24)
- 85 Chłopek K., Frommen C., Léon A., Zabara O., Fichtner M., Synthesis and properties of magnesium tetrahydroborate, Mg(BH₄)₂, *Journal of Materials Chemistry*, **17** (2007) 3496–3503. (Cited on pages 21, 24, and 25)
- 86 Li H.-W., Kikuchi K., Nakamori Y., Ohba N., Miwa K., Towata S., Orimo S., Dehydriding and rehydriding processes of well-crystallized Mg(BH₄)₂ accompanying with formation of intermediate compounds, *Acta Materialia*, **56** (2008) 1342–1347. (Cited on page 25)
- 87 Li H.-W., Kikuchi K., Nakamori Y., Miwa K., Towata S., Orimo S., Effects of ball milling and additives on dehydriding behaviors of well-crystallized Mg(BH₄)₂, *Scripta Materialia*, **57** (2007) 679–682. (Cited on page 25)
- 88 Matsunaga T., Buchter F., Mauron P., Bielman M., Nakamori Y., Orimo S., Ohba N., Miwa K., Towata S., Züttel A., Hydrogen storage properties of Mg[BH₄]₂, *Journal of*

- Alloys and Compound*, **459** (2008) 583–588. (Cited on page 25)
- 89 van Setten M.J., de Wijs G.A., Fichtner M., Brocks G., A Density Functional Study of α -Mg(BH₄)₂, *Chemistry of Materials*, **20** (2008) 4952–4956. (Cited on page 25)
- 90 Wiberg E., Hartwimmer R.Z., *Zeitschrift für Naturforschung B*, **10** (1955) 295. (Cited on page 25)
- 91 Wiberg E., Noth H., Hartwimmer R.Z., *Zeitschrift für Naturforschung B*, **10** (1955) 292. (Cited on page 25)
- 92 Mikheeva V.I., Titov L.V., *Russian Journal of Inorganic Chemistry*, **9** (1964) 789. (Cited on page 25)
- 93 Riktor M.D., Sørby M.H., Chłopek K., Fichtner M., Buchter F., Züttel A., Hauback B.C., *In situ* synchrotron diffraction studies of phase transitions and thermal decomposition of Mg(BH₄)₂ and Ca(BH₄)₂, *Journal of Materials Chemistry*, **17** (2007) 4939–4942. (Cited on pages 25 and 26)
- 94 Nakamori Y., Li H.W., Kikuchi K., Aoki M., Miwa K., Towata S., Orimo S., Thermodynamical stabilities of metal-borohydrides, *Journal of Alloys and Compound*, **446-447** (2007) 296–300. (Cited on page 25)
- 95 Rönnebro E., Majzoub E.H., Calcium borohydride for hydrogen storage: Catalysis and reversibility, *Journal of Physical Chemistry B*, **111** (2007) 12045–12047. (Cited on pages 21, 25, and 26)
- 96 Miwa K., Aoki M., Noritake T., Ohba N., Nakamori Y., Towata S., Züttel A., Orimo S., Thermodynamical stability of calcium borohydride Ca(BH₄)₂, *Physical Review B*, **74** (2006) 155 122. (Cited on page 25)
- 97 Aoki M., Miwa K., Noritake T., Ohba N., Matsumoto M., Li H.-W., Nakamori Y., Towata S., Orimo S., Structural and dehydrogenating properties of Ca(BH₄)₂, *Applied Physics A*, **92** (2008) 601–605. (Cited on pages 25 and 26)
- 98 Kim J.H., Jin S.A., Shim J.H., Cho, Y.W., Thermal decomposition behavior of calcium borohydride Ca(BH₄)₂, *Journal of Alloys and Compound*, **461** (2008) L20–L22. (Cited on page 26)
- 99 Kim J.H., Jin S.A., Shim J. H., Cho Y.W., Reversible hydrogen storage in calcium borohydride Ca(BH₄)₂, *Scripta Materialia* **58** (2008) 481–483. (Cited on page 26)
- 100 Kim J.H., Shim J.H., Cho Y.W., On the reversibility of hydrogen storage in Ti- and Nb-catalyzed Ca(BH₄)₂, *Journal of Power Sources*, **181** (2008) 140–143. (Cited on page 26)
- 101 Bogdanović B., Brand R.A., Marjanović A., Schwickardi M., Tölle J., Metal-doped sodium aluminium hydrides as potential new hydrogen storage materials, *Journal of Alloys and Compounds*, **302** (2000) 36–58. (Cited on pages 26 and 28)
- 102 Bogdanović B., Sandrock G., Catalyzed Complex Metal Hydrides, *MRS Bulletin*, **27** (2002) 712–716. (Cited on page 26)
- 103 Luo W., Rönnebro E., Towards a viable hydrogen storage system for transportation application, *Journal of Alloys and Compounds*, **404-406** (2005) 392–395. (Cited on page 27)
- 104 Satyapal S., Petrovic J., Read C., Thomas G., Ordaz G., The U.S. Department of Energy’s National Hydrogen Storage Project: Progress towards meeting hydrogen-powered vehicle requirements, *Catalysis Today*, **120** (2007) 246–256. (Cited on page 27)
- 105 Ashby M.F., Materials selection in conceptual design, *Materials Science and Technology*, **5** (1989) 517–525. (Cited on page 27)
- 106 Ashby M.F., *Materials selection in mechanical design*, (1992) Pergamon Press, Oxford. (Cited on page 27)
- 107 Ashby M.F., Multi-objective optimization in material design and selection, *Acta Materialia*, **48** (2000) 359–369. (Cited on page 27)
- 108 Ashby M.F., Bréchet Y.J.M., Cebon D., Salvo L., Selection strategies for materials and processes, *Materials & Design*, **25**, (2004) 51–67. (Cited on page 27)
- 109 Allwood J.M., Ashby M.F., Gutowski T.G., Worrell E., Material efficiency: A white paper, *Resources, Conservation and Recycling*, **55** (2011) 362–381. (Cited on page 27)

3 Chapter 3

Synthesis and Characterization Techniques

Abstract. In this chapter the techniques used to develop the experimental work are described: a brief summary of the theory on which every apparatus is based and some technical details are reported. Among the preparation techniques, high energy ball milling was used for hydrides to achieve a nanocrystalline, disordered and dispersed structure, and for carbonaceous materials to increase their surface area. The materials were characterized structurally by means of X-ray diffraction. Microscopy was often used to investigate the morphology of hydrides and carbonaceous materials. Even more details on surfaces could be retrieved from nitrogen adsorption isotherms, applying surface analysis methods. Finally, the kinetics and the thermodynamics of the hydrogen a/d reactions have been studied with a volumetric Sievert's apparatus, while the kinetic performances of storage systems were measured by means of thermal mass flowmeters in dedicated automatic systems.

3.1 Samples Preparation

3.1.1 Ball Milling

High-energy ball milling is a non-equilibrium processing technique that produces powders by repeated fracturing and cold welding of particles via impacts with spheres in a sealed vial. This process is also called mechanical milling when milling components without material transfer or mechanical alloying when milling components with materials transfer, in the case of multicomponent powders. Ball milling can be used, depending on the starting components and on their physicochemical properties to produce several different kinds of solid powders, alloys, intermetallic compounds, multiphase material as well as non-equilibrium solids as quasicrystal, amorphous materials and metastable crystalline phases.

The results are strongly dependent on the initial status of the components: ductile-ductile, ductile-brittle or brittle-brittle. For an exhaustive review see [1].

The process starts loading the powder material along with a grinding medium, generally hard material spheres, into a vial where the powder is milled by effect of repeated collisions. During high-energy milling the particles are continuously flattened, cold welded, fractured and re-welded. Every time there is an impact between two spheres, a number of particle is trapped in between them. The force of the collision plastically deforms the powder particles causing work hardening and fracture. The newly created surfaces allow the particles to stick together and this results in an increase in particle size. In the early stages of milling, if a ductile material is present, soft particles weld together and form larger particles quite frequently. A broad range of particle sizes is obtained, with some three times larger than the starting particles. The composite particles at this stage have a typical layered structure consisting of several combinations of the starting constituents. With consecutive deformations, the particles get work hardened and can fracture by a fatigue-failure mechanism or by the fragmentation of fragile flakes. The fragments created by this mechanism may continue to reduce in size if strong agglomerating forces are not present. At this stage, the frequency of fracture predominates over cold welding. Due to the successive impacts of grinding spheres, the structure of the particles is refined, but the particle size does not change. Consequently, the inter-layer space decreases and the number of layers in a particle increases [1].

After milling for a definite amount of time, a steady equilibrium state is achieved when a balance is reached between the rate of welding, which tends to increase the average particle size, and the rate of fracturing, which tends to decrease it [2]. Smaller particles are able to deform without fracturing and are prone to be welded into larger composites, with a final result of obtaining an intermediate size both from very fine and very large particles [3]. However, it should be noted that the efficiency of particle size reduction is very low: the remaining energy is lost mostly in the form of heat, but a small amount is also utilized in the elastic and plastic deformation of the powder particles [1]. Anyway, the efficiency of the process and the applied energy depend on different parameters, including the type of mill used.

3.1.1.1 Milling Parameters

Ball milling is a complex process and hence it involves optimization of a number of factors. The properties of the final product, particle size distribution, degree of disorder, amorphization, and final stoichiometry, depend on the milling conditions. These parameters are:

type of mill, there are several kinds of mills, that differ in their speed and energy of operation, and material capacity [4]; milling speed and energy are proportional, but there is a limitation due to geometry (especially for rotating devices) and possible overheating;

milling vial, the shape of which is very important for the geometry of the collisions [5]; also the material is to be considered in case of contaminations, hard inert materials are recommended (e. g. ceramics, stainless steel, and tungsten carbide).

grinding medium, with an accurate choice of the diameter of the balls (different sizes together help random collisions), and of the material, that should be the same as

adopted for the vessel;

milling atmosphere, as the gas inside the vial could contaminate the powder or even interact with it on purpose, for instance in reactive milling;

milling environment, because the presence of control agents (e. g. lubricants, surfactants, and protectives) can influence cold welding and alloying processes;

ball-to-powder weight ratio, has a significant effect on the time required to achieve a particular phase in the powder being milled (the higher is the ratio, the shorter the time required);

milling temperature, is another important parameter in the constitution of the milled powder; since diffusion processes are involved in the formation of alloy phases it is expected that the temperature will have a significant effect in any alloy system, irrespective of whether the final product phase is a solid solution, intermetallic, nanostructure, or an amorphous phase;

milling time, the most important parameter, is proportional to the energy transferred to the material; normally it is chosen to achieve a steady state between the fracturing and cold welding of the powder particles, but it should be realized that the level of contamination increases and some undesirable phases could form if the powder is milled for times longer than required [6].

3.1.1.2 Types of Mills

Shaker mills are most commonly used for laboratory investigations, as they mill a quantity of powder in the order of grams. Most of these mills are manufactured by SPEX CertPrep (Metuchen, NJ) and so are the mills used in the experimental activity presented in the next chapters. They have one vial, containing the sample and grinding balls, secured in the clamps and swung energetically back and forth several thousands of times a minute. This motion is combined with lateral movements at the ends of the vial, so that it describes a ∞ shaped trajectory. With each motion of the vial the balls collide against the sample and the sides of the vial, both milling and mixing the material. Because of the amplitude of about 5 cm and the frequency of about 20 s^{-1} of the clamp motion, the ball speed is very high, in the order of 5 m s^{-1} , and consequently it is the force of their impact. Therefore, these mills can be considered as high-energy variety. The machines used in this work are very similar to that shown in figure 3.1, and incorporate forced cooling to permit extended milling times and PLC (programmable logic controller) timer to allow pauses and avoid overheating. The vials were appositely designed and equipped with a valve to control the



Figure 3.1: SPEX 8000 mixer/mill. From [1].

internal atmosphere; they are made of hardened AISI D3 chromium steel. The balls are made of stainless steel and are in a ball-to-powder ratio of 10:1, unless differently reported.

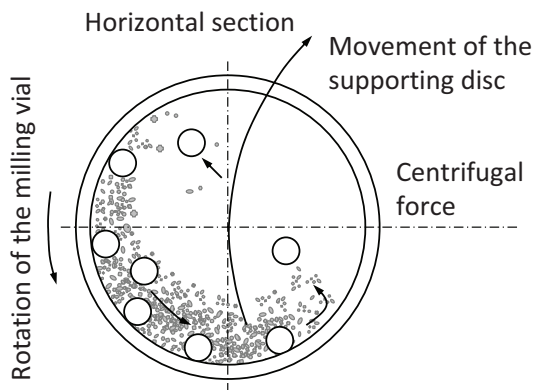


Figure 3.2: Scheme of the spheres motion inside the planetary ball mill. Adapted from [1].

are considered lower energy mills if compared with the shaker ones.

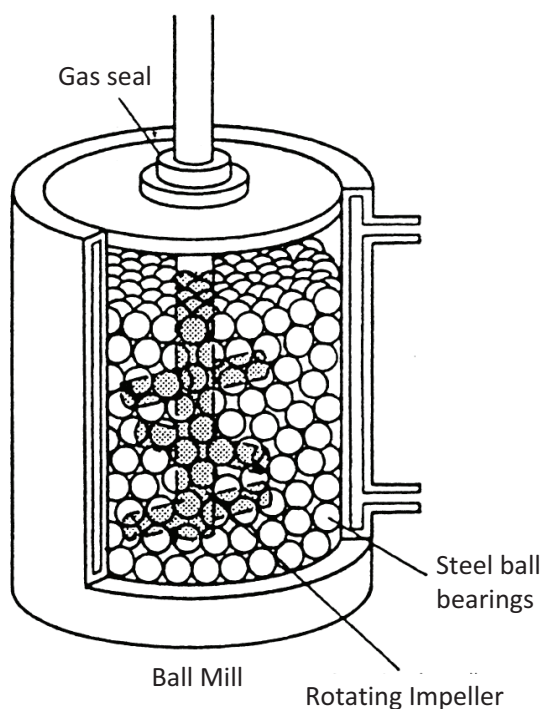


Figure 3.3: Section view of the vial of an attritor ball mill, with rotating arms on a shaft. From [1].

In planetary mills, the vial rotates on his own axis and at the same time in the opposite direction around a central axis, in a planet-like movement. This kind of mills allows to process up to a few hundred grams of powder and the centrifugal forces due to the planetary motion act on the vial content, sample and grinding medium. The opposite rotating directions cause a friction effect, that moves powder and balls together on the walls, and an impact effect, that is responsible for the numerous collision with the opposite inside wall, as it is displayed in figure 3.2. Even if the linear velocity of the spheres is generally higher than in shaker mills, the frequency of the collisions is lower. So, the planetary mills

are considered lower energy mills if compared with the shaker ones.

An attritor mill consists of a vertical stationary vial filled with balls and powder, moved by the stirring action of a vertical rotating central shaft with a series of horizontal arms (impellers). The rotation speed of the central shaft is about 25 rad s^{-1} . In this type of mills it is possible to process larger quantities of powder (from 0.5 to 40 kg). The powder grinding occurs because of impacts between components, interparticle collisions and ball sliding, all exerting both shearing and impact forces on the material. A schematic drawing of the vial of an attritor mill is represented in figure 3.3.

3.1.2 Sample Handling

Most of the materials used in this research work are sensitive to oxygen and water in the atmosphere. This is increased in case of nanostructured powders, which have a higher surface area: the accidental formation of an oxide layer is very compromising for successive reaction kinetics. Furthermore, some metal and complex hydrides

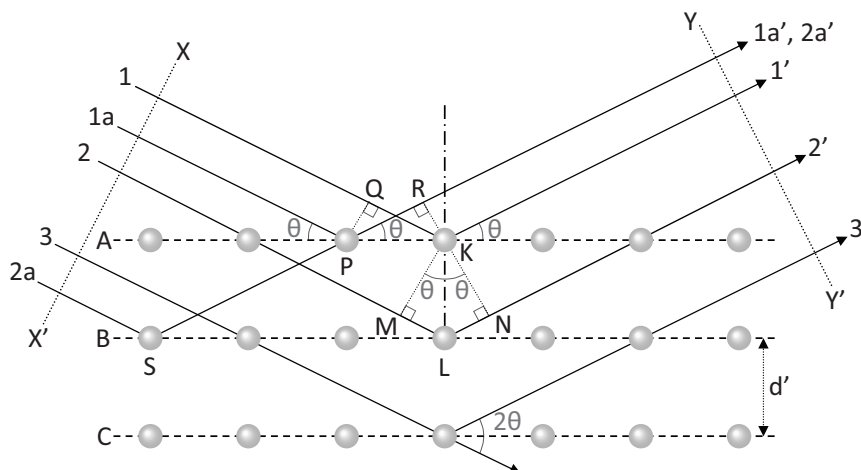


Figure 3.4: Diffraction of X-rays by a crystal. Adapted from [9].

can have fast and exothermic reactions if exposed to air, therefore an inert atmosphere environment is required to handle the samples. For this purpose a MBraun Labstar glove-box with Ar atmosphere was used, where water vapor and oxygen were kept to minimum values (below 0.1 and 10 ppm, respectively). The internal atmosphere is forced by a circulation system into filters, molecular sieves and reducing agents to eliminate the traces of undesired gases from the 0.8 m³ where sample handling is carried out. To exchange material with this closed system, two evacuable/refillable pre-chambers are used.

To prevent the glove-box atmosphere from being contaminated, all the operations involving solvents were performed elsewhere, using Schlenk flasks [7]. This devices allowed safe mixing with solutions, controlled heating and stirring and solvents evaporations; the possibility to prepare and unload the reactive material in the flasks inside the glovebox greatly limited any chance of contamination [8].

3.2 Structural Characterization

3.2.1 X-Ray Diffraction

X-ray diffraction (XRD) is a versatile and non-destructive analytical technique which allows to study the structural and microstructural characteristics of crystalline matter. It is based on the elastic interaction of a electromagnetic radiation, monochromatic X-rays, with a harmonic oscillator lattice, the atomic lattice of the studied matter. This phenomenon was firstly discovered by von Laue in 1912 and later W. L. Bragg implemented it with the necessary conditions.

Considering figure 3.4, rays **1** and **1a** are examined, striking atoms *K* and *P* in the first plane of atoms. The atoms scatter the incident radiation in all directions, but only in the directions **1'** and **1a'** the scattered beams can be in phase reinforcing one another. This only happens if the difference in length of path between the wave fronts *XX'* and *YY'* is equal to

$$QK - PR = KP \cos \theta - PK \cos \theta = 0 \quad (3.1)$$

Similarly, the rays scattered by all the atoms in the first plane in a direction parallel to $\mathbf{1}'$ are in phase and add their contributions to the diffracted beam. This will be true of all the planes separately, and it remains to find the condition for reinforcement of rays scattered by atoms in different planes. Rays $\mathbf{1}$ and $\mathbf{2}$, for example, are scattered by atoms K and L , and the path difference for rays $\mathbf{1K1}'$ and $\mathbf{2L2}'$ is

$$ML + LN = d \sin \theta + d \sin \theta = 2d \sin \theta \quad (3.2)$$

This is also the path difference for the overlapping rays scattered by S and P in the direction shown, since in this direction there is no path difference between rays scattered by S and L or P and K . Scattered rays $\mathbf{1}'$ and $\mathbf{2}'$ will be completely in phase if this path difference is equal to a multiple integer n of λ :

$$n\lambda = 2d \sin \theta \quad (3.3)$$

This equation is known as Bragg's law. It states the essential condition for a monochromatic X-ray radiation to be reflected with constructive interference when hitting on a crystal lattice. The materials influence the reflection — also improperly called *diffraction*¹ — with the interplanar spacing d . The diffractometers hence allow to determine the crystal structures, deformations or amorphous phases, the nature and the distribution of the atoms in the lattice [9]. Most of these apparatuses exploit a monochromatic radiation source (or a source made so thanks to monochromator) and a set-up which is easily approximated by a two-dimensional geometry as the one shown in figure 3.5.

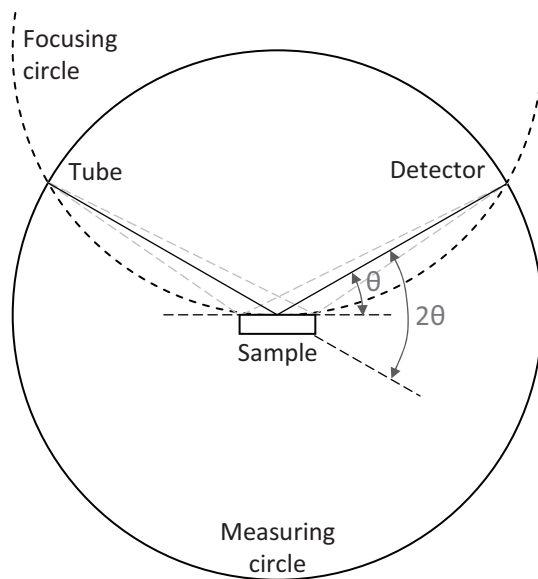


Figure 3.5: Bragg-Brentano geometry.

In the work described in this thesis, different diffractometers have been used. All the instruments made use of the Bragg-Brentano geometry with a $\text{CuK}\alpha$ ($\lambda = 1.54056 \text{ \AA}$) radiation source. This configuration is also called θ - 2θ because the angular velocity of the detector is twice that of the sample; in this way, the incidence and reflection angles remain equal to each other during the scan with respect to the sample plane. This set-up can be obtained both with a fixed source, a θ -moving sample chamber and a 2θ -moving detector, or with a fixed sample, a $-\theta$ -moving X-ray source and a θ -moving detector. In both cases it is a parafocusing geometry, according to which a divergent beam coming from the X-ray tube passes through a divergence slit and a Soller slit collimator before reaching a flat sample; the diffracted beam is

then reflected by the sample to the detector after passing through a second Soller slit and a receiving slit. The parafocusing effect is ensured by the fact that the focus of the X-ray tube and the detector are at the same distance from the axis of the goniometer; it

¹The term *diffraction* has been accepted historical reasons.

is important that the sample is flat and positioned exactly on the axis of the goniometer. Most of the XRD measurements were carried out on samples protected with a thin Kapton (poly-oxydiphenylene-pyromellitimide) foil, which proved to be effective in isolating the samples from the environment and not originating parasitic reflections in the recorded patterns, thanks to its high transmittance to X-rays and very low thickness (8 μm).

In some cases, the qualitative and quantitative analysis of XRD pattern was carried out using the Rietveld method [10, 11]. It is an iterative minimization procedure, based on a function including several structural and microstructural parameters of the system. The method was developed during the 60's and was at the beginning only restricted to the refinement of atomic positions from neutron diffraction profiles [10]. The refinement method is based on individual intensities at every 2θ of a powder diffraction pattern: it relies on the complete diffraction profile, including the background, and originally called *full pattern refinement* for this reason. Basing the calculation on individual intensities is very useful because, especially in the case of powder diffraction, it overcomes the problem of the systematic (due to cubic or trigonal symmetry) and accidental (due to poor resolution) peak overlaps [12]. Using a specific software [13], the information contained in a powder diffraction pattern which can be retrieved by Rietveld refinement include: lattice parameters and space group, derived from peak positions; crystal domain size and residual stress/strain from the broadening and full width at half maximum of the peaks; qualitative and quantitative phase analysis.

3.2.2

Scanning Electron Microscopy

In scanning electron microscopy (SEM) a source of electrons is focused, in vacuum, into a fine probe that is rastered over the surface of the specimen. As the electrons penetrate the surface, a number of interactions occur that can result in the emission of electrons or photons from (or through) the surface. A reasonable fraction of the emitted electrons can be collected by appropriate detectors and elaborated, so that every point stricken by the beam on the sample is mapped directly onto a corresponding point on a screen.

The principal images produced in the SEM are of three types: secondary electron images, backscattered electron images, and elemental X-ray maps. Secondary and backscattered electrons, produced by different mechanisms, are conventionally separated according to their energies. When a high-energy primary electron interacts with an atom, it undergoes either inelastic scattering with atomic electrons or elastic scattering with the atomic nucleus. In an inelastic collision with an electron, some amount of energy is transferred to the other electrons. If the energy transfer is very small, the emitted electron will probably not have energy enough to exit the surface. If the energy transferred exceeds the work function of the material, the emitted electron can exit the solid. When the energy of the emitted electron is less than about 50 eV, by convention is referred to as a secondary electron (SE), or simply a secondary. Most of the emitted secondaries are produced within the first few nm of the surface. Secondaries produced much deeper in the material suffer additional inelastic collisions, which lower their energy and trap them in the interior of the solid [14].

Higher energy electrons are primary electrons that have been scattered without loss of kinetic energy (i. e. elastically) by the nucleus of an atom, although these collisions may occur after the primary electron has already lost some of its energy for interaction with the

electron cloud by inelastic scattering. Backscattered electrons (BSE) are the electrons that exit the specimen with an energy greater than 50 eV. Most BSE have energies comparable to the energy of the primary beam. The higher the atomic number of a material, the more likely the backscattering will occur. Thus as a beam passes from a low-Z (atomic number) to a high-Z area, the signal due to backscattering, and consequently the image brightness, will increase [14]. There is a built in contrast caused by elemental differences.

An additional electron interaction of major importance in the SEM occurs when the primary electron collides with, and ejects a core electron from an atom in the solid. The excited atom will decay to its ground state by emitting either a characteristic X-ray photon or an Auger electron. The X-ray emission signal can be sorted by energy in an energy dispersive X-ray (EDX) detector or by wavelength with a wavelength spectrometer. These distributions are characteristic of the elements that produced them and the SEM can use these signals to produce elemental images that show the spatial distribution of particular elements in the field of view. Both energy-dispersive and wavelength-dispersive X-ray detectors can be used for elemental detection in the SEM.

In this work different SEM apparatuses have been used, so the specific settings will be listed along with details on the considered experiment.

3.2.3

Pores and Surface Characterization

The characterization surface and pore properties of solids uses the process of physical adsorption of a gas on the surface of the solid. It is a spontaneous process dominated by molecular interaction forces (e.g. Van der Waals and dispersion forces) driven by the decrease of entropy, since the molecule in the gas phase have three degrees of freedom, while in the adsorbent phase they have only two. For this reason the process is always exothermic. The physically adsorbed gases on the surface of the solid can be easily removed by evacuation at the same temperature at which adsorption occurred. Adsorption is measured by the volume of adsorbed gas at standard conditions, changing the pressure of the adsorbing gas at a constant temperature. For this reason these measurements are named isotherms.

Usually, volumetric systems are used: in this work a Quantachrome Nova 1200e analyzer has been used, with N_2 as adsorbing gas and liquid nitrogen temperature condition (77 K). The first step in the experimental procedure to get an adsorption isotherm is the sample degassing, needed to remove adsorbed water or other gases on the surface. The amount of used gas is measured with a calibrated volume and an accurate measurement of the pressure with a gauge. Subsequently, N_2 is used for the surface area determination. Its pressure in the sample cell is increased by steps after the equilibrium pressure has been reached each time. The amount of adsorbed gas is recorded at each step. Knowing the effective volume of the system, it is possible to calculate the adsorbed gas volume by measuring the pressure drop with respect to that expected in absence of the sample.

The various theories for surface area and porosity measurements are discussed below.

3.2.3.1 Surface Area

The Brunauer-Emmett-Teller (BET) gas adsorption method [15] has become the most widely used standard procedure for the determination of the surface area of finely-divided and porous materials, in spite of the oversimplification of the model on which the theory

is based [16]. It involves the use of the BET equation

$$\frac{1}{V^{\text{ad}} \left(\frac{p_0}{p} - 1 \right)} \equiv \frac{p}{V^{\text{ad}} (p_0 - p)} = \frac{1}{V_{\text{mono}}^{\text{ad}} C} + \frac{C - 1}{V_{\text{mono}}^{\text{ad}} C} \frac{p}{p_0} \quad (3.4)$$

in which V^{ad} is the adsorbed gas volume at a relative pressure $\frac{p}{p_0}$, and $V_{\text{mono}}^{\text{ad}}$ is the volume of adsorbate constituting a monolayer of surface coverage. The term C , the BET C constant, is related to the energy of adsorption in the first adsorbed layer and consequently its value is an indication of the magnitude of the adsorbent/adsorbate interactions.

The BET method requires a linear plot of the first term of equation (3.4) on p/p_0 , and for most solids (using nitrogen as the adsorbate) is restricted to a limited region of the adsorption isotherm, usually in the range of 0.05 to 0.30. This linear region is shifted to lower relative pressures for microporous materials. The standard multipoint BET procedure requires a minimum of three points in the appropriate relative pressure range. The volume of a monolayer of adsorbate V_{mono} can then be obtained from the slope s and intercept I of the BET plot; extracting them from the equation (3.4):

$$s = \frac{C - 1}{V_{\text{mono}} C} \quad I = \frac{1}{V_{\text{mono}} C} \quad (3.5)$$

V_{mono} can be calculated combining these two equations.

The second step is the calculation of the surface area. The total surface area S_{tot} of the sample can be expressed as:

$$S_{\text{tot}} = \frac{V_{\text{mono}} N_A A_{\text{cs}}}{M_m} \quad (3.6)$$

where N_A is Avogadro's number ($6.022 \times 10^{23} \text{ mol}^{-1}$ [17]) and M_m is the molecular mass of the adsorbate. This also requires the knowledge of the molecular cross-sectional area A_{cs} of the adsorbate molecule: for the hexagonal close-packed nitrogen monolayer at 77 K, the cross-sectional area A_{cs} for nitrogen is 16.2 \AA^2 [18]. The specific surface area (SSA) of the solid can be calculated from the total surface area, simply dividing S_{tot} by the mass of the sample.

3.2.3.2 Porosity by Gas Adsorption

It is expedient to characterize pores according to their sizes [16, 19]:

macropores have openings exceeding 500 \AA in diameter;

mesopores are pores of a diameter between $500\text{--}20 \text{ \AA}$;

micropores is a term used to describe pores with a diameter not exceeding 20 \AA .

Porosity of powders and other porous solids can be conveniently characterized by gas adsorption studies. Two common techniques to describe porosity are the determination of total pore volume and pore size distribution (PSD). For the evaluation of the porosity of most solid materials, nitrogen at 77 K is the most suitable adsorbate. As for the surface area, a mathematical approach is required to deeply understand N_2 adsorption data.

Micropores can be determined by the Dubinin-Radushkevich (DR) method [20, 21], a simple $\log V^{\text{ad}}$ versus $\log^2 \frac{p}{p_0}$ relationship, which linearizes the isotherm based on micropore filling principles; it is based on the Polanyi adsorption potential. A more advanced

formulation is suggested by Saito-Foley (SF) [22, 23], a direct mathematical relationship between relative pressure and pore size. This relationship is calculated from a modified Young-Laplace equation, based on a cylindrical pore geometry, but is restricted to micropore region and sometimes underestimates the true pore size [18].

An intuitive approach leads to the t -plot [24, 25], where the multi-layer formation is modeled mathematically to calculate a layer thickness t as a function of increasing p/p_0 , normally in the 0.2–0.5 range. The resulting t -curve is compared with the experimental isotherm in the form of a t -plot, that is, experimental volume adsorbed is plotted versus statistical thickness for each experimental p/p_0 value. The linear range lies between monolayer and capillary condensation. The slope of the t -plot (V^{ad}/t) is equal to the external area, i. e. the area of those pores that are not micropores: mesopores, macropores and the outside surface are able to form a multilayer, whereas micropores, which have already been filled, cannot contribute further to the adsorption process. Similar background is at the basis of α_S method.

Mesopores are determined from methods based on Kelvin equation (such as BJH–Barrett, Joyner, Halenda [26]). This predicts pressure at which adsorbate will spontaneously condense (and evaporate) in a cylindrical pore of a given size. Condensation occurs in pores that already have some multilayers of adsorbate on the walls. Therefore, the pore size is calculated from the Kelvin equation and the selected statistical thickness (t -plot) equation. It is acceptable for broad size distributions of medium to large mesopores, but it severely underestimates the size of small to medium mesopores [18].

3.2.3.3 Isotherms

An understanding of the surface area and porosity of an adsorbent can be achieved by the construction of an adsorption isotherm. When the quantity of adsorbate on a surface is measured over a wide range of relative pressures at constant temperature, the result is an adsorption isotherm. All adsorption isotherms may be grouped into one of the six types shown in figure 3.6 [27].

Type I or Langmuir isotherms are concave to the p/p_0 axis and the amount of adsorbate approaches a limiting value as p approaches p_0 . Type I physisorption isotherms are exhibited by microporous solids having relatively small external surfaces. The limiting uptake of adsorbate is governed by the accessible micropore volume, rather than by the internal surface area.

Type II isotherms are the normal form of isotherm obtained with a nonporous or macroporous adsorbent. This type of isotherm represents unrestricted monolayer-multilayer adsorption. The start of the linear central section of the isotherm is usually taken to indicate the relative pressure at which monolayer coverage is complete.

Type III isotherms are convex to the P/P_0 axis over its entire range and are rarely encountered; a well-known example is the adsorption of water vapor on nonporous carbons.

Type IV isotherms are associated with capillary condensation in mesopores, indicated by the steep slope at higher relative pressures. The initial part of the type IV isotherm follows the same path as type II.

Type V isotherms are uncommon, corresponding to type III, except that pores in the mesopore range are present.

The former three types are generally reversible, but microporous materials, having type I isotherms can exhibit hysteresis; the latter two types associated with mesoporosity, usually

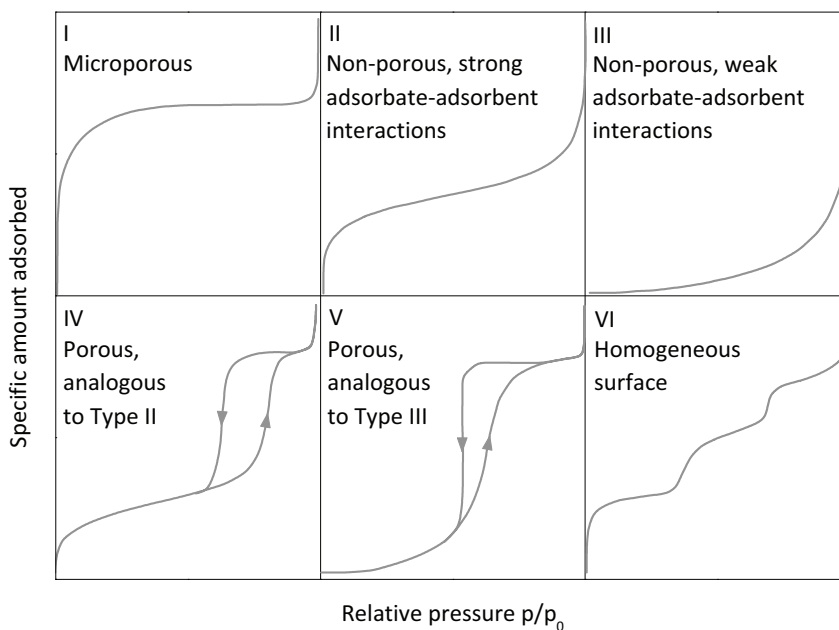


Figure 3.6: The different types of N_2 adsorption isotherms.

exhibit hysteresis between the adsorption and desorption isotherms. Finally, type VI isotherms accounts for materials with homogeneous surface.

3.3 Functional Properties Characterization

3.3.1 Differential Scanning Calorimetry

A number of processes occurring inside physical/chemical systems are connected to heat exchange and thermal effects. In general, the aim of the calorimetry is the evaluation of the amount of heat Q acquired or released by the studied system, when it changes temperature or it is involved in transformations, such as chemical reactions or phase transitions. By measuring both temperature and exchanged heat in isobaric conditions, it is possible to evaluate properties, such as specific heat capacity, latent heat, reaction enthalpies [28]. In a differential scanning calorimetry (DSC) equipment, the temperatures of the sample under investigation and of a reference system are kept almost equal each other, while performing a temperature program (a sequence of temperature controlled stages, such as, heating, isothermal, or cooling), and collecting the data at regular intervals (scanning mode). Usually, the DSC instrument are designed to work with small amounts of samples (up to 100 mg), and this is the case for the DSC instruments used during the experimental work reported on this thesis. The temperatures of the sample T_s and of the reference T_r are measured during the scan by two thermocouples, respectively. On the basis of the difference between T_s and T_r , an electro-thermal device supplies additional heat in order

to make the temperatures coincide. This additional heat is supplied by Joule effect with a filament of resistance R close to the sample or the reference pan. From the intensity of the electric current $i(t)$ on the filament, the additional power $P(t)$ is calculated as:

$$P = i^2 R = \frac{dQ}{dt} \quad (3.7)$$

which is then equal to the heat flux $\frac{dQ}{dt}$. For test performed in isobaric conditions, this amount is also equal to the enthalpy flux, which is the signal in a typical DSC measurement curve.

As explained above, the sample and reference temperatures are kept equal each other by using local heating resistances. For systems in which only heating occurs, at the considered range temperatures, the signal reported on a DSC curve is actually the difference between the heat flux on the sample and the reference:

$$\Delta \left(\frac{dQ}{dt} \right) = \left(\frac{dQ}{dt} \right)_s - \left(\frac{dQ}{dt} \right)_r = \left(\frac{dT}{dt} \right) \left[\left(\frac{dQ}{dT} \right)_s - \left(\frac{dQ}{dT} \right)_r \right] = \beta (m_s c_{p,s} - m_r c_{p,r}) \quad (3.8)$$

where β is the heating rate, m_s , m_r and $c_{p,s}$, $c_{p,r}$ are the masses and the isobaric specific heat capacities of the sample and the reference, respectively. In order to evaluate the specific heat of the sample, once the heating rate and the sample mass are known, the reference contribution

$$\left(\frac{dQ}{dt} \right)_{base} = \beta m_r c_{p,r} \quad (3.9)$$

must be subtracted. This contribution can be evaluated with an analogous measurement with the same reference, but in which the sample pan is empty; the corresponding obtained curve is called *blank*. In the experiment performed during the reported experimental work, no reference sample was used, but the reference pan has been kept empty instead. Moreover, no blank curves were subtracted, as the contribution of the blank (experiment with two empty pans) has been considered negligible with respect to the thermal features shown by the samples. The blank contribution depends on intrinsic properties of the system, such as thermal isolation or temperature controller dynamics, and on the amount of the gas replaced by the sample inside the pan. If the sample undergoes to other processes, besides heating, such as phase transitions, defects annealing or chemical reactions, there would be other contributions to the total enthalpy flux, each of them being generally indicated as:

$$\left(\frac{dQ}{dt} \right) = \Delta H_p m_s \frac{d\alpha}{dt} = \beta \left(\Delta H_p m_s \frac{d\alpha}{dT} \right) \quad (3.10)$$

where α is the process progress fraction and $\frac{d\alpha}{dt}$ is the process progress rate. Once the onset temperature is reached, the process starts with a small rate, then it accelerates up to a maximum rate, and finally it ends again with a small rate. For this reason, the single process is represented by a peak. In a DSC plot, the correspondence of the acquired heat (endothermic process) with the sign of the y -axis must be specified. Endothermic features can indicate processes such as melting, vaporization or, in case of hydrogen storage materials, hydrogen release, as well as decomposition in general. The annealing of the material surface and bulk defects are indicated by exothermic features, due to the release of the energy excess present in unordered systems with respect to the corresponding ordered structures. It is to note from equation (3.10) that the specific enthalpy of a process can

be evaluated by integrating the corresponding peak, once the heating rate and the sample mass are known. In order to reduce or eliminate the possibility of degradation for the oxygen and moisture sensitive materials studied, sealed sample holders or pans have been used during the experiments: they have been filled with the sample and sealed inside a glove-box.

3.3.2 Hydrogen Adsorption/Desorption Characterization

An important step in the experimental research is the analysis of the H₂ storage efficiency for the new materials, and the study of their a/d kinetics and thermodynamics. There are three kinds of experimental approach. At a desired temperature, the sample is contained in a chamber at a certain H₂ pressure and the quantity of absorbed hydrogen is evaluated by:

- thermogravimetric techniques, that is by measuring the variation of the sample mass by a microbalance;
- volumetric techniques, that is by measuring the H₂ pressure variation in a reaction chamber;
- flowmetric techniques, that is by measuring the H₂ flows going to and/or coming from a reaction chamber.

The accuracy of volumetric techniques is potentially greater compared to that of thermogravimetric techniques, since large changes in gas pressure are measured, rather than small changes in mass: this advantage is particularly marked when the gas involved is hydrogen [29]. Flowmetric techniques are usually the least accurate for laboratory-scale samples and found their application only with tank systems. In this setup, normally, the volume of gas exchanged by the system is too large for a closed volume and so is the mass of the sample.

3.3.2.1 Volumetric Sievert's Apparatus

In the simplest design, the volumetric apparatus records the change of the H₂ pressure within a fixed sample volume resulting from the reaction progress [30]. In more sophisticated volumetric devices the H₂ gas pressure in the reaction chamber is maintained constant during the experiment, by modifying, for example, the length of a bellows that is part of the reaction chamber [31]. In this work the hydrogen a/d reaction characterization was accomplished by means of a Sievert's volumetric apparatus of the former type. The Gas Reaction Controller (GRC), provided by Advanced Materials Corporation (Pittsburgh, Pennsylvania), allows both kinetics and thermodynamics measurements. It is provided with a LabView-based software to manage the experiments and the setup; the user interface schematically represents the internal organization of the apparatus (figure 3.7), where it is possible to point out:

Sample CH1: the sample chamber, with an internal volume of about 2 cm³, is external and detachable. It can be inserted in a furnace to be heated up to 500 °C, in a thermostatic bath or in a cryogenic bath (a liquid nitrogen dewar). Temperature is measured with a type K thermocouple displaying TC1 and pressure is displayed in HP1. All the HP pressure sensors have an accuracy of 0.01 atm (approx. 1 kPa)

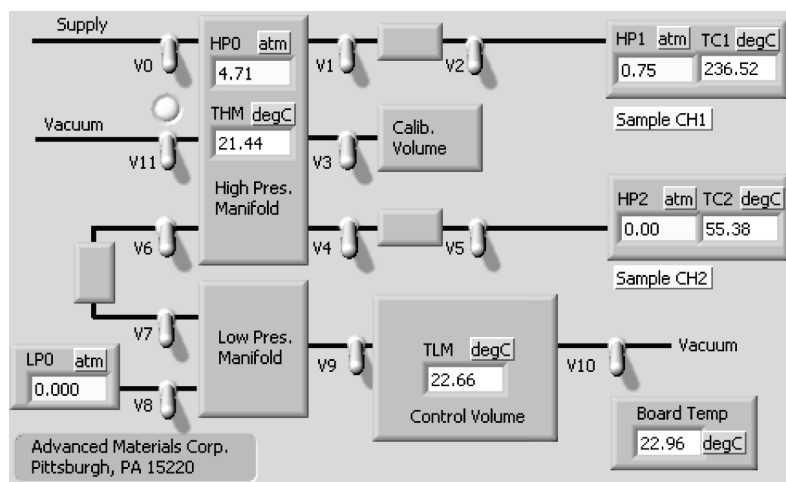


Figure 3.7: GRC software user interface, schematizing volumes, components and sensors.

Sample CH2: a second channel for a sample holder.

High Pressure Manifold: is connected to the calibration volume (Calib. Volume, 40 cm³), to the rotary vacuum pump and to the gas supply. It is provided with HP0 pressure sensors and THM type K thermocouple.

Low Pressure Manifold: is also connected to the vacuum pump by the Control Volume (500 cm³), where TLM temperature is measured, and to low pressure sensor LP0, which allows an accuracy of 0.001 atm (approx. 0.1 kPa).

V₀₋₁₁: solenoid valves that can withstand up to 20 MPa unidirectionally. For this reason, in some connections they are coupled on the same flow line.

The valves can be manually opened, but normally the software operates in automatic standard procedures, which set the sequence and timing of valves operation. The main procedures are:

Soak/Release: the valves between High Pres. Manifold and Sample CH1 open at regular time intervals, allowing the gas to flow between the volumes. The Δp allows to measure the quantity of sorbed gas, but modifies the starting pressure in the manifold, because with this setup the two volumes behaves as a closed system.

PCI absorption/desorption: this measure allows the determination of the pressure-composition equilibrium isotherm (described in section 2.1.2) during absorption and desorption. The Δp occurs in small steps to maintain a quasi-equilibrium state, and the pressure in the manifold is regulated for this purpose.

Evacuation: this step connects the sample chamber with the vacuum pump, thus evacuating the volume.

The temperature settings allow both static set points and temperature gradients. Moreover, the software allows to repeat operations or operations sequences in loops, to investigate the cyclability of the considered samples.

Kinetic Measurements These experiments are obtained with soak/release procedures. During the tests the sample is exposed to a pressure p , which must be respectively higher/lower than the plateau pressure p_{eq} at a given temperature, to have some driving force for the reaction. Knowing the sum of the volumes, V , it is easy to calculate the moles n of absorbed/released hydrogen from Δp differencing the virial third-order approximate equation:

$$\frac{pV}{nRT} = 1 + B\frac{n}{V} + C\left(\frac{n}{V}\right)^2 + D\left(\frac{n}{V}\right)^3 + \dots \quad (3.11)$$

where R is the gas constant, T the absolute temperature and $B(T)$, $C(T)$ and $D(T)$ are respectively first, second and third order virial coefficients. In case of a temperature ramp performed during the measure, these experiments are usually called temperature programmed absorption and desorption (TPA and TPD, respectively).

Thermodynamic Measurements These experiments allow the determination of thermodynamic properties, by means of PCI curves (see section 2.1.2). To operate as close as possible to the thermodynamic equilibrium state, the pressure variations dp are very small: in a real system it is difficult to stabilize p and T over time due to sample reaction. Every point in the isotherm is the result of a small series of kinetics measurements: when there is no driving force for the reaction at the desired pressure the sample is considered at equilibrium. The procedure continues until the desired pressure value is reached. In addition to plateau pressure values, from these measurements it is possible to obtain more precise H_2 storage capacity, due to the reached equilibrium state.

3.3.2.2 Flowmeters

As previously mentioned, samples that are able to exchange large volumes of gas, require a measuring system that allows gas to flow. Normally these measuring stations are designed and built specifically for the particular storage system, so a detailed description will be provided case by case, when such measuring stations are encountered in the experimental work.

However, the basics of operation are common for flow measurements. All gas flow sensors operate according to the same principle: they are operating on heat transfer by sensing the ΔT along a heated section of a capillary tube. Part of the total flow is forced through the capillary by means of a laminar flow device in the main stream generating a difference in pressure. The design of the laminar flow device is such that flow conditions in both the capillary and laminar flow device are comparable, thereby resulting in proportional flow rates through the meter. The ΔT , sensed by the upstream and downstream temperature sensors on the capillary, depends on the amount of heat absorbed by the gas flow. The transfer function, between gas mass flow and signal, can be described by the equation:

$$\Delta T = k c_p \Phi_m \quad (3.12)$$

where k is a constant, c_p is the isobaric specific heat capacity and Φ_m the specific mass flow.

References

- 1 Suryanarayana C., Mechanical alloying and milling, *Progress in Materials Science*, **46** (2001) 1–184. (Cited on pages 36, 37, and 38)
- 2 Lee P.Y., Yang J.L., Lin H.M., Amorphization behaviour in mechanically alloyed Ni–Ta powders, *Journal of Material Science*, **33** (1998) 235–239. (Cited on page 36)
- 3 Benjamin J.S., Mechanical alloying, *Scientific American*, **234** (1976) 40–48. (Cited on page 36)
- 4 Kerr I., Laboratory mills for mechanical alloying, *Metal Powder Report*, **48** (1993) 36–38. (Cited on page 36)
- 5 Harringa J.L., Cook B.A., Beaudry B.J., Effects of vial shape on the rate of mechanical alloying in Si₈₀Ge₂₀, *Journal of Material Science*, **27** (1992) 801–804. (Cited on page 36)
- 6 Suryanarayana C., Does a disordered γ -TiAl phase exist in mechanically alloyed Ti–Al powders?, *Intermetallics*, **3** (1995) 153–160. (Cited on page 37)
- 7 Schlenk W., in: *Die Methoden der organischen Chemie*, Weyl T., Houben J. (eds), (1924) Thieme Verlag, Stuttgart. Vol. **IV**, 720–978. (Cited on page 39)
- 8 Shriver D.F., Drezdon M.A., *The Manipulation of Air-Sensitive Compounds*, 2nd ed. (1986) John Wiley & Sons, Inc., New York. (Cited on page 39)
- 9 Cullity B.D., Stock S.R., *Elements of X-ray Diffraction*, 3rd ed. (2001) Prentice-Hall, Upper Saddle River. (Cited on pages 39 and 40)
- 10 Rietveld H.M., Line profiles of neutron powder-diffraction peaks for structure refinement, *Acta Crystallographica*, **22** (1967) 151–152. (Cited on page 41)
- 11 Rietveld H.M., A profile refinement method for nuclear and magnetic structures, *Journal of Applied Crystallography*, **2** (1969) 65–71. (Cited on page 41)
- 12 Young R.A., Willes D.B., Profile shape functions in Rietveld refinements, *Journal of Applied Crystallography*, **15** (1982) 430–438. (Cited on page 41)
- 13 Lutterotti L., Scardi P., Maistrelli P., LSI — a computer program for simultaneous refinement of material structure and microstructure, *Journal of Applied Crystallography*, **25** (1992) 459–462. (Cited on page 41)
- 14 Brundle C.R., Evans C.A., Wilson S. (eds), *Encyclopedia of Materials Characterisation — Surfaces, Interfaces, Thin Films*, (1992) Butterworth-Heinemann, Stoneham. (Cited on pages 41 and 42)
- 15 Brunauer S., Emmett P.H., Teller E., Adsorption of Gases in Multimolecular Layers, *Journal of the American Chemical Society*, **60** (1938) 309–319. (Cited on page 42)
- 16 Sing K.S.W., Everett D.H., Haul R.A.W., Moscou L., Pierotti R.A., Rouquerol J., Siemieniewska T., Reporting physisorption data for gas/solid systems with special reference to the determination of surface area and porosity (Recommendations 1984), *Pure and Applied Chemistry*, **57** (1985) 603–619. (Cited on page 43)
- 17 Mohr P.J., Taylor B.N., Newell D.B., CODATA Recommended Values of the Fundamental Physical Constants: 2006, *Reviews of Modern Physics*, **80** (2008) 633–730. (Cited on page 43)
- 18 Lowell S., Shields J.E., Thomas M.A., Thommes M., *Characterization of Porous Materials and Powders: Surface Area, Pore Size and Density*, (2006) Springer-Verlag, Berlin Heidelberg. (Cited on pages 43 and 44)
- 19 Rouquerol J., Avnir, D., Fairbridge C.W., Everett D.H., Haynes J.H., Pernicone N., Ramsay J.D.F., Sing K.S.W., Unger K.K., Recommendations for the Characterization of Porous Solids, *Pure and Applied Chemistry*, **66** (1994) 1739–1758. (Cited on page 43)
- 20 Dubinin M.M., Radushkevich L.V., The equation of the characteristic curve of the activated charcoal, *Proceedings of the USSR Academy of Sciences*, **55** (1947) 331–337. (Cited on page 43)
- 21 Dubinin M.M., *Russian Journal of Physical Chemistry*, **39** (1965) 697–704. (Cited on page 43)
- 22 Saito A., Foley H.C., Curvature and parametric sensitivity in models for adsorption in micropores, *AIChE Journal*, **37** (1991) 429–436. (Cited on page 44)
- 23 Parent M.A., Moffat J.B., A Comparison of Methods for the Analysis of Adsorption-Desorption Isotherms of Microporous Solids, *Langmuir*, **11** (1995) 4474–4479. (Cited on page 44)
- 24 Halsey G., Physical Adsorption on Non-Uniform Surfaces, *Journal of Chemical Physics*, **16** (1948) 931–938. (Cited on page 44)

- 25 de Boer J.H., Linsen B.G., Plas Th., Zondervan G.J., Studies on pore systems in catalysts: VII. Description of the pore dimensions of carbon blacks by the *t* method, *Journal of Catalysis*, **4** (1969) 649–653. (Cited on page 44)
- 26 Barrett E.P., Joyner L.G., Halenda P.P., The Determination of Pore Volume and Area Distributions in Porous Substances. I. Computations from Nitrogen Isotherms, *Journal of the American Chemical Society*, **73** (1951) 373–380. (Cited on page 44)
- 27 Brunauer S., Deming L.S., Deming W.S., Teller E., On a Theory of the van der Waals Adsorption of Gases, *Journal of the American Chemical Society*, **62** (1940) 1723–1732. (Cited on page 44)
- 28 Höhne G., Hemminger W.F., Flammersheim H.-J., *Differential Scanning Calorimetry*, 2nd ed. (2003) Springer-Verlag, Berlin Heidelberg. (Cited on page 45)
- 29 Checchetto R., Trettel G., Miotello A., Sievert-type apparatus for the study of hydrogen storage in solids, *Measurement Science and Technology* **15** (2004) 127–130. (Cited on page 47)
- 30 Ryan D.H., Coey J.M.D., Thermopiezic analysis: gas absorption and desorption studies on milligram samples, *Journal of Physics E: Scientific Instruments*, **19** (1986) 693–694. (Cited on page 47)
- 31 Gerard N., Belkbir L., Joly E., High accuracy volumetric device for hydrogen sorption kinetic studies, *Journal of Physics E: Scientific Instruments*, **12** (1979) 476–477. (Cited on page 47)

4

Chapter 4

Nanosupported Borohydride Compounds

Abstract. This chapter concerns with the study on borohydrides, among the highest capacity materials available, but still unavailable for practical purposes due to different issues. An attempt to improve the decomposition kinetics of lithium borohydride has been made dispersing this material on the surface of modified nanotubes and graphite, enhanced by high energy ball milling. The outcome showed a decreased decomposition temperature as regard to pure material and further decreasing was observed with increased the surface of the supports. The interpretation proposed for this behaviour is the heterogeneous nucleation of decomposition products of intermediate phases on the carbon surface coming from liquid borohydrides. A similar experiment was performed to investigate this effect in combination with the advantage of a reactive hydride composite, where two materials are combined to obtain a mixture with a lower decomposition enthalpy. The effect of the mixture was positive in presence of the support, due to lower temperature melting. For calcium borohydride a tailored mesoporous carbon was used after chemical activation. The increased wettability of this support resulted in lower decomposition temperature and improved reversibility for a number of cycles at different pressure values.

As assessed in the previous chapters, an essential component for successful clean power technologies is hydrogen storage in a convenient way, especially for on-board applications. At present, targets for reversible hydrogen storage materials require characteristics that will finally give a gravimetric capacity of 5.5 wt.% H₂ to storage devices [1, 2]. As it is not likely that capacities higher than 6 wt.% H₂ can be obtained in transition metal hydride materials, research and studies have focused on complex hydrides of few light elements, for instance alanates, amides and borohydrides. In this case, the selection of the class of materials is motivated by this specific need and the top right corner of graph in figure 2.7 is being explored. As anticipated in section §2.4, the materials found in this region present the drawback of high decomposition temperatures.

However, following the materials selection approach, in this chapter borohydrides are analyzed, exploiting their peculiarities to try to obtain more useful compounds. In par-

ticular, the possibility to dissolve their powders in organic solvents allowed new samples preparation pathways. Again, this perspective is similar to exploiting the property of some materials to be formed in shapes that are more convenient for their application in mechanical design [3].

4.1

Advantages of Nanosupports

Borohydrides have been already described in subsections from 2.3.1 to 2.3.4, underlining both their very high storage density and the problems connected to the decomposition conditions and scanty reversibility.

In order to overcome these limitations and improve thermodynamics and kinetics of dehydrogenation of light metal hydrides, it has been proposed to confine the hydrides in nanoporous scaffolds [4], exploiting the favourable properties of nanostructured materials which can be employed to tailor the size, surface and morphology features of hydride reactants [5], besides to avoid sintering and agglomeration during cycling.

In recent papers it has been shown that LiBH_4 milled with carbon nanotubes [6] and included in mesoporous carbon [7] displays a decrease of dehydrogenation temperature. Beneficial effects of carbon addition on the dehydrogenation kinetics were also observed for the Li–B–Mg–H system [8] or using nanoporous carbon [9].

In this chapter it is shown that LiBH_4 deposited on carbon nanotubes, previously modified by ball milling, exhibits a lower dehydrogenation temperature compared to the pure material. It is also shown that, even if the thermodynamics remains unchanged with respect to the pure LiBH_4 , dehydrogenation temperature is lower when the SSA of the support is larger. This improvement may be correlated to a heterogeneous nucleation process of the solid decomposition products of reaction (2.18) on the surface of carbon.

In section 2.1.3 it was also discussed how the thermodynamic properties of a storage material can be also controlled getting chemical stability of the dehydrogenated state, thus diminishing the enthalpy for dehydrogenation [10, 11]. Destabilization of complex hydrides with reactive composite systems allows to increase dramatically the performances of individual materials [12, 13], creating new dehydrogenation mechanisms [14]. The second experiment presented in this chapter is an attempt to show the synergistic effects of the two mentioned destabilization methods [15]: it is shown that ball milled mixtures of LiBH_4 and $\text{Mg}(\text{BH}_4)_2$ deposited on graphite exhibit a lower onset dehydrogenation temperature compared to supported individual materials or unsupported reactive mixtures.

Finally, $\text{Ca}(\text{BH}_4)_2$ is considered, a material which has been already proved to be partially reversible [16]. According to suggestions in similar works [9], the third experiment tries to achieve reversibility in more moderate conditions, reducing the particle size of $\text{Ca}(\text{BH}_4)_2$ to nanoscale with its confinement into specifically synthesized ordered mesoporous carbon (MC).

4.2

Preparation and Characterization of Samples

4.2.1

Lithium, Magnesium and Mixed Borohydrides

Commercial multi-walled carbon nanotubes (MWCNTs), provided by CNT Co. Ltd. (Korea), were modified by high energy ball milling in order to increase the SSA. They were used as received (CNT-0) and milled for 15, 90, 600 and 600 °C (in this last case 660 min adding 10 min pause every hour) obtaining the samples CNT-1, CNT-2 and CNT-3, respectively. In the same way, starting from commercial graphite (purchased from Carlo Erba Reagenti) as received (GRA-0), microporous graphite was obtained by milling for the same amounts of time, yielding to samples GRA-1, GRA-2 and GRA-3, respectively.

The modified MWCNTs were then poured into a 0.1 M solution of LiBH_4 (Sigma-Aldrich, purity > 95 %) in methyl tert-butyl ether (MTBE, Sigma-Aldrich, anhydrous, 99.8 %). The suspension was stirred for 12 h and the solvent was then removed by evaporation under rotary pump vacuum. In order to understand the effect of carbon on the dehydrogenation kinetics of LiBH_4 better, samples were prepared using the different MWCNTs: in the following discussion these samples will be called $\text{L}_{\text{CNT-0}}$, $\text{L}_{\text{CNT-1}}$, $\text{L}_{\text{CNT-2}}$ and $\text{L}_{\text{CNT-3}}$ with respect to the nanotubes used. Moreover, three samples with different LiBH_4 :MWCNTs mass ratios were prepared using CNT-2: sample $\text{L}_{\text{CNT-2}}$ (1:1.8), sample $\text{L}'_{\text{CNT-2}}$ (1:0.9) and sample $\text{L}''_{\text{CNT-2}}$ (1:0.45).

In the following step, the same LiBH_4 was used with magnesium borohydride synthesized from MgBut_2 and BH_3SMe_2 [18] following the method described in [19]. Mixtures of these two products, LiBH_4 : $\text{Mg}(\text{BH}_4)_2$ with stoichiometric ratios 1:0, 2:1, 1:1, 1:2, 0:1 were obtained by ball milling in Ar atmosphere for 15 h. The masses of the starting materials used for a typical throughput of 1 g are reported in table 4.1. Samples L and M are the initial materials after ball milling.

Smaller amounts of pure and mixed samples, typically a tenth of a gram, were soluted in 50 ml of MTBE and stirred for 24 h in protective atmosphere vials. The milled graphite was degassed at 300 °C in rotary vacuum and then poured into the solution of borohydride mixtures in MTBE and stirred for further 24 h. Afterwards it was dried using a Schlenk flask connected to rotary pump vacuum and, finally, heated to 100 °C for 3 h.

TPD and PCI measurements were performed on the produced samples by means of the volumetric apparatus described in section 3.3.2.1. Before the TPD measurements, the sample chamber with the sample inside was evacuated at room temperature. The total volume of the Sievert's device was assumed to be large enough to avoid kinetics being affected by the increase of hydrogen pressure during the measurements. Then the temperature was raised from ambient to 500 °C at a heating rate of 2.5 °C min⁻¹. XRD patterns of milled, mixed and impregnated samples were obtained using a Philips PW1820/00

Label	Ratio	LiBH_4 (g)	$\text{Mg}(\text{BH}_4)_2$ (g)
L	1:0	1.000	0.000
$\text{LM}^{2:1}$	2:1	0.449	0.551
$\text{LM}^{1:1}$	1:1	0.289	0.711
$\text{LM}^{1:2}$	1:2	0.169	0.831
M	0:1	0.000	1.000

Table 4.1: Masses used for ball-milling of un-mixed and mixed borohydrides, with a throughput of 1 g.

and a Bruker D8 Advance diffractometer. The surface area of as-received and ball-milled MWCNTs and graphite was determined from N_2 adsorption experiments applying the multi-point BET method, while the graphite micropore area was derived with statistical thickness method as described in section 3.2.3. The samples were degassed for at least 12 h at $300\text{ }^\circ\text{C}$ to remove any moisture or adsorbed contaminants that might be present on the surface. SEM micrographs were acquired with a JEOL JSM-6490 microscope operated at 20 kV.

DSC measurements were performed using a DSC-1 Mettler Toledo instrument with a heating rate of $5\text{ }^\circ\text{C min}^{-1}$. The samples were charged inside 40 μl aluminium pans, which were sealed by cold welding, using a suitable press. The temperature and enthalpy calibrations for the DSC instrument were checked by measuring melting temperature and enthalpy of tin and indium standards [20].

4.2.2 Calcium Borohydride on MC

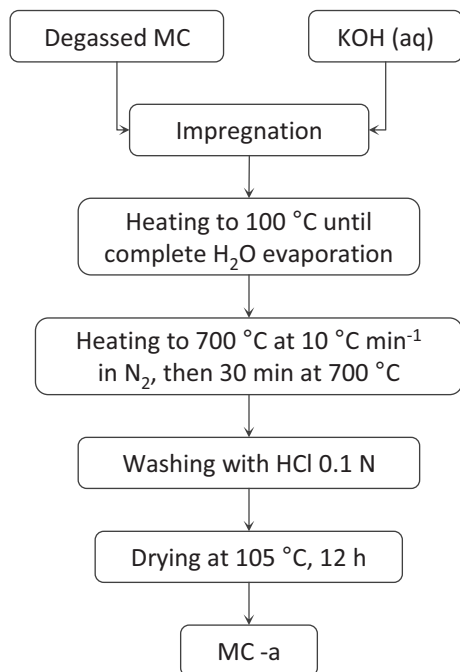


Figure 4.1: Scheme of activation procedure steps for activated mesoporous carbon.

MC was synthesized by soft-templating using phloroglucinol-formaldehyde resins, with a pyrolyzation temperature of $650\text{ }^\circ\text{C}$ in flowing N_2 . In a typical synthesis 1.25 g phloroglucinol and 1.25 g Pluronic F127 (the soft-template) were added to a mixture of $\text{EtOH}:\text{H}_2\text{O}$ 10:9 by weight stirring until complete dissolution. A catalytic amount (0.09 cm^3) of HCl was then added and the mixture was further stirred for an additional half an hour. A light pink colour appeared after 30 min and 1.25 cm^3 of formaldehyde was added to the reaction beaker while stirring. The mixture turned cloudy and after other 2 h stirring, the products separated into a polymeric layer at the bottom and an aqueous layer on top, which was easily eliminated. The stirring continued overnight and the result was a soft monolith, which was transferred into an oven at $100\text{ }^\circ\text{C}$ for 24 h air curing. Several monoliths, produced in this way, turned dark-red after this last treatment and were transferred into an oven for treatment at high temperatures ($600, 650, 700$

and $850\text{ }^\circ\text{C}$) in N_2 atmosphere to obtain carbonaceous materials denoted MC 600, MC 650, MC 700 and MC 850, respectively.

Chemical activation was carried out using an aqueous KOH solution (5 M) and subsequent heat treatment in N_2 atmosphere at $700\text{ }^\circ\text{C}$, as schematized in figure 4.1. The final quality of an activated carbon depends ultimately on two factors: the starting materials and synthesis route conditions [21, 22, 23]. A chemical activation with KOH was chosen,

since a physical activation with CO_2 would act more like a hole-driller and expander in the pores: carbon dioxide reacts with elementary graphite micro-crystallites and burns off the carbon atoms at the sides of the pores, resulting in a heterogeneous structure with various types of pores. On the other hand, chemical activation with KOH has some advantages concerning the final properties of the carbonaceous material since it enhances its surface area, pore volume and textural properties and is relatively easily applied [22, 24, 25]. Surface area and pore size analysis, carried out on these activated carbons, denoted as MC 600-a, MC 650-a, MC 700-a and MC 850-a, is described in section 4.3.1.3, and led to the choice of MC 650-a as support for impregnation of $\text{Ca}(\text{BH}_4)_2$ (Sigma-Aldrich, purity > 95 %).

Composites $\text{Ca}(\text{BH}_4)_2/\text{MC 650-a}$ (labeled as $\text{C}_{\text{MC 650-a}}$) were obtained by the incipient wetness method in an Ar atmosphere by impregnating a 0.1 M $\text{Ca}(\text{BH}_4)_2/\text{MTBE}$ solution in MC 650-a. In a typical impregnation 0.057 g of $\text{Ca}(\text{BH}_4)_2$ and 0.100 g MC 650-a were used. MTBE was chosen as it does not form dangerous peroxides, owing to its bulky chemical structure.

The surface area and pore size analysis (see data in table 4.3) performed in particular on sample MC 650-a showed a pore volume of $1.01 \text{ cm}^3 \text{ g}^{-1}$. This means that the available pore volume found in 0.1 g MC 650-a was $0.1 \text{ g} \times 1.01 \text{ cm}^3 \text{ g}^{-1} \cong 0.1 \text{ cm}^3$. The density of $\text{Ca}(\text{BH}_4)_2$, $\sim 1.1 \text{ g cm}^{-3}$, was evaluated considering that at RT it consisted of a mixture of α -phase (87 %, 1.094 g cm^{-3}) and β -phase (13 %, 1.118 g cm^{-3}) [26]. An amount of $\text{Ca}(\text{BH}_4)_2$ suitable to fill ~ 50 % of the available carbon pore volume was used. A slight MTBE excess (~ 25 %) served to counteract the evaporation process and continuing stirring until the complete borohydride dissolution.

Pure $\text{Ca}(\text{BH}_4)_2$ was used as a reference for comparison, as well as a $\text{Ca}(\text{BH}_4)_2/\text{graphite}$ composite ($\text{C}_{\text{GRA-3}}$) obtained impregnating 0.1 g commercial ball-milled graphite GRA-3 with 0.05 g $\text{Ca}(\text{BH}_4)_2$ in MTBE solution, following the method already used in section 4.2.1. Carbonaceous sample and solvent handling was performed in an Ar filled glove box (less than 100 ppm H_2O and 0.1 % O_2) and, for the most reactive products, the Labstar glove box was used (see section 3.1.2 at page 38).

XRD patterns of $\text{C}_{\text{MC 650-a}}$ and reaction mixtures, after several hydrogen a/d cycles (both absorbed and desorbed samples) were obtained with a Bruker D8 diffractometer. SSA, pore volume and PSD were deduced from sorption isotherms, recorded on the prepared MC before and after chemical activation. TPA and TPD measurements, with a heating rate of $2.5 \text{ }^\circ\text{C min}^{-1}$ at temperatures up to $550 \text{ }^\circ\text{C}$, were performed on $\text{Ca}(\text{BH}_4)_2$, $\text{C}_{\text{GRA-3}}$, $\text{C}_{\text{MC 650-a}}$. The hydrogen amounts reported in the following are percentage weights of H_2 in the $\text{C}_{\text{MC 650-a}}$ composite as a whole.

4.3

Analysis of Experimental Outcomes

4.3.1

Characterization of Carbonaceous Supports

4.3.1.1 Carbon Nanotubes

Table 4.2 reports the effect of ball milling on the SSA of MWCNTs, which increases with ball milling time and is more than twice after 600 min milling with respect to the

Milling time (min)	Nanotubes		Graphite		
	Sample	External SSA (m ² g ⁻¹)	Sample	External SSA (m ² g ⁻¹)	Micropore area (m ² g ⁻¹)
0	CNT-0	201	GRA-0	9	0
15	CNT-1	229	GRA-1	55	7
90	CNT-2	263	GRA-2	256	73
600	CNT-3	408	GRA-3	182	115

Table 4.2: BET surface area of MWCNTs as a function of high energy ball milling time.

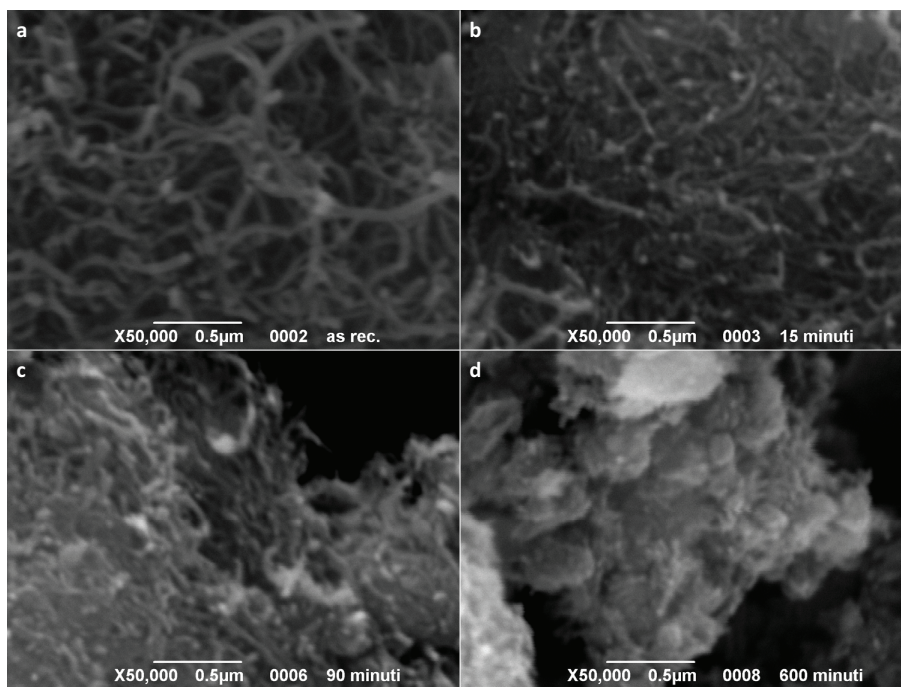


Figure 4.2: SEM micrographs of MWCNTs as received (a) and high energy ball milled for 15 (b), 90 (c) and 600 min (d). See table 4.2.

as-received material. From the SEM micrographs shown in figure 4.2 it is possible to see the evolution of nanotubes morphology with ball milling time. Figure 4.2 a shows the morphology of the as-received nanotubes CNT-0 with an average diameter of about 60 nm. As already reported in [27, 28], carbon nanotubes are shortened by the ball milling process, while the average diameter remains unchanged. This is shown in figures 4.2 b and 4.2 c for CNT-1 and CNT-2, respectively. In both cases, the material looks more compact with respect to CNT-0 (figure 4.2 a). After 600 min ball milling the structure of nanotubes vanishes (CNT-3, figure 4.2 d), resulting in the typical morphology of an amorphous-like carbon.

4.3.1.2 Graphite

The results of morphological characterization of the milled graphite, to be used as support of the borohydrides, are reported in table 4.2 and figure 4.3.

The results of BET and micropore analysis are summarized in table 4.2. The values of SSA are increasing with longer milling time, due to the presence of micropores, but

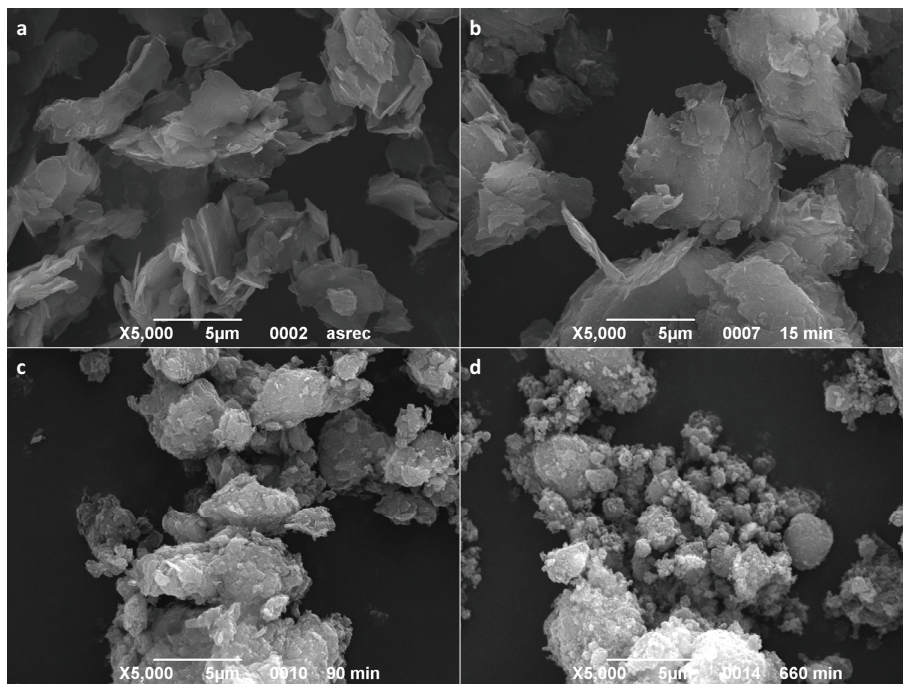


Figure 4.3: SEM micrographs for graphite as received (a) and high energy ball milled for 15 (b), 90 (c) and 600 min (d). See table 4.2.

the external surface area, in particular from sample GRA-2 to GRA-3, is not following this trend. The cause can be better understood observing the SEM pictures of figure 4.3. It is clearly visible how the pristine structure of the as received graphite is still visible after milling by 15 min, but destroyed after 90 min and especially after 600 min, when the lamellar particles are completely replaced by a disordered powder with rough and eventually porous surface.

4.3.1.3 Mesoporous Carbon

The effect of the carbonization temperature on the properties of the as-prepared and activated carbons can be deduced from the isotherms of figure 4.4. According to the computed data of table 4.3, the temperature provides a fine-tuning of the microporous-mesoporous

Sample	SSA ($\text{m}^2 \text{g}^{-1}$)	V_t ($\text{cm}^3 \text{g}^{-1}$)	V_m ($\text{cm}^3 \text{g}^{-1}$)	V_m / V_t (%)
MC 600	620	0.87	0.11	12.6
MC 600-a	1946	1.14	0.60	52.6
MC 650	521	0.75	0.10	13.3
MC 650-a	1780	1.01	0.67	66.3
MC 700	563	0.85	0.09	10.5
MC 700-a	1340	1.05	0.39	37.1
MC 850	518	0.71	0.08	11.2
MC 850-a	874	0.96	0.21	21.8

Table 4.3: Pore and surface parameters for MC before and after activation.

volumes, while the chemical activation greatly enhances the microporous region, especially for the carbons as MC 600 and MC 650 having already a considerable amount of micropores. As seen, a well developed hysteresis loop evolves from 600 to 850 °C. Comparing the loops of MC and activated MC samples at the same temperature, it is evident in figure 4.4 a that for 850 °C carbonization the activation process does not change the hysteresis loop, influencing only the pore texture and the surface area. For 700 °C carbonization (figure 4.4 b) this last effect is higher and the loop exhibits a lower hysteresis.

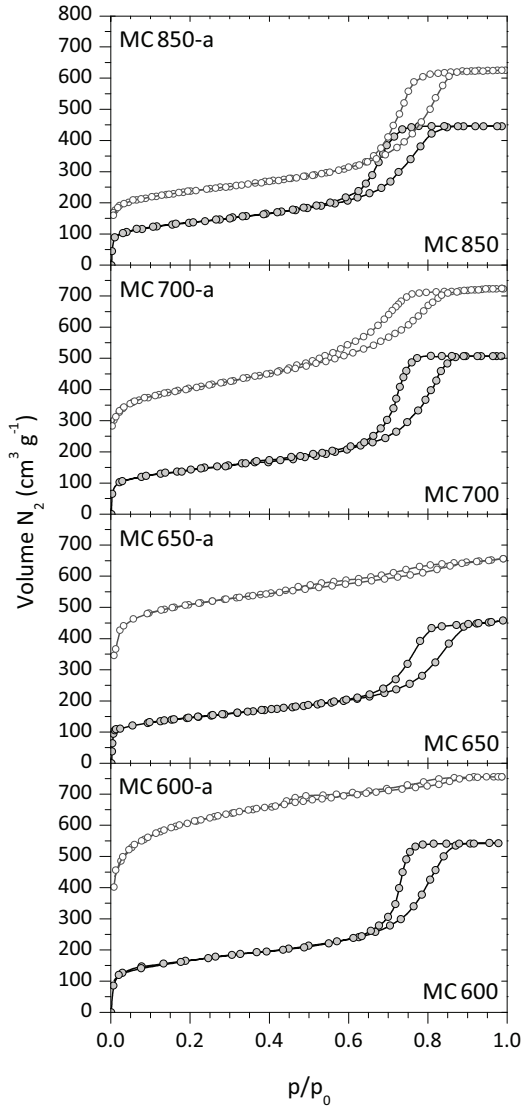


Figure 4.4: N_2 adsorption isotherms of different MC samples before (filled symbols) and after activation (empty symbols).

best range of application. Moreover, in the present case, micropore volumes (V_m in table 4.3) have been computed by the DR method, while pore volumes (V_t in table 4.3) with the t -plot method.

As said before, the MC 650 sample was chosen since it showed, according to table 4.3, the highest percentage of micropores among the initial carbon samples (13.3%), and it was

Finally, for 650 and 600 °C carbonization (figures 4.4 c and 4.4 d) a higher value of the SSA is obtained after activation and the hysteresis is minimized. The pore diameter increases with the carbonization temperature, so the lower the carbonization temperature, the smaller the resulting pores. On the other hand, since the pore volume decreases globally with higher temperature, the highest number of smaller pores is found for specimens treated at lower temperature. For all these reasons the MC 650-a support was chosen for impregnation, since it exhibits a very high surface area ($1780 \text{ m}^2 \text{ g}^{-1}$ in the region of relative pressures $p/p_0 = 0-0.25$) and pore diameters and volume suitable for incorporation of a borohydride.

For activated carbons, it is widely accepted [29] that the use of BET analysis yields an overestimation of the SSA, due to the quasi-capillary condensation effect. However, one may account for this overestimation using a similar formalism, restricting the relative pressure range to 0.01–0.05 and checking the linearity of the plot, in order to evaluate the entity of microporous surface area, which influences the mentioned effect. The methods used to determine the PSD discussed thoroughly in section 3.2.3, have been applied to the adsorption branch of the isotherm to avoid possible pore network and tensile strength effects. In figure 4.5 the PSD derived from SF and BJH methods are presented in their

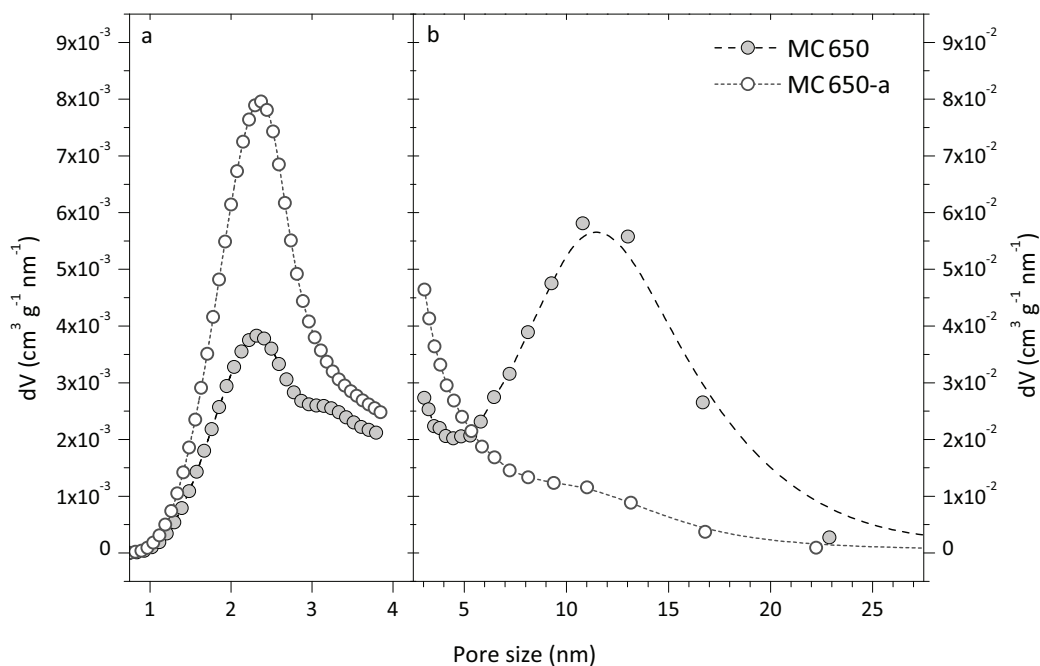


Figure 4.5: PSD of MC 650 and MC 650-a: (a) lower size range between 0.5 to 4 nm computed with the SF method; (b) higher size range between 5 to 20 nm computed with the BJH method.

expected to be the sample possessing the highest micropore percentage after activation, confirmed by the 66.3% value in the table. The pore volume was computed as a single-point pore volume, at the relative pressure $p/p_0 \simeq 0.99$. The corresponding isotherms also show a slightly more resolved hysteresis loop for the MC 650-a rather than for MC 600-a, thus pore blocking issues are more likely to be present in the latter. The samples MC 700-a and MC 850-a have a broader PSD, as suggested by the shape of their condensation step.

4.3.2

Properties of Studied Borohydride Mixtures

The XRD patterns shown in figure 4.6 belong to the as-milled mixtures of borohydrides at different ratios. Samples L and M display the diffraction peaks of the low temperature stable phases for starting borohydrides: in the pattern of sample L all the peaks for orthorhombic phase of LiBH_4 are labelled and the pattern of sample M is almost completely attributable to $\alpha\text{-Mg}(\text{BH}_4)_2$ phase with minor contribution of $\beta\text{-Mg}(\text{BH}_4)_2$ phase. In all milled samples, a small loss of crystallinity can be noticed with respect to the as-received or as-synthesized products, causing little broadening, shift and differences in the intensity ratios of peaks. To improve the diffraction patterns and the characterization of the samples a mild annealing treatment has been tried, heating the samples at 150°C in H_2 atmosphere for 6 h. The patterns obtained after this treatment added no further information to those shown in figure 4.6, so they are not reported.

The XRD patterns of the mixed borohydrides can be described as a combination of the already identified stable phases: going from $\text{LM}^{2:1}$ to $\text{LM}^{1:2}$ there is an increasing contribution of $\alpha\text{-Mg}(\text{BH}_4)_2$ and an obvious decrease of LiBH_4 peaks. There is no evidence of any

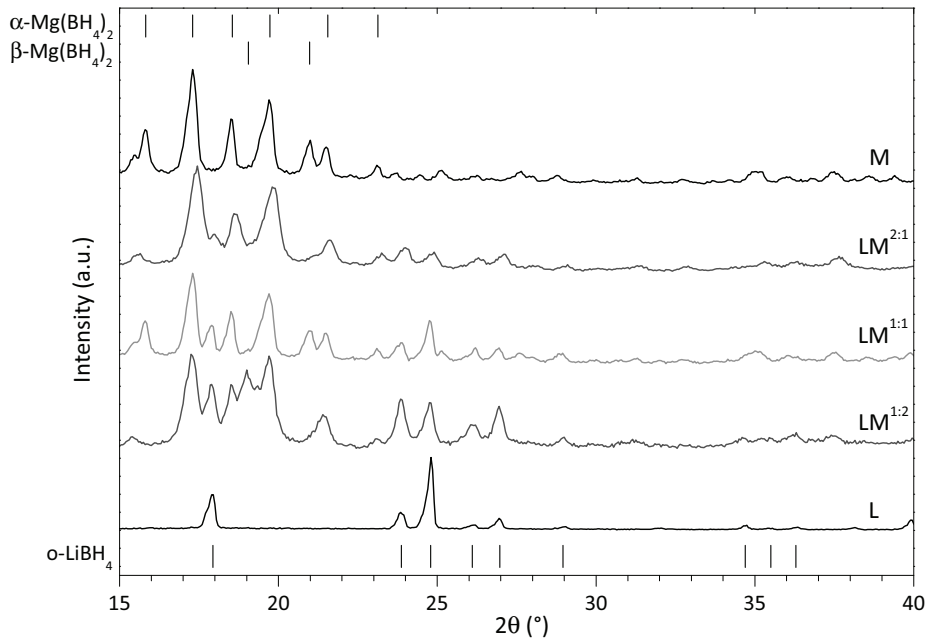


Figure 4.6: XRD patterns of ball milled borohydrides and borohydride mixtures (labelled as in table 4.1).

dual-cation borohydride formation in the process of milling, as proposed by Fang *et al.* [30] and already confuted by Bardají *et al.* [31].

In figure 4.7 the TPD analysis profiles performed on the five different samples are reported: lines L and M represent pure LiBH_4 and pure $\text{Mg}(\text{BH}_4)_2$, respectively, while the other lines refer to mixed samples, which give intermediate desorption properties between the pure borohydrides. It was analyzed in section 2.3.1.1 how the electronegativity χ_p of the cation is influencing the enthalpy of the considered borohydride. That is resulting in the relationship shown in figure 2.5 for a group of materials, later updated in a following work, where χ_p is also put in correlation with the temperature of desorption T_d [32]. According to a development based on this phenomenon [33], the electronegativity of the mixed cations in $\text{MM}'_{m-n}(\text{BH}_4)_m$ borohydrides can be calculated with the following equation:

$$\chi_{\text{MM}'} = \frac{\chi_{\text{M}} + \chi_{\text{M}'}(m-n)}{1 + (m-n)} \quad (4.1)$$

where χ_{M} and $\chi_{\text{M}'}$ are the electronegativities of the two cations, and $\chi_{\text{MM}'}$ is the resulting value for the mixed one. The link between T_d and χ_p is assumed to be valid also for mixed borohydrides [33]. Considering Li ($\chi_{\text{Li}} = 1.0$) and Mg ($\chi_{\text{Mg}} = 1.3$) in the mixed borohydride $\text{MgLi}_{m-2}(\text{BH}_4)_m$, $\chi_{\text{MM}'}$ can be calculated for the different mixture, concluding that (following this procedure) desorption temperature should stay between the two T_d of the pure borohydrides. The experimental validation of this hypothesis was performed for Zn and Li, preparing $\text{ZrLi}(\text{BH}_4)_5$ and $\text{ZrLi}_2(\text{BH}_4)_6$ by mechanical milling of LiBH_4 – ZrCl_4 mixtures in appropriate molar ratios. In that work, it was possible to observe a dehydrogenation temperature decrease of the dual-cation borohydrides, with respect to LiBH_4 .

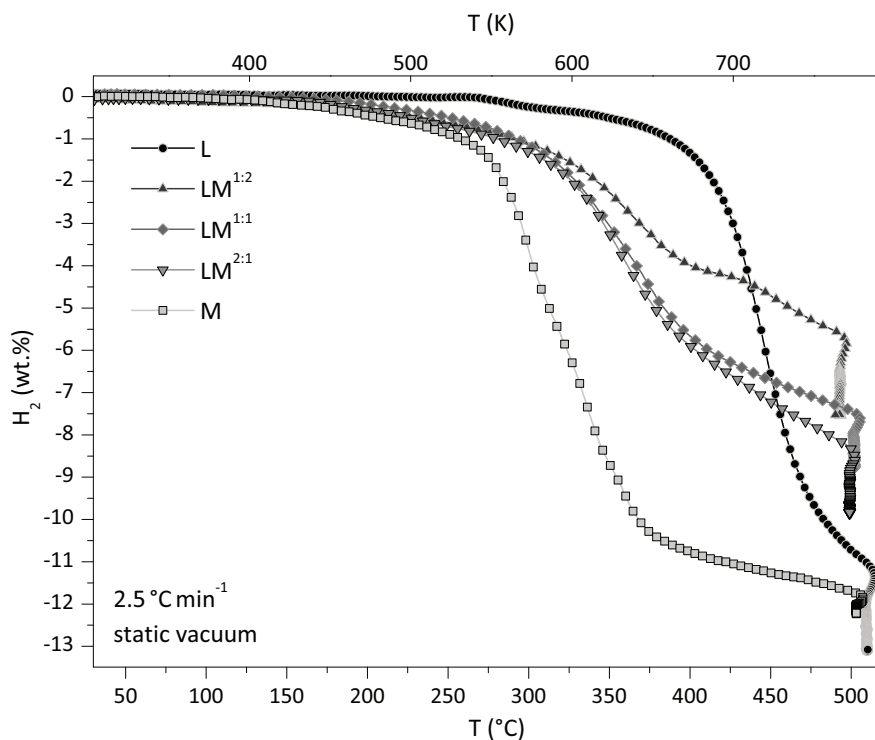


Figure 4.7: TPD profiles of milled borohydrides and physical borohydride mixtures (see table 4.1 for labels) at a heating rate of 2.5 °C min^{-1} and starting in vacuum.

The result suggests that the hydrogen desorption temperature of metal borohydrides can be precisely adjusted by the appropriate combination of cations [33].

The lack of evidence of the presence of a dual-cation compound in the physical mixture, however, do not allow to rely completely on the application of the formula (4.1) for the considered experiment.

Nevertheless, in this case, it is not possible to notice the improvement claimed in analogous experimental works [31, 34], despite the very similar starting conditions. Moreover, if the final amount of released hydrogen is lower than expected, some event has hindered its complete release, too. Presumably, the milling process carried out here with a shaker mill, more energetic than the planetary mills used in [30, 31, 34], produced a slight contamination or caking of powders due to increase of local temperature. There is the possibility that a too energetic milling is not effective to create a mixture where the polymorphic transformations are assisted by the presence of the second component.

4.3.3 Nanoconfined Samples and Mixtures

Figure 4.8 shows that the dehydrogenation reaction of supported LiBH_4 has almost the same two-step behaviour for samples $\text{L}_{\text{CNT-2}}$, $\text{L}'_{\text{CNT-2}}$ and $\text{L}''_{\text{CNT-2}}$: the first onset occurs at about 270 °C both for all the infiltrated samples and for pure LiBH_4 obtained after recrystallization in MTBE; the second onset occurs at about 340 °C , i. e. 600 °C lower than the one of pure LiBH_4 . The results are in agreement with those reported by Yu *et al.* [6].

The XRD patterns of sample $\text{L}_{\text{CNT-2}}$ as-prepared and after complete dehydrogenation are

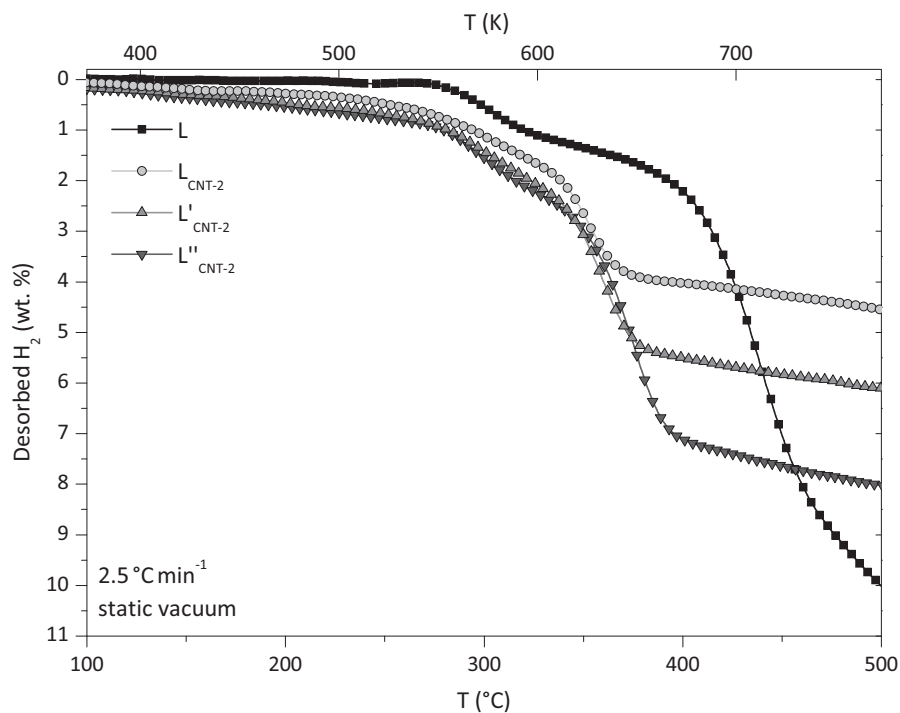


Figure 4.8: Comparison of dehydrogenation profiles of samples with different MWCNTs ratios L_{CNT-2} , L'_{CNT-2} , L''_{CNT-2} , and pure $LiBH_4$ re-crystallized with MTBE. The wt.% of desorbed H_2 is related to the total weight of the sample.

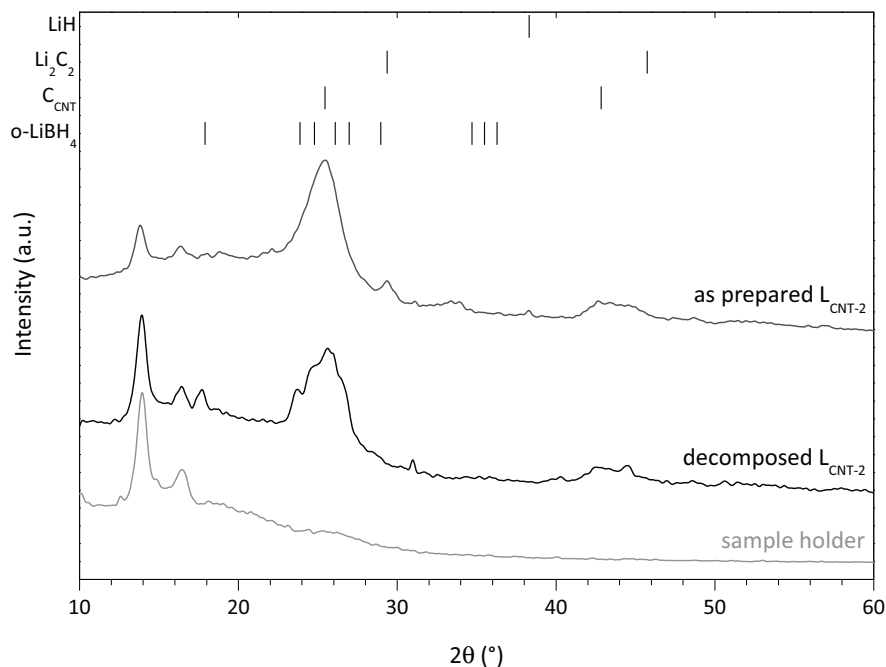


Figure 4.9: Comparison of the XRD patterns of sample L_{CNT-2} as prepared (a) and after dehydrogenation (b). The XRD profile of Kapton foil and sample holder is also reported.

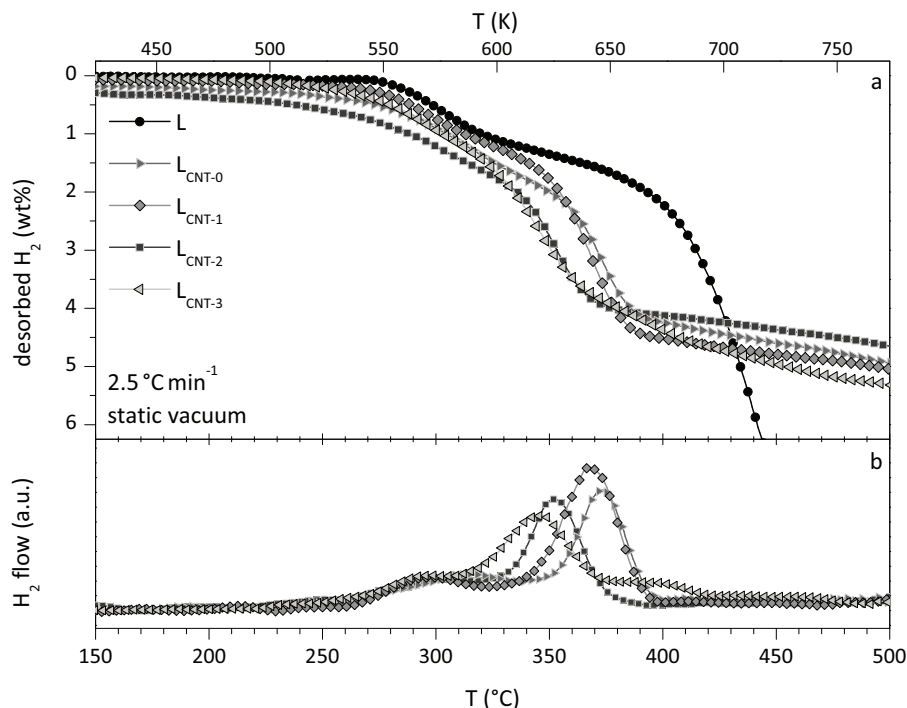


Figure 4.10: Dehydrogenation profiles of samples L_{CNT-0}, L_{CNT-1}, L_{CNT-2} and L_{CNT-3} (a) and corresponding dehydrogenation rates (b). The wt.% of desorbed H₂ is related to the total weight of the sample.

reported in figure 4.9. The as-prepared sample displays the broad peaks of carbon along with peaks of LiBH₄, while the decomposed sample presents, in addition to the peaks of carbon, weak peaks of LiH and Li₂C₂.

It is clearly evident from figure 4.10 that increasing the SSA of the carbonaceous support leads to the decrease of the onset temperature of the main dehydrogenation process, going from about 350 °C in the case of the as-received MWCNTs (L_{CNT-0}) to about 310 °C in the case of L_{CNT-3}. Hence, the SSA of the carbonaceous support seems to have an important effect on the dehydrogenation kinetics of LiBH₄.

The TPD curves in figure 4.11, as well, represent a clear evidence of lowering the hydrogen release temperature when a hydride is impregnated into a high SSA material. The higher the SSA, the stronger is this effect: the temperature for the main release (when most of the H₂ is released at the fastest rate) is shifted by almost 100 °C in the sample L_{GRA-3} if compared with L (not impregnated LiBH₄). Of course, the use of milled graphite is decreasing the storage gravimetric capacity; with L_{GRA-0}, the use of as received graphite seems to have even a detrimental effect in the temperature, but this is due to the lower released amount that stretches the curve with respect to L.

It is possible to conclude that the as received graphite is having almost no effect on release temperature, due to the low specific surface area. This is better comprehensible looking at the derivative of the desorption profiles, that give a qualitative representation of the hydrogen flow and confirm what stated before. On the basis of the results shown in figure 4.11, the 600 min milled graphite (GRA-3) was chosen as the most convenient scaffold for impregnation of mixed and unmixed borohydrides.

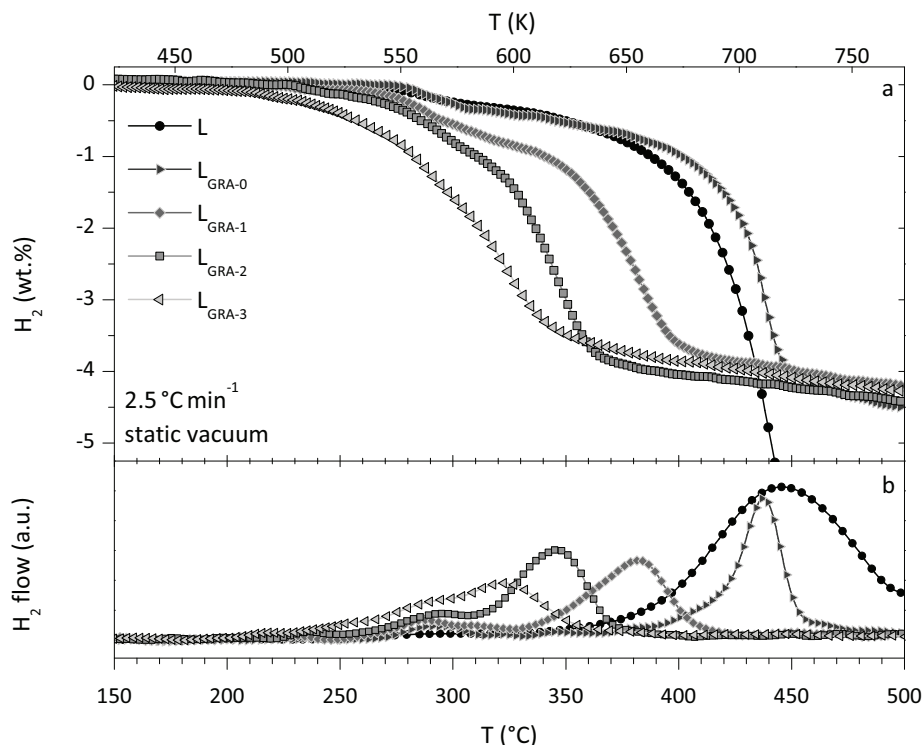


Figure 4.11: TPD curves (a) and corresponding derivative (b) for sample L (see table 4.1) on different SSA graphite supports (see table 4.2), at a heating rate of 2.5 °C min^{-1} and starting in vacuum.

Figure 4.12 shows the results of XRD analysis of these samples, as well as the pattern of GRA-3. The effect of confinement is clearly evident in all samples, particularly in those containing a higher percentage of $\text{Mg}(\text{BH}_4)_2$. Starting from pattern $\text{L}_{\text{GRA-3}}$, where all the peaks for LiBH_4 are broad, moving to higher magnesium borohydride content, a slight increase in the intensity of background profile (centered at about $2\theta = 25^\circ$) can be observed. In pattern $\text{LM}_{\text{GRA-3}}^{2:1}$ it is hard to detect traces of $\alpha\text{-Mg}(\text{BH}_4)_2$, which become more visible in $\text{LM}_{\text{GRA-3}}^{1:1}$ and then disappear in pattern $\text{LM}_{\text{GRA-3}}^{1:2}$, where are replaced by a second hump at lower angles. Pattern of sample $\text{M}_{\text{GRA-3}}$ (not shown) is similar to this last one, where no phases were detectable besides graphite. A plausible reason for this behaviour is that $\alpha\text{-Mg}(\text{BH}_4)_2$ is more prone to nucleate as small particles or amorphous material inside the graphite.

The TPD analysis on dispersed borohydrides is shown in figure 4.13. Starting from sample $\text{L}_{\text{GRA-3}}$ (i. e. the same shown in figure 4.11), the desorption temperature is lowered of further tens of degrees. Sample $\text{M}_{\text{GRA-3}}$ (pure supported $\text{Mg}(\text{BH}_4)_2$) displays a TPD profile starting after 200 °C with a maximum of flow at 275 °C , while the samples $\text{LM}_{\text{GRA-3}}^{2:1}$ and $\text{LM}_{\text{GRA-3}}^{1:2}$ present a broad flow profile with a maximum around 300 °C : the shape indicates that desorption starts at a lower temperature and occurs in a wide interval of time. The best behaviour in terms of lowering the temperature is that of sample $\text{LM}_{\text{GRA-3}}^{1:1}$, the flow peak of which is at about 260 °C .

All the samples have a gravimetric capacity between 3 and 4 wt.% H_2 , except for $\text{L}_{\text{GRA-3}}$, which is one point higher.

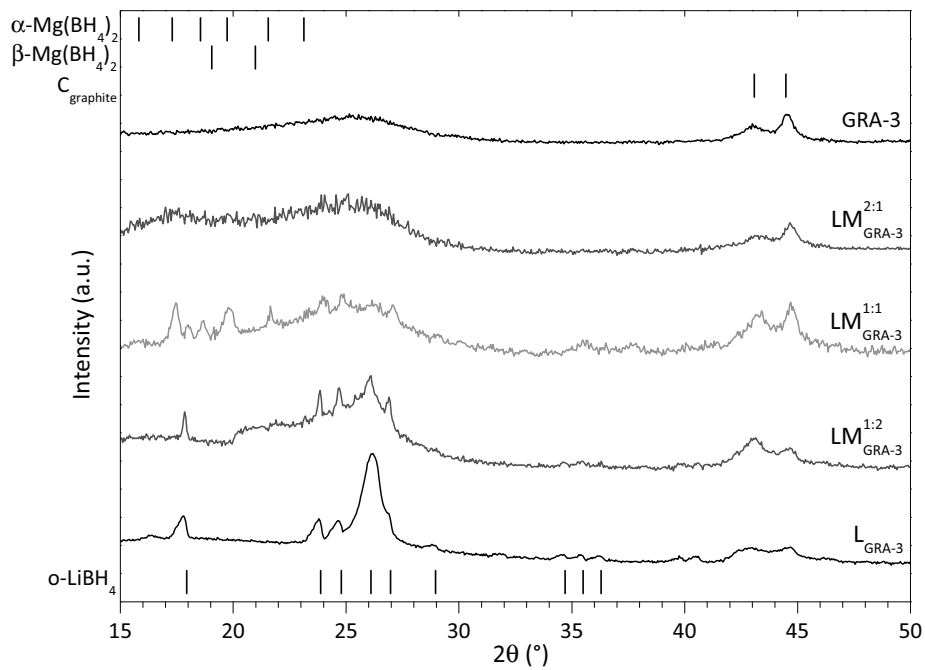


Figure 4.12: XRD patterns of samples $L_{\text{GRA-3}}$, $LM_{\text{GRA-3}}^{2:1}$, $LM_{\text{GRA-3}}^{1:1}$, $LM_{\text{GRA-3}}^{1:2}$, after impregnation in the milled graphite, represented by pattern GRA-3 (see tables 4.1 and 4.2).

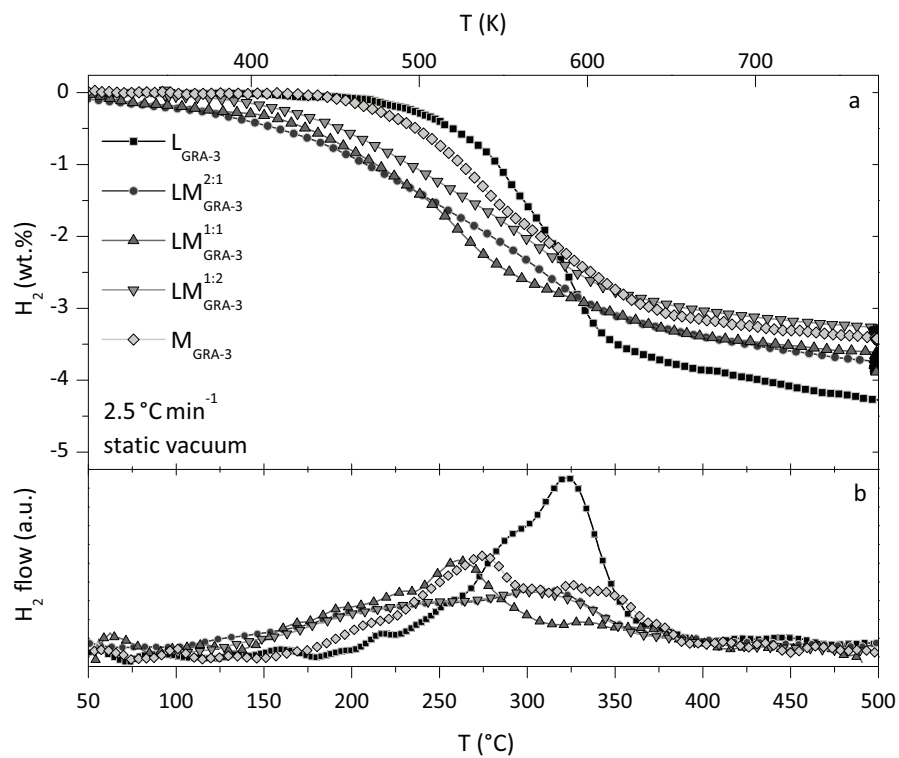


Figure 4.13: TPD curves (a) and corresponding derivative (b) for base materials and mixed samples on GRA-3 at a heating rate of 2.5 °C min^{-1} and starting in vacuum.

4.3.3.1 Interpretation of Reaction Improvement

This effect may be explained considering the surface of the support not only as a mean to disperse the active material, but also as a nucleation centre for the solid decomposition products of borohydrides. LiBH_4 melts at 268 °C [35] then, when dehydrogenation starts, some solid LiH and B particles start nucleating from liquid LiBH_4 along with hydrogen desorption. The high surface area of the carbonaceous material probably acts as a centre for heterogeneous nucleation of the decomposition products. Considering a spherical cluster having radius r that nucleates from the melt, the free energy needed for its nucleation is

$$\Delta G = \frac{4}{3}\pi r^3 \Delta G_v + 4\pi r^2 \sigma \quad (4.2)$$

where ΔG_v is the free energy gain for volume unit and σ is the interfacial energy [36]. To increase the radius of the nuclei, the system needs free energy and if $\frac{dG}{dr} > 0$ the growth of the nuclei is limited by nucleation. This occurs when the radius is less than the critical radius r^* defined as

$$r^* = -\frac{2\sigma}{\Delta G_v} \quad (4.3)$$

to which corresponds a maximum of free energy:

$$\Delta G^* = \frac{16\pi\sigma^3}{3(\Delta G_v)^2} \quad (4.4)$$

When the nuclei reach the radius r^* , the energy barrier ΔG^* for nucleation has been overcome and nucleation proceeds [37]. If the products nucleate on a surface, wetting it with a contact angle θ , the heterogeneous nucleation process occurs and the energy barrier for nucleation is

$$\Delta G_{\text{heterogeneous}}^* = \Delta G_{\text{homogeneous}}^* \cdot s(\theta) = \Delta G^* \cdot s(\theta) \quad (4.5)$$

where $s(\theta)$ is the shape factor defined as

$$s(\theta) = \frac{1}{2} - \frac{3}{4} \cos \theta - \frac{1}{4} \cos^3 \theta \quad (4.6)$$

It corresponds to the ratio between the volume of the particle nucleated on the surface and the volume of a sphere having the same radius of curvature r ; therefore, it is smaller than 1. This means that in this case the nuclei that can overcome the nucleation energy barrier have the same critical radius, but need a much smaller volume. Hence, it is obvious that increasing the available surface for heterogeneous nucleation (the SSA of the support), it is possible to increase the reaction kinetics. According to this interpretation, it could be possible, in principle, to reduce the dehydrogenation temperature of a borohydride further, by choosing a support with the same SSA on which the contact angle of solid decomposition products is smaller.

An attempt to find an experimental evidence to confirm this hypothesis could be made assuming that the wetting contact angle θ of melted borohydrides on graphite differs from that on nanotubes. Comparing the effect of CNT-2 with that of GRA-3 on LiBH_4 is the best option, because the two mentioned supports have a very similar SSA (see table 4.2). However, the difference between the decomposition temperature of $\text{L}_{\text{CNT-2}}$ and $\text{L}_{\text{GRA-3}}$ is not so high: θ depends mainly on the interaction between the liquid and the solid surface.

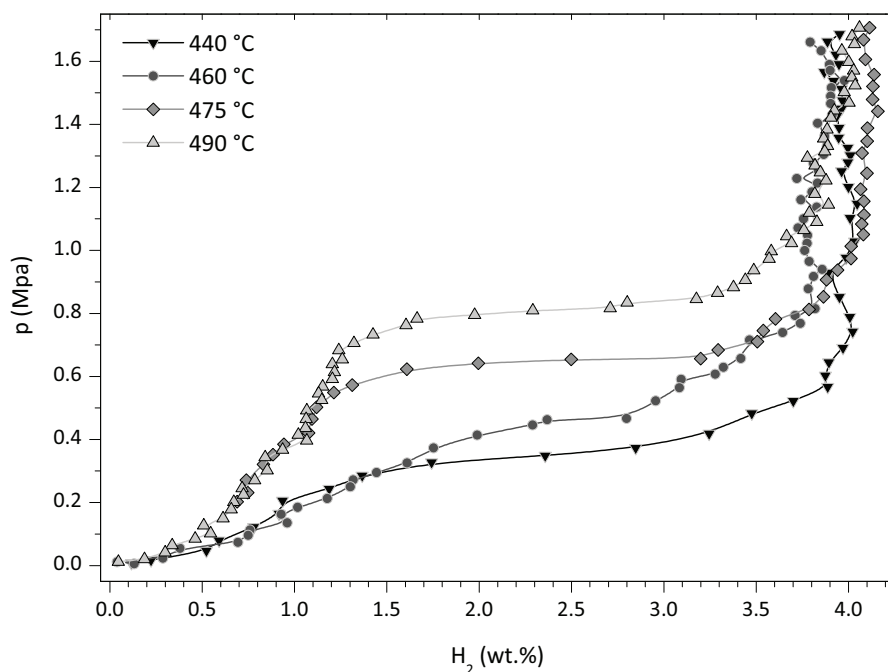


Figure 4.14: PCI (desorptions) obtained during dehydrogenation of sample LCNT-3.

It is plausible to consider nanotubes and graphite to have a very similar response, as they have the same chemistry, similar structure and they went through the same milling treatment. Apparently the only reasonable variation to justify the small temperature difference can be found in the surface curvature (assuming a flat graphite and convex nanotubes). An enhanced nucleation effect may be possible activating the surfaces to increase the wettability, i. e. using activated carbon for the infiltration of borohydrides [38].

4.3.3.2 Thermodynamic Behaviour

In the previous discussion only kinetics has been considered. Anyway, the infiltration of LiBH_4 in a high surface area material could also lead to the formation of nanoparticles that, due to a size effect, could show modified and favourable thermodynamic properties. In order to check this possibility, the PCI curves of figure 4.14 have been measured at different temperatures during the desorption of sample LCNT-3. Usually, the poor kinetics of LiBH_4 hinders fast measurements of equilibrium pressures, but in this case it was possible thanks to the improved kinetics. The corresponding van't Hoff plot is shown in figure 4.15. The estimated values

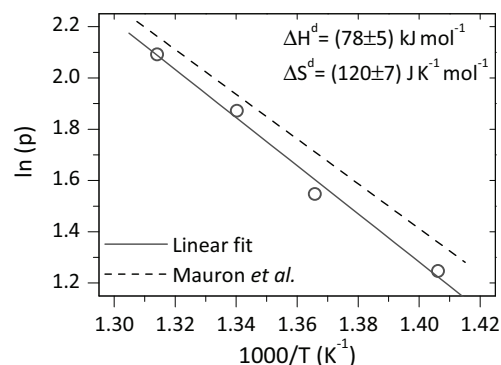


Figure 4.15: Van't Hoff plot pertinent to PCI of figure 4.14. The plot published in [39] is also shown.

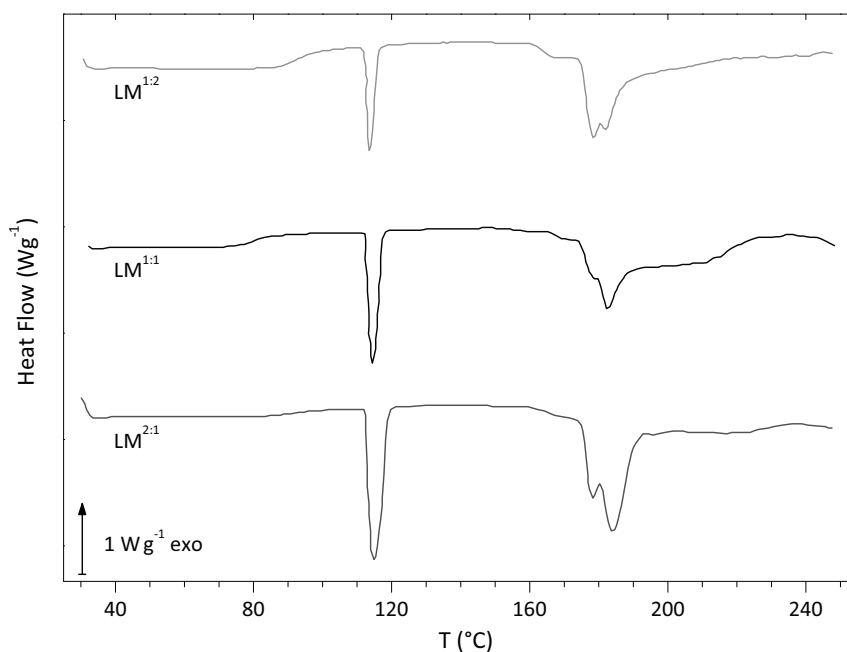


Figure 4.16: DSC profiles of the mixed samples (see table 4.1 for stoichiometry), with a heating ramp of $5\text{ }^{\circ}\text{C min}^{-1}$ in 80 ml min^{-1} Ar flow.

for dehydrogenation enthalpy and entropy changes obtained by fitting the experimental data with the van't Hoff law (2.6) are $\Delta H_d = (78 \pm 5)\text{ kJ mol}^{-1}\text{ H}_2$ and $\Delta S_d = (120 \pm 7)\text{ J K}^{-1}\text{ mol}^{-1}\text{ H}_2$. The equilibrium pressure p_{eq} for each PCI has been evaluated at the inflection point of the curve. The estimated values are in good agreement with $\Delta H_d = 74\text{ kJ mol}^{-1}\text{ H}_2$ and $\Delta S_d = 115\text{ J K}^{-1}\text{ mol}^{-1}\text{ H}_2$, recently calculated for pure LiBH_4 by Mauron *et al.* using the same law [39]. In this case the equilibrium pressure looks slightly lower, probably because of a not perfectly reached equilibrium, due to poor kinetics, especially at lower temperatures. This means that the dispersion of borohydrides on high SSA carbonaceous supports does not lead to thermodynamic destabilization of the material as argued by Yu *et al.* [6].

In figure 4.16, the DSC profiles in the range $30\text{--}240\text{ }^{\circ}\text{C}$ of samples simply mixed in a mortar are reported. It is possible to observe the endothermic polymorphic transformation of LiBH_4 at approximately $113\text{ }^{\circ}\text{C}$ and a second two peaks endothermic event at about $180\text{ }^{\circ}\text{C}$. The first is probably generated by the shifting of the $\text{Mg}(\text{BH}_4)_2$ phase transformation, as suggested in [31]. The other peak corresponds to the melting of the mixture. This low melting temperature is supposed to be one of the causes of the lower decomposition temperature of the studied borohydride mixture, when this is nanoconfined on high SSA supports: heterogeneous nucleation of decomposition products can occur from melted borohydride. The tentative phase diagram reported in [31] is showing, in fact, that a possible eutectic point is situated close to the stoichiometry of sample $\text{LM}^{1:1}$, which is the one with lower desorption temperature. It was already discussed how the decomposition is also probably aided by sites where the nucleation energy gap can be overcome, and this provide another evidence that decomposition from liquid can benefit of a **nanosupport**.

On the other hand, in the not supported mixtures the lower melting point does not affect the dehydrogenation, as an early nucleation is still energetically precluded. To further support the impregnation hypothesis, single point BET surface area measurements were carried out on nanoconfined samples. The results provided values one order of magnitude lower than those measured on the as-milled graphite (about $8 \text{ m}^2 \text{ g}^{-1}$ in comparison with values in table 4.2). This can suggest that the active material, the mixed borohydride, was effectively dispersed on the available surface filling the micropores. Further investigations are in progress to clarify this point.

4.3.3.3 Desorbed Gas Analysis

Interestingly, nanoconfinement of hydrides has been suggested as a way to effectively control the released gases, limiting undesired desorptions [40]. To detect desorbed gas thermal desorption spectroscopy (TDS) has been applied using a quadrupole mass spectrometer (MS, Catlab Hiden). In fact, along with hydrogen also other gases are desorbed from the borohydride samples: BH_3 , H_2O and B_2H_6 , respectively with M/Z ratios of 11–13, 18 and 26–27. These compound have been detected during desorption in several works [10, 17, 41]. Due to the nature of the samples, a comparison with data for $\text{Mg}(\text{BH}_4)_2$ [42], was also useful. Analyzing the research carried out on very analogous mixtures [31] it is found that the fragments of diborane have to be controlled, too. In order to analyze the full range of masses which might be observed, it has first been measured the sample L in scanning mode, figure 4.17. In this configuration the MS is able to scan all the spectrum of M/Z in a range between two set ratios at each temperature during the heating treatment. The chosen range was 4–30, excluding the signals of He (the carrier) and H_2 to identify the secondary masses better. It has been detected that the sample contained some water (M/Z = 18) and, during the heating, some 27–28–29 and 15–16 M/Z masses have been released, corresponding to B_2H_6 and BH_3 . From that moment all the analyses are carried monitoring one of each group of these masses along with M/Z = 2 (hydrogen).

In the following TDS the milled samples show a continuous release of borane that could be confused with the background. In the impregnated samples, a decrease in borane emission was expected, but the results show that there is still some release which takes place in two steps, one at low temperature and one corresponding to the desorption of hydrogen.

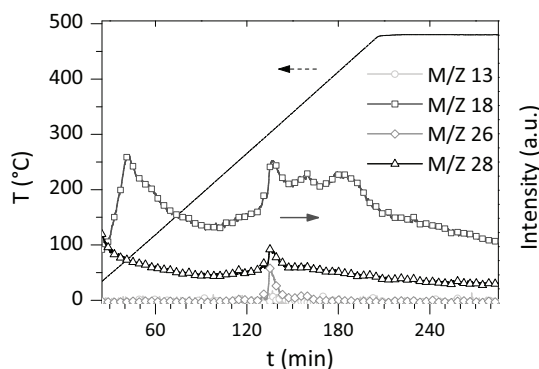


Figure 4.17: MS spectrum of secondary masses desorbed by sample L during TDS.

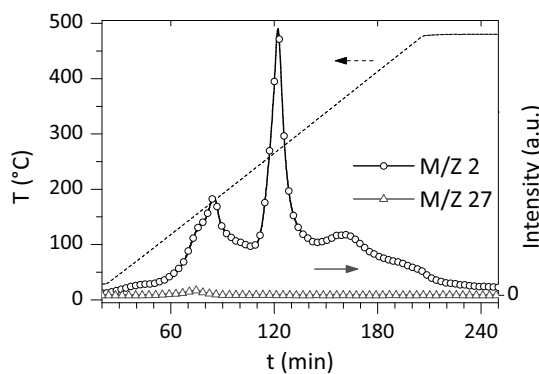


Figure 4.18: TDS spectra of LM^{1:2} sample: M/Z 2 (hydrogen) and 27 (borane).

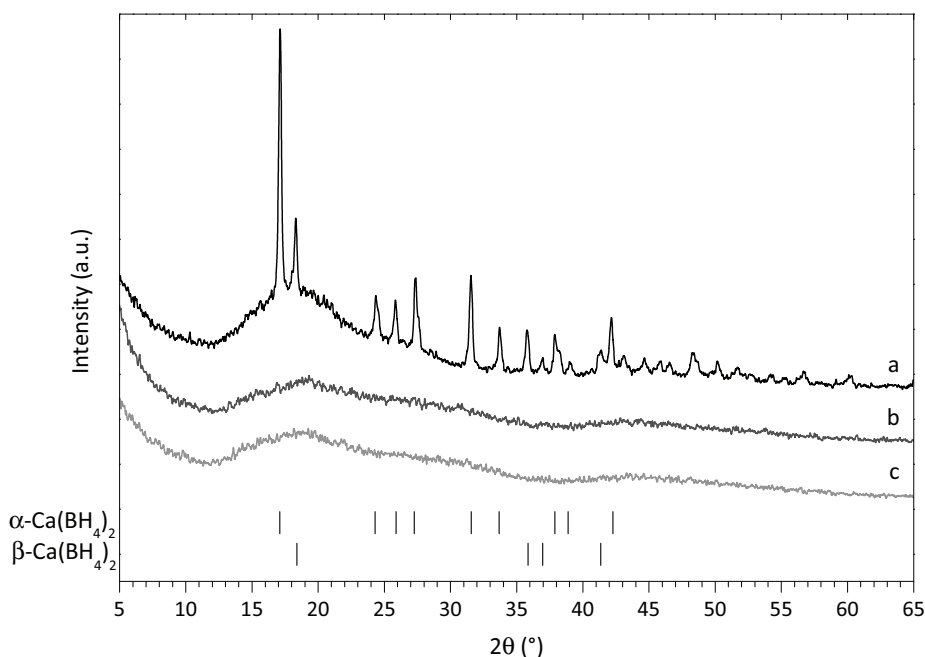


Figure 4.19: XRD patterns of $C_{MC\ 650-a}$: (a) as impregnated, (b) desorbed, and (c) absorbed, after 18 hydrogen a/d cycles.

The amount of emitted borane of impregnated samples is generally equal to or slightly higher than the milled ones, even if the hydrogen is desorbed in a lower quantity. For all the samples, anyway, the signal of borane can be considered an impurity in comparison to the hydrogen released, as it is shown in figure 4.18.

4.3.4 $Ca(BH_4)_2$

4.3.4.1 Infiltration of $Ca(BH_4)_2$ into MC-a

XRD patterns of the $Ca(BH_4)_2$ impregnated into the MC 650-a support in figure 4.19 show that a part of the borohydride crystallized outside the pores, since net peaks are displayed in the pattern of the as-impregnated sample. Therefore, only part of the borohydride was effectively introduced into the carbonaceous framework. All the sharp peaks belong to and phases of the borohydride, while the broad hump situated between 15° and 25° is due to the support. In the same figure 4.19 the XRD patterns after 18 hydrogen a/d cycles give evidence of the absence of crystalline phases both in the absorbed and desorbed state, proving the amorphous nature or nanoconfinement of the borohydride particles and of the dehydrogenation products inside the support.

4.3.4.2 Hydrogen a/d and Reversibility of the Infiltrated $Ca(BH_4)_2$

Figure 4.20 shows the TPD behaviour of $C_{MC\ 650-a}$ composite in the first desorption, along with the release profiles of the reference composite and of the pure borohydride. The hydrogen release profile starts at about $100^\circ C$ with a first desorption step, which accounts

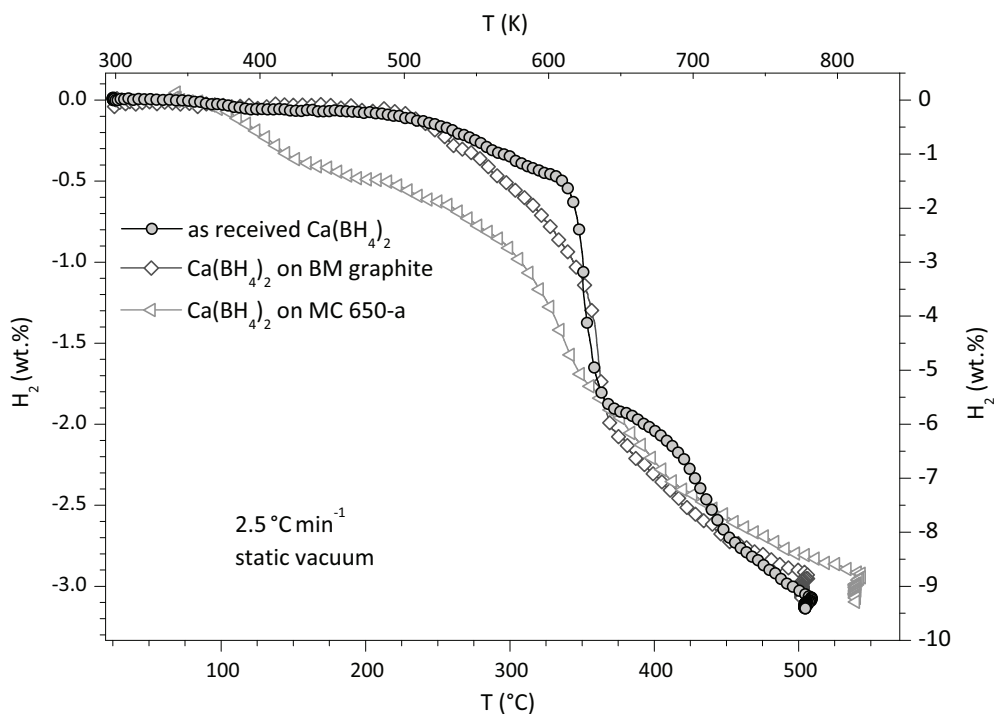


Figure 4.20: TPD curves of $\text{Ca}(\text{BH}_4)_2$, with a heating rate of $2.5\text{ }^\circ\text{C min}^{-1}$. Use vertical scale on the right for as-received material C (filled symbols); use scale on the left for $\text{C}_{\text{GRA-3}}$ and for $\text{C}_{\text{MC650-a}}$ (empty symbols).

for a small hydrogen amount, followed by the main release step starting around $280\text{ }^\circ\text{C}$. For $\text{Ca}(\text{BH}_4)_2$ alone this main step, measured both with a volumetric system and a gravimetric apparatus [43], is sharper and occurs at approximately $350\text{ }^\circ\text{C}$. Even in the case of the borohydride/graphite composite, where the release behaviour is smoother and the profile starts somehow lower than for pure material, the release temperature is about $350\text{ }^\circ\text{C}$.

Considering that both the composites contain about one third of $\text{Ca}(\text{BH}_4)_2$, the amount of hydrogen released is likely to result close to the $9.6\text{ wt.}\%$ theoretical values of reaction (2.21). A very similar result is obtained for the unsupported $\text{Ca}(\text{BH}_4)_2$ (also comparable with the one in [43]) leading to a quite good superimposition of the last parts of the curves in the plot in figure 4.20, taking into account the two different vertical scales.

Figure 4.21 shows the TPA behaviour of the hydrogen a/d cycles (1 to 18) at various pressures. The first TPA at 4.5 MPa H_2 shows a very sharp initial behaviour followed by a second step leading to a final re-hydrogenation value of $2.7\text{ wt.}\%$. The second hydrogenation at 4.5 MPa H_2 appears relatively fast and maximum hydrogenation is achieved during the temperature ramp in less than 4 h. With ongoing cycles and at lower pressure this performance is worsening. However, it can be noted that after five cycles, using a hydrogen pressure of only 2.5 MPa , $2.4\text{ wt.}\%$ H_2 is absorbed in 6.5 h, corresponding to a $\text{Ca}(\text{BH}_4)_2$ reversibility (considering from the previous calculations that the as-prepared composite contained about $36\text{ wt.}\%$ of $\text{Ca}(\text{BH}_4)_2$) of $6.6\text{ wt.}\%$ H_2 . This means that at least $6.6/9.6 = 68.75\%$ of the $\text{Ca}(\text{BH}_4)_2$ behaves reversibly, improving the result obtained by Kim *et al.* [16] on $\text{Ca}(\text{BH}_4)_2$ (50% reversibility at $350\text{ }^\circ\text{C}$ and 9 MPa of hydrogen). This is encouraging, since it was obtained without any catalyst; the possible role of catalysts

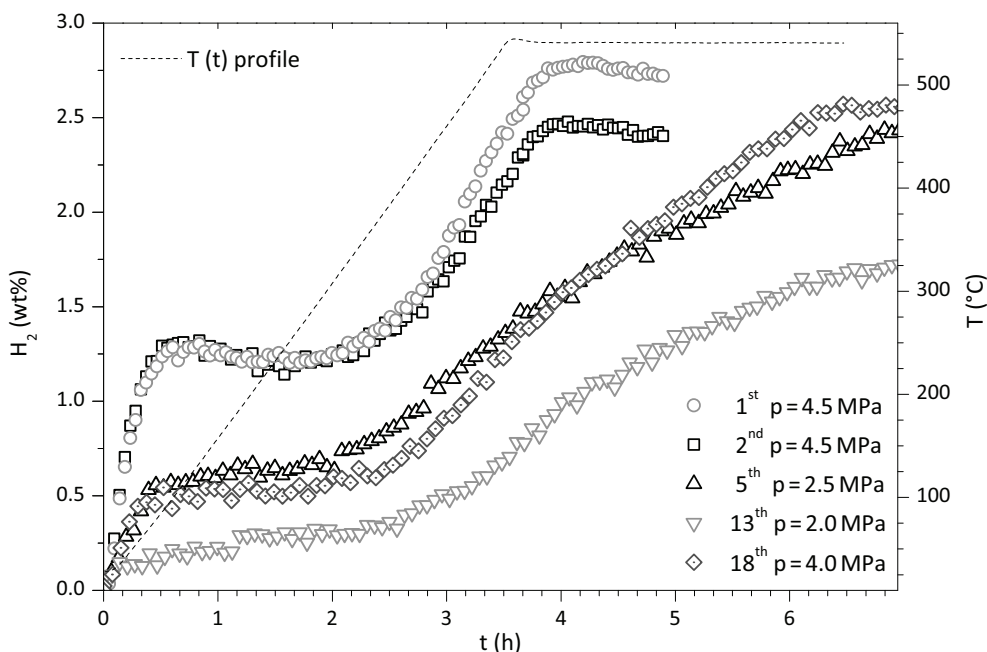


Figure 4.21: TPA curves of nano-composite $C_{MC650-a}$ for successive hydrogenation cycles at different pressures.

in kinetics improvement of $C_{MC650-a}$ composites is still to be tested

A few additional cycles (up to the 13th) and a further decrease of pressure resulted in a significant loss of storage capacity and absorption rate, but the previous performance was recovered by setting the pressure above 4 MPa H_2 : the composite absorbed 2.4 wt.% of hydrogen reversibly up to 18 cycles.

4.4

Observations on Nanosupported Borohydrides

In this chapter, it has been shown that $LiBH_4$ dispersed on MWCNTs by solvent infiltration shows a decreased dehydrogenation temperature with respect to the pure material by more than 60 °C. The dehydrogenation temperature of $LiBH_4$ further decreases with increasing the SSA of MWCNTs. The dispersion of $LiBH_4$ on the high SSA of the MWCNTs does not seem to lead to thermodynamic destabilization with respect to pure material due to a size effect.

In order to investigate the effect of confinement in nanoporous supports on mixed borohydride systems too, composites of $LiBH_4$ and $Mg(BH_4)_2$ borohydrides in five different ratios have been prepared by ball milling and dispersed on a high SSA graphite. While TPD analysis of the physical mixture has not shown improvements in this case, it has been observed by volumetric measurements that the confinement lowers the dehydrogenation temperature with respect to not confined samples. There is a link between the available surface and pores area of the support and the release temperature of the system: it has been found that the support used in this investigation decreased the dehydrogenation tem-

perature with respect to the pure material by more than 100 °C. The process appears to be facilitated by the heterogeneous nucleation of decomposition products or intermediate phases from melted borohydrides on the graphite surface and pores. The experiment performed with carbon nanotubes and the related results can be found in the literature [44]. The outcomes of the research on borohydride mixtures, comprehending their infiltration in the graphite, were the subject of another paper [45].

The possibility to enhance this phenomenon by means of activated surfaces was also studied. $\text{Ca}(\text{BH}_4)_2$ /activated MC composites were prepared by infiltration of $\text{Ca}(\text{BH}_4)_2$ into an activated mesoporous carbon MC 650-a (SSA 1780 $\text{m}^2 \text{g}^{-1}$, pore volume $\sim 1 \text{ cm}^3 \text{g}^{-1}$ and more than 60 % of micropores) synthesized by soft-templating and activated chemically. The infiltration was done by incipient wetness of an etherate (MTBE) solution of $\text{Ca}(\text{BH}_4)_2$ into the carbon framework. The composite desorbed reversibly up to 18 cycles 2.4 wt.% of hydrogen during dehydrogenation measurements up to 550 °C. Starting at about 100 °C, the hydrogen release of the composite was significantly improved with respect to bulk material and previous literature data. This procedure of borohydride nanoconfinement apparently led also to the reduction of dehydrogenation activation energies, enhancing the overall reaction kinetics. Aiming at higher hydrogen storage capacity composites, work is in progress on impregnation of complex borohydrides in higher pore volume carbon ($> 2 \text{ cm}^3 \text{g}^{-1}$) and using additives to promote faster reaction kinetics. The work performed on the $\text{Ca}(\text{BH}_4)_2$ /activated MC was also published in a paper [46].

From these studies on borohydrides and attempts to reduce their decomposition temperature by means of infiltration in nanostructured supports, it is possible to draw some general statements. Nano-confinement is a viable solution to reduce the hydrogen release temperature and, in some measure, to limit the amount of undesired gas desorbed. The reversibility of the reactions in mild conditions was only improved in the case of calcium borohydride, but it was not possible to achieve it with the other compounds analyzed. This is a major drawback for the practical application of this class of materials, however, confinement is a promising research line for this goal as well.

References

- 1 Satyapal S., Petrovic J., Read C., Thomas G., Ordaz G., The U.S. Department of Energy's National Hydrogen Storage Project: Progress towards meeting hydrogen-powered vehicle requirements, *Catalysis Today*, **120** (2007) 246–256. (Cited on page 53)
- 2 DoE *Targets for onboard hydrogen storage systems for light-duty vehicles*, Rev. 4.0 (2009), retrieved from: <http://www.eere.energy.gov/>¹ (on 30/06/11). (Cited on page 53)
- 3 Ashby M.F., Overview No. 92: Materials and shape, *Acta Metallurgica et Materialia*, **39** (1991) 1025–1039. (Cited on page 54)
- 4 de Jongh P.E., Adelhelm P., Nanosizing and nanoconfinement: new strategies towards meeting hydrogen storage goals, *ChemSusChem*, **3** (2010) 1332–1348. (Cited on page 54)
- 5 Vajo J.J., Olson G.L., Hydrogen storage in destabilized chemical systems, *Scripta Materialia*, **56** (2007) 829–834. (Cited on page 54)
- 6 Yu X.B., Wu Z., Chen Q.R., Li Z.L., Weng B.C., Huang T.S., Improved hydrogen storage properties of LiBH₄ destabilized by carbon, *Applied Physics Letter*, **91** (2007) 034106. (Cited on pages 54, 63, and 70)
- 7 Cahen S., Eymery J.B., Janot R., Tarascon J.M., Improvement of the LiBH₄ hydrogen desorption by inclusion in mesoporous carbon, *Journal of Power Sources*, **189** (2009) 902–908. (Cited on page 54)
- 8 Wang P.J., Fang Z.Z., Ma L.P., Kang X.D., Wang P., Effect of carbon addition on hydrogen storage behaviors of Li–Mg–B–H system, *International Journal of Hydrogen Energy*, **35** (2010) 3072–3075. (Cited on page 54)
- 9 Gross A.F., Vajo J.J., van Atta S.L., Olson G.L., Enhanced Hydrogen Storage Kinetics of LiBH₄ in Nanoporous Carbon Scaffolds, *Journal of Physical Chemistry B*, **112** (2008) 5651–5657. (Cited on page 54)
- 10 Vajo J.J., Skeith S.L., Mertens F., Reversible Storage of Hydrogen in Destabilized LiBH₄, *Journal of Physical Chemistry B*, **109** (2005) 3719–3722. (Cited on pages 54 and 71)
- 11 Durojaiye T., Ibikunle A., Goudy A.J., Hydrogen storage in destabilized borohydride materials, *International Journal of Hydrogen Energy*, **35** (2010) 10329–10333. (Cited on page 54)
- 12 Bösenberg U., Doppiu S., Mosegaard L., Borgschulte A., Eigen N., Barkhordarian G., Jensen T.R., Cerenius Y., Gutfleisch O., Klassen T., Dornheim M., Bormann R., Hydrogen sorption properties of MgH₂-LiBH₄ composites, *Acta Materialia*, **55** (2007) 3951–3958. (Cited on page 54)
- 13 Crosby K., Shaw L.L., Dehydrogenating and re-hydrogenating properties of high-energy ball milled LiBH₄+MgH₂ mixtures, *International Journal of Hydrogen Energy*, **35** (2010) 7519–7529. (Cited on page 54)
- 14 Yu X.B., Grant D.M., Walker G.S., A new dehydrogenation mechanism for reversible multicomponent borohydride systems — The role of Li–Mg alloys, *Chemical Communications*, (2006) 3906–3908. (Cited on page 54)
- 15 Nielsen T.K., Bösenberg, Gosalawit R., Dornheim M., Cerenius Y., Besenbacher F., Jensen T.R., A Reversible Nanoconfined Chemical Reaction, *ACS Nano*, **4** (2010) 3903–3908. (Cited on page 54)
- 16 Kim J.H., Jin S.A., Shim J.H., Cho Y.W., Reversible hydrogen storage in calcium borohydride Ca(BH₄)₂, *Scripta Materialia*, **58** (2008) 481–483. (Cited on pages 54 and 73)
- 17 Liu X., Peaslee D., Jost C.Z., Majzoub E.H., Controlling the Decomposition Pathway of LiBH₄ via Confinement in Highly Ordered Nanoporous Carbon, *Journal of Physical Chemistry C*, **114** (2010) 14036–14041. (Cited on page 71)
- 18 Zanella P., Crociani L., Masciocchi N., Giunchi G., Facile high-yield synthesis of pure, crystalline Mg(BH₄)₂, *Inorganic Chemistry*, **46** (2007) 9039–9041. (Cited on page 55)
- 19 Zanella P., Crociani L., Giunchi G., *Process for the preparation of crystalline magnesium borohydride*, (2007) U.S. Patent US 7 678 356. (Cited on page 55)
- 20 Grønvold F., Enthalpy of fusion and temperature of fusion of indium, and redetermination of the enthalpy of fusion of tin, *Journal of Chemical Thermodynamics*, **25** (1993) 1133–1144. (Cited on page 56)
- 21 Hu Z., Srinivasan M.P., Ni Y., Preparation of Mesoporous High-Surface-Area Activated Carbon, *Advanced Materials*, **12** (2000) 62–65. (Cited on page 56)

¹http://www1.eere.energy.gov/hydrogenandfuelcells/storage/pdfs/targets_onboard_hydro_storage_explanation.pdf

- 22 Ryoo R., Joo S.H., Kruk M., Jaroniec M., Ordered Mesoporous Carbons, *Advanced Materials*, **13** (2001) 677–681. (Cited on pages 56 and 57)
- 23 Lillo-Ródenas M.A., Marco-Lozar J.P., Cazorla-Amorós D., Linares-Solano A., Activated carbons prepared by pyrolysis of mixtures of carbon precursor/alkaline hydroxide, *Journal of Analytical and Applied Pyrolysis*, **80** (2007) 166–174. (Cited on page 56)
- 24 Lillo-Ródenas M.A., Cazorla-Amorós D., Linares-Solano A., Understanding chemical reactions between carbons and NaOH and KOH: An insight into the chemical activation mechanism, *Carbon*, **41** (2003) 267–275. (Cited on page 57)
- 25 Maciá-Agulló J.A., Moore B.C., Cazorla-Amorós D., Linares-Solano A., Activation of coal tar pitch carbon fibres: Physical activation vs. chemical activation, *Carbon*, **42** (2004) 1367–1370. (Cited on page 57)
- 26 Filinchuk Y., Ronnebro E., Chandra D., Crystal structures and phase transformations in $\text{Ca}(\text{BH}_4)_2$, *Acta Materialia*, **57** (2009) 732–738. (Cited on page 57)
- 27 Pierard N., Fonseca A., Konya Z., Willems I., van Tendeloo G., Nagy J.B., Production of short carbon nanotubes with open tips by ball milling, *Chemical Physics Letter*, **335** (2001) 1–8. (Cited on page 58)
- 28 Pierard N., Fonseca A., Colomer J.F., Bossuot C., Benoit J.M., van Tendeloo G., Pirard J.P., Nagy J.B., Ball milling effect on the structure of single-wall carbon nanotubes, *Carbon* **42** (2004) 1691–1697. (Cited on page 58)
- 29 Stoeckli F., Centeno T.A., On the determination of surface areas in activated carbons, *Carbon*, **43** (2005) 1184–1190. (Cited on page 60)
- 30 Fang Z.Z., Kang X.D., Wang P.J., Li H.W., Orimo S., Unexpected dehydrogenation behavior of $\text{LiBH}_4/\text{Mg}(\text{BH}_4)_2$ mixture associated with the in situ formation of dual-cation borohydride, *Journal of Alloys and Compound*, **491** (2010) L1–L4. (Cited on pages 62 and 63)
- 31 Bardají E.G., Zhao-Karger Z., Boucharat N., Nale A., van Setten M.J., Lohstroh W., Röhm E., Catti M., Fichtner M., $\text{LiBH}_4\text{--Mg}(\text{BH}_4)_2$: a physical mixture of metal borohydrides as hydrogen storage material, *Journal of Physical Chemistry C*, **115** (2011) 6095–6101. (Cited on pages 62, 63, 70, and 71)
- 32 Nakamori Y., Li H.-W., Kikuchi K., Aoki M., Miwa K., Towata S., Orimo S., Thermodynamical stabilities of metal-borohydrides, *Journal of Alloys and Compounds*, **446–447** (2007) 296–300. (Cited on page 62)
- 33 Li H.-W., Orimo S., Nakamori Y., Miwa K., Ohba N., Towata S., Züttel A., Materials designing of metal borohydrides: Viewpoints from thermodynamical stabilities, *Journal of Alloys and Compounds*, **446–447** (2007) 315–318. (Cited on pages 62 and 63)
- 34 Nale A., Catti M., Bardají E.G., Fichtner M., On the decomposition of the 0.6 LiBH_4 – 0.4 $\text{Mg}(\text{BH}_4)_2$ eutectic mixture for hydrogen storage, *International Journal of Hydrogen Energy*, **36** (2011) 13676–13682. (Cited on page 63)
- 35 Lide D.R. (ed.), *Handbook of Chemistry and Physics*, 84th ed. (2003) CRC Press, Boca Raton. (Cited on page 68)
- 36 Abraham F.F., *Homogeneous Nucleation Theory*, (1974) Academic Press, New York. (Cited on page 68)
- 37 Oxtoby D.W., Homogeneous nucleation: theory and experiment, *Journal of Physics: Condensed Matter*, **4** (1992) 7627. (Cited on page 68)
- 38 Fichtner M., Zhao-Karger Z., Hu J., Roth A., Weidler P., The kinetic properties of $\text{Mg}(\text{BH}_4)_2$ infiltrated in activated carbon, *Nanotechnology*, **20** (2009) 204029. (Cited on page 69)
- 39 Mauron Ph., Buchter F., Friedrichs O., Remhof A., Biemann M., Zwicky C.N., Züttel A., Stability and Reversibility of LiBH_4 , *Journal of Physical Chemistry B*, **112** (2008) 906–910. (Cited on pages 69 and 70)
- 40 Liu X., Peaslee D., Jost C.Z., Baumann T.F., Majzoub E.H., Systematic pore-size effects of nanoconfinement of LiBH_4 : elimination of diborane release and tunable behavior for hydrogen storage applications, *Chemistry of Materials*, **23** (2011) 1331–1336. (Cited on page 71)
- 41 Au M., Jurgensen A., Modified Lithium Borohydrides for Reversible Hydrogen Storage, *Journal of Physical Chemistry B*, **110** (2006) 7062–7067. (Cited on page 71)
- 42 Hanada N., Chłopek K., Frommen C., Lohstroh W., Fichtner M., Thermal decomposition of $\text{Mg}(\text{BH}_4)_2$ under He flow and H_2 pressure, *Journal of Material Chemistry*, **18** (2008) 2611–2614. (Cited on page 71)
- 43 Kim J.H., Jin S.A., Shim J.H., Cho, Y.W., Thermal decomposition behavior of calcium

- borohydride, *Journal of Alloys and Compound*, **461** (2008) L20–L22. (Cited on page 73)
- 44 Agresti F., Khandelwal A., Capurso G., Lo Russo S., Maddalena A., Principi G., Improvement of dehydrogenation kinetics of LiBH_4 dispersed on modified multi-walled carbon nanotubes, *Nanotechnology*, **21** (2010) 065 707. (Cited on page 75)
- 45 Capurso G., Agresti F., Crociani L., Rossetto G., Schiavo B., Maddalena A., Lo Russo S., Principi G., Nanoconfined mixed Li and Mg borohydrides as materials for solid state hydrogen storage, *International Journal of Hydrogen Energy*, **37** (2012) 10 768–10 773. (Cited on page 75)
- 46 Comănescu C., Capurso G., Maddalena A., Nanoconfinement in activated mesoporous carbon of calcium borohydride for improved reversible hydrogen storage, *Nanotechnology*, **23** (2012) 385 401. (Cited on page 75)

5 Chapter 5

Magnesium Hydride Based Materials and Systems

Abstract. This chapter deals with different studies on magnesium hydride based systems: to improve its sluggish kinetics a zirconium-nickel alloy was tested and appeared to be quite promising in its enhancement of the reaction rate, both in absorption and desorption. The degradation of another magnesium hydride powder, catalyzed with niobium pentoxide, in experimental reactors was a motivation to study pellets with the addition of aluminium powder as binding agent, to obtain mechanical consistency and structure, still allowing hydrogen diffusion. Each pellet should behave as an independent system, so they were also used in a small reactor, designed and built to demonstrate the effectiveness of the compacted system. A number of hydrogen a/d cycles was carried out to compare the behaviour of the small reactor with the laboratory data obtained on small amounts of powdered and pelletized samples.

Moving further in the employment of hydride-based storage technology to applications, the requirement of reversibility becomes a key aspect for both stationary and vehicular uses [1]. The attribute of a good resistance to hydrogenation/dehydrogenation cycles is among the different positive assets of magnesium hydride [2], listed also in section 2.2.2. This makes the materials based on MgH_2 better candidates for an immediate practical application than other highest H_2 capacity compounds. The efforts in the research are focused on the improvement of the a/d properties, looking for a viable catalyst, and on the feasibility of storage reactors, facing the challenge of thermal management, heat dissipation and material deterioration. One of the promising solutions is the realization of a composite material, using components able to improve thermal and mechanical properties without lowering the functionality too much. As for engineered composite materials [3, 4], the optimal selection of a material to be combined should produce an enhancement, rather than a compromise, in the overall performances.

5.1 Seeking a Novel Catalyst

The possibility to catalyze magnesium hydride successfully was already discussed in section 2.2.2.1, showing that the comminution of the hydride particles by high energy milling along with the use of additives can significantly improve the hydrogen a/d kinetics. Starting from that perspective, this section deals with a deeper insight of catalytic effects of transition metals [5, 6]. Recently, attention has been paid to investigations on properties of multicomponent alloys composed by these elements [7, 8, 9].

Dehouche *et al.* observed that MgH_2 ball-milled with some Zr–Ni alloys exhibited an improved a/d kinetics, which also depended on the stoichiometry of the alloy [10]. More precisely, the eutectoid composition $\text{Zr}_{36}\text{Ni}_{64}$ formed by the two crystalline phases $\text{Zr}_7\text{Ni}_{10}$ and $\text{Zr}_8\text{Ni}_{21}$ [11] showed a faster kinetics than $\text{Zr}_7\text{Ni}_{10}$ and $\text{Zr}_9\text{Ni}_{11}$, motivating the question about the influence of the $\text{Zr}_8\text{Ni}_{21}$ phase on the hydrogen a/d kinetics. Additionally, in a study of hydride-forming alloys in nickel-metal batteries Ruiz *et al.* observed that $\text{Zr}_8\text{Ni}_{21}$ had a better charge/discharge performance than $\text{Zr}_7\text{Ni}_{10}$ and $\text{Zr}_9\text{Ni}_{11}$ [12].

On the basis of the previous considerations, MgH_2 powders ball milled with $\text{Zr}_8\text{Ni}_{21}$ were studied, analyzing the corresponding activation process and a/d hydrogen kinetics and thermodynamic properties.

5.1.1 Preparation of $\text{Zr}_8\text{Ni}_{21}$ -Catalyzed MgH_2 Samples

The $\text{Zr}_8\text{Ni}_{21}$ alloy was prepared by arc-melting the elements Zr and Ni under Ar atmosphere inside a water cooled copper crucible in order to avoid contamination. The purity was 99.9% for Zr and Ni, and 99.999% for Ar. A reduction of contamination from the furnace atmosphere was obtained by melting a sacrificial button before Zr and Ni melting. The arc was established by a torch with tungsten tip. The additive was re-melted three times to ensure homogeneity. Then, it was wrapped in a Ta foil, which is a oxygen getter, and annealed for 30 days at 1000 °C inside an evacuated quartz capsule. Thereafter, several cycles of heating and cooling from ambient temperature to 250 °C at 1.5 MPa H_2 were performed on the alloy to make it brittle and so facilitate its reduction into small pieces by crushing.

MgH_2 powder, supplied by Th. Goldschmidt GmbH (95% MgH_2 + 5% Mg), was ball milled for 20 h under Ar atmosphere with the obtained $\text{Zr}_8\text{Ni}_{21}$ grains, in the amounts indicated below. Five different MgH_2 - x (wt.%) $\text{Zr}_8\text{Ni}_{21}$ compounds, with $x = 12.5, 10, 7.5, 5$ and 3 , labelled $\text{Mg}^{\text{Z}12.5}, \dots, \text{Mg}^{\text{Z}3}$, respectively, were synthesized. Sample handling was carried out inside the glove box.

Before each a/d measurement performed in the volumetric apparatus the samples were dehydrogenated for 1 h at 250 °C and 40 Pa. Powder XRD patterns were measured by a Philips PW 1820/00 diffractometer. SEM observations were performed by using a Cambridge Stereoscan 440 SEM equipped with Philips PV5800 EDS.

5.1.2 Analysis of Experimental Results

The catalyzed hydride powders obtained after 20 h milling display a homogeneous distribution of the additive particles, which can be well distinguished from the MgH_2 in the SEM

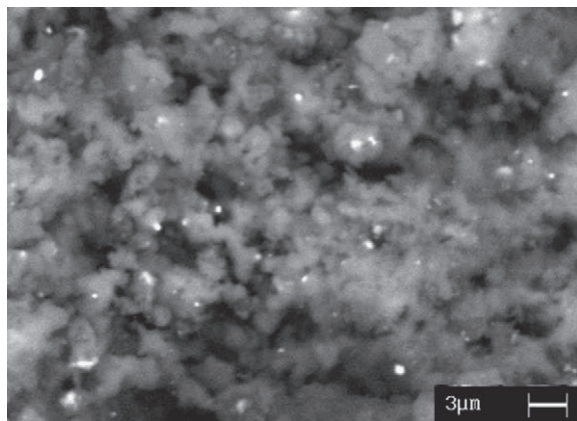


Figure 5.1: SEM image of MgH_2 -10 wt.% $\text{Zr}_8\text{Ni}_{21}$ obtained with BSE. The white spots correspond to the additive particles and the grey regions to the MgH_2 matrix.

image of sample $\text{Mg}^{\text{Z}10}$ reported in figure 5.1. The white spots, with size not exceeding $1\ \mu\text{m}$, are due to the elastic collisions of backscattered electrons with the heavy nuclei of zirconium, while the grey weak region is due to the light nuclei of magnesium hydride.

5.1.2.1 Activation of Samples

Ten cycles of hydrogen a/d at $250\ ^\circ\text{C}$ were performed for the activation of all samples and an extra cycle at $300\ ^\circ\text{C}$ in the special case of sample 3 cat. The result of the activation cycles was a stabilized absorption kinetics. In figure 5.2 the absorption curves for the 1st, 5th, and 10th cycles of sample $\text{Mg}^{\text{Z}10}$ at $250\ ^\circ\text{C}$ and $1\ \text{MPa H}_2$ are shown. The hydrogen absorbed within 1 min was 4.8, 5.2 and 5.7 wt.%, respectively, which is an increment of 19% after 10 cycles. This can be due to the mechanical stress produced by expansion and contraction during cycling that may comminute the magnesium particles by cracking and change their surface extension and characteristics. This transformation may allow hydrogen to react with material that was previously inaccessible. Dehouche *et al.* suggested that in their Zr–Ni doped compounds rougher surfaces may be due to the formation of nano-channels that facilitate the hydrogen access to the particle bulk [10]. The improvement continues up to 10 cycles and then a steady state is reached, as seen with subsequent cycles from the 10th to the 16th. The need of a/d cycles to reach the optimal sorption properties has been reported for other Mg-based hydrides (e. g. the $\text{Mg} + \text{Mg}_2\text{Ni}$ composite [5]).

The milling and activation processes also introduce changes in the crystalline structure and chemical composition. In figure 5.4, the XRD patterns of an as-milled (bottom) and an activated (top) hydrided sample are shown. The broad peaks of the as milled sample are due to the reduced size of the grains, the lattice strain and the structural defects produced by high energy milling. There is a major contribution of β - MgH_2 and

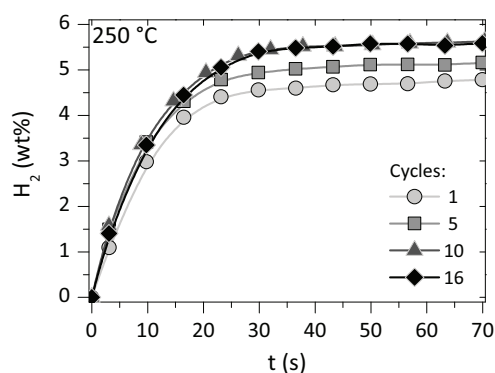


Figure 5.2: Absorption curves at $250\ ^\circ\text{C}$ and $1\ \text{MPa}$ for the sample MgH_2 -10 wt.% $\text{Zr}_8\text{Ni}_{21}$.

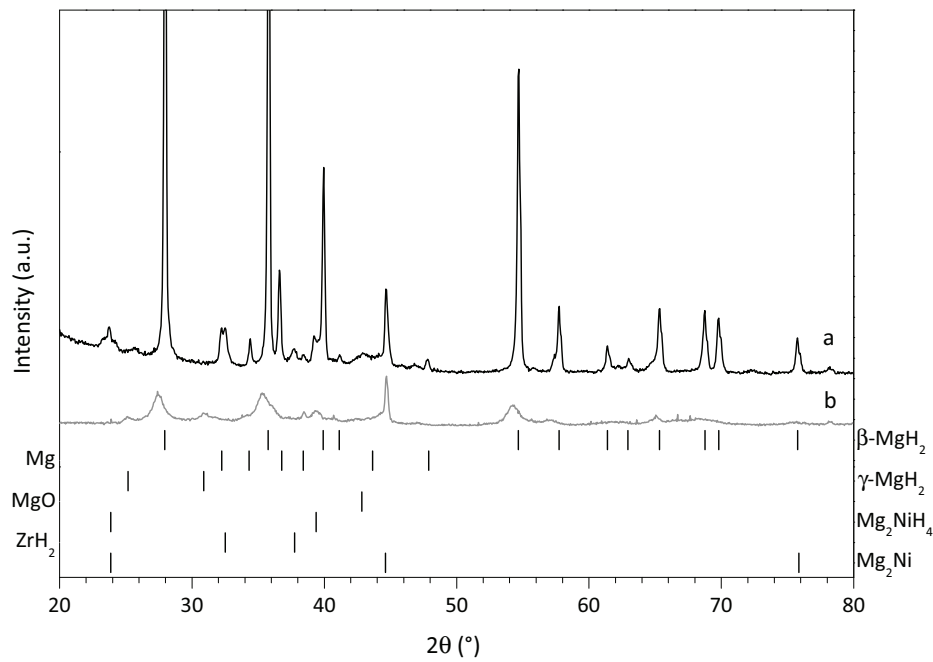


Figure 5.4: Diffraction patterns of MgH_2 -10 wt.% $\text{Zr}_8\text{Ni}_{21}$ as-milled (bottom) and hydrided after cycling (top).

a lower one of $\gamma\text{-MgH}_2$: the former is the equilibrium phase of magnesium hydride, the latter is a high pressure metastable phase typically generated by milling. The pattern exhibits low intensity peaks of pure Mg, present in the commercial magnesium hydride, and also a peak of Mg_2Ni . The Mg_2Ni may be originated by a mechanically driven solid-state displacement reaction, where Ni moves from the $\text{Zr}_8\text{Ni}_{21}$ additive into MgH_2 .

The Mg_2Ni formation was also found by other authors in similar experiments [5, 10]. Little contributions of MgO by air contamination during material handling, milling process or X-ray measurements cannot be ruled out.

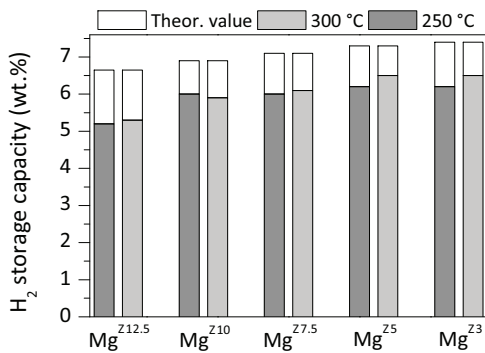


Figure 5.3: Hydrogen storage capacity of catalyzed MgH_2 samples as a function of additive amount and temperature. The empty portion of the bars corresponds to the theoretical capacity (see text).

After activation with hydrogen a/d cycles, the diffraction peaks of a hydrided sample are sharper, owing to the relaxation of strain and the reduction of structural defects. The disappearance of $\beta\text{-MgH}_2$ peaks testifies that magnesium hydride relaxed completely to the β -phase. The increment in Mg_2Ni intensity and formation of Mg_2NiH_4 indicate that Ni continues reacting with Mg during a/d cycling. The peak of ZrH_2 , not observed in the as-milled

sample, may be produced by the remaining Zr after the mentioned Mg–Ni reaction, the

possibility of which is also suggested by experiments on ball-milled Mg and Ni [13]. Their differential scanning calorimetry measurements showed that the Mg–Ni reaction was thermally activated at 250 °C, the temperature at which the a/d cycles were performed. The Mg₂Ni is possibly produced in the present case at the interfaces between MgH₂ and Zr₈Ni₂₁ particles, yielding MgH₂ particles superficially covered by Mg₂Ni. This is a possible explanation of part of the improved sorption properties which will be reported in the following. Finally, diffraction peaks corresponding to MgO and de-hydrated Mg and Mg₂Ni are also observed, accounting for the hydrogen capacity reduction in comparison with the theoretical value.

In figure 5.3 it is shown the weight percentage of hydrogen reversibly absorbed by the five compounds at a reservoir pressure of 1 MPa H₂ for 1 h, period long enough to ensure the saturation of all samples. The dark and light grey bars correspond to the sample temperatures of 250 and 300 °C, respectively. The empty portion of the bars represents the extra capacity that would have been measured if all the magnesium of the compound had been hydrided. Taking into account that magnesium hydride theoretically stores 7.6 wt.% H₂, the resulting capacity is $7.6 \left(\frac{1-x}{100} \right)$ wt.% H₂. As said, the discrepancies between the two values are due to the presence of MgO and unreacted material. The storage capacity is almost the same at both temperatures: for the sample Mg^Z₁₀ the values are 6.1 and 5.9 wt.% H₂ for 250 and 300 °C, respectively, in agreement with the values reported for magnesium hydride doped with 10 wt.% Zr₃₆Ni₆₄ [10]. According to figure 5.3, the highest storage capacity of 6.5 wt.% H₂ is found for samples Mg^Z₃ and Mg^Z₅.

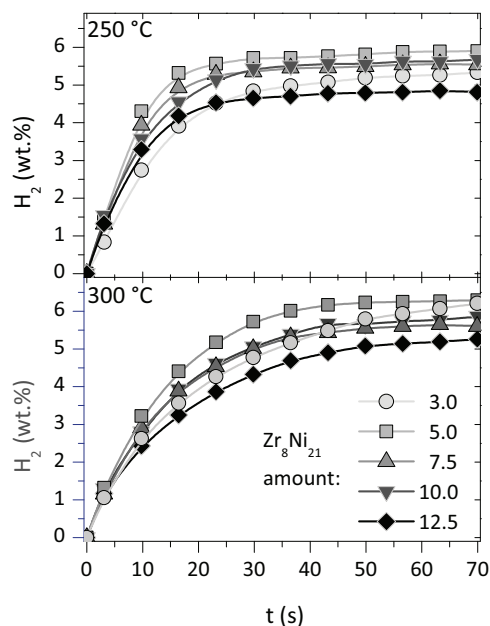


Figure 5.5: Hydrogen absorption at 1 MPa of catalyzed MgH₂ for different additive amounts.

5.1.2.2 Effect of the Additive Amount on Kinetics of Activated Samples

The absorption kinetics of magnesium hydride with Zr₈Ni₂₁ additive at 250 and 300 °C and 1 MPa H₂ is shown in figure 5.5. The best rate at 250 °C is obtained with 5 wt.% of Zr₈Ni₂₁: 5.3 wt.% H₂ in 16 s. It is observed that the absorption kinetics does not depend strongly on the additive amount and that all the samples reached 80 % of the storage capacity in 30 s and 90 % in 60 s at both temperatures. Since the absorption rate depends on the difference between the reservoir and equilibrium pressures, a slowing down of kinetics is expected at a temperature of 300 °C, as it is seen in figure 5.5. For instance, sample Mg^Z₁₀ reaches 80 % of the storage capacity in 25 s at 300 °C and in 19 s at 250 °C. These values are slightly better than those reported for absorption measurements in similar conditions of 0.2 mol % Nb₂O₅ doped MgH₂ milled for 20 h or more [14].

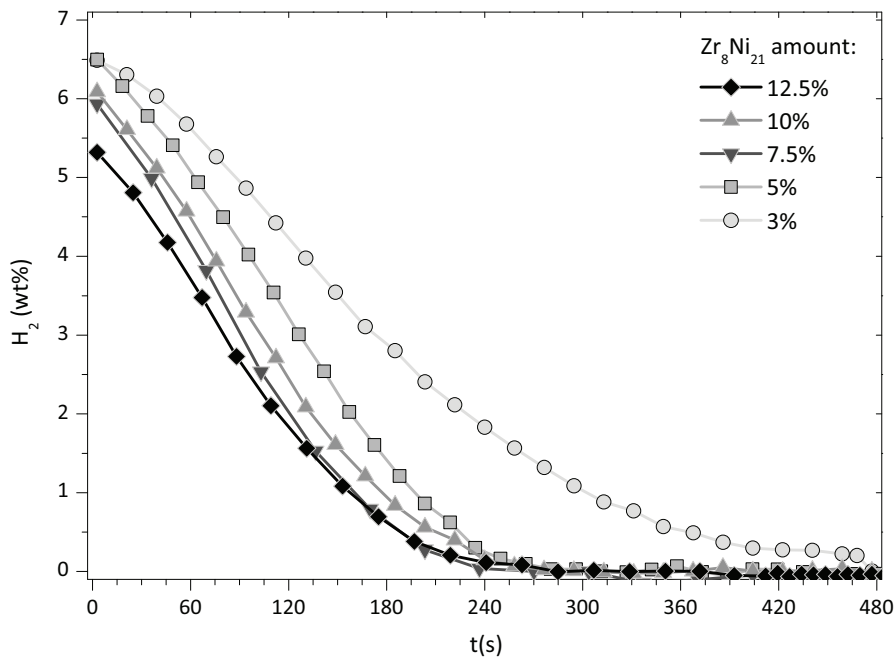


Figure 5.7: Hydrogen desorption of catalyzed MgH_2 at $300\text{ }^\circ\text{C}$ and 10 kPa .

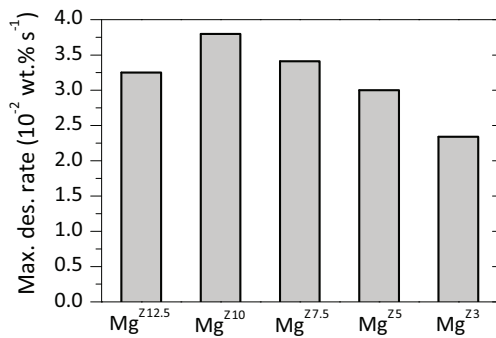


Figure 5.6: Maximum desorption rate at $300\text{ }^\circ\text{C}$ and 10 kPa catalyzed MgH_2 .

The most interesting results are observed during desorption. In figure 5.7, which reports the amount of hydrogen desorbed by completely hydrided samples connected to a reservoir at 10 kPa and $300\text{ }^\circ\text{C}$, it is shown that all samples desorb completely in 4 min, except the sample $\text{Mg}^{\text{Z}3}$ that took 8 min. The maximum desorption rate (calculated from the minimum of the numerical derivative of each curve) is reported in figure 5.6 as a function of the amount of additive, showing that the best value of $3.8\text{ wt.}\% \text{ H}_2 \text{ s}^{-1}$ is obtained for

sample $\text{Mg}^{\text{Z}10}$. A higher additive amount may not introduce extra benefits but only reduction of storage capacity. The samples were desorbed in a finite volume reservoir, where pressure increased lightly during desorption, so the reported kinetics might be underestimated. Similar values of desorption kinetics are reported for $0.2\text{ mol}\% \text{ Nb}_2\text{O}_5$ doped MgH_2 milled for 20 h or more [14].

5.1.2.3 Thermodynamic Behaviour

Figure 5.8 shows the absorption and desorption PCI at 250 and $300\text{ }^\circ\text{C}$. The pressure of coexistence between the partially hydrided compound and the gaseous hydrogen is given by the plateau pressure calculated by averaging all the plateau points at the given temperature. At $250\text{ }^\circ\text{C}$ the absorption and desorption plateaux pressure are very close,

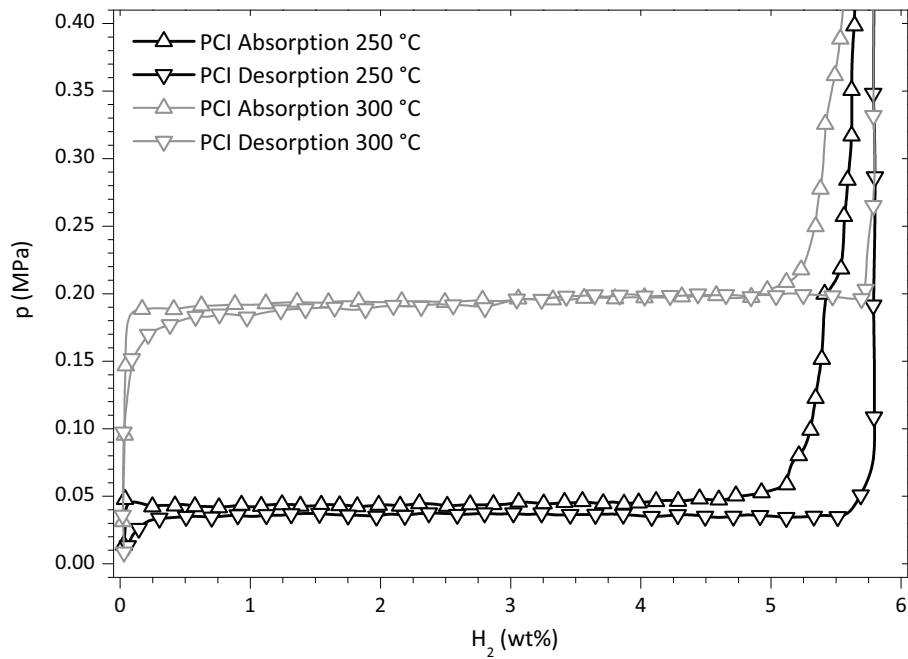


Figure 5.8: PCI curves at 250 and 300 °C for MgH_2 -10 wt.% $\text{Zr}_8\text{Ni}_{21}$.

44 and 37 kPa, respectively. At 300 °C both pressures have, within the experimental error, the same value of 194 kPa. This means that for the MgH_2 catalyzed by the $\text{Zr}_8\text{Ni}_{21}$ alloy, there is a small hysteresis between absorption and desorption curves measured at the same temperature. The hysteresis is originated by strain and disorder of the MgH_2 lattice, due to expansion during absorption, higher if compared with relaxed strain and disorder during desorption: higher strain and disorder increase the plateau pressure, which is lowered by their relaxation [15].

The low hysteresis in the present case may be due to the presence of the additive which, being unstable, favours lattice mobility and therefore less stress during the formation of MgH_2 . The lattice mobility is higher at high temperature and consequently the hysteresis decreases. Hints of a second plateau is suggested by the shoulder in the absorption curve, produced by hydriding of little amounts of Mg_2Ni , seen also in the corresponding XRD pattern of figure 5.4, which has a higher plateau pressure than magnesium hydride. The formation of Mg_2Ni was also reported for other MgH_2 samples with additives containing Ni (see e. g. references [16, 17, 18]).

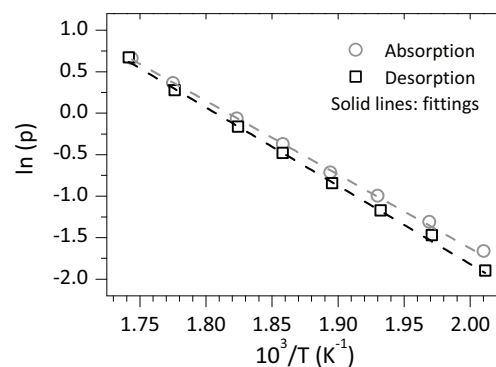


Figure 5.9: Van't Hoff plots of hydrogen a/d for MgH_2 -10 wt.% $\text{Zr}_8\text{Ni}_{21}$.

The enthalpy and entropy of the reaction were obtained by the van't Hoff plots of Fig. 9

figure 5.9, resulting to be $\Delta H = 73.9 \pm 0.7$ and $77.7 \pm 0.8 \text{ kJ mol}^{-1}$ and $\Delta S = 134.2 \pm 1.2$ and $141.8 \pm 1.5 \text{ J K}^{-1} \text{ mol}^{-1}$ for absorption and desorption, respectively, in agreement with previous data (e. g. [18]), proving once more that the use of an additive to MgH_2 does not change the thermodynamic properties of hydrogen a/d process.

It can be concluded that hydrogen absorption and desorption kinetics of MgH_2 could be improved adding $\text{Zr}_8\text{Ni}_{21}$ as reaction catalyst up to the limit of 10 wt.%. For this composition the maximum desorption rate was found to be $3.8 \text{ wt.}\% \text{ s}^{-1}$ and complete desorption occurred in 4 min at 300°C and 10 kPa of hydrogen pressure. These values are similar to the best results found in literature. A hydrogen storage capacity of 5.9 wt.% at 250°C and of 6.1 wt.% at 300°C vs. the theoretical value of 6.8 wt.% was found, due to the presence of Mg oxide and inactive Mg and Mg_2Ni . The highest hydrogen reversible capacity of 6.5 wt.% at 300°C was obtained with the samples with less additive amount. The kinetic behaviour did not change after 10 hydrogen a/d cycles onwards. The thermodynamic properties of MgH_2 are not modified by the additive, within the experimental error. The results presented in this section have been published in [19].

5.2

Development of MgH_2 -Based Pellets

The efforts made to find a solution for the shortcomings of MgH_2 , by using it in nanocrystalline form obtained by high energy milling [20] and using transition metal oxides as catalysts [21, 22], can address only the issue of sluggish a/d kinetics (with a little reduction in the gravimetric capacity). In particular, it has already been pointed out how the addition of Nb_2O_5 catalyst during milling results in one of the fastest kinetics [14, 23, 24, 25]. This section, starting from one of this improved materials, discuss the possibility to address the issues coming from its practical application in storage systems larger than the samples used in laboratory.

During scaling up studies of MgH_2 -based powders in a specially designed reactor it was observed that the hydrogen storage capacity as well as the a/d kinetics decreased with the ongoing cycles [26, 27]. It was argued that this degradation was due to a close compaction of the powder particles inside the reaction chamber associated with local overheating, with the detrimental effect of strongly reducing the free flow of hydrogen through the storage material. The compaction of the powders was probably due to a pressure gradient that built up during the first stages of hydrogen absorption process given by the difficult gas transport through the Mg bed.

These observations were a motivation to study MgH_2 based powders moderately pressed in the form of pellets with the addition of some binding agent in order to retain stable mechanical consistency and structure with persistent free paths for hydrogen diffusion. The use of pellets instead of powder should improve the hydrogen transport inside the storage vessel avoiding pressure gradients and further compaction of the material. Moreover, in principle, each pellet should behave as an independent system reducing scaling up effects on the a/d kinetics.

In the work presented in this section MgH_2 catalyzed ball-milled powders were tested, mixed with Al powder as a binder pressed with an electro-mechanical press, following an approach already preliminarily studied [28]. The crystalline structure, the hydrogen a/d properties and the mechanical strength of the samples have been analyzed before and

after hydrogen a/d cycling. Recently, different studies have reported the improvement of thermal conductivity in case of compacted MgH_2 -based disks by incorporation of expanded natural graphite [29, 30, 31]. In the present case, the incorporation of aluminium is supposed to enhance further the thermal conductivity in the pellets.

5.2.1

Preparation of Pellets

MgH_2 powder (as-received from Th. Goldschmidt GmbH, 95 % purity with residual 5 % metallic Mg) mixed with Nb_2O_5 (0.5 mol % \simeq 5 wt.%) as catalysts of the gas-solid reaction and graphite (1 wt.%), acting as a lubricant of milling [24], was ball-milled for 20 h. Hereafter as-milled MgH_2 mixed with Nb_2O_5 and graphite is referred to as catalyzed MgH_2 and denoted as $\text{Mg}^{\text{N}05}$. To avoid oxygen contamination, milling was carried out under a little over-pressure of argon atmosphere and samples were handled in glove-box. This study was performed on two types of pellets. One made up of as-milled $\text{Mg}^{\text{N}05}$ powder and in the other case 5 and 20 wt.% Al powder was homogeneously mixed by ball milling for 5 min with $\text{Mg}^{\text{N}05}$ to act as a binding agent (hereafter these last two types of samples are referred to as $\text{Mg}_{5\text{Al}}^{\text{N}05}$ and $\text{Mg}_{20\text{Al}}^{\text{N}05}$, respectively). All pellets (weighing about 0.3 g and with diameter of 7 mm and average height of 7 mm) were obtained pressing the powders in Ar atmosphere with a uniaxial pressure of 180 MPa by means of an Instron 1121 tester.

The load was applied with a constant displacement rate of 1 mm min^{-1} up to 180 MPa, then the level of strain was kept constant for 60 s and a second step of compression, under the same conditions of displacement rate and final pressure, was performed to compensate the partly reduced stress. Structural characterization of the as-prepared powders and of the pellets after a number of hydrogen a/d cycles was done using a Philips PW 1820/00 X-ray diffractometer. Kinetic and thermodynamic tests were performed with the GRC apparatus. Annealing of samples containing Al powder was performed at 450°C in the same apparatus for 10 min under rotary pump vacuum before starting the hydrogen a/d cycles. Environmental SEM pictures were acquired with a FEI XL 30 ESEM instrument operated at 20 kV. In order to test the compressive strength resistance of the pellets after different a/d cycles, compression tests were performed using the same Instron 1121 tester at the compressive strain rate of 1 mm min^{-1} controlled by the automation software CatMan.

5.2.2

Pellets Properties Characterization

5.2.2.1 Hydrogen a/d Cycling

For all samples the hydrogen release processes were performed at the temperature of 320°C and a pressure of 120 kPa H_2 , while the soak processes were performed at the same temperature and 1.5 MPa H_2 . Figure 5.11a shows the release kinetics for the pellet of $\text{Mg}^{\text{N}05}$ and indicates that the maximum stored and released hydrogen in this case was 5.6 wt.%, which remained stable for all the hydrogen a/d cycles. The time for a 90 % desorption after 20 cycles reduced to 660 s compared to 790 s for the first desorption cycle. During cycling, the pellet lost gradually its mechanical consistency and after 20 cycles got completely powdered. This behaviour is in agreement with the observed continuous reduction of desorption time by cycling, considering that a not close compacted powder

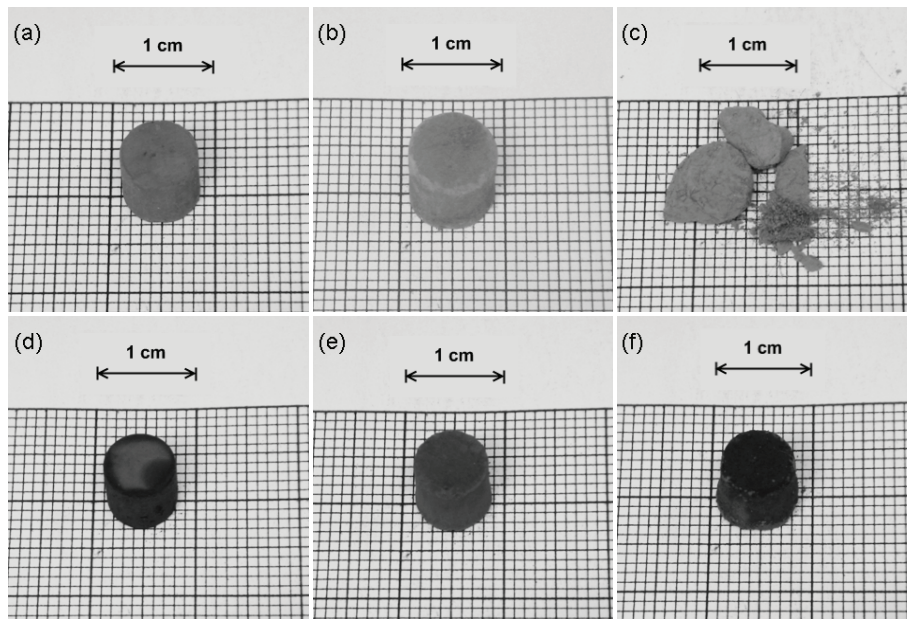


Figure 5.10: Pictures of hydrogenated pellets: (a), (b) and (c) are the $\text{Mg}^{\text{N}05}$ pellets after 10, 20 and 50 hydrogen a/d cycles, respectively, while (d), (e) and (f) are the $\text{Mg}_{5\text{Al}}^{\text{N}05}$ pellets preheated at 450°C after 10, 20 and 50 hydrogen a/d cycles, respectively.

favours the hydrogen flow through the material. The breaking of the pellets is due to the stress induced during absorption with an increase of 32 % of the volume for the host Mg forming MgH_2 . Figure 5.11 b gives the desorption curves for pellet $\text{Mg}_{20\text{Al}}^{\text{N}05}$, where is shown that the time for 90 % desorption is about 1000s and the hydrogen content goes from the initial 4.3 wt.% to about 3.6 wt.% after 50 cycles. This decrease can be explained in terms of Mg–Al phases formation during cycling, slowly reacting with hydrogen due to a higher plateau pressure with respect to pure magnesium. Moreover, it was observed that the compactness of the pellet started degrading before 20 cycles and was completely lost before 50 cycles. Another similar pellet was then first heated in vacuum at 450°C , for 10 min, in order to facilitate, according to the Mg–Al phase diagram [32], the formation of some intermetallic phases and/or solid solution and then submitted to 50 a/d cycles. As shown in figure 5.11 c, the maximum hydrogen content of this pellet was about 3.3 wt.% and the time for 90 % desorption increased to 1320 s. The hydrogen content was now almost constant under cycling, in contrast to the pellet without pre-heating, and the degradation of mechanical compactness resulted less. However, the pellet started to degrade before about 50 cycles.

$\text{Mg}_{5\text{Al}}^{\text{N}05}$ were cycled under similar conditions after pre-heating as in the previous case. Figure 5.11 d shows that in this case almost all the absorbed hydrogen (5.3 wt.%) was released in about 1500s. The desorption behaviour became almost stable just after 10 cycles and the pellet remained mechanically consistent and hard even after 50 cycles.

Pictures of the cycled $\text{Mg}^{\text{N}05}$ and $\text{Mg}_{5\text{Al}}^{\text{N}05}$ pellets are shown in figure 5.10. It is visible that the pellets not containing aluminium have a larger volume after 10 and 20 cycles compared to the pellets containing 5 wt.% Al, due to a more advanced disgregation process of pellets without Al. After 50 a/d cycles, the pellet containing aluminium is still intact, while the one without aluminium got powdered.

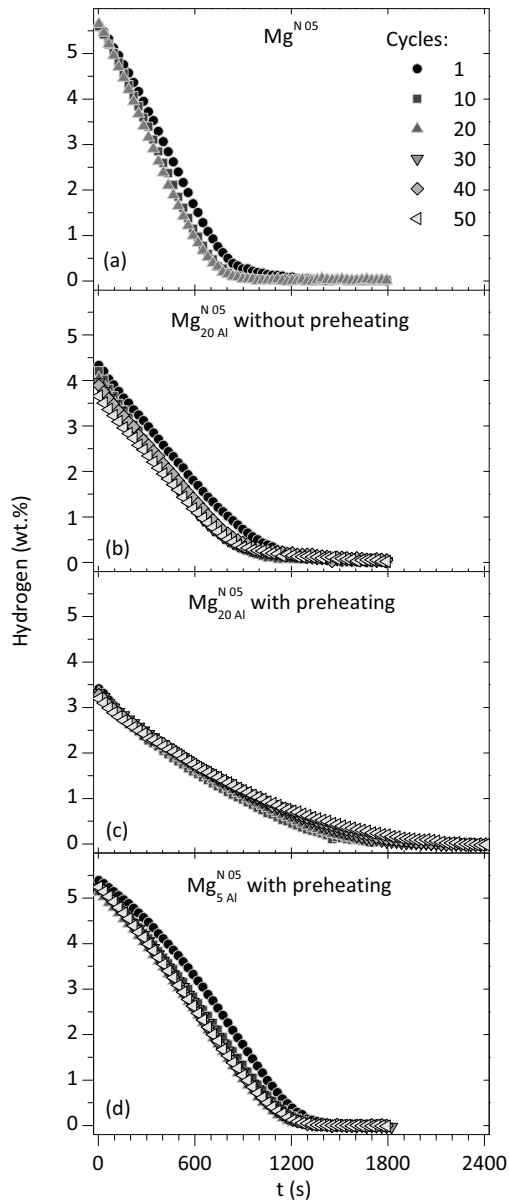


Figure 5.11: Desorption cycles of pellets $\text{Mg}^{\text{N}05}$ (a), $\text{Mg}_{20\text{Al}}^{\text{N}05}$ without preheating (b), $\text{Mg}_{20\text{Al}}^{\text{N}05}$ with preheating (c) and $\text{Mg}_{5\text{Al}}^{\text{N}05}$ with preheating (d).

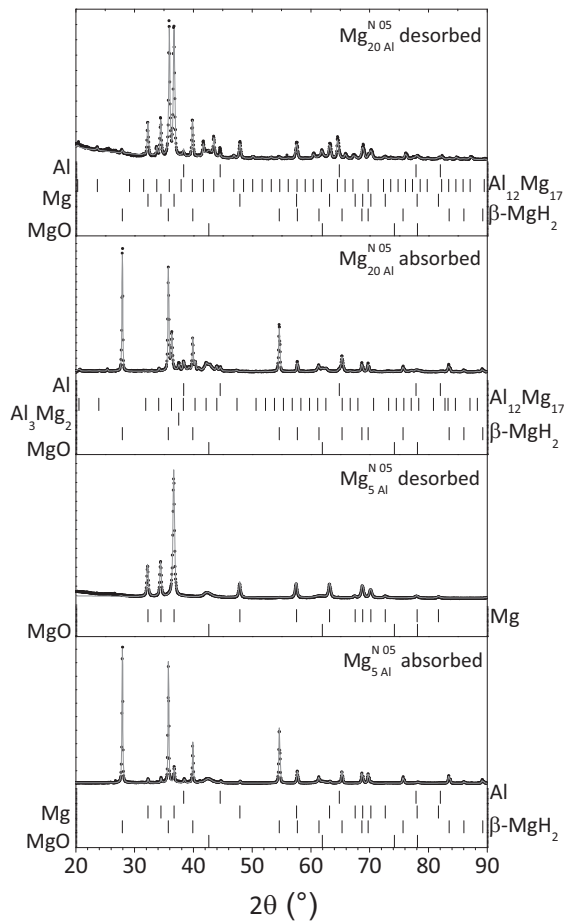


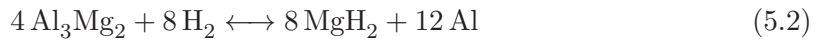
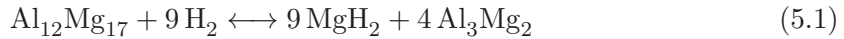
Figure 5.12: XRD patterns (points) and Rietveld fit (line) of preheated $\text{Mg}_{20\text{Al}}^{\text{N}05}$ and $\text{Mg}_{5\text{Al}}^{\text{N}05}$ pellets in the dehydrogenated and hydrogenated states after 50 hydrogen a/d cycles.

Sample	β -MgH ₂ (wt.%)	Mg (wt.%)	MgO (wt.%)	Al (wt.%)	Al ₃ Mg ₂ (wt.%)	Al ₁₂ Mg ₁₇ (wt.%)
Mg _{20Al} ^{N05} (dehydrogenated)	< 2	39 (2)	14 (2)	< 3	–	43 (2)
Mg _{20Al} ^{N05} (hydrogenated)	51 (2)	–	17 (2)	4 (1)	15 (2)	13 (1)
Mg _{5Al} ^{N05} (dehydrogenated)	5 (1)	73 (2)	22 (1)	–	–	–
Mg _{5Al} ^{N05} (hydrogenated)	72 (1)	7 (1)	18 (1)	< 3	–	–

Table 5.1: Relative amount of crystalline phases in heat treated pellets after 50 hydrogen a/d cycles obtained by Rietveld refinement of the XRD patterns. The uncertainty of the values is given in parenthesis.

5.2.2.2 Structural Characterization

Figure 5.12 shows the XRD patterns of Mg_{5Al}^{N05} and Mg_{20Al}^{N05} hydrogenated and dehydrogenated pellets after heat treatment and 50 hydrogen a/d cycles. The relative abundance of the phases has been estimated by means of the Rietveld refinement performed with the software MAUD [33] and is reported in table 5.1. The Mg_{20Al}^{N05} sample displays the Mg phase (39 wt.%), intense peaks of the intermetallic eutectic phase Al₁₂Mg₁₇ (43 wt.%) and other residual phases as MgH₂, MgO plus a small amount of Al (< 3 wt.%). In the pattern of the Mg_{20Al}^{N05} sample hydrogenated after 50 a/d cycles, it is possible to notice the presence of Al₁₂Mg₁₇ phase (13 wt.%) along with the Al₃Mg₂ phase (15 wt.%) in addition to the obvious presence of MgH₂ (51 wt.%). This agrees with the study of hydrogenation process of ball-milled Mg–Al powders by Crivello *et al.* [34, 35], which occurs in two completely reversible steps:



Reaction (5.2) did not reach completion in the operating conditions considered here, probably due to the higher relevant plateau pressure. The estimated amount of Al (4 wt.%) in the Mg_{20Al}^{N05} hydrogenated sample is larger than in the case of dehydrogenated sample. This is due to the fact that a certain amount of Al is in solid solution in the structure of Mg and during hydrogenation is expelled, according to the disproportionation reaction [36]



In the XRD pattern of Mg_{5Al}^{N05} dehydrogenated pellet, after heat treatment and 50 a/d cycles, there is no evidence of the presence of any Mg–Al intermetallic phase. According to the Mg–Al phase diagram, the smaller amount of Al is not sufficient for the precipitation of the eutectic phase and leads only to a solid solution of Al in Mg. The presence of Al in solid solution is also supported by the fact that the estimated amount of Al in the dehydrogenated sample is negligible. In the XRD profile of the same sample after hydrogenation there is no evidence of the presence of Mg–Al intermetallic phases. But, accordingly, to the behaviour for the Mg_{20Al}^{N05} sample, the observed amount of Al (< 3 wt.%) is anyway more than in the dehydrogenated sample, in agreement with reaction (5.3). It is not possible to evaluate the actual amount of Al possibly incorporated into the residual Mg (7 wt.%) and maybe into some intermetallic phases not detected by XRD.

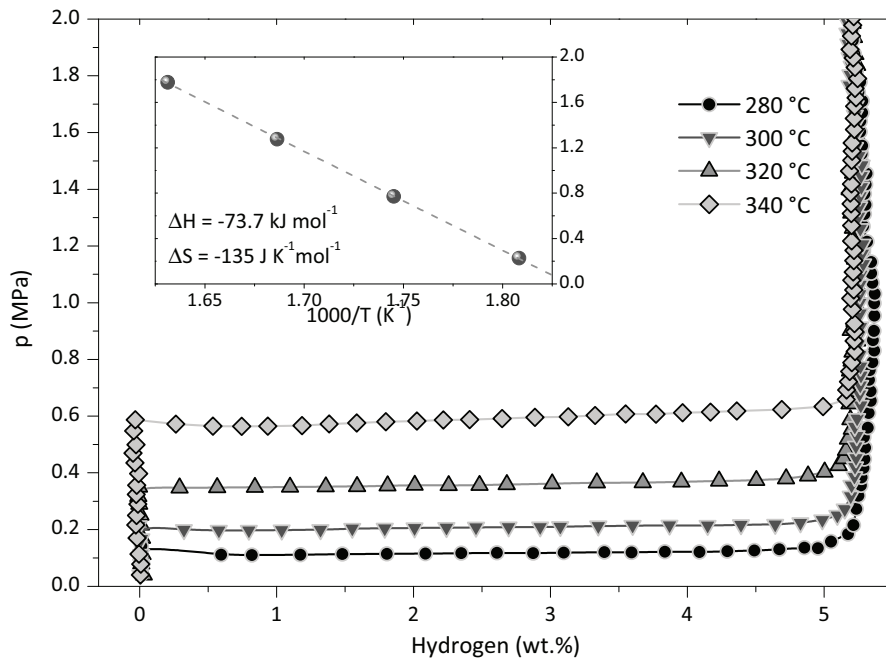


Figure 5.14: PCI at different temperatures for the $\text{Mg}_{5\text{Al}}^{\text{N}05}$ pellet preheated at 450 °C. The inset shows the corresponding van't Hoff plot.

The lattice parameters of Mg estimated by Rietveld refinement for some of the dehydrogenated samples are shown in figure 5.13. These values are smaller compared to those of pure Mg (taken from the PDF sheet 35–821) and this is certainly due to the presence of Al in Mg(Al) solid solution, considering the smaller metallic radius of Al compared to that of Mg [37]. The smallest lattice parameters are observed for the $\text{Mg}_{5\text{Al}}^{\text{N}05}$ sample after heat treatment and 50 a/d cycles, which shows that in this case Al prefers to enter the Mg(Al) solid solution instead of forming Mg–Al intermetallic phases. On the contrary, in the case of the $\text{Mg}_{20\text{Al}}^{\text{N}05}$ sample the precipitation of the eutectic phase $\text{Al}_{12}\text{Mg}_{17}$ slows down the formation of Mg(Al) and the lattice parameters of Mg are larger. The reported values of lattice parameters result higher than those corresponding to the maximum Al solubility in Mg(Al) (5 wt.%) [32] most probably because the actual structural situation is far from equilibrium.

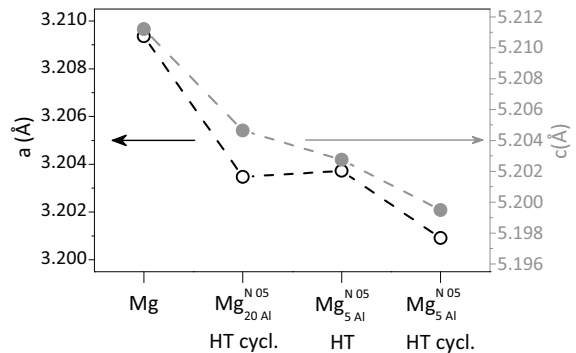


Figure 5.13: Lattice parameters of Mg estimated by Rietveld refinement for some of the studied dehydrogenated samples. The values are compared to the lattice parameters of pure Mg.

5.2.2.3 Thermodynamic Characteristics

PCI of the $\text{Mg}_{5\text{Al}}^{\text{N}05}$ pellet preheated at 450°C are reported in figure 5.14, showing a single plateau in correspondence to the equilibrium pressure of pure MgH_2 phase at a given temperature. There is not a second plateau corresponding to the reaction of intermetallic phases with hydrogen, which would further justify the above discussion [35]. Moreover, the values of the enthalpy (ΔH) and the entropy (ΔS) changes, as deduced from the van't Hoff plot (inset of figure 5.14), are -73 kJ mol^{-1} and $-135\text{ J K}^{-1}\text{ mol}^{-1}$, respectively, in good agreement with the values for pure MgH_2 phase [38].

5.2.2.4 Mechanical Characterization

The better mechanical resistance to a/d cycles of the dehydrogenated $\text{Mg}_{5\text{Al}}^{\text{N}05}$ samples with respect to the $\text{Mg}_{20\text{Al}}^{\text{N}05}$ samples is probably related to the presence in the first case of Al only in solid solution and, in the second case, of Al also in the $\text{Al}_{12}\text{Mg}_{17}$ intermetallic phase. This is supported by the following considerations. Solutioning of Al in Mg results in the strengthening of bulk polycrystalline materials because of the increase of the critical resolved shear stress, i. e. the stress needed to start the slip of crystal planes along the basal plane [39]. However, at the same time the critical resolved shear stress for the prismatic slip is reduced, with improvement of ductility and then of the resistance of the material to fracture. In particular, the strengthening of Mg–Al alloys increases proportionally to the presence of Al up to 10 wt.%, while the elongation (ductility) shows a maximum around 4 wt.% Al [36]. The best compromise between hardness and ductility is estimated to be around 6 wt.% Al. It has also been reported that the presence of Al in solid solution favours the superplasticity of Mg at temperatures $> 300^\circ\text{C}$ [40, 41, 42], meaning that at these temperatures the material presents a high deformability before fracture. It should also be taken into account that the eutectic phase $\text{Al}_{12}\text{Mg}_{17}$, being fragile, can cause a general embrittlement of the material. Therefore, the ductility of the material can be improved by reducing the amount of this phase [43], even in view of its localization along grain boundaries of the hosting Mg alloy [44]. Finally, since the bcc structure of $\text{Al}_{12}\text{Mg}_{17}$ is not compatible with the hcp structure of Mg, this leads to the embrittlement of the Mg / $\text{Al}_{12}\text{Mg}_{17}$ interface [45].

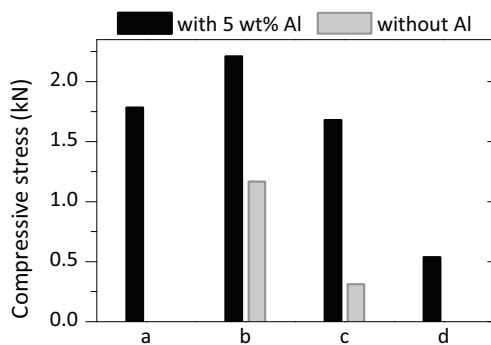


Figure 5.15: Results of the compression tests to estimate the mechanical strength of the pellets without and with 5 wt.% Al.

Figure 5.15 shows the results of the mechanical tests for hydrogenated pellets without Al and with 5 wt.% Al after 0 and 50 a/d cycles. It is evident the better behaviour of pellets containing Al, while, in absence of aluminium, a stress of 30.1 N mm^{-2} and of 8.1 N mm^{-2} is sufficient to break the pellet after 10 and 20 a/d cycles, respectively. As before said and shown in figure 5.10, it is not possible to recover the pellet after 50 a/d cycles. The better behaviour of samples containing Al can be attributed to the presence, according to reaction (5.3), of an Al matrix surrounding the MgH_2 particles. Anyway, also in this case the strength decreases, likely

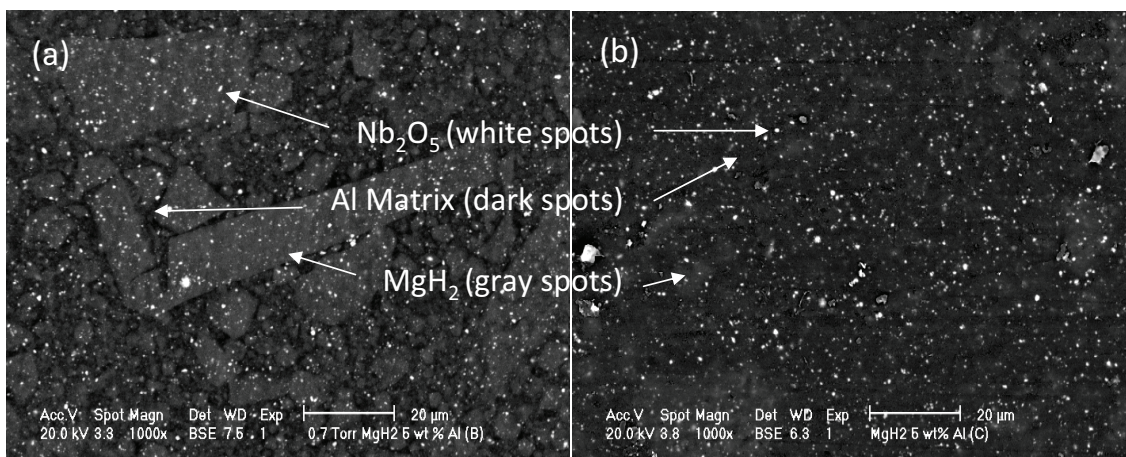


Figure 5.16: Environmental SEM micrographs for the hydrogenated $\text{Mg}_{5\text{Al}}^{\text{N}0.05}$ pellet (a) preheated at $450\text{ }^{\circ}\text{C}$ and (b) after 50 hydrogen a/d cycles. The gray scale contrast of the above images is influenced by the presence of carbon in the starting powder mixture.

due to the progressive increase of porosity: 43.7 N mm^{-2} and 13.9 N mm^{-2} after 20 and 50 cycles, respectively.

Figure 5.16 shows the SEM micrograph of the $\text{Mg}_{5\text{Al}}^{\text{N}0.05}$ pellet after heat treatment at $450\text{ }^{\circ}\text{C}$. The formation of the aluminium matrix, mentioned above to justify the improvement of mechanical properties of hydrogenated samples, is shown along with the grey regions, corresponding to MgH_2 and the white spots corresponding to well dispersed Nb_2O_5 particles. Figure 5.16 gives the SEM micrograph for the same pellet after 50 a/d cycles, showing that the cycling increases the homogeneity of the observed aluminium matrix and the MgH_2 phase.

5.2.3

Overall Properties of MgH_2 -Based Pellets

The mechanical strength of pellets made by catalyzed MgH_2 mixed with crystalline aluminium powder as binding agent has been tested after hydrogen a/d cycles. It is found that a pre-heating treatment of the pellet to the temperature sufficient to form intermetallic phases and/or a solid $\text{Mg}-\text{Al}$ solution ($450\text{ }^{\circ}\text{C}$) increases the resulting performance of the material, as concerns both functional and mechanical stability. The pellets with 20 wt.% Al degrade by cycling and, moreover, the hydrogen capacity is low and decreases with the ongoing cycles. A good mechanical stability has been observed instead in the case of pellets with 5 wt.% Al. These pellets show a constant 5.3 wt.% H_2 capacity up to 50 cycles and constant kinetics after 10 cycles. The enhanced stability of the pellets in this case has been attributed to the presence of the Al in solid solution with Mg when the pellet is dehydrogenated and to the formation of an Al matrix surrounding the MgH_2 particles when the pellet is hydrogenated. The microstructural evolution of the pellets in the different stages of a/d cycling requires a higher resolution investigation to be more deeply understood.

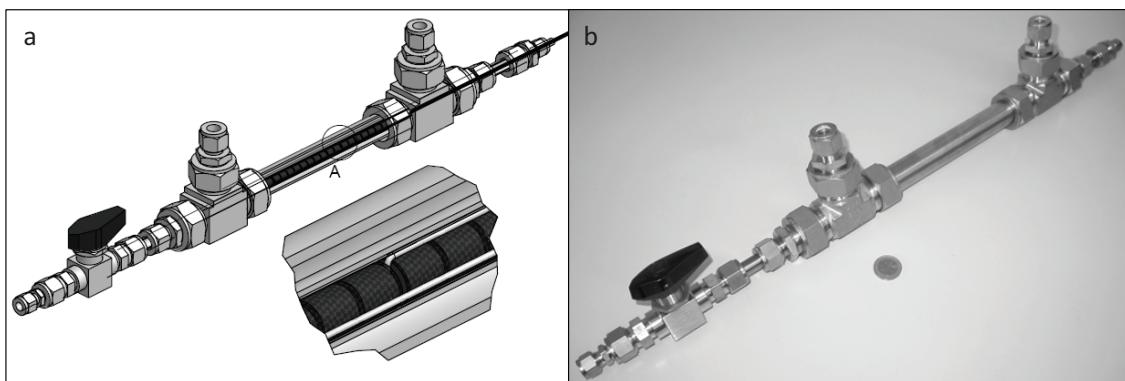


Figure 5.17: Design sketch of the reactor representing a detail of inner placement of pellets (a) and picture of the same after manufacturing (b).

5.2.4

Experimental Reactor for MgH_2 -Based Pellets

The preparation of a small vessel to study the hydrogen a/d behaviour of a metal hydride in form of pellets instead of powder, in order to overcome the shortcomings of the scaling up effects, is described in the following.

Scaling-up studies of magnesium hydride based powders in reactors as systems for solid state hydrogen storage have been recently reported [46, 47, 48], showing that the performances of those systems can degrade quickly with hydrogen a/d cycles [26]. A small experimental reactor was then conceived to evaluate the scale-up effects on the previously developed MgH_2 -based composite material sintered in pellets, which showed good cycling behaviour and mechanical strength stability. The design of this first experimental reactor containing hydride pellets was based on simplicity in its realization and on the possibility to adopt a modular concept.

The $\text{Mg}_{5\text{Al}}^{\text{N}05}$ pellets, were produced following the details already described in section 5.2.1. To increase the production volume, the thermal treatment under rotary pump vacuum was performed in a small furnace heated at 5°C min^{-1} up to 450°C for about 120 min. Three batches of 12 pellets were used in this annealing operation after which a 10% mass loss was observed: this was due both to dehydrogenation and to some probable Mg alloy evaporation (the furnace chamber resulted coated by a thin layer of this metal). Out of the total number of pellets, 32 were inserted in the reactor, resulting in 9.6 g.

The experimental reactor (figure 5.17) was composed of an AISI 304 steel pipe (outer diameter 12 mm, wall thickness 1.5 mm) inserted in a larger one of the same material (outer diameter 25 mm, wall thickness 2 mm). The interspace between the two pipes allowed heat exchange fluid to flow to control temperature. All the connections and the inlet valve were of Swagelok type. Opposite to the gas inlet three K-type thermocouples entered the inner pipe to measure the temperature of the pellets in different positions of the reactor during the test.

To improve the thermal conductivity between the pellets and between the pellets and heat exchanger, carbon mat from R&G Faserverbundwerkstoffe GmbH-Composite Technology was inserted between one pellet and another and rolled around a group of them. The final setup resulted in four equal group of wrapped pellets. In order to insert the pellets inside the reactor in the correct position the extremities of the thermocouples were bent appropriately.

Automated facilities developed at the ERSE labs [26] and schematized in figure 5.18 were utilized to test the reactor: that allows performing hydrogen a/d cycles at desired temperatures, heating and cooling rate, gas flow rate and pressure. The test system had two different circuits. The gas circuit, equipped with control and measuring instruments (provided by Bronkhorst High-Tech B.V., El-Flow and El-Press series), shut and safety valves, was connected to the inner pipe of the reactor. The oil circuit, working with Solutia Therminol 72 oil and including oil reservoir, pump, expansion tank and electrical heater, was connected with the external pipe.

The reactor was inspected before and after 50 cycles of hydrogen a/d by means of radiographic equipment Bosello SRE80 MAN with a XRG130 IT generator, 0.2 mm focal spot and 19° aperture angle. Voltage and current values of 90 kV and 2.80 mA, respectively, were used as initial settings and slightly adjusted to optimize the contrast.

5.2.5 Performances of the Reactor

Once the reactor had been connected to the test device, the first operation was hydrogen absorption, because during the heat treatment the pellets were dehydrogenated as a result of a combined action of temperature and rotary pump evacuation.

The first a/d cycles were operated manually to test the effectiveness of the chosen operating parameters, and later the automatic mode started.

In absorption mode the operating values were the following: hydrogen pressure 0.8 MPa, flow rate between a maximum of 0.7 Nl min^{-1} and a minimum of 270°C , temperature 0.8 MPa. The absorption started automatically when the established temperature was reached and the gas valve opened to let the chosen maximum hydrogen flow in the reactor. This lasted as long as the reaction kinetics slowed down and the gas flow decreased, then the flow rate was measured with the valve fully opened up to the moment when the minimum flow rate was reached. The amount of stored hydrogen was calculated from the flow rate measurements, while the difference between inlet and outlet oil temperatures, oil heat capacity and flow rate allowed the calculation of the heat generated by the exothermic absorption reaction.

The selected operating values for the desorption steps were: discharge hydrogen pressure of 0.12 MPa, minimum hydrogen flow rate of 0.01 Nl min^{-1} and temperature of 310°C .

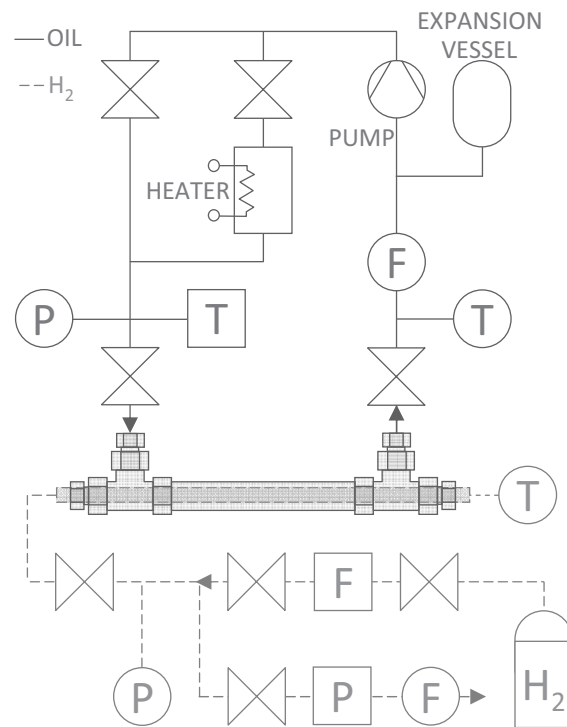


Figure 5.18: Simplified schematic drawing of the experimental setup coupled with the reactor. Circles are measuring instruments and squares are measuring and control instruments. Letters F, T, and P indicate flow, temperature and pressure, respectively.

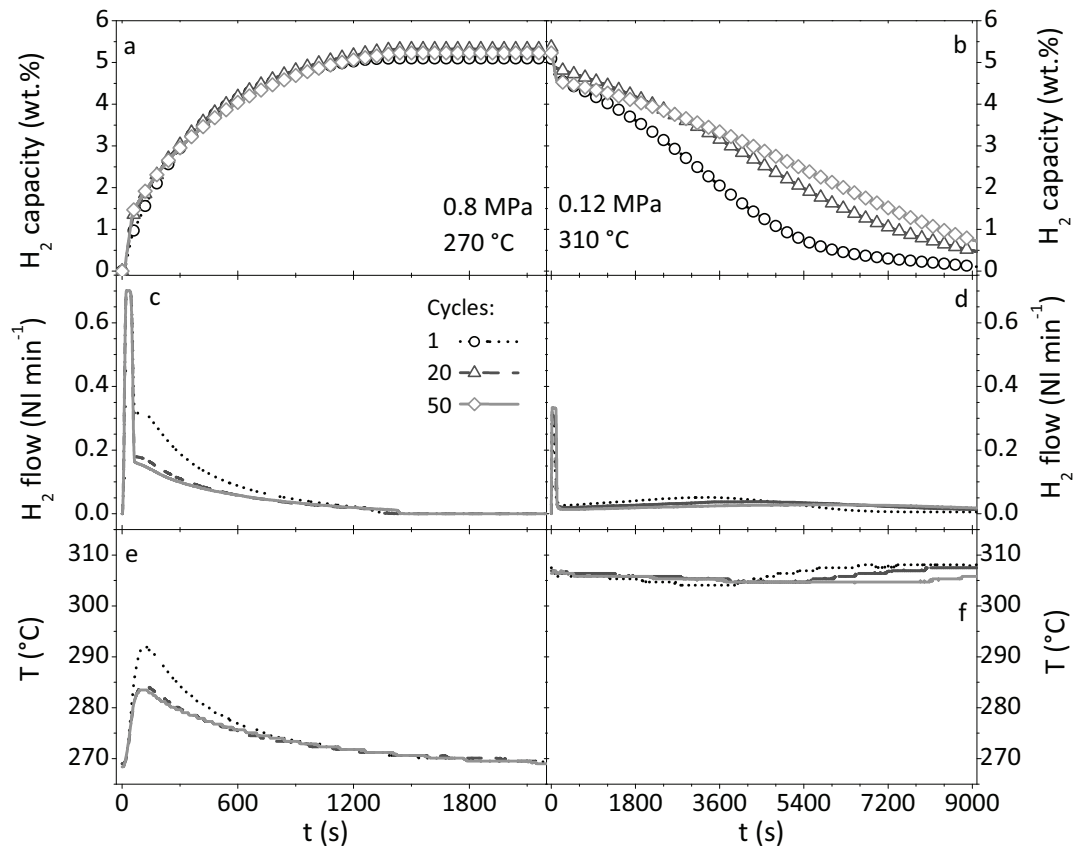


Figure 5.19: Absorption (a, c, e) and desorption (b, d, f) data vs. time for first, intermediate and last hydrogen a/d cycles. Hydrogen content plots (a and b) were obtained from flow data (c and d) retrieved from instruments during the test. Temperatures (e and f) were those registered in the central part of the reactor.

In these steps too, the operation started when the set temperature was reached: the hydrogen outlet valve opened and a pressure controller maintained the hydrogen pressure to the established value. As for absorption, the desorption lasted as long as the minimum hydrogen flow rate value was reached.

The instrumental flow data were elaborated to obtain the wt.% H_2 vs. time plots shown in figures 5.19 a and b. A comparison with the data measured for a single Mg_{5Al}^{N05} pellet (figure 5.11 d) shows clearly that the desorption kinetics is worsen, but anyway better than for the scaling-up tests carried out with a reactor containing powder not previously pressed. These differences may be in part attributed to an inhomogeneous hydrogen gas flow and heat exchange rate in the scaled-up systems with respect to the single pellet experiments. The absorption behaviour in the present small reactor is similar to that of a single compacted pellet. It can be seen that with the ongoing cycles the maximum hydrogen gravimetric capacity is stable, around 5.2 wt.%, but that desorption kinetics is slowing down. It is to be noted that the flow measurements and the thermal fluid heating, used in the present case, have different performances and settings compared to the Sievert's apparatus and the electrical heating used to test a single pellet (section 5.2.1). For instance, the GRC apparatus releases the gas in small amounts, thus leaving to the

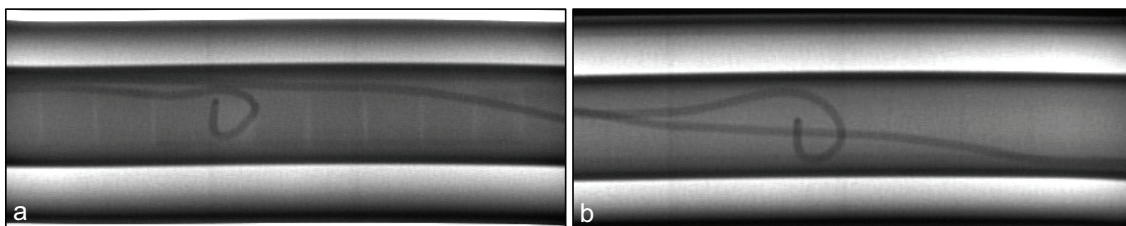


Figure 5.20: Radiographs of the central part of reactor before (a) and after (b) 50 hydrogen a/d cycles.

sample at least 6 s between one step and another to react and stabilize, while a continuous flow of gas does not allow any settling or relaxation of temperatures and stresses. As a matter of fact, the kinetics of hydrogen release is approximately an order of magnitude slower for a number of pellets in the reactor rather than for a single pellet in the sample holder of the volumetric apparatus.

Both absorption and desorption graphs display a first part where almost 1 wt.% of hydrogen is shown to react: this is mostly due to the shape of the flow profiles of figure 5.19 c, where the initial sudden hydrogen flow, due to the 0.8 MPa pressure, is limited by the controller and then the valve is fully opened. Figure 5.19 d represents the flows during hydrogen release, where the minimum useful pressure of 0.12 MPa limits the flow to lower values and causes slow desorption kinetics: in fact the first flow peak does not reach the value of 0.7 Nl min^{-1} (instrumental limit) and the subsequent decrease of flow is more rapid than in figure 5.19 c.

The figures 5.19 e and f display the temperatures registered by the central thermocouple (clearly visible in the radiographs of figure 5.20) placed inside the reactor. Most significantly, figure 5.19 e shows how temperature increases suddenly with the exothermic hydrogen absorption, but just a maximum difference of about 20°C was detected between the central part of the reactor and the sides. The thermocouples placed at the extremity of the reactor registered only small variations in temperature (and so not reported in the figure), because they were in contact with just one pellet and in a position of higher heat dispersion: the central thermocouple was more affected by the contact with the pellets and, moreover, the steel pipe could disperse heat less easily than at the sides. This was a really localized effect, in fact the oil temperature was not affected appreciably and the heat flow was below 65 W for absorption. In contrast, previously developed reactors containing a comparable amount of powder were suffering of almost 80°C of local over-heating (figure 11 in ref. [26]). The data for hydrogen a/d in a larger reactor containing not previously compressed hydride powder show both a decrease in kinetics (the time for complete reaction is doubled) and in storage capacity which drops from 5.5 to 3 wt.% H_2 (figure 9 in ref. [26]).

In the release process of the present experiment the slow kinetics allows the material to complete the endothermic reaction without a significant change in temperature: a loss of few degrees of temperature was detected only by the central thermocouple.

The radiographic picture of figure 5.20 a shows the ordered disposition of the pellets assembled inside the reactor and how they are separated by the carbon mat; darker zones correspond to denser material, the pellets, while a lighter shade of grey corresponds to carbon mat. The same central zone of the reactor, examined after 50 cycles and reported in figure 5.20 b, shows a reversed contrast between pellets and carbon mat regions and a considerable decrease of the interspaces thickness. The reason for this is twofold: the increase

of the volume of pellets after cycling and migration of part of the metallic component of the pellets to their surface. This agrees with previous observations on the aluminium under cycling of single pellets (section 5.2.2). It is easy to foresee that the behaviour of the system might be significantly improved with wider interspaces between pellets inside the reactor filled with a light good heat conductor, as the carbon fibers used in the present case.

5.2.6 Towards MgH₂-Based Tanks

This experiment was carried out to evaluate the scaling up performances of a MgH₂-based composite material pressed in form of cylindrical pellets. The hydrogen a/d tests, performed on a reactor containing a number of pellets, behave differently from previous experiments on a single pellet: slightly lower gravimetric capacity and worse desorption kinetics. Nevertheless, the use of Mg_{5Al}^{N05} pellets in a reactor (well separated e. g. by carbon-fiber mat) instead of a powder bed, facilitates the heat exchange and avoids local overheating and subsequent detrimental strong compaction of the powder which has been seen in previous experiments to lead to rapid degradation of performances.

The experiment performed on the pellets and the profitable discussion arisen from the results, especially concerning the microstructural evolution of the composite in the a/d process, have been subject of a publication [49], successively completed by a shorter communication relative to the design and testing of the small reactor [50]. The realization of the same was a small step further to the realization of practical devices, especially if the requirements for vehicles (in the order of kg H₂) and the maximum hydrogen content in this reactor (about 0.5 g) are compared. Considering that the work started with a modest laboratory scale, the final results were significant, because it was incremented of almost two orders of magnitude.

Larger tanks are being developed with magnesium based materials [51, 52], they all contain compacted powder in pellets or discs and the presence of an additive is fundamental to help the thermal management of the tank. The operative temperatures are far from ambient condition, but these tanks can work if coupled with a device operating at medium-high temperature, e. g. solid oxide or molten carbonate fuel cells, heat co-generation or other industrial processes. They are particularly suitable for stationary applications, where weight and volume of the storage system do not represent a limitation.

References

- 1 McWhorter S., Read C., Ordaz G., Stetson N., Materials-based hydrogen storage: Attributes for near-term, early market PEM fuel cells, *Current Opinion in Solid State and Materials Science*, **15** (2011) 29–38. (Cited on page 81)
- 2 Dornheim M., Doppiu S., Barkhordarian G., Bösenberg U., Klassen T., Gutfleisch O., Bormann R., Hydrogen storage in magnesium-based hydrides and hydride composites, *Scripta Materialia*, **56** (2007) 841–846. (Cited on page 81)
- 3 Ashby M.F., Criteria for selecting the components of composites, *Acta Metallurgica et Materialia*, **41** (1993) 1313–1335. (Cited on page 81)
- 4 Lahaie D.J., Embury J.D., Ashby M.F., Scale dependent composite design charts, *Scripta Metallurgica et Materialia*, **32** (1995) 133–138. (Cited on page 81)
- 5 Liang G., Boily S., Huot J., van Neste A., Schulz R., Mechanical alloying and hydrogen absorption properties of the Mg–Ni system, *Journal of Alloys and Compounds*, **267** (1998) 302–306. (Cited on pages 82, 83, and 84)
- 6 Liang G., Huot J., Boily S., van Neste A., Schulz R., Catalytic effect of transition metals on hydrogen sorption in nanocrystalline ball milled MgH_2 –Tm (Tm = Ti, V, Mn, Fe and Ni) systems, *Journal of Alloys and Compounds*, **292** (1999) 247–252. (Cited on page 82)
- 7 Jain A., Jain R.K., Agarwal S., Ganesan V., Lalla N.P., Phase D.M., Jain I.P., Synthesis characterization and hydrogenation of $\text{ZrFe}_{2-x}\text{Ni}_x$ ($x = 0.2, 0.4, 0.6, 0.8$) alloys, *International Journal of Hydrogen Energy*, **32** (2007) 3965–3971. (Cited on page 82)
- 8 Agarwal S., Aurora A., Jain A., Jain I.P., Montone A., Catalytic effect of ZrCrNi alloy on hydriding properties of MgH_2 , *International Journal of Hydrogen Energy*, **34** (2009) 9157–9162. (Cited on page 82)
- 9 Yu X.B., Yang Z.X., Liu H.K., Grant D.M., Walker G.S., The effect of a Ti–V-based bcc alloy as a catalyst on the hydrogen storage properties of MgH_2 , *International Journal of Hydrogen Energy*, **35** (2010) 6338–6344. (Cited on page 82)
- 10 Dehouche Z., Peretti H.A., Hamoudi S., Yoo Y., Belkacemi K., Effect of activated alloys on hydrogen discharge kinetics of MgH_2 nanocrystals, *Journal of Alloys and Compounds*, **455** (2008) 432–439. (Cited on pages 82, 83, 84, and 85)
- 11 Nash P., Jayanth C.S., The Ni–Zr system, *Bulletin of Alloy Phase Diagrams*, **5** (1984) 144–147. (Cited on page 82)
- 12 Ruiz F.C., Castro E.B., Peretti H.A., Visintin A., Study of the different Zr_xNi_y phases of Zr-based AB_2 materials, *International Journal of Hydrogen Energy*, **35** (2010) 9879–9887. (Cited on page 82)
- 13 Ebrahimi-Purkani A., Kashani-Bozorg S.F., Nanocrystalline Mg_2Ni -based powders produced by high-energy ball milling and subsequent annealing, *Journal of Alloys and Compounds*, **456** (2008), 211–215. (Cited on page 85)
- 14 Barkhordarian G., Klassen T., Bormann R., Kinetic investigation of the effect of milling time on the hydrogen sorption reaction of magnesium catalyzed with different Nb_2O_5 contents, *Journal of Alloys and Compounds*, **407** (2006) 249–255. (Cited on pages 85, 86, and 88)
- 15 Flanagan T.B., Park C.N., Oates W.A., Hysteresis in solid state reactions, *Progress in Solid State Chemistry*, **23** (1995) 291–363. (Cited on page 87)
- 16 Hanada N., Ichikawa T., Fujii H., Catalytic effect of nanoparticle 3d-transition metals on hydrogen storage properties in magnesium hydride MgH_2 prepared by mechanical milling, *Journal of Physical Chemistry B*, **109** (2005) 7188–7194. (Cited on page 87)
- 17 Palade P., Sartori S., Maddalena A., Principi G., Lo Russo S., Lazarescu M., Schintei G., Kuncser V., Filoti G., Hydrogen storage in Mg–Ni–Fe compounds prepared by melt spinning and ball milling, *Journal of Alloys and Compounds*, **415** (2006) 170–176. (Cited on page 87)
- 18 Molinas B., Ghilarducci A.A., Melnichuk M., Corso H.L., Peretti H.A., Agresti F., Bianchin A., Lo Russo S., Maddalena A., Principi G., Scaled-up production of a promising Mg-based hydride for hydrogen storage, *International Journal of Hydrogen Energy*, **34** (2009) 4597–4601. (Cited on pages 87 and 88)
- 19 Pighin S.A., Capurso G., Lo Russo S., Peretti H.A., Hydrogen sorption kinetics of magnesium hydride enhanced by the addition of

- Zr₈Ni₂₁ alloy, *Journal of Alloys and Compounds*, **530** (2012) 111–115. (Cited on page 88)
- 20 Mushnikov N.V., Ermakov A.E., Uimin M.A., Gaviko V.S., Terent'ev P.B., Skripov A.V., Tankeev A.P., Soloninin A.V., Buzlukov A.L., Kinetics of Interaction of Mg-based mechanically activated alloys with hydrogen, *Physics of Metals and Metallography*, **102** (2006) 421–431. (Cited on page 88)
 - 21 Polanski M., Bystrzycki J., Plocinski T., The effect of milling conditions on microstructure and hydrogen absorption/desorption properties of magnesium hydride (MgH₂) without and with Cr₂O₃ nanoparticles, *International Journal of Hydrogen Energy*, **33** (2008) 1859–1867. (Cited on page 88)
 - 22 Schulz R., Huot J., Liang G., Boily S., Lalande G., Denis M.C., Dodelet J.P., Recent developments in the applications of nanocrystalline materials to hydrogen technologies, *Materials Science and Engineering: A*, **267** (1999) 240–245. (Cited on page 88)
 - 23 Barkhordarian G., Klassen T., Bormann R., Fast hydrogen sorption kinetics of nanocrystalline Mg using Nb₂O₅ as catalyst, *Scripta Materialia*, **49** (2003) 213–217. (Cited on page 88)
 - 24 De Piccoli C., Dal Toé S., Lo Russo S., Maddalena A., Palade P., Saber A., Sartori S., Principi G., Hydrogen storage in magnesium hydride doped with niobium pentaoxide and graphite, *Chemical Engineering Transactions*, **4** (2004) 343–347. (Cited on pages 88 and 89)
 - 25 Friedrichs O., Aguey-Zinsou F., Ares Fernández J. R., Sánchez-López J. C., Justo A., Klassen T., Bormann R., Fernández A., MgH₂ with Nb₂O₅ as additive, for hydrogen storage: Chemical, structural and kinetic behavior with heating, *Acta Materialia*, **54** (2006), 105–110. (Cited on page 88)
 - 26 Verga M., Armanasco F., Guardamagna C., Valli C., Bianchin A., Agresti F., Lo Russo S., Maddalena A., Principi G., Scaling up effects of Mg hydride in a temperature and pressure-controlled hydrogen storage device, *International Journal of Hydrogen Energy*, **34** (2009) 4602–4610. (Cited on pages 88, 96, 97, and 99)
 - 27 Verga M., Guardamagna C., Valli C., Principi G., Molinas B., Sistemi di accumulo di idrogeno ad idruri di magnesio: verifica sperimentale degli effetti di scala, *La Metallurgia Italiana*, **1** (2009) 59–67. (Cited on page 88)
 - 28 Glage A., Ceccato R., Lonardelli I., Girardi F., Agresti F., Principi G., Molinari A., Gialanella S., A powder metallurgy approach for the production of a MgH₂–Al composite material, *Journal of Alloys and Compounds*, **478** (2009) 273–280. (Cited on page 88)
 - 29 Chaise A., de Rango P., Marty Ph., Fruchart D., Miraglia S., Olivès R., Garrier S., Enhancement of hydrogen sorption in magnesium hydride using expanded natural graphite, *International Journal of Hydrogen Energy*, **34** (2009) 8589–8596. (Cited on page 89)
 - 30 Pohlmann C., Röntzsch L., Kalinichenka S., Hutsch T., Kieback B., Magnesium alloy-graphite composites with tailored heat conduction properties for hydrogen storage applications, *International Journal of Hydrogen Energy*, **35** (2010) 12829–12836. (Cited on page 89)
 - 31 Pohlmann C., Röntzsch L., Kalinichenka S., Hutsch T., Weissgärber T., Kieback B., Hydrogen storage properties of compacts of melt-spun Mg₉₀Ni₁₀ flakes and expanded natural graphite, *Journal of Alloys and Compounds*, **509**, (2011), S625–S628. (Cited on page 89)
 - 32 Murray J.L., “Aluminum – Magnesium”, in *ASM Handbook*, (1992) ASM International. Vol. **3** – *Alloy Phase Diagrams*, 305–306. (Cited on pages 90 and 93)
 - 33 Lutterotti L., Matthies S., Wenk H.R., Goodwin M., Combined texture and structure analysis of deformed limestone from time-of-flight neutron diffraction spectra, *Journal of Applied Physics*, **81** (1997) 594–600. (Cited on page 92)
 - 34 Crivello J.-C., Nobuki T., Kato S., Abe M., Kuji T., Hydrogen absorption properties of the γ-Mg₁₇Al₁₂ phase and its Al-rich domain, *Journal of Alloys and Compounds*, **446** (2007) 157–161. (Cited on page 92)
 - 35 Crivello J.-C., Nobuki T., Kuji T., Improvement of Mg–Al alloys for hydrogen storage applications. *International Journal of Hydrogen Energy*, **34** (2009) 1937–1493. (Cited on pages 92 and 94)
 - 36 Andreasen A., Hydrogenation properties of Mg–Al alloys, *International Journal of Hydrogen Energy*, **33** (2008) 7489–7497. (Cited on pages 92 and 94)
 - 37 Raynor G.V. (ed.), *The Physical Metallurgy of Magnesium and Its Alloys*, (1959) Pergamon Press, New York. (Cited on page 93)
 - 38 Bogdanović B., Bohmhammel K., Christ B., Reiser A., Schlichte K., Vehlen R., Wolf U., Thermodynamic investigation of the

- magnesium-hydrogen system, *Journal of Alloys and Compounds*, **282** (1999) 84–92. (Cited on page 94)
- 39 Cáceres C.H., Rovera D.M., Solid solution strengthening in concentrated Mg–Al alloys, *Journal of Light Metals*, **1** (2001) 151–156. (Cited on page 94)
- 40 Ceschini L., Balloni L., Boromei I., Mehtedi M.El, Morri A., Comportamento superplastico della lega di magnesio AZ31 prodotta mediante twin roll casting, *Metallurgia Italiana*, **9** (2007) 5–11. (Cited on page 94)
- 41 Ceschini L., Mehtedi M.El, Morri A., Sambogna G., Spigarelli S., Superplastic Deformation of Twin Roll Cast AZ31 Magnesium Alloy, *Materials Science Forum*, **604-605** (2008) 267–277. (Cited on page 94)
- 42 Watanabe H., Tsutsui H., Mukai T., Kohzu M., Tanabe S., Higashi K., Deformation mechanism in a coarse-grained Mg–Al–Zn alloy at elevated temperatures, *International Journal of Plasticity*, **17** (2001) 387–397. (Cited on page 94)
- 43 Kleiner S., Beffort O., Wahlen A., Uggowitzer P. J., Microstructure and mechanical properties of squeeze cast and semi-solid cast Mg–Al alloys. *Journal of Light Metals*, **2** (2002) 277–280. (Cited on page 94)
- 44 Kostka A., Coelho R.S., Dos Santos J., Pyzalla A.R., Microstructure of friction stir welding of aluminium alloy to magnesium alloy, *Scripta Materialia*, **60** (2009) 953–956. (Cited on page 94)
- 45 Zhang L., Cao Z.Y., Liu Y.B., Su G.H., Cheng L.R., Effect of Al content on the microstructure and mechanical properties of Mg–Al alloys, *Material Science and Engineering: A*, **508** (2009) 129–133. (Cited on page 94)
- 46 de Rango P., Chaise A., Charbonnier J., Fruchart D., Jehan M., Marty Ph., Miraglia S., Rivoirard S., Skryabina N., Nanostructured magnesium hydride for pilot tank development, *Journal of Alloys and Compounds*, **446-447** (2007) 52–57. (Cited on page 96)
- 47 Chaise A., de Rango P., Marty Ph., Fruchart D., Experimental and numerical study of a magnesium hydride tank, *International Journal of Hydrogen Energy*, **35** (2010) 6311–6322. (Cited on page 96)
- 48 de Rango P., Garrier S., Chaise A., Fruchart D., Miraglia S., Marty Ph., MgH₂ tank tested under various experimental conditions, *Diffusion and Defect Data Part B: Solid State Phenomena*, **170** (2011) 342. (Cited on page 96)
- 49 Khandelwal A., Agresti F., Capurso G., Lo Russo S., Maddalena A., Gialanella S., Principi G., Pellets of MgH₂-based composites as practical material for solid state hydrogen storage, *International Journal of Hydrogen Energy*, **35** (2010) 3565–3571. (Cited on page 100)
- 50 Capurso G., Agresti F., Lo Russo S., Maddalena A., Principi G., Cavallari A., Guardamagna C., Performance tests of a small hydrogen reactor based on Mg–Al pellets, *Journal of Alloys and Compounds*, **509** (2011) S646–S649. (Cited on page 100)
- 51 Garrier S., Chaise A., de Rango P., Marty Ph., Delhomme B., Fruchart D., Miraglia S., MgH₂ intermediate scale tank tests under various experimental conditions, *International Journal of Hydrogen Energy*, **36** (2011) 9719–9726. (Cited on page 100)
- 52 Delhomme B., de Rango P., Marty Ph., Bacia M., Zawilski B., Raufast C., Miraglia S., Fruchart D., Large scale magnesium hydride tank coupled with an external heat source, *International Journal of Hydrogen Energy*, **37** (2012) 9103–9111. (Cited on page 100)

6

Chapter 6

Room Temperature Hydride Storage System

Abstract. The topic of this chapter concerns with the feasibility of a vehicular hydrogen tank system, using a commercial interstitial metal hydride as storage material. The tank was designed to feed a fuel cell in a light prototype vehicle and the material, Hydralloy C5 by GfE, was expected to be able to absorb and desorb hydrogen in a range of pressure suitable for that. A systematic analysis of the material in laboratory scale is useful to make an extrapolation of the thermodynamic and reaction kinetics data. The development of the tank was done according to the requirements of the prototype vehicle propulsion system. The task for static tests (measurements with automatic flow control and constant settings) is to evaluate whether the requirements for desorption are met by this tank set-up. Moreover the settings for the most convenient reloading of the tank were experimented. The following step was the design and the application of dynamic tests, where the requirements were still met and the hydrogen flow, provided by the tank, was fluctuating following a hypothetical on-road test. It was possible to underline the thermal issues of high-demanding performances and to propose a solution for that. Different cycles were performed on the tank to find the ideal setting for high average and peak flow in a realistic experiment.

After considering the materials for hydrogen storage and the possible solutions to the hydrogen capacity, kinetic, thermodynamic issues and hydrogen a/d reversibility, the technological challenge is moved to the realization of a storage system for practical applications. In chapter 5 the first attempt to build a working system was outlined, but the focus was still on the hydride behaviour inside the reactor, rather than on the system itself. The material selection for a hydride-based tank is a crucial aspect and involves a higher number of parameters than the material choice in a laboratory scale: among the several factors listed in section 2.1.4, heat and mass transport move up from almost negligible aspects to become the main impediments to the optimal functionality. In fact, it was already mentioned how most of the efforts are focused to increase the thermal conductivity.

Furthermore, the tank system design must follow specific criteria for the selected material, trying to optimize the aforesaid parameters in combination with mass, pressure resistance and several requirements related to the application. Different analytical approaches are available to assist the selection process also in this field of technical studies [1, 2].

6.1 Introduction

The compounds used for the development of storage systems belong to different classes of the materials analyzed in chapter 2. The minimum requirement that has to be fulfilled is a very good reversibility of the process in feasible conditions, hence most of the complex hydrides are ruled out. Sodium alanate is a remarkable exception and many researchers dedicated their studies to the developments of models [3, 4] and experiments with this material [5]. The optimization of a tank involves the seek of the best material to minimize the final weight of the system, as well [6]. Apart from reversibility, the advantage of NaAlH_4 is an operative temperature around 125°C , which allowed experimentation in full-scale (3 kg H_2 were stored in a four module system [7]), or using exclusively an air-cooling system [8].

Air-cooling is a very positive asset if the coupling with a high temperature PEM fuel cell is considered, for instance. In fact, this technical solution has been undertaken for magnesium hydride based material too [9], even if for this hydride the choice of a different thermal fluid is more often considered, especially in the case of stationary application [10, 11]. Magnesium hydride is seldom taken into account for vehicular applications, as it does not have the capacity to exploit just the waste heat of the propulsion system to reach an equilibrium hydrogen pressure suitable to feed a PEM fuel cell [12].

On the other hand, among the various intermetallic hydrides it is easy to find compounds able to deliver an acceptable hydrogen amount at ambient temperature. For example, LaNi_5 has been used in different experiments [13, 14], and AB_2 Laves phases (see the dedicated section at page 17) found their application also in vehicular tests [15]. Due to the low storage capacity of the intermetallic hydrides, anyway, a hybrid application with high-pressure storage vessel has been proposed for this class of material [16].

6.1.1 Purpose

Along with the progress of the world economy, mobility is likely to expand further in the future. The environmental and energetic concerns raised in the introduction (chapter 1) strongly apply to means of transport, as they consume about one quarter of the world total energy and are imputable for exhaust emission. In the case of automobiles with internal combustion engines, a large part of the fuel energy is emitted as heat due to friction loss and exhaust gas: higher efficiency technologies such as fuel cell vehicles are expected to improve this field [17].

Most of experimental activity described in this chapter was developed at Helmholtz-Zentrum Geesthacht (HZG)¹ in the frame of the Nios project. The Nios concept is a fully

¹A five months period was spent there during the doctoral studies.

Name	Supplier	Composition wt. %	Plateau pressure MPa	Hydrogen wt. %
Hydralloy C 5	GfE	Al 0.27, Ti 27.13, V 13.95,	2 (abs. 44 °C)	1.81 (abs.)
		Mn 51.31, Fe 2.98, Zr 2.97	1.26 (des. 44 °C)	1.77 (des.)
Hydralloy E 60/0	GfE	La 18.4, Ce 8.2, Pr 1.6,	0.456 (abs. 22 °C)	1.42 (abs.)
		Ni 64.2, Nd 3.2, Sn 3.6	0.211 (des. 19 °C)	1.38 (des.)
Hy-Stor	MPD Tech.Co.	LaNi ₅	0.135	1.37
Ecka	Eckart-Weeke	95 (Ti, V, Fe, Mn) + 5 Al	-	-

Table 6.1: Comparison of the available data of commercial room temperature alloys for selection.

working prototype of a hydrogen-fueled city car². The vehicle took part in the 2010 Shell Eco Marathon in the *Urban Concept Cars* category where it took home the Autodesk Design Award for its outstanding design and ergonomics. As an entrant in the Urban Concept Cars class, the Nios had to be viable for use in the real-world. The electric motor of the vehicle is powered by an advanced hydrogen fuel cell system, which was coupled, for the competition, with a pressurized cylinder provided by the organizers. The task assigned to HZG was the design and realization of a hydride-based tank for the Nios prototype, according to the fuel cell H₂ supply demand and the available volume constraints.

6.2

Material Choice

The material to serve as hydride bed inside the storage tank was to be chosen among some commercial room temperature alloys, already present at the research institute as stock. In this early stage, for the conception of the system a maximum loading hydrogen pressure of 3 MPa was adopted, while a value of 0.2 MPa for released hydrogen was assumed as adequate to feed the fuel cell. According to the available data, reported in table 6.1, Hydralloy C 5 was chosen. Apart from the relatively high H₂ capacity, it is supposed to provide a sufficient pressure difference in both the considered processes, thus ensuring a good driving force for a/d reactions.

The alloy belongs to the Hydralloy C group of products by Gesellschaft für Elektrometallurgie, a class of pseudo-binary AB₂ alloys with different composition and performances. They were studied since early years of hydrogen storage research [18, 19], and suggested for the niche application of self-sufficient energy systems [20]. The literature concerning the specific C 5 alloy is not abundant [21], therefore some laboratory scale test have been performed to accompany and explain the data coming from the scaled-up system.

6.2.1

Structural Characterization

X-Ray diffraction measurements were performed with a Philips X'Pert MPD. The XRD patterns shown in figure 6.1 confirmed the Laves phase structure of the sample, the hexag-

²It was developed by a team of students and professors at three German universities and colleges: the University of Art and Design in Halle, the Technical University Chemnitz, and the College of Further Education in Merseburg, in collaboration with automotive supplier Strähle & Hess, and Fortis Saxonia.

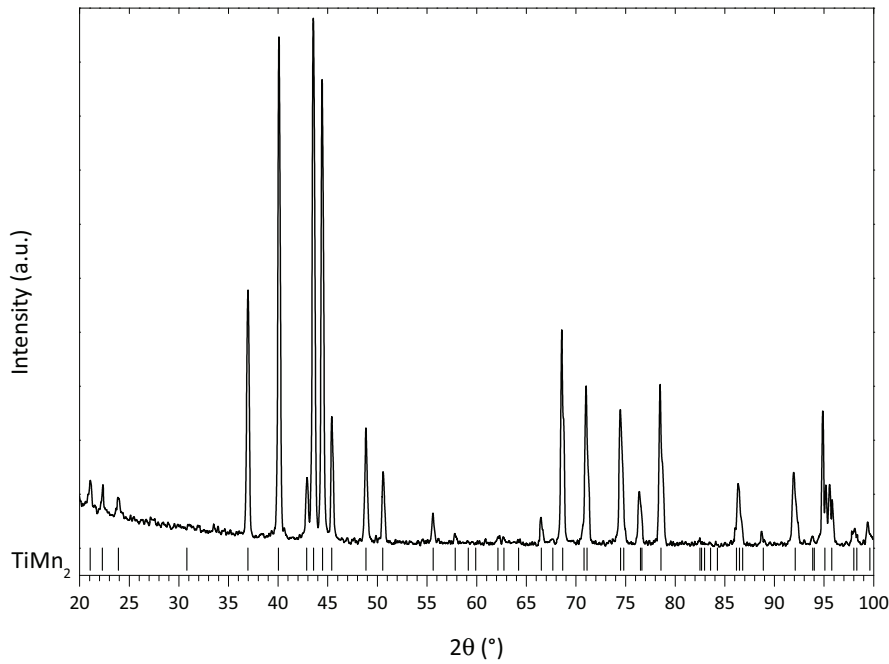


Figure 6.1: XRD pattern of Hydralloy C5, with the representative Laves phase peaks highlighted.

Micrograph	Position	Al	Ti	V	Mn	Fe	Zr	Ce
		wt. %						
	Sample average values	0.5	31.2	15.5	45.4	3.6	3.0	0.8
figure 6.2 a	Spots 1-2-3-4: mean values	0.4	27.9	14.0	50.9	3.3	2.9	0.6
figure 6.2 b	Spots 1-2-3: mean values	0.9	57.6	17.2	21.2	2.5	-	0.5

Table 6.2: EDX analysis results for Hydralloy C5. See figure 6.2 for the position of the spots.

onal (C14) lattice shared with the representative MgZn_2 . Microscopic analysis were performed with an EVO 40 Carl Zeiss, equipped with a Pentafet Link EDX microanalysis system. SEM micrographs, shown in figures 6.2a and b, together with EDX were used to verify the homogeneity of the samples. The global composition of the alloy (reported in table 6.2) is similar to that declared by the supplier and can be written as $\text{Ti}(\text{Mn},\text{V})_2$ with traces of other elements. The results of elemental analysis of the main constituent phase (figure 6.2a) are listed in table 6.2. It was also possible to detect some Ti-rich spots (figure 6.2b) of an unknown phase the components of which are listed in table 6.2, too. However, they represent a negligible fraction in the sample.

6.2.2 Hydrogen a/d Properties

Several PCI were measured to accurately derive thermodynamics properties and to have an experimental evidence of the pressures in different conditions with respect to the data of the supplier and those available in the literature [21]. The curves are shown in fig-

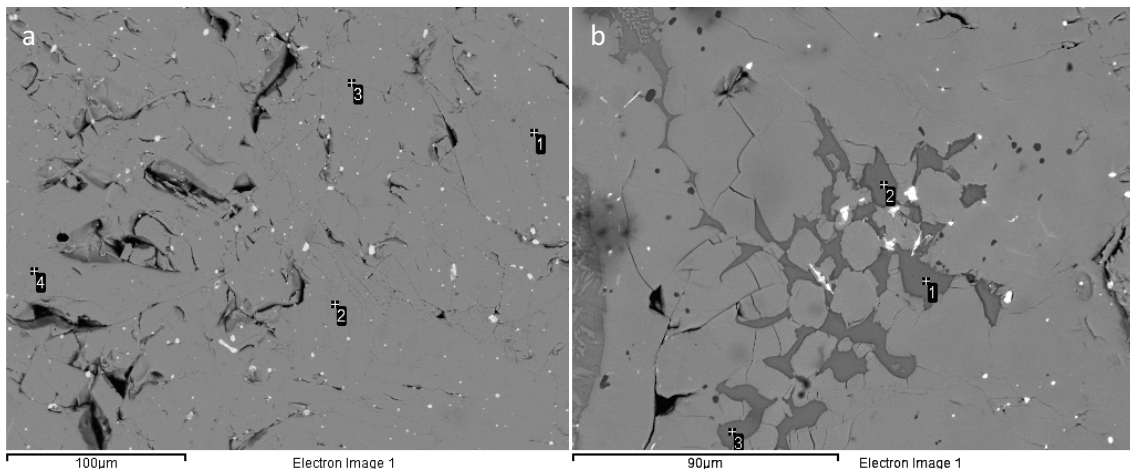


Figure 6.2: SEM micrographs of Hydralloy C5: main phase (a) and Ti-rich phase (b). The spots used for EDX analysis are marked in the pictures.

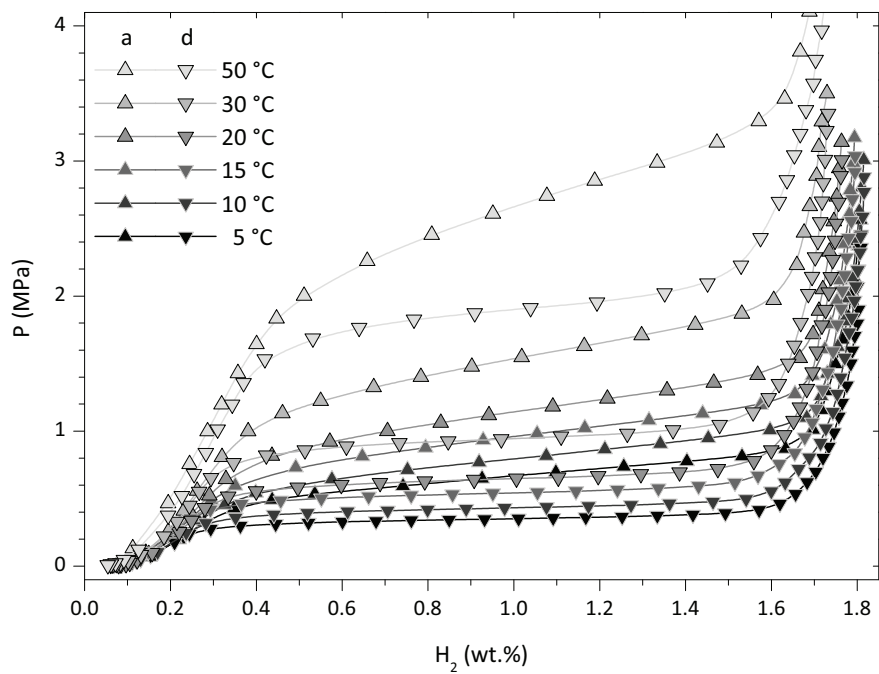


Figure 6.3: PCI for Hydralloy C5 in the 5–50 °C temperature range.

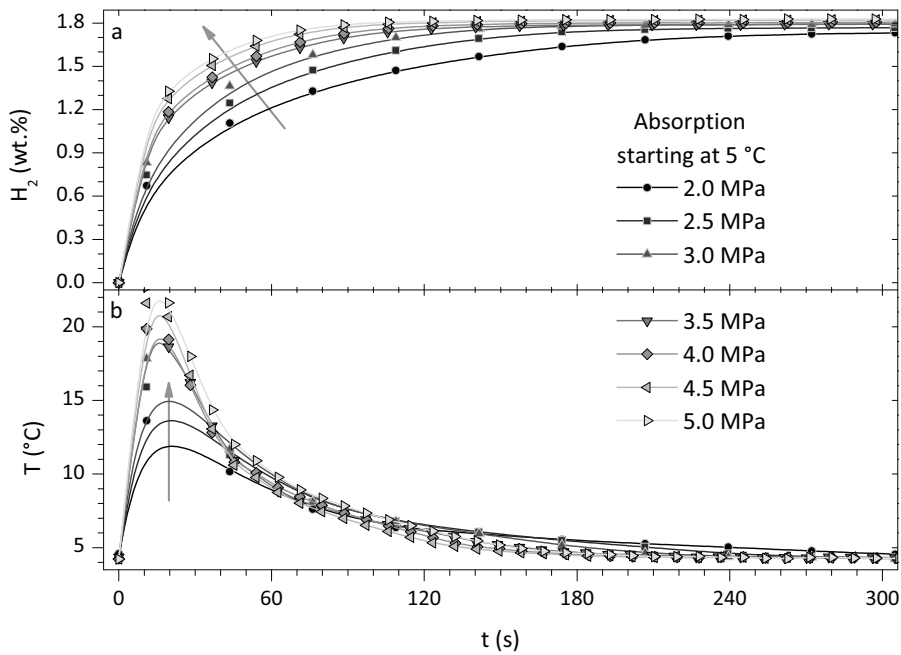


Figure 6.5: Absorption cycles starting at 5 °C and different pressures (a) and their temperature profiles (b).

ure 6.3 for several temperatures in the range from 5 to 50 °C. The desorption pressure is quite higher than 200 kPa even at 5 °C, and extrapolation from the van't Hoff plot reported in figure 6.4 (in good agreement with data in reference [21]) shows an equilibrium pressure $p_{eq} \approx 200$ kPa for desorption at a temperature as low as -7 °C. Apart from the expected regular increment of the plateau pressures with the temperature, it is possible to notice a moderate increase in the slope and inter-distance of the absorption and desorption curves, resulting in an augmented hysteresis at higher temperatures.

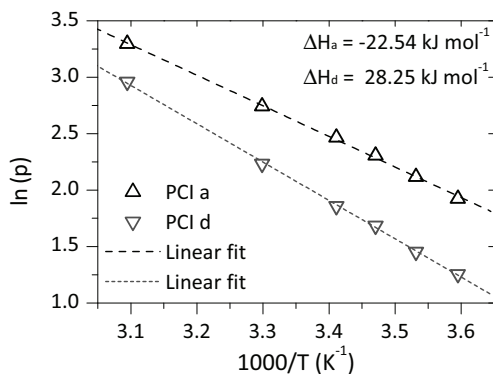


Figure 6.4: Van't Hoff plot derived from PCI in figure 6.3. The thermodynamic properties for Hydralloy C 5 are also reported.

This is resulting in a required pressure higher than 1 MPa to complete the absorption at a temperature just higher than 10 °C.

In kinetic measurements it is possible to clearly notice the effects of the thermodynamic properties, i. e. of the distance from p_{eq} , in the driving force of the reaction. For low temperatures the absorption is quite fast and can be completed within 5 min, as in figure 6.5 a. At 20 °C a pressure of 1 MPa is confirmed to be already not enough to complete the absorption (figure 6.6 a) and with higher pressure it is possible to notice a decrease in the kinetics with respect to that at 5 °C. This is even more evident at

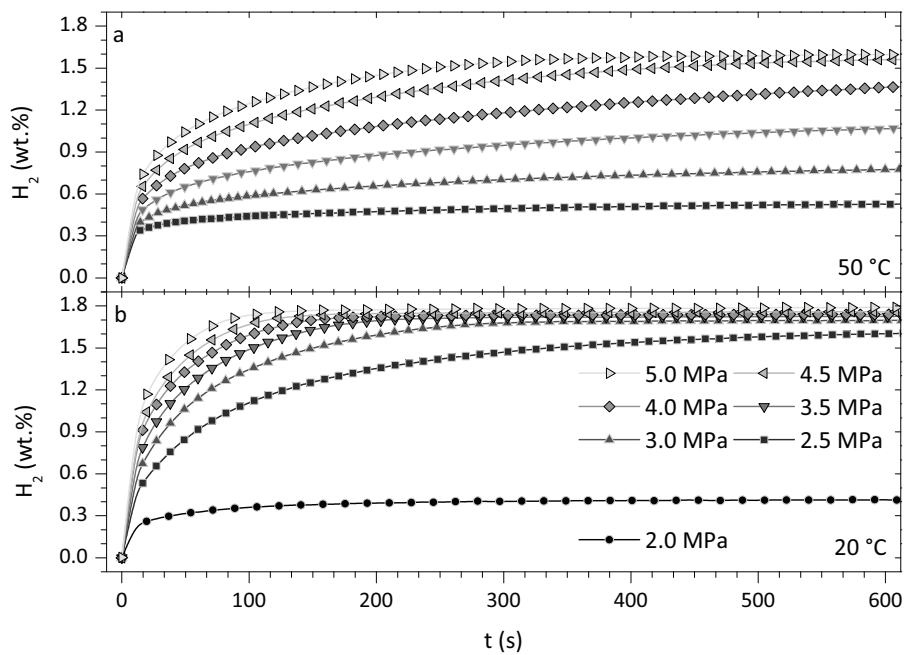


Figure 6.6: Absorption cycles starting at 20 °C (a) and at 50 °C (b) at different pressures.

40 °C and 50 °C (figures 6.7 a and 6.6 b, respectively), because in the latter the only pressure able to complete the absorption is 5 MPa, but the maximum hydrogen content can only reach 1.7 wt.% in a longer time.

Considering desorption curves, it is not possible to notice an effect of the ultimate pressure of the previous absorption figure 6.8 a; on the other hand the final pressure reached during the release process can influence the kinetics and the final quantity too, as shown in figure 6.8 b. For desorptions at fixed pressure values, the influence of the temperature is much more evident, as displayed in figure 6.9

It is very interesting to see the evolution of the samples temperature with the development of the gas-solid reaction. The processes are quite fast and both in adsorption and in desorption the temperature offset can be higher than 20 °C, as shown in figures 6.5 b, 6.7 b for absorption and in figures 6.10 a and b for desorption. Moreover, in figure 6.10 a, the effect of previous absorption pressure is presented, resulting in a temperature drop due to sudden hydrogen release, while in figure 6.10 b the effect of the desorption pressure is considered. Considering the thermodynamic state, when the samples are approaching the equilibrium pressure the driving force for the reaction is reducing and so is the exchanged heat, self-balancing the system. In a laboratory scale, however, this temperature difference is restored within minutes.

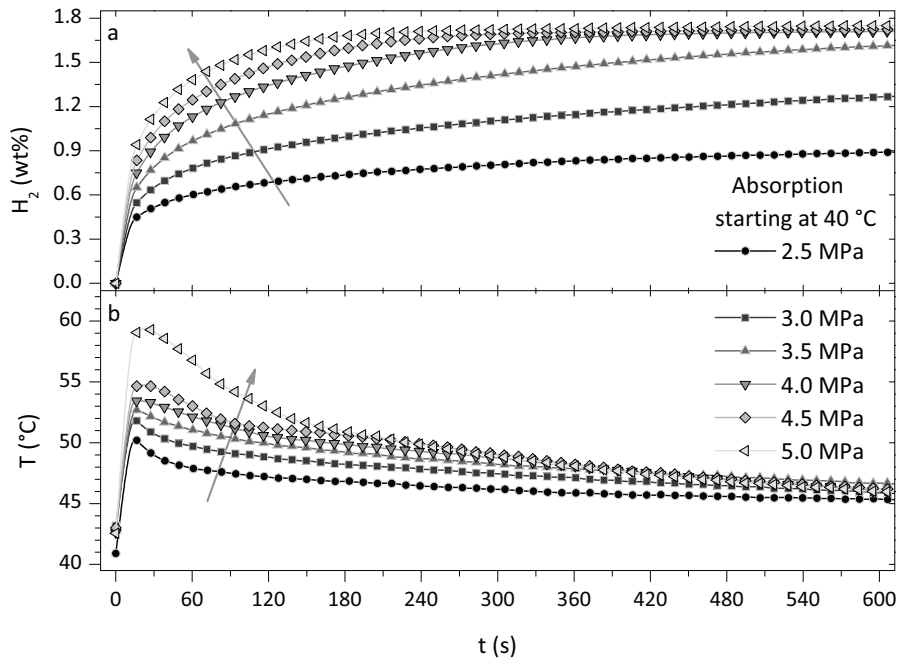


Figure 6.7: Absorption cycles starting at 40 °C and different pressures (a) and their temperature profiles (b).

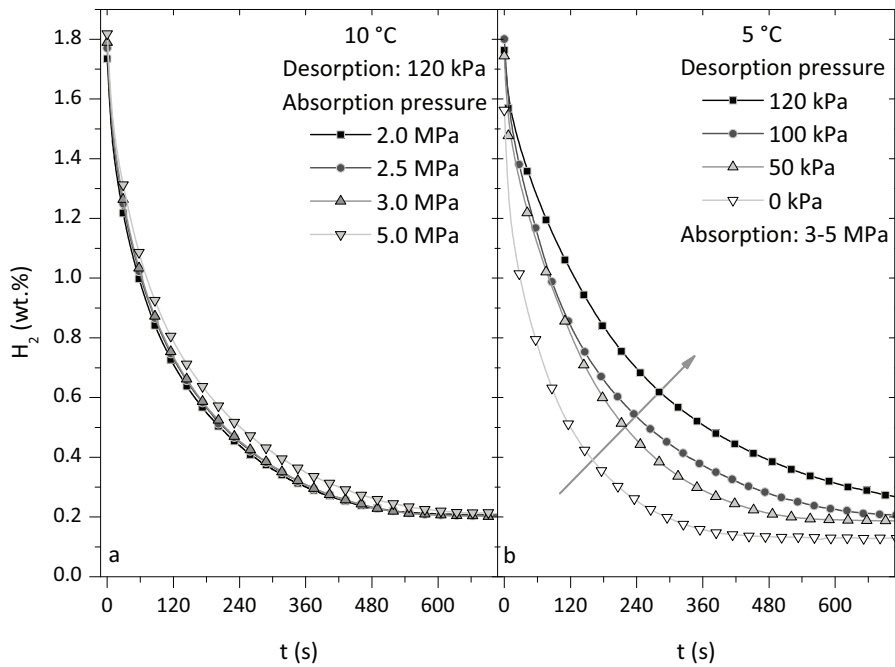


Figure 6.8: Desorption cycles starting at 10 °C and from different pressures (a) at 5 °C and at different pressures (b).

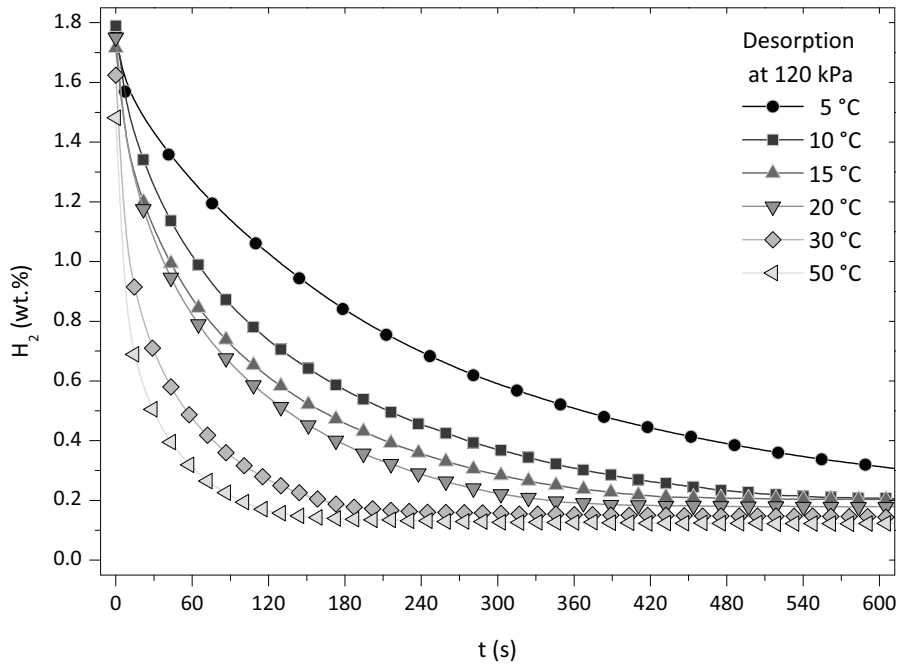


Figure 6.9: Desorption cycles starting at 120 kPa and at different temperatures.

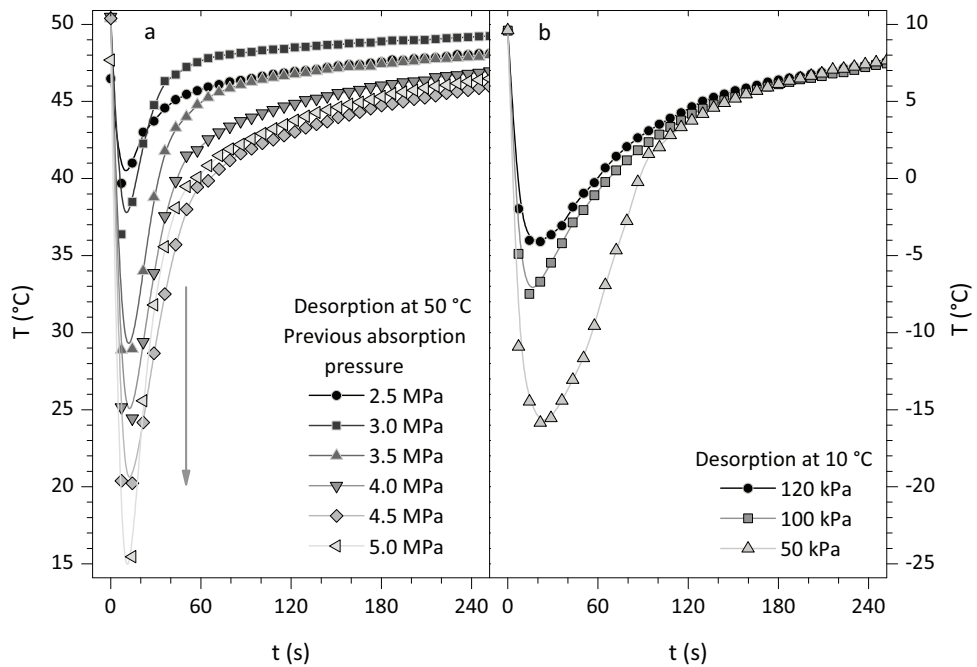


Figure 6.10: Desorption temperature profiles from different pressures at 50 °C (a) and at different pressure and 10 °C (b).

6.3 Storage System Development

6.3.1 Requirements

The initial performances required for the tank are a minimum total released hydrogen volume of 400 Nl in one hour (equivalent to $6.67 \text{ Nl H}_2 \text{ min}^{-1}$), with an initial peak to start-up of $25 \text{ Nl H}_2 \text{ min}^{-1}$ for at least one minute. The available room inside the vehicle is about 48 dm^3 to fit the complete system, including closure and safety valves, connecting pipes, and any additional accessory of the tank. The prototype is not supposed to be equipped with a liquid heat-exchange system, but no particular restraints were imposed regarding the maximum weight. The choice of the Nios light-weight wooden frame (only 18.5 kg), resulted in a total mass of about 400 kg, allowing to consider room temperature hydride, requiring a much simpler set-up, despite of the higher mass of the active material. Moreover, considering the limited range of the prototype and the consequent limited amount of hydrogen required, it is convenient to avoid heavy auxiliary parts.

The mentioned requirements were used to design the tank, in a scaling-up process described in a following section, and in the first set of tests. The task for these *static* tests (measurements with automatic flow control and constant settings) is to evaluate if the minimum requirements for desorption are met by this tank setup and in which conditions this is happening. Furthermore, the settings for the most convenient reloading of the tank will be experimented.

After the first set of tests the feasibility of the fuel cell supply for the Eco Marathon needed to be evaluated. The tank is conceived to be coupled in the vehicle with a fuel cell derived from the commercial Horizon H2000.

This generated new requirements, apart from the unvaried total quantity. During the race there is one acceleration phase per lap at maximum power (2 kW) for approximately 30 sec and 1 kW power is required some more times each lap; a race consists of 7 laps. The above conditions can be summarized as follows:

400 l in 60 min	$= 400 \text{ l h}^{-1}$	$\simeq 6.67 \text{ Nl min}^{-1}$ of average flow
7 laps in 60 min	$= 514 \text{ s}$ each lap	$\simeq 500 \text{ s}$ per cycle
2000 W of power for 30 s	$= 29 \text{ l min}^{-1}$ for 30 s	$\simeq 30 \text{ Nl min}^{-1}$ for 30 s per cycle
1000 W for re-accelerations	$= 15 \text{ l min}^{-1}$ some times a lap	$\simeq 2 \cdot (15 \text{ Nl min}^{-1})$ per cycle

These requirements were used for *dynamic* tests, where flow settings were changed cyclically to simulate the driving performances.

6.3.2 Experimental Set-Up

The stages of preparation of the tank preceding the testing have already been reported in detail in a previous work [22], so they will be briefly described here, stressing the necessary adjustments performed to obtain the best experimental data.

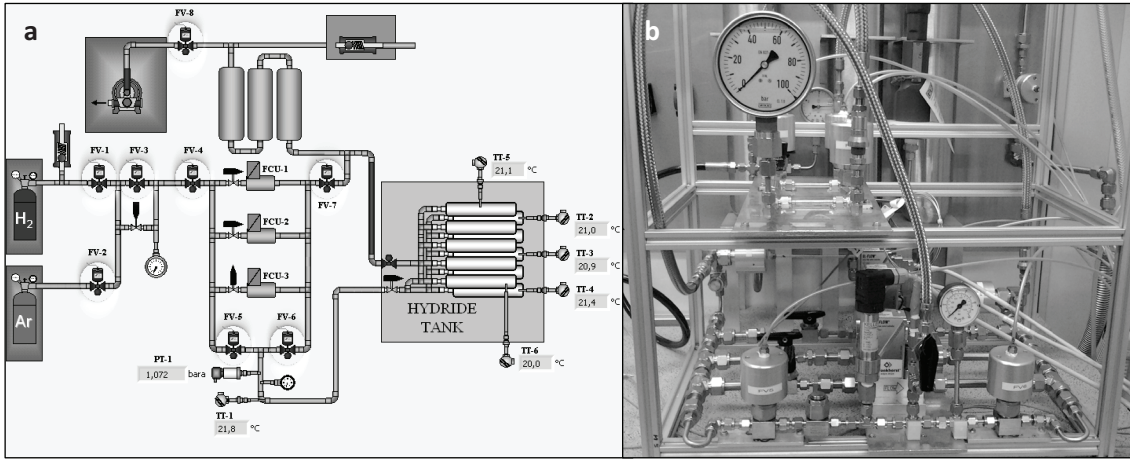


Figure 6.11: Snapshot of the software interface (a), showing schematically the layout, and picture of the test station (b).

6.3.2.1 Test Station

The use of a volumetric apparatus for testing a storage system expected to deliver at least 400 Nl h^{-1} would require a very impractical reference volume. Therefore, a hydrogen tank station was modified and adopted. The set up shown in figure 6.11 allowed the quantitative evaluation of hydrogen a/d process measuring temperature, pressure and gas mass flow. The amount of hydrogen exchanged by the hydride between two different times t_0 and t_1 is calculated from the hydrogen mass (m_{H_2}) balance on the gaseous phase in the tank:

$$\int_{t_0}^{t_1} \dot{m}_{\text{H}_2} dt = \left(V_{\text{g}} \rho_{\text{H}_2}(T, p) \right)_{t_0} + \int_{t_0}^{t_1} \dot{m}_{\text{H}_2} dt - \left(V_{\text{g}} \rho_{\text{H}_2}(T, p) \right)_{t_1} \quad (6.1)$$

where the mass flow \dot{m}_{H_2} is directly derived from the specific one Φ_m (see equation (3.12)), the gas density ρ_{H_2} is calculated by means of the van der Waals equation (1.2) considering T and p of the tank, and the volume of the gaseous phase V_{g} is calculated using an equation derived from (6.1) for the case of Ar, used in the calibration. The first and third terms on the right side of (6.1) correspond to the hydrogen present in gaseous phase at times t_0 and t_1 , respectively. The second one accounts for the total H_2 flown between the corresponding interval [23].

Therefore, the flow control units (Bronkhorst El-Flow series, labelled FCU-1 and FCU-2; a third one was installed but not calibrated) are the fundamental part of the measuring station and have two different operative ranges: $0.1\text{--}10 \text{ Nl min}^{-1}$ and $10\text{--}200 \text{ Nl min}^{-1}$, respectively. The pressure is measured with a Keller piezoresistive transducer (PT-1) and visually monitored with analog manometers. The flowing temperature is measured with an in-line type K thermocouple (TT-1), while the tank is equipped with 5 surface K thermocouples applied in different external positions (TT-2 to TT-6). Eight pneumatic valves (FV) are manually controlled and used to set the station for the desired test mode, considering that the flow measurement is unidirectional. Three safety valves have been installed and one was already after the buffer volume (12 dm^3) to release the excess gas. To go below atmospheric pressure, a rotary vacuum pump is connected after the buffer volume too. All pipes are stainless steel with an internal diameter large enough to avoid pressure drops.

The control of the operations is managed with a LabView based software, that provides safety blocks to prevent hardware damage. Apart from that and an algorithm to adjust the flow when a minimum pressure is reached, the control is completely manual.

6.3.2.2 Powder Activation

The Hydralloy C 5 is received from the supplier in form of flakes, small stones with a size distribution around 15 mm. A mechanical milling process was supposed to be used to improve the hydrogen sorption kinetics of the as received material, but the estimation on the final required quantity made the use of a shaker mill unfeasible. Other kinds of mill were tried in unsuccessful attempts to obtain a fine powder: not applying a high energy technique, all the processes were unable to comminute the samples without an excessive overheating. Even if both planetary and attritor mills were able to manage the desired quantity in acceptable times, they were discarded due to the temperature increase.

Thus, because there was no mechanical way to process the quantity of flakes, the possibility to fill the tank directly with the original sized material was investigated. Some preliminary hydrogen sorption cycles were performed on a small quantity of material in order to cause the *hydrogen decrepitation* phenomenon. In fact, during a/d cycles hydrogen diffuses inside the material causing internal stress and subsequent cracks that cause particle size reduction and specific surface area increase (see section 2.1.1). Hydrogen decrepitation is actually an alternative route, with respect to other mechanical syntheses, to prepare high surface area alloys [24].

The a/d cycles were performed at ambient temperature and between 3 and 0.2 MPa of pressure and the fine powder obtained confirmed the possibility to use the as-received flakes directly. Moreover, the result showed that the accidental contact with air (the supplied batch was contained in a plastic bag inside an unsealed metal can) did not affect the material performances.

6.3.2.3 Preliminary Tests and Tank Design

In order to obtain the necessary information for the subsequent design of the tank, some tests were performed on a 500 cm³ internal volume cylinder, charged with about 1 kg of Hydralloy C 5, previously used for another prototype from Fortis Saxonia, called Sax 3. From the data recorded using that first tank, some conservative hypothesis were assumed in the design process [22]:

1. the hydrogen desorption rate was derived from the average rate obtained on the 500 cm³ Sax 3 tank considering part of the process with a linear behaviour;
2. the final capacity was considered reduced to a value of 1.2 wt.% H₂, even if the measured one was 1.35 wt.% H₂ for the range of pressure from 3 and 0.2 MPa;
3. the active alloy density was assumed closer to the value for the material in flakes;
4. the powder expansion inside the tank during the hydrogenation process was supposed to be 20 %;
5. the maximum filling ratio of the hydrogenated powder, was only the 80 % of the cylinder internal volume.

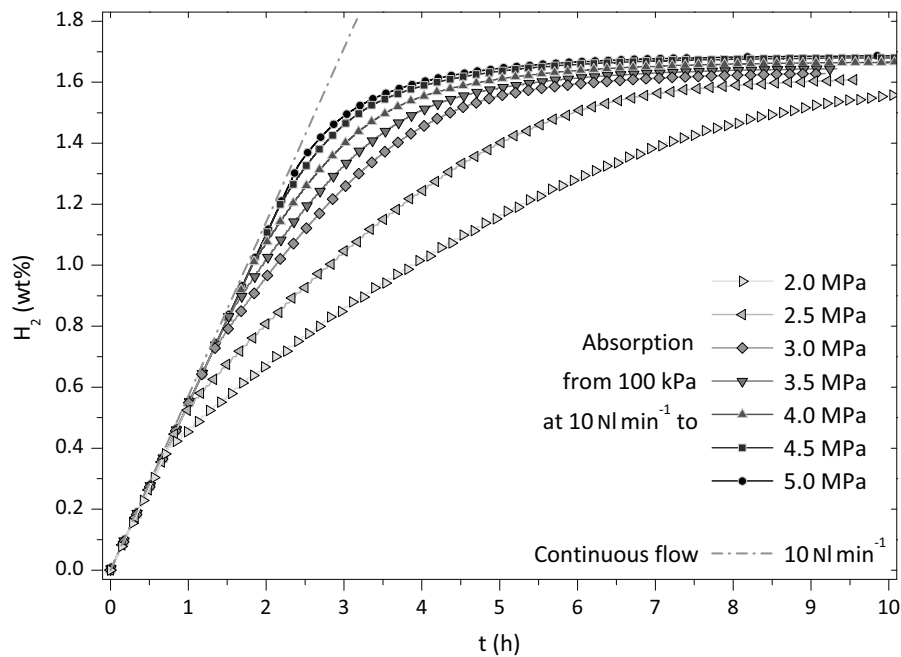


Figure 6.12: Absorption at fixed flow rate, up to different pressures.

Each hypothesis reported above affected the calculation of the tank final volume: the first assumption regarded the total amount of material needed to meet the requirement for H_2 supply rate; the second hypothesis related to the total capacity requirement; all the other points helped adjusting the determined value. The calculation outcomes gave total mass of about 12.6 kg of alloy, with a final available hydrogen volume of more than 1800 NL. Finally, the release kinetics of the alloy, rather than its hydrogen capacity, represented the limiting factor in the scaling up of the system. The resulting tank should have an internal volume of 3700 cm³, compatible with the available space inside the vehicle. In order to optimize the use of the available space commercial Swagelok® pipes and fittings were selected and TPED³ compliant stainless steel cylinders with a 300 cm³ internal volume were chosen to host the material. Intermediate testing, with one and two modules of five cylinders each, showed that the hypothesis were cautiously conservative and the quantity of about 9.5 kg of material⁴, in ten cylinders, was accepted as a starting point for the tests.

6.3.3 Static Tests

The experiments with constant (automated) settings cover different ranges of flow and pressure, both for absorption and desorption, and are organized in such a way that it is possible to compare the influence of one of the parameters at once.

In figure 6.12 it is possible to examine the influence of pressure in the loading (absorp-

³ Acronym for Transportable Pressure Equipment Directive.

⁴ The exact mass of the inserted alloy is 9450.8 g.

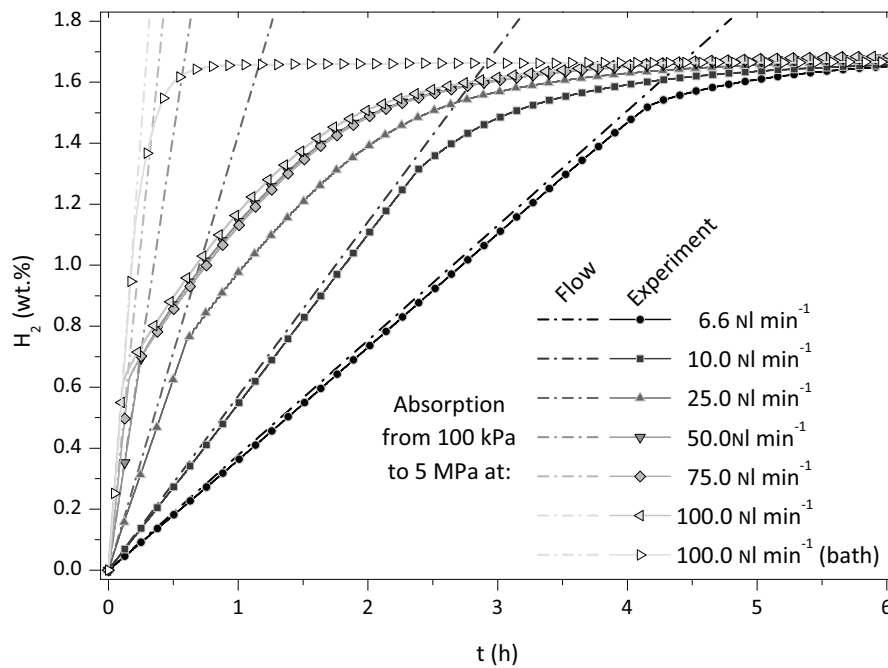


Figure 6.13: Absorption at different flow-rates, with fixed maximum pressure.

tion) step. The hydrogen flow was set at 10 Nl min^{-1} because it is the highest measurable value by the most precise flowmeter FCU-1. The continuous flow is indicated by the dashed line and it is possible to see how all these absorptions follow the ideal flow to a point when the desired pressure is reached; then a slower process occurs, due to the time needed to absorb H_2 in the material. Of course, 5 MPa of pressure is the fastest setting and the more effective in terms of quantity. The final quantity is obviously influenced by the starting pressure: as seen in figure 6.14 after a complete evacuation and starting from 0 kPa the tank can store up to 1.8 wt.% of hydrogen (out of a theoretical capacity of the material of 1.83 wt.% H_2), but considering an outlet pressure of 250 kPa the quantity is reduced to 1.63 wt.%.

Keeping fixed the maximum loading pressure to 5 MPa, it is possible to underline also the effect of the change of flow in the loading operation, as shown in figure 6.13. With a low hydrogen flow ($6.6 \text{ Nl min}^{-1} \approx 400 \text{ Nl h}^{-1}$) almost all the tank is filled up with a constant flow, meaning that the absorption reaction is slow enough to be in equilibrium with the flow until the pressure is reached. On the other hand flows greater than or equal to 50 Nl min^{-1} are very similar in the first segment and in the following curve, too: the pressure is increasing rapidly and the exothermic absorption reaction is increasing the temperature, thus setting the equilibrium pressure to higher values. This effect is avoided if the tank is immersed in a bath of water that buffers the temperature: in this case a satisfactory filling is achieved in less than an hour.

Dealing with the desorption, using a similar approach, leads to results that are apparently very similar one to another, thus reducing the influence of the loading pressure. This is mainly due to the time scale (x axis) in the graph in figure 6.15 a and to the instrumental apparatus settings. It is possible to separate the contribution of the pressurized hydrogen

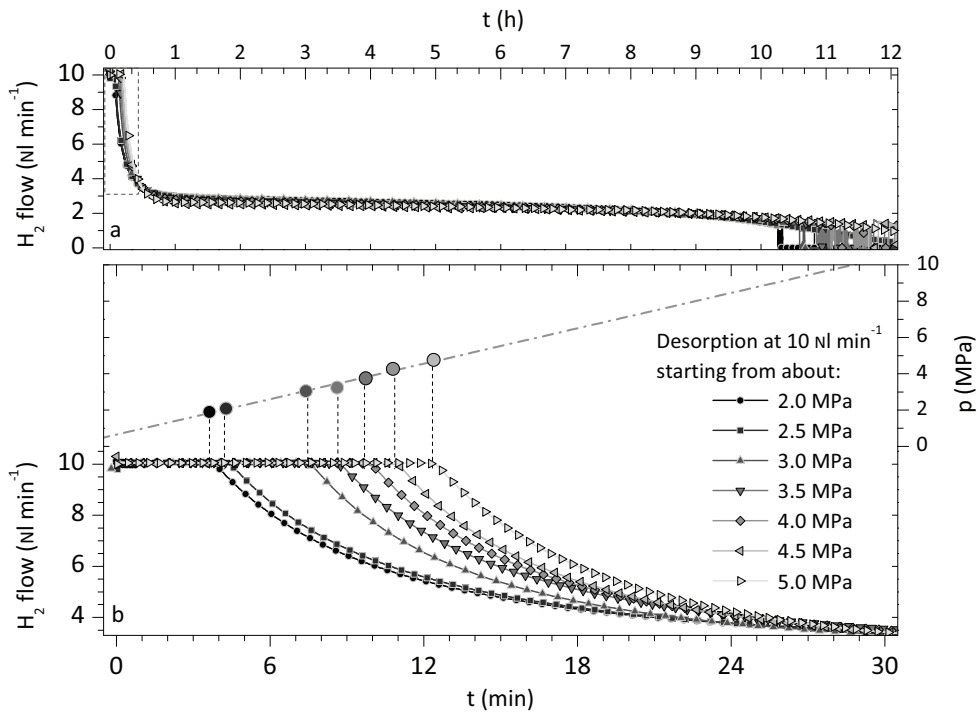


Figure 6.15: Desorption at 10 NL min^{-1} starting from different pressures. Overall process (a) and a detail of the first 30 min (b).

from that of the hydrogen that is released by the Hydralloy C 5 for a longer time and at a quasi-constant flow below 3 NL min^{-1} . In figure 6.15 b a zoom in the previous graph is shown, where it is possible to see the influence of the initial pressure and to make a rough evaluation of the possible effects of higher pressure: even loading the tank with 10 MPa the 10 NL min^{-1} hydrogen flow should not last longer than 30 min.

The curves in figure 6.16 a represent the desorption at 6.6 NL min^{-1} and look very similar to those at 10 NL min^{-1} . Also in this case, from the first part shown in figure 6.16 b it is possible to notice the contribution of the pressure and calculate the effect of higher pressures: 10 MPa would last for almost 1 h. The unsatisfactory behaviour of the tank in this flow regimes is mainly due to a hardware limit of the instruments: the flowmeter FCU-1 is more precise in the lower values, but most probably the section of the internal pipe limits the flow to a value according to the pressure. This is well evidenced considering the flow change with pressure: 10 NL min^{-1} flow requires more than 1.25 MPa left in the tank and for 6.6 NL min^{-1} about 0.83 MPa are needed; lower pressures will deliver insufficient gas flows.

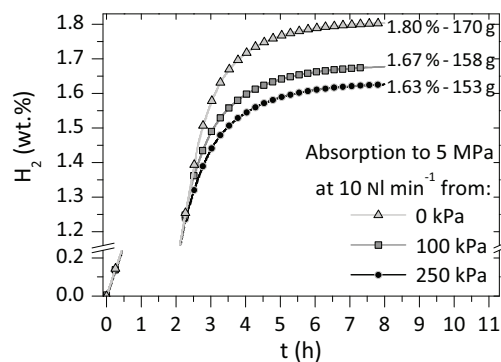


Figure 6.14: Absorption at fixed flow-rate and final pressure, starting from different values.

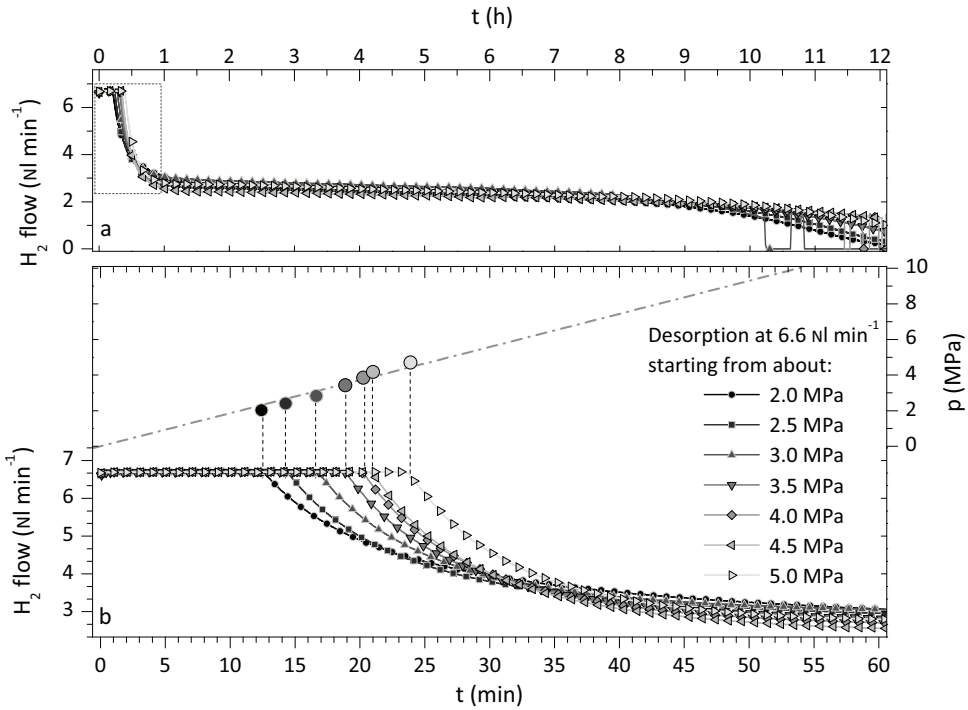


Figure 6.16: Desorption at 6.6 NL min⁻¹ starting from different pressures. Overall process (a) and a detail of the first 60 min (b).

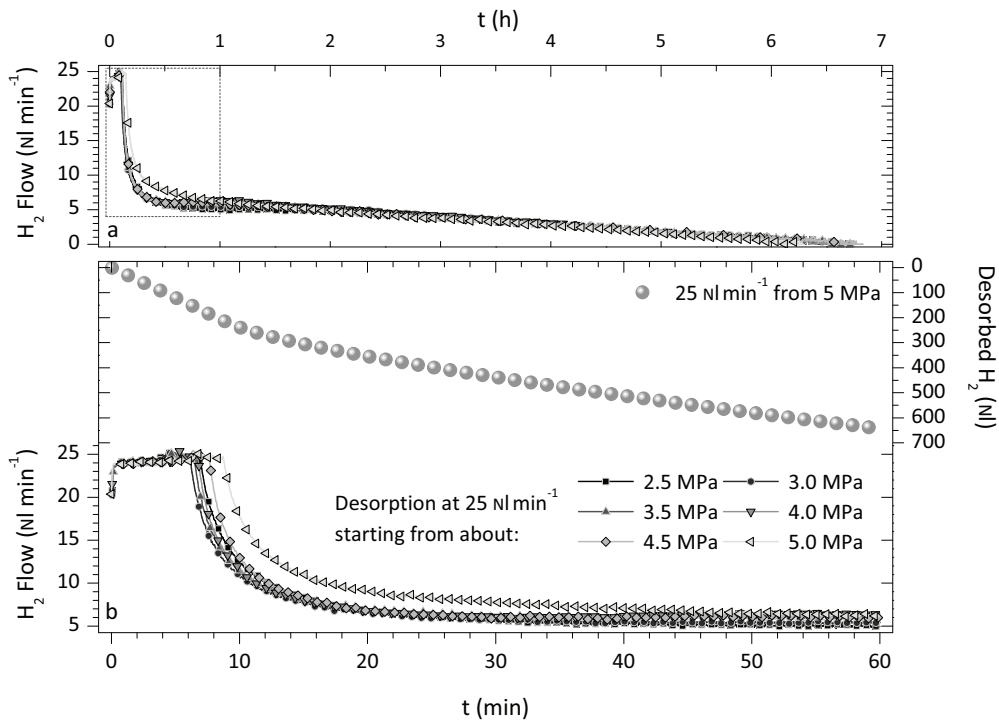


Figure 6.17: Desorption at 25 NL min⁻¹ starting from different pressures. Overall process (a) and a detail of the first 60 min (b).

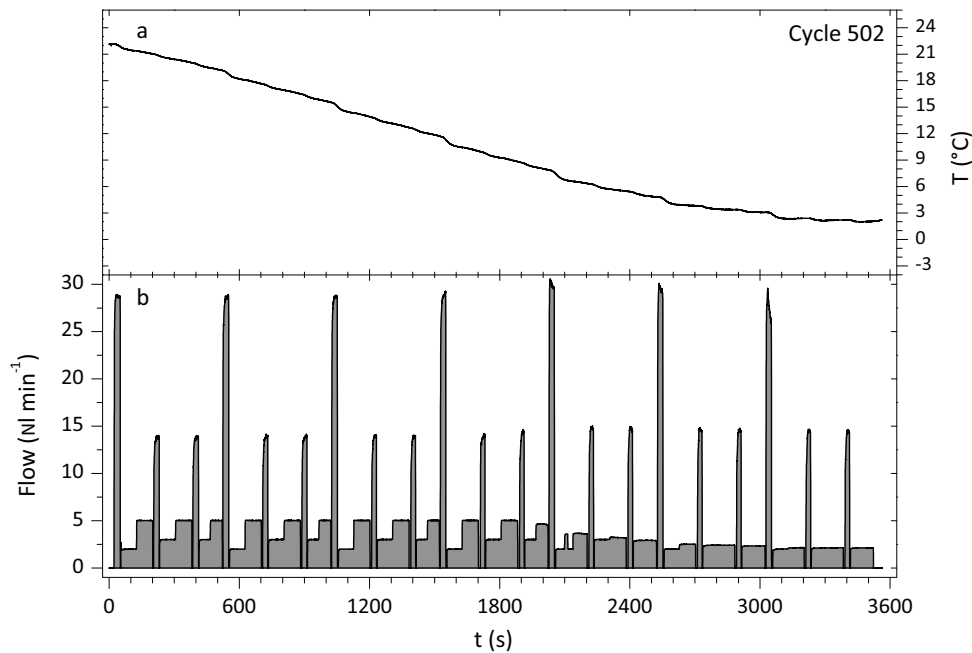


Figure 6.18: Cycle 502 results: average temperature of the tank (a) and hydrogen flow (b).

Desorbing the hydrogen with a flow of 25 Nl min^{-1} and using the bigger flowmeter, a different regime of flow is originated: keeping in mind that the vertical scale is more than doubled, in figure 6.17 a it is easy to see that the hydrogen gas flows much more efficiently than before. The reason for this is explained by the fact that the flowmeter FCU-2 allows higher flows of gas with much smaller Δp . Even if it is possible to have some drawbacks in the loss of accuracy, this setting is more adequate for the test. In fact, in the first hour of operation in figure 6.17 b, it is possible to see that with all the loading pressures, the flow is always higher than 5 Nl min^{-1} . In particular, the measured desorbed quantity with a loading pressure of 5 MPa was higher than 600 Nl.

6.3.4 Dynamic Tests

The second set of requirements mentions the race and the fact that acceleration is needed for every lap, thus setting a new challenging condition for the tank: the 29 Nl min^{-1} flow step must be repeated even when the pressurized hydrogen is over and the tank temperature is lower due to the endothermic desorption reaction. The dynamic tests were designed to match both the requirements and the actual possibilities of the system. Real driving cycles are very demanding and are barely fulfilled by larger tanks [7]. The cycles are labeled 50x, where the first part indicates the duration ($\sim 500 \text{ s}$) and the second part is a progressive number.

The first cycle (501) was designed taking in account all the parameters, the shape of some European standard driving cycles linked to the fact that the fuel cell and DC engine have a fast response to the H_2 flow [25]. The average flow obtained with this cycle was

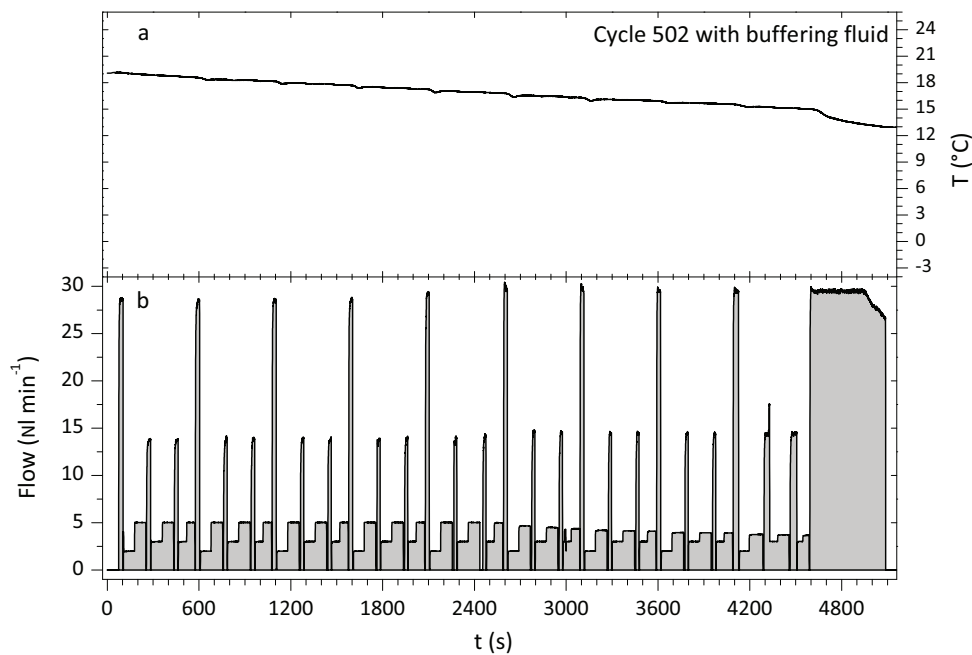


Figure 6.19: Cycle 502 results with a buffering bath: average temperature of the tank (a) and hydrogen flow (b).

satisfactory (6.6 Nl min^{-1} out of designed 8.3 Nl min^{-1}), however the repeatability of the single cycle was very low, due to the several manual operation to follow the designed ramps.

The second cycle (502) was designed trying to take in account the previous errors: there are no ramps and the flow is increasing with easily reproducible steps. The flow was exactly calculated to give the target result. With that trial it was possible to learn that there is some delay in the flowmeter response, due to the pipe opening; this can be noticed in figure 6.18 b, when switching from one flowmeter to the other, because some 0-flow gaps occur. The repeatability was good: the cycles were performed in two different sets (here just one is displayed) with extremely similar results. The average H_2 flow (5.3 Nl min^{-1}) was unsatisfactory, in fact starting with the 5th cycle the pressure gradient was not enough for the steps in FCU-1. The temperature played a fundamental role (figure 6.18 a), in fact the average value dropped below 3°C . The previous unsuccessful trials motivated the use of a water bath to buffer the lowering temperature; the results of this modification are shown in figure 6.19. With this setting there were almost no losses using FCU-1 and, after 9 continuous cycles, the temperature was still above 12°C and it was possible to release more than 200 Nl H_2 in 500 s using FCU-2. Therefore, if the average flow was lower than the target (5.6 Nl min^{-1}), it is because of hardware delays and the real flow slightly lower than the desired one: the design of the experiment was not suitable to make the tank meet the requirements.

To improve the performances on this kind of step-increased cycles, higher flow was lasting longer in this new cycle design (503) and thus the average designed flow is 8.3 Nl min^{-1} (the same of cycle 501, that was actually giving positive, but irregular results). Even if this

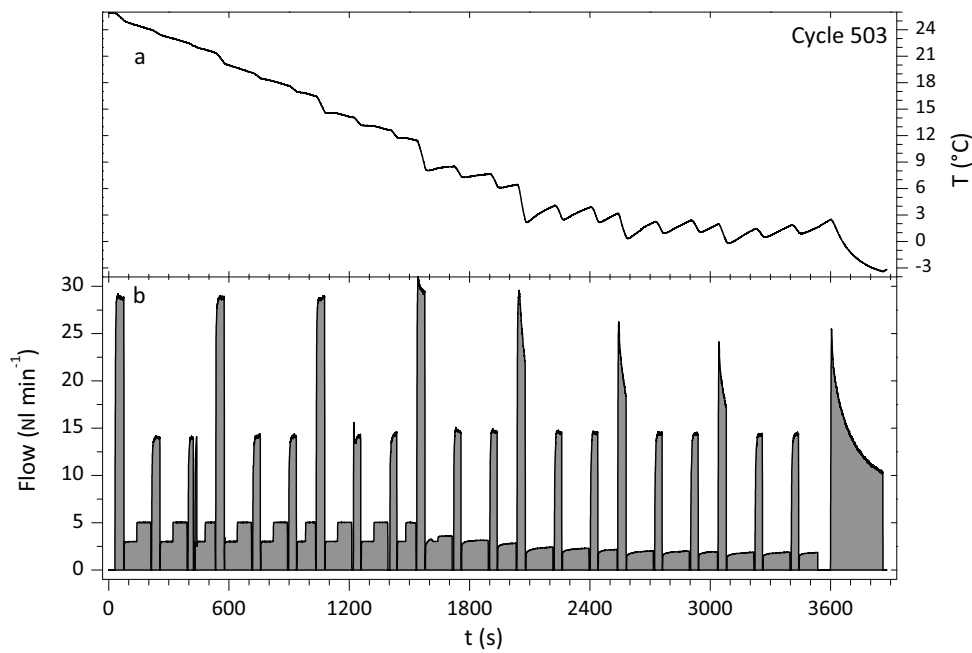


Figure 6.20: Cycle 503 results: average temperature of the tank (a) and hydrogen flow (b).

test was suffering some losses both in high and low flows, the average flow was higher and approaching the desired results (figure 6.20 b). In this case the design of the experiment was suitable, but the response of the tank was not fully satisfactory, due to temperature-related issues. In figure 6.20 a it is possible to notice how every flow peak corresponds to a heat loss for a final temperature below -3°C . Hence, the water bath was used once again with good results: the requirements for 7 laps were fulfilled and after 8 cycles the systems still made available an interesting amount of H_2 at 29 Nl min^{-1} . Of course the water bath is not suitable for a vehicular application, due to the extra weight of the liquid. Instead of using an unpractical liquid bath, two small fans were applied to the tank in the last cycle, for a total power consumption of 40 W. In figure 6.21 b, it is possible to see how the system was fulfilling the requirements as in the previous case, with an average flow of 6.9 Nl min^{-1} , but this time the extra release was less effective and there was a drop in the minimum flow. The temperature was not buffered as in figure 6.19 a, in fact the heat losses are still noticeable in figure 6.21 a and the final temperature is not negative. Anyway, it did not represent a problem for the completion of the task.

Other arrangements were tried: the graph in figure 6.22 summarizes most of the dynamic tests performed on the tank. It plots the average flow on y -axis versus the cycle number on x -axis; as references, the first item on the x -axis is the design value and the last is the average value of the considered set of cycles. It is possible to see how all the experiments experienced a loss between the design value and the first cycle (where pressurized hydrogen is still 100%): therefore the 502 type, with a design value of $6.7 \text{ Nl H}_2 \text{ min}^{-1}$, could never fulfill the requirements. It is also clear that, after the pressurized hydrogen is over, most of the experiments evidences a drop of flow; this is not very intense in 502 and 503 type, but is much more severe in 504. The exception to this phenomenon are the cycles with a

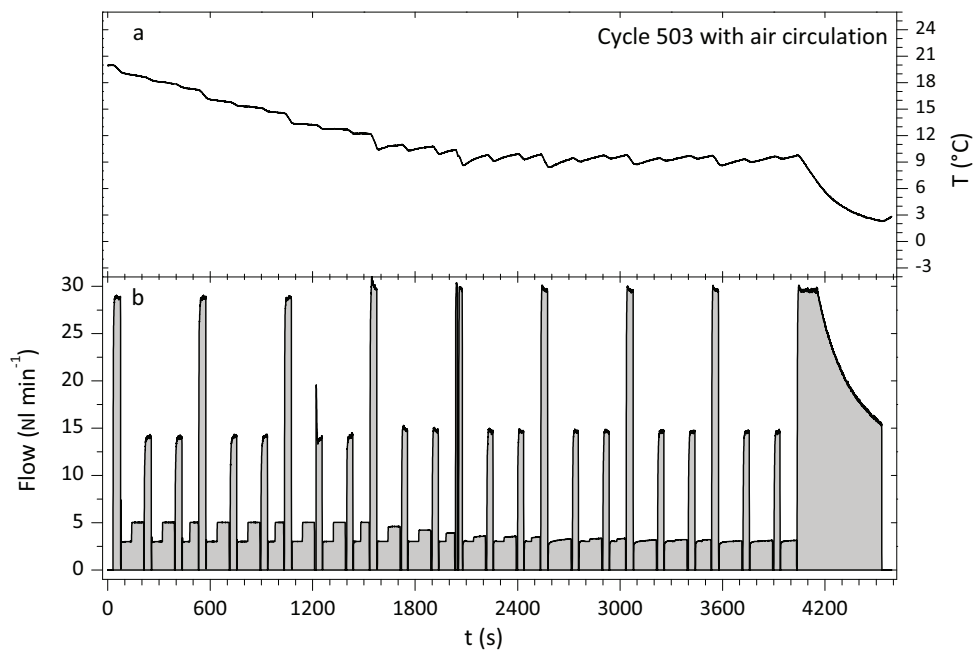


Figure 6.21: Cycle 503 results with air circulation: average temperature of the tank (a) and hydrogen flow (b).

thermal improvement in the settings, for which the decrease in the flow is minimum.

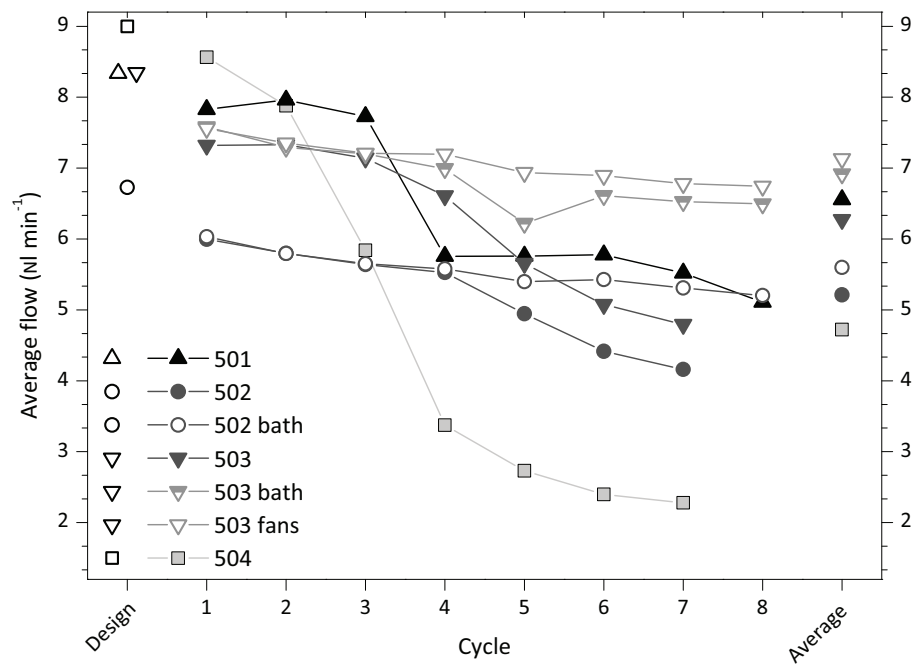


Figure 6.22: Cycles results summary: designed and average values are reported, too.

6.4 Conclusions

This chapter dealt with the development and testing of a room temperature hydride tank. The chosen material, the commercial Hydralloy C 5, was also characterized in laboratory scale, in order to obtain important information about its behaviour. This measurements evidenced the possibility to use the material in a suitable range of temperature, even considering the effects of endothermic and exothermic reactions occurring during cycling. The tank design was also briefly outlined, too, on the basis of the requirements for the vehicular application.

The tank setup with 10 cylinder is already fulfilling the general requirements, in fact in figure 6.17 it is evident that more than 600 Nl of hydrogen can be released in an hour, with a 25 Nl min^{-1} initial hydrogen flow which lasts 10 min, in case of 5 MPa loading. Moreover, the maximum loading capacity achieved is 1.80 wt.% H_2 (the theoretical one is 1.83 wt.%), with 1.65 wt.% H_2 released at a pressure above the fuel cell requirements. In absolute terms, the useful hydrogen stored is about 155 g or $> 1700 \text{ Nl}$; considering the bulk density of Hydralloy C 5 ($\approx 6.3 \text{ g cm}^{-3}$), the volumetric hydrogen capacity of the alloy resulted to be 115 g dm^{-3} , similar to that of MgH_2 .

All the results of several static tests are highly reproducible and a complete loading can be achieved in 4 h, that is drastically reduced ($< 1 \text{ h}$) using a fluid bath to buffer the temperature increase. The heat dissipation is evidently a key aspect in the operative conditions, even with continuous regular flows.

The racing requirements were more challenging and the repeated peak flows might have represented a problem for the actual storage system. However, the tank met the

requirements in some of the designed experiments with losses in a low flow regime which were mainly due to the test apparatus. The storage setup is ready to be tested directly on the Nios car, eventually a third line of cylinders can be added later if the on-board tests should be unsuccessful. Considering the energetic content of hydrogen, the first hour of continuous operation delivered about 8.2 MJ ($\simeq 2.3$ kWh), while a dynamic use could provide about 5.2 MJ ($\simeq 1.5$ kWh). In the particular application, the fuel cell efficiency reduces these figures.

In conclusion, in this chapter it was showed how a hydride-tank can be successfully used in a prototypal vehicular application. Of course, there is room for improvements acting on the system and, in minor part, on the material.

The application of a pressure reducer can change and enhance the performances, avoiding the waste of pressurized hydrogen, very useful for acceleration peaks. Following this outlook, the maximum loading pressure can be increased to 10 MPa, thus exploiting the empty volume inside the cylinders and obtaining a system closer to a hybrid one [16]. The waste heat from fuel cell could be profitably used to increase the desorption rate thanks to a small forced ventilation system. The fans used improved the overall performances, consuming just about 2.5% of the total power.

Once again, even if dealing with room temperature hydrides, the thermal management has to be thoroughly designed [26]. The temperatures registered on the steel surface of the wall were not below (or above, in absorption) the equilibrium T for the target pressure, but the core of the hydride bed inside the vessel was presumably unable to continue the reaction efficiently. The process is self-balancing, but a more effective heat flow would avoid detrimental deceleration in the reaction rate. Also with AB_2 materials there are different researches for the improvement of the vessel heat flow with metallic fins [27] or a circulating fluids [28]. Finally, the material could be compacted in form of pellets with the addition of a conductivity-enhancing element: this possibility renewed the interest in Hydralloy C5 and very recent studies are investigating in this direction, even assessing the geometrical stability of pellets with cycling [29, 30].

References

- 1 Yang F.S., Wang G.X., Zhang Z.X., Meng X.Y., Rudolph V., Design of the metal hydride reactors — A review on the key technical issues, *International Journal of Hydrogen Energy*, **35** (2010) 3832–3840. (Cited on page 106)
- 2 Pasini J.M., van Hassel B.A., Mosher D.A., Veenstra M.J., System modeling methodology and analyses for materials-based hydrogen storage, *International Journal of Hydrogen Energy*, **37** (2012) 2874–2884. (Cited on page 106)
- 3 Lozano G.A., Na Ranong C., Bellosta von Colbe J.M., Bormann R., Fieg G., Hapke J., Klassen T., Dornheim M., Empirical kinetic model of sodium alanate reacting system (I). Hydrogen absorption, *International Journal of Hydrogen Energy*, **35** (2010) 6763–6772. (Cited on page 106)
- 4 Lozano G.A., Na Ranong C., Bellosta von Colbe J.M., Bormann R., Fieg G., Hapke J., Klassen T., Dornheim M., Empirical kinetic model of sodium alanate reacting system (II). Hydrogen desorption, *International Journal of Hydrogen Energy*, **35** (2010) 7539–7546. (Cited on page 106)
- 5 Lozano G.A., Bellosta von Colbe J.M., Bormann R., Klassen T., Dornheim M., Enhanced volumetric hydrogen density in sodium alanate by compaction, *Journal of Power Sources*, **196** (2011) 9254–9259. (Cited on page 106)
- 6 Lozano G.A., Na Ranong C., Bellosta von Colbe J.M., Bormann R., Hapke J., Fieg G., Klassen T., Dornheim M., Optimization of hydrogen storage tubular tanks based on light weight hydrides, *International Journal of Hydrogen Energy*, **37** (2012) 2825–2834. (Cited on page 106)
- 7 Johnson T.A., Jorgensen S.W., Dedrick D.E., Performance of a full-scale hydrogen-storage tank based on complex hydrides, *Faraday Discussions*, **151** (2011) 327–352, discussion 385–397. (Cited on pages 106 and 121)
- 8 Utz I., Schmidt N., Wörner A., Hub J.J., Zabara O., Fichtner M., Experimental results of an air-cooled lab-scale H₂ storage tank, *International Journal of Hydrogen Energy*, **36** (2011) 3556–3565. (Cited on page 106)
- 9 Garrier S., Chaise A., de Rango P., Marty Ph., Delhomme B., Fruchart D., Miraglia S., MgH₂ intermediate scale tank tests under various experimental conditions, *International Journal of Hydrogen Energy*, **36** (2011) 9719–9726. (Cited on page 106)
- 10 Guardamagna C., Cavallari A., Malvaldi V., Soricetti S., Pontarollo A., Molinas B., Andreasi D., Lo Russo S., Capurso G., Magistri L., Monteverde M., Nava R., Mazzanti V., Innovative Systems for Hydrogen Storage, *Advances in Science and Technology*, **72** (2010) 176–181. (Cited on page 106)
- 11 Delhomme B., de Rango P., Marty Ph., Bacia M., Zawilski B., Raufast C., Miraglia S., Fruchart D., Large scale magnesium hydride tank coupled with an external heat source, *International Journal of Hydrogen Energy*, **37** (2012) 9103–9111. (Cited on page 106)
- 12 Eberle U., Arnold G., von Helmolt R., Hydrogen storage in metal-hydrogen systems and their derivatives, *Journal of Power Sources*, **154** (2006) 456–460. (Cited on page 106)
- 13 Laurencelle F., Goyette J., Simulation of heat transfer in a metal hydride reactor with aluminium foam, *International Journal of Hydrogen Energy*, **32** (2007) 2957–2964. (Cited on page 106)
- 14 Souahlia A., Dhaou H., Askri F., Sofiene M., Jemni A., Ben Nasrallah S., Experimental and comparative study of metal hydride hydrogen tanks, *International Journal of Hydrogen Energy*, **36** (2011) 12918–12922. (Cited on page 106)
- 15 Töpler J., Feucht K., Results of a Test Fleet with Metal Hydride Motor Cars, *Zeitschrift für Physikalische Chemie*, **164** (1989) 1451–1461. (Cited on page 106)
- 16 Takeichi N., Senoh H., Yokota T., Tsuruta H., Hamada K., Takeshita H. T., Tanaka H., Kiyobayashi T., Takano T., Kuriyama N., “Hybrid hydrogen storage vessel”, a novel high-pressure hydrogen storage vessel combined with hydrogen storage material, *International Journal of Hydrogen Energy*, **28** (2003) 1121–1129. (Cited on pages 106 and 126)
- 17 Mori D., Hirose K., Recent challenges of hydrogen storage technologies for fuel cell vehicles, *International Journal of Hydrogen Energy*, **34** (2009) 4569–4574. (Cited on page 106)
- 18 Hagström M.T., Lund P.D., Vanhanen J.P., Metal hydride hydrogen storage for near-ambient temperature and atmospheric pressure applications, a PDSC study, *International Journal of Hydrogen Energy*, **20** (1995) 897–909. (Cited on page 107)

- 19 Hagström M.T., Vanhanen J.P., Lund P.D., AB₂ metal hydrides for high-pressure and narrow temperature interval applications, *Journal of Alloys and Compounds*, **269** (1998) 288–293. (Cited on page 107)
- 20 Vanhanen J.P., Lund P.D., Hagström M.T., Feasibility study of a metal hydride hydrogen store for a self-sufficient solar hydrogen energy system, *International Journal of Hydrogen Energy*, **21** (1996) 213–221. (Cited on page 107)
- 21 Skripnyuk V.M., Ron M., Hydrogen desorption kinetics in intermetallic compounds C2, C5₁ and C5₂ with Laves phase structure, *International Journal of Hydrogen Energy*, **28** (2003) 303–309. (Cited on pages 107, 108, and 110)
- 22 Schiavo B., *Solid state hydrogen storage: a study on different materials and development of an applicative system*, (2012) PhD thesis, Università degli Studi di Palermo. (Cited on pages 114 and 116)
- 23 Lozano Martinez G.A., *Development of Hydrogen Storage Systems using Sodium Alanate*, (2010) PhD thesis, Helmholtz-Zentrum Geesthacht, Zentrum für Material- und Küstenforschung GmbH. (Cited on page 115)
- 24 Kianvash A., Harris I.R., Hydrogen decrepitation as a method of powder preparation of a 2:17-type, Sm(Co, Cu, Fe, Zr)_{8.92} magnetic alloy, *Journal of Material Science*, **20** (1985) 682–688. (Cited on page 116)
- 25 Maxoulis C.N., Tsinoglou D.N., Koltsakis G.C., Modeling of automotive fuel cell operation in driving cycles, *Energy Conversion and Management*, **45** (2004) 559–573. (Cited on page 121)
- 26 Melnichuk M., Silin N., Guidelines for thermal management design of hydride containers, *International Journal of Hydrogen Energy*, **37** (2012) 18080–18094. (Cited on page 126)
- 27 Oi T., Maki K., Sakaki Y., Heat transfer characteristics of the metal hydride vessel based on the plate-fin type heat exchanger, *Journal of Power Sources*, **125** (2004) 52–61. (Cited on page 126)
- 28 Visaria M., Mudawar I., Coiled-tube heat exchanger for high-pressure metal hydride hydrogen storage systems — part 1. Experimental study, *International Journal of Heat and Mass Transfer*, **55** (2012) 1782–1795. (Cited on page 126)
- 29 Pohlmann C., Röntzsch L., Weißgärber T., Kieback B., Heat and gas transport properties in pelletized hydride-graphite-composites for hydrogen storage applications, *International Journal of Hydrogen Energy*, **38** (2013) 1685–1691. (Cited on page 126)
- 30 Pohlmann C., Röntzsch L., Heubner F., Weißgärber T., Kieback B., Solid-state hydrogen storage in Hydralloy-graphite composites, *Journal of Power Sources*, **231** (2013) 97–105. (Cited on page 126)

7 Chapter 7

Final Remarks

Abstract. This last short chapter contains the final remarks, summarizing the outcomes obtained during the experimental work and trying to draw a conclusion from the suggestions coming from those results.

The research described in this thesis was focused on the development of suitable materials for solid state hydrogen storage. The storage represents one of the improvable points to transform the idea of a hydrogen based economy in a possible reality. A sustainable energetic future, as the one described in the utopian book by Rifkin [1], is still far to be accomplished. As today, there are many technological issues that hinder the large diffusion of hydrogen as energy carrier and in particular of solid state hydrogen systems. In most cases the problem is related to the adopted material, to its intrinsic properties or the way the technology is applied. Züttel *et al.* analyzed the volumetric and gravimetric energy density of the most important energy carriers, thus evidencing both the physical limits of hydrogen storage systems, if compared to some classical fuels, and the need for a novel synthetic carrier, which can still exploit hydrogen in a more complex cycle (involving CO₂ sequestration) similar to natural photosynthesis [2].

Nevertheless, there are evidences that the hydrogen solid state storage presents some advantages in comparison to different kinds of electrochemical batteries [2] and also to physical storage of hydrogen, in high pressure cylinders or in cryostats [3]. The current technologies have severe disadvantages (especially in volumetric and safety terms), and the storage of hydrogen in light-weight solids could be the solution.

Keeping in mind the limitations of hydrogen storage, it is still possible to focus efforts and researches to improve the most promising systems.

Among the studied materials, borohydrides are the category with the highest hydrogen content. The drawback in their possible application is represented by the high operative temperatures needed to release hydrogen and the scarce reversibility of the hydrogen a/d process.. The path followed to enhance the desorption behaviour of this class of compounds involves the use of carbonaceous nano-supports, following a highly developing trend in this field [4]. Lithium borohydride infiltrated in modified nanotubes showed a marked decrease in the desorption temperature and it was possible to notice a correlation

between the surface characteristics of the support and the observed improvements. A confirmation came from the use of modified graphite to achieve the same positive effect. In the attempt to enhance their characteristics, this concept was also applied to group II borohydrides, which have been proved reversible [5]. At first, mixtures of magnesium and lithium borohydride were tested and infiltrated in enhanced graphite, effectively proving the effect of the heterogeneous nucleation sites to the decomposition from melted material. In fact, the mixtures have a lower melting point and benefit from the effect of carbonaceous support. Finally, calcium borohydride was accurately infiltrated in activated mesoporous carbon. This support was tailored choosing from different synthesis and taken at its best with specific treatments to maximize pores and surface area. The increased wettability of the support is promoting both lower decomposition temperature and higher reversibility amount.

Moving towards more mature systems, different magnesium based materials were studied. The seek for a novel efficient catalyst found a plausible candidate in a zirconium nickel alloy, which displayed an interesting effect on the milled magnesium hydride powder. The effect of the quantity of such a catalyst was analyzed, to find the optimal combination to enhance the kinetics without decreasing the storable amount of hydrogen. The thermodynamic properties were unaltered by the addition of the transition metal catalyst. Exploiting a metal oxide catalysts, small hydride pellets were tested, too. The purpose of such a compacted system is to avoid further undesired sintering in scaled-up systems. Laboratory scale experiments allowed to focus on the addition of aluminium as a binding agent. All that was required to improve the mechanical resistance of the pellets. The quantity of aluminium was investigated and selected to exploit the metallurgical combination with magnesium. The pellets, conceived to prevent detrimental aggregation in storage vessel, were also tested in an experimental reactor where a number of cycles was performed. The a/d properties of the material in the reactor were quite stable and overheating was avoided.

The thermal management is a central issue in the realization of hydrogen storage tanks, using metal and complex hydrides, because the involved reactions can involve considerable amounts of heat [6]. This challenge was faced also testing a room temperature hydride for a prototypal vehicular application. A modular tank, previously designed and realized according to specific requirements, was tested in static and dynamic conditions. The former set of tests evidenced the correlation between flow-rate, pressure and temperature, providing a starting point for the following procedures. Moreover, the requirements concerning the delivered quantity were met. The latter group of tests followed more challenging requirements, in a simulation of application on the road. Continuous cycles drained the storage system and lowered the temperature, requiring a buffer fluid or forced ventilation to complete the task. The influence of temperature was highlighted in laboratory scale tests, where the exothermic and endothermic reactions of small quantities of material were already causing temperature differences in the order of tens of degrees. Anyway, the tank was able to fulfill the requirements in particular conditions, storing a substantial quantity of energy. None of the studied materials represents a unique answer to the hydrogen storage issue. However, from the most advanced compounds to more mature systems, they were selected trying to satisfy a specific need. In a limited number of application is already possible to use hydride-based technology profitably. To improve this subject, find new fields of application and increase the number of employable materials as well as the basic knowledge, the joint efforts of scientists and engineers are required.

References

- 1 Rifkin J., *The Hydrogen Economy: The Creation of the Worldwide Energy Web and the Redistribution of Power on Earth*, (2003) Penguin Putnam Inc., New York. (Cited on page 129)
- 2 Züttel A., Remhof A., Borgschulte A., Friedrichs O., Hydrogen: the future energy carrier, *Philosophical Transaction of the Royal Society A*, **368** (2010) 3329–3342. (Cited on page 129)
- 3 Jepsen J., Bellosta von Colbe J.M, Klassen T., Dornheim M., Economic potential of complex hydrides compared to conventional hydrogen storage systems, *International Journal of Hydrogen Energy*, **37** (2012) 4204–4214. (Cited on page 129)
- 4 Vajo J.J., Influence of nano-confinement on the thermodynamics and dehydrogenation kinetics of metal hydrides, *Current Opinion in Solid State and Materials Science*, **15** (2011) 52–61. (Cited on page 129)
- 5 Rönnebro E., Development of group II borohydrides as hydrogen storage materials, *Current Opinion in Solid State and Materials Science*, **15** (2011) 44–51. (Cited on page 130)
- 6 Jorgensen S.W., Hydrogen storage tanks for vehicles: Recent progress and current status, *Current Opinion in Solid State and Materials Science*, **15** (2011) 39–43. (Cited on page 130)

Nomenclature

a/d	absorption/desorption
BET	Brunauer-Emmett-Teller
BJH	Barrett, Joyner, Halenda
BSE	Backscattered Electrons
DFT	Density Functional Theory
DR	Dubinin-Radushkevich
DSC	Differential Scanning Calorimetry
EDX	Energy Dispersive X-ray spectroscopy
GRC	Gas Reaction Controller
HZG	Helmoltz-Zentrum Geesthacht
MC	Mesoporous Carbon
MS	Mass Spectrometry
MTBE	Methyl Tert-Butyl Ether
MWCNTs	Multi-Walled Carbon Nanotubes
PCI	Pressure-Composition Isotherm
PEM	Proton Exchange Membrane or, equivalently, Polymer Electrolyte Membrane
PSD	Pore Size Distribution
SE	Secondary Electrons
SEM	Scanning Electron Microscopy
SF	Saito-Foley
SSA	Specific Surface Area
TDS	Thermal Desorption Spectroscopy
TPA	Temperature Programmed Absorption
TPD	Temperature Programmed Desorption
TPED	Transportable Pressure Equipment Directive
XRD	X-Ray Diffraction

Curriculum Vitæ

Giovanni Capurso was born in Venice (Italy) on 25 April 1984.

Education

- **Ph. D.** Materials Science and Engineering
January 2010–December 2012
University of Padova, Padova, Italy
Thesis title: *Innovative Materials and Systems for Solid State Hydrogen Storage*
Advisors: Prof. Amedeo Maddalena and Prof. Giovanni Principi
- Visiting Ph. D. Student
September 2011–February 2012
Helmholtz-Zentrum Geesthacht, Geesthacht, Germany
Project title: *Static and dynamic performance tests on room temperature hydride tank.*
Advisor: Dr. Martin Dornheim.
- **M. S.** Materials Science and Engineering
110/110 cum laude
October 2006–April 2009
University of Padova, Padova, Italy
Thesis title: *Development of an experimental system for solid state hydrogen storage.*
- Education Abroad Program
September 2006–June 2007
University of California, Los Angeles UCLA
Los Angeles, CA, U.S.A.
- **B. S.** Materials Engineering
110/110 cum laude
October 2003–July 2006
University of Padova, Padova, Italy
Thesis title: *Hygroscopic characterization of epoxy matrix composite materials for ALMA radio-telescope.*

List of Publications

- Agresti F., Khandelwal A., Capurso G., Lo Russo S., Maddalena A., Principi G., Improvement of dehydrogenation kinetics of LiBH_4 dispersed on modified multi-walled carbon nanotubes, *Nanotechnology*, **21** (2010) 065 707.
- Khandelwal A., Agresti F., Capurso G., Lo Russo S., Maddalena A., Gialanella S., Principi G., Pellets of MgH_2 -based composites as practical material for solid state hydrogen storage, *International Journal of Hydrogen Energy*, **35** (2010) 3565–3571.

- Guardamagna C., Cavallari A., Malvaldi V., Soricetti S., Pontarollo A., Molinas B., Andreasi D., Lo Russo S., Capurso G., Magistri L., Monteverde M., Nava R., Mazzanti V., Innovative Systems for Hydrogen Storage, *Advances in Science and Technology*, **72** (2010) 176–181.
- Schiavo B., Girella A., Agresti F., Capurso G., Milanese C., Ball-milling and AlB_2 addition effects on the hydrogen sorption properties of the $\text{CaH}_2+\text{MgB}_2$ system, *Journal of Alloys and Compounds*, **509** (2011) S714–S718.
- Capurso G., Agresti F., Lo Russo S., Maddalena A., Principi G., Cavallari A., Guardamagna C., Performance tests of a small hydrogen reactor based on Mg–Al pellets, *Journal of Alloys and Compounds*, **509** (2011) S646–S649.
- Pighin S.A., Capurso G., Lo Russo S., Peretti H.A., Hydrogen sorption kinetics of magnesium hydride enhanced by the addition of $\text{Zr}_8\text{Ni}_{21}$ alloy, *Journal of Alloys and Compounds*, **530** (2012) 111–115.
- Capurso G., Agresti F., Crociani L., Rossetto G., Schiavo B., Maddalena A., Lo Russo S., Principi G., Nanoconfined mixed Li and Mg borohydrides as materials for solid state hydrogen storage, *International Journal of Hydrogen Energy*, **37** (2012) 10 768–10 773.
- Comănescu C., Capurso G., Maddalena A., Nanoconfinement in activated mesoporous carbon of calcium borohydride for improved reversible hydrogen storage, *Nanotechnology*, **23** (2012) 385 401.
- Capurso G., Naik M., Lo Russo S., Maddalena A., Saccone A., Gastaldo F., De Negri S., Study on La–Mg Based Ternary System for Hydrogen Storage, *Journal of Alloys and Compounds*, submitted (2013).

Presentations at Scientific Meetings

- 4th Symposium Hydrogen and Energy — January 2010, Wildhaus, Switzerland.
 - *Pellets of MgH_2 -based composites as practical material for solid state hydrogen storage* Khandelwal A., Agresti F., Capurso G., Lo Russo S., Maddalena A., Gialanella S., Principi G.
 - *Improvement of dehydrogenation kinetics of LiBH_4 dispersed on modified MWCNTs* Agresti F., Khandelwal A., Capurso G., Lo Russo S., Maddalena A., Principi G., (poster presentation).
- 18th World Hydrogen Energy Conference 2010 — May 2010, Essen, Germany.
 - *Pellets of MgH_2 -based composites as practical material for solid state hydrogen storage* Khandelwal A., Agresti F., Capurso G., Lo Russo S., Maddalena A., Gialanella S., Principi G.
- International Symposium on Metal-Hydrogen Systems, MH 2010 — July 2010, Moscow, Russia.
 - *Performance tests of a small hydrogen reactor based on Mg–Al pellets* Capurso G., Agresti F., Lo Russo S., Maddalena A., Principi G., Cavallari A., Guardamagna C., (poster presentation).

- Faraday Discussion 151: Hydrogen Storage Materials — April 2011, Didcot, U.K.
 - *Dehydrogenation behaviour of mixed borohydrides dispersed on high specific surface area carbons*
Capurso G., Agresti F., Crociani L., Rossetto G., Schiavo B., Maddalena A., Lo Russo S., Principi G., (poster presentation).
- Hydrogen-Metal Systems Gordon Research Conference — July 2011, Easton MA, U.S.A.
 - *Dehydrogenation and reversibility behavior of light metal borohydrides supported by high SSA carbons*
Capurso G., Comănescu C., Maddalena A., Lo Russo S., Principi G., (poster presentation).
- 4th World Hydrogen Technologies Convention 2011 — September 2011, Glasgow, U.K.
 - *Nanoconfined mixed Li and Mg borohydrides as materials for solid state hydrogen storage*
Capurso G., Agresti F., Crociani L., Rossetto G., Schiavo B., Maddalena A., Lo Russo S., Principi G.
 - *Reversible hydrogen storage in calcium borohydride supported on mesoporous carbon*
Comănescu C., Capurso G., Maddalena A.
 - *Hydrogen sorption kinetics of magnesium hydride enhanced by the addition of Zr_8Ni_{21} alloy*
Pighin S.A., Capurso G., Lo Russo S., Peretti H.A., (poster presentation).
- International Symposium on Metal-Hydrogen Systems, MH2012 — October 2012, Kyoto, Japan.
 - *Study on La–Mg Based Ternary System for Hydrogen Storage*
Capurso G., Naik M., Lo Russo S., Maddalena A., Saccone A., Gastaldo F., De Negri S., (poster presentation).
- 34° Convegno Nazionale AIM — November 2012, Trento, Italy.
 - *Leghe di Mg per lo stoccaggio di idrogeno in stato solido,*
Saccone A., Gastaldo F., De Negri S., Naik M., Capurso G., Lo Russo S., Maddalena A., Principi G.

Acknowledgments

My most sincere gratitude goes to Prof. Giovanni Principi for his patient and meticulous assistance and his ever-present guidance in these years; I am deeply grateful to Prof. Amedeo Maddalena for his valuable advices and helpfulness and to Prof. Sergio Lo Russo for his continuous support and encouragement. Many thanks also to Filippo Agresti and Ashish Khandelwal for introducing me to the laboratory, when I was not yet planning to start my Ph.D. studies. All members of the research group gave me important basic knowledge, continuous help and also the curiosity to proceed with my work.

Of course, an important role was played by visiting scientists and students like Santiago Pighin, Cezar Comănescu and, just recently, Mehraj-ud-din Naik and Pukazh Selvan Dharmakkon. I would like to thank Benedetto Schiavo for our long-distance collaboration and for the great job designing the tank and Chiara Milanese for her kindness and help. Nicolò Campagnol did a very good job on our samples while visiting Joint Research Centre in Petten, so I must thank also Renato Campesi and Francesco Dolci for being very patient, too.

I am grateful to Andrea Cavallari and Cristina Guardamagna for allowing the use of their test station and collaborating in different projects. Prof. Adriana Saccone provided many metallurgical samples and very thoughtful advices. Thanks also to Katya Brunelli for SEM pictures.

My acknowledgment goes also to Martin Dornheim and Thomas Klassen for the opportunity to spend a very useful and profitable period in their institute in Geesthacht. I had the chance to go to HZG thank to Gustavo Lozano and working on the tank was great because of him, José Bellosta von Colbe and Julian Jepsen. I would like to thank also Claudio, Christian, Oliver, Klaus, Nina and Fahim.

Finally, I truly appreciated the friendly and motivating environment in the department, I owe this to my colleagues in the department: Giulio and Marta since the first year of engineering, Marco, Giovanni, Enrico, Laura, Erika, Mauro, Gioia, Michela, Jlenia and Alex. Mauro deserves a particular thank, too.

My parents deserve an important place on this list, for supporting and loving me unconditionally: for this reason I dedicated these pages to them.